

# Development of Oxidatively Stable Battery Materials

Solid-State and Diffusional Nuclear  
Magnetic Resonance Investigations of  
Oxidatively Stable Materials  
for Sodium Batteries

Christopher J. Franko

A Thesis Submitted to the School of Graduate Studies in Partial  
Fulfilment of the Requirements for the Degree Doctor of Philosophy

McMaster University, Hamilton, Ontario

Doctor of Philosophy (2022) Chemistry and Chemical Biology

Title: Solid-State and Diffusional Nuclear Magnetic Resonance Investigations of  
Oxidatively Stable Materials for Sodium Batteries

Author: Christopher J. Franko, B.Sc (McMaster University)

Supervisor: Professor Gillian R. Goward

Number of Pages: (xxv, 262)

## Lay Abstract

The continued development of rechargeable batteries is paramount in reducing the world's reliance on fossil fuels, as they allow for the storage of electrical energy produced by renewable sources. This work primarily examines sodium-based batteries systems, such as the sodium-oxygen battery (NaOB) and sodium-ion battery (SIB), which are possible alternatives to the currently used lithium-ion battery (LIB) system.

In order to produce energy, NaOBs produce sodium superoxide ( $\text{NaO}_2$ ) during the discharge process, which is formed on the carbon cathode. However,  $\text{NaO}_2$  is inherently unstable to carbon materials, causing degradation of the battery overtime.  $\text{Ti}_4\text{O}_7$  is investigated as a stable coating material in NaOBs, used to coat the carbon cathode to make the system more stable to  $\text{NaO}_2$  degradation. The degradation processes in NaOBs are characterized by solid state nuclear magnetic resonance (ssNMR) spectroscopy, which uses strong superconducting magnets to probe the magnetic properties of, and consequently identify, the chemical species formed within the battery. It is found that the addition of the  $\text{Ti}_4\text{O}_7$  coating inhibits  $\text{NaO}_2$  degradation, producing longer lifetime NaOBs.

Subsequently, both Li-bis(trifluoromethanesulfonyl)imide (LiTFSI), and NaTFSI, in adiponitrile (ADN) electrolytes are examined for their use in LIBs and SIBs, respectively. Electrolytes facilitate stable ion transport within the cell, and ADN electrolytes specifically allow for the use of higher voltage cathode materials, which can result in a higher energy density battery. The transport properties of LiTFSI in ADN electrolytes are studied by a pulsed-field gradient (PFG) NMR technique, that

allows for the measurement of the rate of ion transport in the electrolyte. It is found that the mechanism of ion transport significantly depends on electrolyte concentration, which suggests significant changes to the electrolyte solution structure at high concentration.

The electrochemical ramifications of this are studied for the NaTFSI in ADN electrolyte in SIBs. It is found that the electrolyte becomes substantially more stable at high concentrations, leading to more favourable charging and discharging behaviours when tested in SIBs.

The work presented in this thesis illustrates the development of more stable, longer lifetime, batteries over a number of cell chemistries, using a variety of NMR and electrochemical characterization techniques.

## Abstract

This thesis focuses on the development of oxidatively stable cathode and electrolyte materials for sodium-based battery systems. This is primarily achieved through the use of solid-state nuclear magnetic resonance (ssNMR) and pulsed-field gradient (PFG) NMR spectroscopy.

ssNMR is used to diagnose the primary failure mode of the NaOB. It is found through a combined  $^{23}\text{Na}$  and  $^{19}\text{F}$  study that the main discharge product of the cell,  $\text{NaO}_2$ , oxidizes both the carbon and polyvinylidene fluoride (PVDF) binder of the cathode to produce parasitic  $\text{Na}_2\text{CO}_3$  and  $\text{NaF}$ . In a subsequent study,  $\text{Ti}_4\text{O}_7$ -coated carbon paper cathodes are implemented in an attempt to stabilize  $\text{NaO}_2$ . The  $^{23}\text{Na}$  triple quantum magic angle spinning (3QMAS) and  $^1\text{H}$  to  $^{23}\text{Na}$  dipolar heteronuclear multiple quantum correlation ( $^{23}\text{Na}\{^1\text{H}\}$  D-HMQC) experiments are used to diagnose the failure modes of carbon-coated, and  $\text{Ti}_4\text{O}_7$ -coated cathodes. It is found that electrochemically formed  $\text{NaO}_2$  is significantly more stable in  $\text{Ti}_4\text{O}_7$ -coated cathodes, leading to longer lifetime NaOBs.

Oxidatively stable electrolyte materials are also examined. Lithium and sodium bis(trifluoromethanesulfonyl)imide (TFSI) in adiponitrile (ADN) electrolytes exhibit extreme oxidative resistance, but are unusable in modern cells due to Al corrosion by TFSI, and spontaneous ADN degradation by Li and Na metal. PFG NMR is used to investigate the transport properties of LiTFSI in ADN as a function of LiTFSI concentration. By measuring the diffusion coefficient of  $\text{Li}^+$  and TFSI as a function of diffusion time ( $\Delta$ ), diffusional behaviour is encoded as a function of length scale to study the short- and long-range solution structure of the electrolyte. It is found that at

high concentrations, LiTFSI in ADN transports  $\text{Li}^+$  primarily through an ion-hopping mechanism, in contrast to the typical vehicular mechanism observed at low concentrations. This suggests significant structural changes in solution at high concentrations.

The NaTFSI in ADN analogue is examined for its electrochemical properties in Na-ion and Na- $\text{O}_2$  batteries. It is found that the oxidative resistance of ADN to Na metal is significantly increased at high concentrations, leading to reversible Na deposition and dissolution in cyclic voltammetry (CV) experiments. Linear sweep voltammetry (LSV) and chronoamperometry (CA) experiments on Al current collectors show that Al corrosion by TFSI is similarly suppressed at high concentration. This culminates in high concentration NaTFSI in ADN being able to reversibly intercalate  $\text{Na}_3\text{V}_2(\text{PO}_4)_2\text{F}_3$  (NVPF) cathodes in SIB half-cells for multiple cycles.

The knowledge gained from exploring oxidatively stable cathode and electrolyte materials can be used in tandem for the development of a longer lifetime, more oxidatively stable, NaOB in the future.

## Acknowledgements

My utmost thanks go to Gillian Goward, who was enthusiastic in supporting me in every stage of this thesis. She encouraged me to pursue new and interesting avenues, while offering guidance and direction when I strayed off course. Outside of research, Gillian was consistently patient, understanding, and supportive during difficult times in my life, and for that I am ever grateful.

Thank you to my committee members: Dr. David Emslie, and Dr. Giuseppe Melacini. Your continued guidance and advice throughout my graduate school, and undergrad, career has been invaluable.

I am also grateful for the mentors I have had throughout my research. Kris Harris, Zoë Reeve, Sergey Krachkovskiy, Zoya Sadighi, and Kevin Sanders all have taught me indispensable research skills inside and outside of the lab. Particular thanks is given to Kris Harris and Zoë Reeve, who were instrumental in developing the NMR and electrochemical expertise needed for the research in this thesis.

The McMaster NMR facility, Bob Berno, Hilary Jenkins, and Megan Fair, deserve a world of thanks for doing the enormous amount of work it takes to keep the NMR facility running, without which this research would not have been possible. Specifically, I want to thank Bob Berno for the multitude of discussions we have had over the past several years about interesting NMR phenomena. Your genuine passion for the technique is contagious, and sparked my drive to try new and interesting pulse sequences for improved data collection (although admittedly, sometimes just for fun).

Thank you to everyone in the Goward COVID gang who hasn't already been mentioned, and who went through this wild ride with me together: Mengyang Cui,

Taiana Pereira, Amanda Ciezki, Walker Zheng, Malaika Hussain, Breanna Pinto, and Olivia Velanosi. You all made this crazy time in our lives a fun experience. I'm nostalgic for those late nights in lab, working (and procrastinating) with the random assortment of people who were assigned to the night shift on a given day due to the COVID-capacity restrictions.

Thank you to the older generation, “The Brains”: Blossom Yan, David Bazak, Adam MacIntosh, Annica Freytag, and Danielle Smiley. You're an amazing group of friends who helped me through this thesis more than you know. I'm going to finally get my pope hat, and Annica, I didn't graduate first, you win.

Thank you to the boys as well: Jiwon, Ali, and Rob. This journey would have ended at 2<sup>nd</sup> year analytical without you guys; as well as the other boys: Phil, Phill, and Chris, who listened to many rants about how “I was never going to have a *real* job” over the past 6 years.

Thank you to Sara, who was willing to suffer endless socially-distanced outdoor winter dates and freezing patio dinners during the COVID lockdowns, just to listen to me vent about failed experiments.

Thank you to my family, especially my parents, Karen and Jim Franko. You have always supported me through any direction I wanted to take in life. I couldn't have done this without you.

Particular thanks goes out to Ferbie, who is a constant reminder to not stress about the little things, and to just be excited for the day, no matter the circumstance.

# Table of Contents

<b>1 – Introduction</b> .....	<b>1</b>
1.1 – Rechargeable Batteries .....	2
1.1.1 – The Li-ion Battery & Battery Fundamentals .....	2
1.1.2 – From Li-Ion to Na-Ion Batteries .....	11
1.1.3 – Na-O <sub>2</sub> Batteries & Their (Many) Challenges .....	17
1.2 – Cathode Choice in Na-O <sub>2</sub> Batteries .....	27
1.2.1 – Carbon Allotropes .....	27
1.2.2 – Catalysts in NaOBs .....	29
1.2.3 – Introduction to Ti <sub>4</sub> O <sub>7</sub> .....	31
1.3 – Concentrated Electrolytes in Li- and Na-Batteries .....	37
1.3.1 – High Voltage Adiponitrile Electrolytes .....	38
1.3.2 – Ultraconcentrated Electrolytes .....	41
1.4 – Thesis Outline .....	45
1.5 – References .....	47
<b>2 – Methods</b> .....	<b>53</b>
2.1 – Solid-State NMR Spectroscopy .....	53
2.1.1 – The Zeeman Effect & The Origin of NMR Signal .....	53
2.1.2 – The Basic NMR Experiment .....	59
2.2 – Nuclear Spin Interactions .....	64
2.2.1 – Chemical Shielding .....	65
2.2.2 – Dipolar Coupling .....	69
2.2.3 – Quadrupolar Coupling .....	73
2.2.4 – Magic Angle Spinning .....	79
2.3 – Pulse Sequences .....	83
2.3.1 – The Spin Echo .....	83

2.3.2 – Dipolar Heteronuclear Multiple Quantum Correlation (D-HMQC)	86
2.3.3 – Triple Quantum Magic Angle Spinning Spectroscopy (3QMAS)	91
2.3.4 – ssNMR Practical Challenges	96
2.3 – Pulsed Field Gradient NMR Spectroscopy	97
2.3.1 – The Pulsed Field Gradient Stimulated Echo Experiment (PGSTE)	98
2.3.2 – PFG Pulse Sequence Additions	102
2.3.3 – Practical Challenges	104
2.4 – Electrochemical Impedance Spectroscopy (EIS)	104
2.4 – References	109
<b>3 – Characterising Carbon Cathode Decay in Sodium-Oxygen Batteries by Solid-State NMR Spectroscopy</b>	<b>111</b>
3.1 – Introduction	113
3.2 – Experimental	115
3.2.1 – NaO <sub>2</sub> Synthesis	115
3.2.2 – Preparation and Electrochemical Characterization of Composite CB / PVDF Cathodes	115
3.2.3 – Preparation and Electrochemical Characterization of Surface-Modified CC Cathodes	116
3.2.4 – Physical Characterizations	117
3.3 – Results & Discussion	118
3.3.1 – NaO <sub>2</sub> Synthesis & Characterization	118
3.3.2 – <sup>23</sup> Na NMR of Discharged NaOB Composite Cathodes	121
3.3.3 – Reactivity of NaO <sub>2</sub> to Composite Cathodes	123
3.3.4 – Surface-Modified Binder-Free Carbon-Cloth Cathodes	126
3.4 – Conclusions	130
3.5 – References	132

<b>4 – Ti<sub>4</sub>O<sub>7</sub>-Enhanced Carbon Supports to Stabilize NaO<sub>2</sub> in Sodium-Oxygen Batteries .....</b>	<b>134</b>
4.1 – Introduction.....	135
4.2 – Experimental .....	140
4.2.1 – Ti <sub>4</sub> O <sub>7</sub> Synthesis.....	140
4.2.2 – Cathode Preparation .....	140
4.2.3 – Electrochemical Characterization .....	141
4.2.4 – Cathode Characterization.....	142
4.3 – Results and Discussion .....	143
4.3.1 – Ti <sub>4</sub> O <sub>7</sub> Synthesis & Stability .....	143
4.3.2 – NaOB Long-Term Cycle-Life .....	145
4.3.3 – Characterization of Discharge Products.....	150
4.3.4 – Characterization of Cell Death.....	155
4.3.5 – Discharge Mechanism .....	161
4.4 – Conclusions.....	163
4.5 – Supporting Information.....	164
4.5.1 – Further Details on Cathode Manufacturing .....	164
4.5.2 – Details on NMR pulse sequences.....	165
4.5.3 – NaO <sub>2</sub> Synthesis and Reaction Test.....	166
4.5.4 – Ti <sub>4</sub> O <sub>7</sub> on Ni Foam Tests .....	167
4.5.5 – Additional Figures.....	167
4.6 – References .....	174
<b>5 – Concentration Dependent Solution Structure and Transport Mechanism in High Voltage LiTFSI – Adiponitrile Electrolytes .....</b>	<b>177</b>
5.1 – Introduction.....	178
5.2 – Experimental .....	182
5.2.1 – Electrolyte Preparation.....	182
5.2.2 – Electrolyte Preparation.....	182

5.2.3 – Low Temperature XRD measurement of LiTFSI-ADN solutions .....	183
5.2.4 – NMR Spectroscopy .....	184
5.3 – Results and Discussion .....	184
5.3.1 – Conductivity - Phase Diagram Relationship .....	184
5.3.2 – Diffusional Perspective .....	190
5.3.3 – Diffusion Length as a Structural Probe .....	193
5.3.4 – Solvation Structure & Transport Mechanism .....	197
5.3.5 – Cyclic Voltammetry and Li-O <sub>2</sub> cells Proof of Concept .....	199
5.4 – Conclusions .....	202
5.5 – Supporting Information .....	203
5.5.1 – Phase Diagram Construction .....	203
5.5.2 – Fitting of the conductivity isotherm .....	212
5.5.3 – Calculated Eutectic Composition .....	212
5.5.4 – Radial Distribution Functions .....	213
5.6 – References .....	216
<b>6 – Highly Concentrated NaTFSI – Adiponitrile Electrolytes for Na-Ion and Na-O<sub>2</sub> Batteries .....</b>	<b>219</b>
6.1 – Introduction .....	220
6.2 – Experimental .....	224
6.2.1 – Electrolyte Preparation .....	224
6.2.2 – Electrode Preparation .....	224
6.2.3 – Electrochemical Characterization .....	225
6.3 – Results and Discussion .....	226
6.3.1 – Transport and Physical Properties .....	226
6.3.2 – Electrochemical Stability .....	232
6.3.3 – Application to Na-O <sub>2</sub> Batteries .....	236
6.3.4 – Aluminum Corrosion Resistance .....	239
6.3.5 – Half Cell Cycling .....	241

6.4 – Conclusions.....	245
6.5 – Supporting Information .....	246
6.5.1 – Differential Scanning Calorimetry & Phase Diagram Construction .....	246
6.5.2 – NMR Characterization .....	248
6.5.3 – Additional Cyclic Voltammetry Data.....	251
6.5.4 – MOPAC simulations .....	251
6.6 – References .....	253
<b>7 – Outlook.....</b>	<b>256</b>
7.1 – Conclusions.....	256
7.2 – Future Work .....	259
7.3 – References .....	262

# List of Figures

<b>Figure 1.1.</b> [a] General schematic of a typical Li-ion cell employing a graphite anode, a LiNMC cathode, and a liquid electrolyte. †[b] Representative galvanostatic charge / discharge curves of a Gr    NMC (Gr = graphite) full cell employing a variety of electrolyte systems. LP40 = 1 M LiPF <sub>6</sub> in EC / DEC, LP30 = 1 M LiPF <sub>6</sub> in EC / DMC, M9F1 = 1 M LiPF <sub>6</sub> in methyl propionate / fluoroethylene carbonate (FEC). †Reprinted with permission from ACS Energy Lett. 2021, 6, 5, 2016–2023 © 2021 American Chemical Society. <sup>8</sup> .....	3
<b>Figure 1.2.</b> Molecular structures of LiPF <sub>6</sub> , EC, and DEC.....	10
<b>Figure 1.3.</b> Cycling curve of an NVPF cathode, emphasizing the phase transformations during the charging process, where NVPF is deintercalated. <sup>33</sup> †Reprinted with permission from Journal of Power Sources 256 (2014) 258 – 263 © 2014 Elsevier. ....	15
<b>Figure 1.4.</b> [a] General schematic of a typical Na-O <sub>2</sub> cell employing a Na-metal anode, a carbon cathode, and a liquid electrolyte. †[b] Representative galvanostatic discharge / charge curves of a NaO <sub>2</sub> producing NaOB cycled at varying current densities. †Reprinted with permission from Nature Mater 12, 228–232 (2013) © 2013 Nature Publishing Group. <sup>40</sup> .....	18
<b>Figure 1.5.</b> †[a] SEM image of NaO <sub>2</sub> crystallites that have deposited on the surface of the bulk carbon fibres of a carbon cloth NaOB cathode. ††[b] TEM of exfoliated graphene layers of a LIB cathode after Li <sup>+</sup> intercalation. †Reprinted with permission from J. Phys. Chem. Lett. 2017, 8, 19, 4794–4800 © 2017 American Chemical Society. <sup>42</sup> ††Reprinted with permission from Carbon 2012, 50, 10, 3836–3844 © 2012 Elsevier. <sup>43</sup> .....	19
<b>Figure 1.6.</b> †[a] Solution-based formation and decomposition mechanism for NaO <sub>2</sub> showing the proton phase transfer catalyst. †Reprinted with permission from Nature Chemistry volume 7, pages 496–501 (2015) © 2013 Nature Publishing Group. <sup>45</sup> .....	22
<b>Figure 1.7.</b> Molecular structures of NaOTf and DEGDME. ....	26
<b>Figure 1.8.</b> NaOB discharge / charge profiles utilizing †[a] un-doped carbon cathodes, ††[b] Pt-doped graphene nanosheets cathodes, and ††[c] RuO <sub>2</sub> -doped rGO cathodes. †Reprinted with permission from J Phys Chem Lett. 2016, 7, 23, 4841–4846 © 2016 American Chemical Society. <sup>58</sup> ††Reprinted with permission from J. Mater. Chem. A, 2015, 3, 2568-2571 © 2016 Royal Society of Chemistry. <sup>71</sup> †Reprinted with permission from Adv. Funct. Mater. 2017, 27, 1700632 © 2017 John Wiley & Sons. <sup>72</sup> .....	30
<b>Figure 1.9.</b> [a] Rutile TiO <sub>2</sub> . [b / c] Corundum Ti <sub>2</sub> O <sub>3</sub> view along the c-axis, and parallel to the c-axis, respectively. [d] Magneli-phase Ti <sub>4</sub> O <sub>7</sub> structure, showing the rutile chains connected by face sharing shear planes. Reprinted with permission from Sci Rep 6, 28871 (2016) © 2016 Nature Publishing Group. <sup>78</sup> .....	32
<b>Figure 1.10.</b> CVs of various MEAs in PEMFC fuel cells. [a] Pt/C MEA with a C GDL. [b] Pt/Ti <sub>4</sub> O <sub>7</sub> MEA with a C GDL. [c] Pt/C MEA with a Ti GDL. [d] Pt/ Ti <sub>4</sub> O <sub>7</sub> MEA with a Ti GDL. In the original figure labels, “XC72-HTT” refers to the type of carbon used. Reprinted with permission from ECS Trans. 11 (2007) 1041 © 2007 The Electrochemical Society. <sup>82</sup> .....	34
<b>Figure 1.11.</b> Cyclic voltammograms of [a] a Ti <sub>4</sub> O <sub>7</sub> on glassy carbon electrode in an O <sub>2</sub> saturated 6 M KOH <sub>(aq)</sub> electrolyte for Zn-Air batteries, and [b] a nanosphere Ti <sub>4</sub> O <sub>7</sub> on Ni-foam electrode in a 1 M LiNO <sub>3</sub> – DMC electrolyte for LiOBs. Reprinted with permission from Electrochem Acta 50, 20 (2010) 5891-5898 © 2010 Elsevier. <sup>84</sup> Reprinted with permission from ACS Catal. 2018, 8, 2601–2610 © 2018 American Chemical Society. <sup>85</sup> .....	35
<b>Figure 1.12.</b> Intercalation voltage ranges of LiNMC (LiNi <sub>1/3</sub> Mn <sub>1/3</sub> Co <sub>1/3</sub> O <sub>2</sub> ), <sup>91</sup> LMNO (LiNi <sub>0.5</sub> Mn <sub>1.5</sub> O <sub>4</sub> ), <sup>90</sup> and LNP (LiNiPO <sub>4</sub> ) cathodes, <sup>89</sup> With high voltage limits of various organic solvents varieties appearing as dotted lines. ....	39
<b>Figure 1.13.</b> LSV of Li <sub>(s)</sub>    Al <sub>(s)</sub> using different concentrations of LiTFSI in EC electrolytes. <sup>104</sup> Reprinted with permission from Journal of Power Sources 231 (2013) 234-238 © 2013 Elsevier. <sup>103</sup> .....	44

<b>Figure 2.1.</b> Zeeman splitting of a $I = 12$ and a $I = 32$ nuclear spin into non-degenerate spin-states in the presence of an external magnetic field, $B_0$ . <sup>1,2</sup> .....	57
<b>Figure 2.2.</b> Simple “onepulse” pulse sequence showing a $\pi/2$ pulse on nucleus $I$ with a phase of $x$ . The resulting free-induction decay is shown as $I$ precesses in the $x - y$ plane. $D_1$ is the delay time parameter, and is the time allowed for magnetization to relax before each scan. ....	60
<b>Figure 2.3.</b> Simulated powder pattern with CSA contributions with $\delta_{iso} = 0$ ppm, $\Delta = 100$ ppm, and $\eta = 0.5$ . Each of the contributions from the $z$ , $x$ , and $y$ primary axis are highlighted. Simulated in ssNake V1.3. <sup>4</sup> .....	68
<b>Figure 2.4.</b> Simulated dipolar coupling powder pattern, showing the manifestation of CD in the spectrum. <sup>2</sup> Reprinted with permission from <i>Solid State NMR Spectroscopy: Principles and Applications</i> . John Wiley & Sons: Cambridge, 2001 © 2001 John Wiley & Sons. <sup>2</sup> .....	72
<b>Figure 2.5.</b> The perturbation of $I = 32$ Zeeman energy states by QC interactions of the first order ( $QC^1$ ) and second order ( $QC^2$ ). .....	75
<b>Figure 2.6.</b> Simulated quadrupolar lineshapes with various parameter sets. [a] $CQ = 0.377$ MHz, $\eta = 0$ nucleus. [b] $CQ = 2.48$ MHz, $\eta = 0$ nucleus with a broad spectral width. [c] $CQ = 2.48$ MHz, $\eta = 0$ nucleus with an enhanced spectral width. [d] $CQ = 2.48$ MHz, $\eta = 0.65$ nucleus. Simulated in ssNake V1.3. <sup>4</sup> .....	77
<b>Figure 2.7.</b> Simulated solid-state MAS spectra of an $I = 32$ nucleus under primarily [a – d] chemical shielding anisotropy and [e – h] quadrupolar coupling. Simulated in ssNake V1.3. <sup>4</sup> .....	81
<b>Figure 2.8.</b> [a] One-pulse and [b] Hahn-echo pulse sequences. The pulse sequence “blocks” where magnetization evolution is effectively “on” or “off” are identified below each sequence. ....	84
<b>Figure 2.9.</b> Pulse sequence of the $^{23}\text{Na}\{^1\text{H}\}$ D-HMQC experiment used in this thesis. <sup>16</sup> .....	86
<b>Figure 2.10.</b> [a] 1D $^{23}\text{Na}$ , [b] 1D $^1\text{H}$ , and [c] 2D $^{23}\text{Na}\{^1\text{H}\}$ D-HMQC spectrum of $\text{NaH}_2\text{PO}_4$ . Each spectrum was collected at a field of 11.7 T at a spinning rate of 30 kHz MAS. ....	90
<b>Figure 2.11.</b> Pulse sequence of the $z$ -filtered 3QMAS experiment, with the coherence order of the magnetization over the course of the pulse sequence plotted below. <sup>2,6</sup> .....	93
<b>Figure 2.12.</b> [a] 1D onepulse spectrum of $\text{Na}_2\text{CO}_3$ [b] 2D 3QMAS spectrum of $\text{Na}_2\text{CO}_3$ . [c] Projection of the direct dimension giving the 1D $\text{Na}_2\text{CO}_3$ spectrum with isotropic and anisotropic contributions. [d] Projection of the indirect dimension giving the 1D pure isotropic $\text{Na}_2\text{CO}_3$ spectrum. This spectrum was collected at a magnetic field of 19.9 T at a MAS spinning rate of 30 kHz. ....	95
<b>Figure 2.13.</b> [a] PGSTE pulse sequence. <sup>20</sup> The $I$ channel represent typical RF pulses, while the $G$ channel represents gradient pulses. [b] Illustration of spatially-dependant phase encoding during the PGSTE sequence. ....	99
<b>Figure 2.14.</b> Diffusional decay curve of 1 M $\text{NaCl}_{(aq)}$ . Measured datapoints are in blue and are each the result of an individual PGSTE experiment using a gradient strength $g$ . The computed gaussian decay model fit to extract $D$ is in red. ....	101
<b>Figure 2.15.</b> PGSTE experiment implementing bipolar pulse pairs, spoiler gradient pulses, and a longitudinal eddy delay. <sup>22-24</sup> .....	103
<b>Figure 2.16.</b> [a] Nyquist plot and [c] EEC model for a solution-state ion conductor. [b] Nyquist plot and [d] EEC model for a solid-state ion conductor. <sup>29-31</sup> .....	106
<b>Figure 3.1.</b> PXRD diffractogram of synthesized $\text{NaO}_2$ , along with a calculated reference pattern (ICSD 87176). Adapted with permission from the <i>Journal of the American Chemical Society</i> 2017, 139, 2, 595–598 © 2016 American Chemical Society. <sup>1</sup> .....	119
<b>Figure 3.2.</b> [a] $^{23}\text{Na}$ NMR spectrum of synthesized $\text{NaO}_2$ . The $\text{NaO}_2$ Asterisk symbols in the NMR spectrum denote spinning side bands. [b] $\text{NaO}_2$ $^{23}\text{Na}$ NMR spectra at varying temperatures from 300 K to 350 K. $\Delta\delta_{dia}$ represents the unchanging shift of a diamagnetic impurity in the sample. Adapted with permission from the <i>Journal of the American Chemical Society</i> 2017, 139, 2, 595–598 © 2016 American Chemical Society. <sup>1</sup> .....	120
<b>Figure 3.3.</b> [a] Representative galvanostatic discharge curve of NaOBs studied by $^{23}\text{Na}$ NMR discharged at a current density of $75 \text{ mAh g}^{-1}$ . The $100 \text{ mAh g}^{-1}$ and $750 \text{ mAh g}^{-1}$ points are marked. [b] $^{23}\text{Na}$ MAS	

ssNMR spectra of the NaOB cathodes discharged to a capacity of 100 and 750 mAh g <sup>-1</sup> . [c] and [d] <sup>23</sup> Na MAS ssNMR spectra of expected electrochemical discharge products in NaOBs. Adapted with permission from the Journal of the American Chemical Society 2017, 139, 2, 595–598 © 2016 American Chemical Society. <sup>1</sup> .....	122
<b>Figure 3.4.</b> <sup>23</sup> Na NMR spectrum of NaO <sub>2</sub> ground with CB, and spectra of relevant reference compounds. Adapted with permission from the Journal of the American Chemical Society 2017, 139, 2, 595–598 © 2016 American Chemical Society. <sup>1</sup> .....	123
<b>Figure 3.5.</b> [a] <sup>23</sup> Na NMR [b] <sup>19</sup> F NMR, and [c] <sup>19</sup> F SeISat NMR spectrum of NaO <sub>2</sub> ground with PVDF, and spectra of relevant reference compounds. Adapted with permission from the Journal of the American Chemical Society 2017, 139, 2, 595–598 © 2016 American Chemical Society. <sup>1</sup> .....	124
<b>Figure 3.6.</b> <sup>1</sup> H MAS ssNMR spectra of hydrophilic and hydrophobic CC cathodes. Adapted with permission from the Journal of Physical Chemistry Lett 2017, 8, 19, 4794–4800 © 2017 American Chemical Society. <sup>2</sup> .....	126
<b>Figure 3.7.</b> [a] Galvanostatic cycling curves for a single cycle of hydrophobic and hydrophilic cathodes in NaOBs. [b - e] SEM micrographs of the [b / c] hydrophobic cathode and the [d / e] hydrophilic cathode at varying resolutions. Adapted with permission from the Journal of Physical Chemistry Lett 2017, 8, 19, 4794–4800 © 2017 American Chemical Society. <sup>2</sup> .....	127
<b>Figure 3.8.</b> [a] PXRd diffraction patterns of discharged hydrophobic and hydrophilic cathodes. [b - c] <sup>23</sup> Na ssNMR spectra of discharged [b] hydrophobic and [c] hydrophilic cathodes through time as the reaction mixture aged after discharging. Adapted with permission from the Journal of Physical Chemistry Lett 2017, 8, 19, 4794–4800 © 2017 American Chemical Society. <sup>2</sup> .....	129
<b>Figure 4.1.</b> [a] PXRd diffractograms of the Ti <sub>4</sub> O <sub>7</sub> synthesis products. [b] <sup>23</sup> Na NMR spectrum of Ti <sub>4</sub> O <sub>7</sub> ground with NaO <sub>2</sub> . .....	144
<b>Figure 4.2.</b> [a] Discharge capacity achieved as a function of cycle number for NaOB assembled with cathodes of varying Ti <sub>4</sub> O <sub>7</sub> weight percentage. All cells are limited to a discharge capacity of 0.28 mAh cm <sup>-2</sup> and are cycled at a current density of 0.1 mA cm <sup>-2</sup> . Data points are offset with each series for visibility. [b - f] Galvanostatic discharge/charge curves for NaOB assembled with cathodes of varying Ti <sub>4</sub> O <sub>7</sub> weight percentage. [b] 0%-Ti <sub>4</sub> O <sub>7</sub> , [c] 40%-Ti <sub>4</sub> O <sub>7</sub> , [d] 60%-Ti <sub>4</sub> O <sub>7</sub> , [e] 80%-Ti <sub>4</sub> O <sub>7</sub> , [f] 90%-Ti <sub>4</sub> O <sub>7</sub> . .....	147
<b>Figure 4.3.</b> PXRd diffractograms of single-discharge 0%-Ti <sub>4</sub> O <sub>7</sub> and 90%-Ti <sub>4</sub> O <sub>7</sub> cathodes. The reference patterns of NaO <sub>2</sub> and Na <sub>2</sub> O <sub>2</sub> ·2H <sub>2</sub> O are shown below, as well as the pattern of the empty air-free sample holder used for discharged cathode data collection. The reflections of the sample holder are also marked by “x” symbols in the discharged cathode diffractograms. ....	150
<b>Figure 4.4.</b> <sup>23</sup> Na ssNMR spectra of discharged [a] 0%-Ti <sub>4</sub> O <sub>7</sub> and [b] 90%-Ti <sub>4</sub> O <sub>7</sub> cathodes (blue is 2.66 hours after discharge, black is 1 month). Each includes the reference spectra of Na <sub>2</sub> CO <sub>3</sub> (pink), NaOTF that has been wet with DEGDME (purple), and synthesised NaO <sub>2</sub> (green). [c-d] Time dependant <sup>23</sup> Na ssNMR spectrum showing the decay of NaO <sub>2</sub> in the discharged [c] 0%-Ti <sub>4</sub> O <sub>7</sub> and [d] 90%-Ti <sub>4</sub> O <sub>7</sub> cathodes. [e] The NaO <sub>2</sub> integral taken from the <sup>23</sup> Na spectra of the discharged NaOB cathodes plotted over time. ....	152
<b>Figure 4.5.</b> SEM and EDS characterization of pristine and discharged NaOB cathodes. [a] SEM and C Kα1, 2 EDS of a Pristine 0%-Ti <sub>4</sub> O <sub>7</sub> cathode. [b] SEM and C Kα1, 2 EDS of a Discharged 0%-Ti <sub>4</sub> O <sub>7</sub> cathode. [c] SEM and Ti Kα1 EDS of a Pristine 90%-Ti <sub>4</sub> O <sub>7</sub> cathode. [d] SEM and Ti Kα1 EDS of a Discharged 90%-Ti <sub>4</sub> O <sub>7</sub> cathode. ....	154
<b>Figure 4.6.</b> [a] 1D <sup>23</sup> Na and [b] 1D <sup>1</sup> H ssNMR spectra of lifetime-cycled 0%-Ti <sub>4</sub> O <sub>7</sub> and 90%-Ti <sub>4</sub> O <sub>7</sub> cathodes. The asterisk in the NaFormate spectrum marks an impurity in the sample. ....	157
<b>Figure 4.7.</b> 2D <sup>23</sup> Na{ <sup>1</sup> H} D-HMQC spectra of [a] lifetime-cycled 0%-Ti <sub>4</sub> O <sub>7</sub> cathode, [b] lifetime-cycled 90%-Ti <sub>4</sub> O <sub>7</sub> cathode, and [c] combined NaFormate, NaBicarbonate, and dried NaOTF in DEGDME reference materials. ....	158
<b>Figure 4.8.</b> 2D 3QMAS spectra of [a] lifetime-cycled 0%-Ti <sub>4</sub> O <sub>7</sub> cathode, [b] lifetime-cycled 90%-Ti <sub>4</sub> O <sub>7</sub> cathode, and [c] combined NaFormate, NaBicarbonate, Na <sub>2</sub> CO <sub>3</sub> , and dried NaOTF in DEGDME reference materials. ....	159

<b>Figure 4.9.</b> Proposed schematic on the mechanism by which $Ti_4O_7$ increases cycle-life. [a] Cell discharge; $O_2$ is reduced at the carbon surface and $NaO_2$ precipitates on both the carbon and $Ti_4O_7$ surfaces via the well-studied solution-based phase transfer catalyst mechanism. [b] Degradation; $NaO_2$ in contact with the carbon surface decays. [c] Cell charge; $NaO_2$ solvates into solution and $O_2^-$ is oxidized at the carbon surface in the reverse phase transfer catalyst mechanism. ....	162
<b>Figure 4.10S.</b> $^{23}Na$ reference spectra of various Na-containing species expected to form in NaOBs. Spectra in [a] include: $Na_2CO_3$ , NaBicarbonate, Dry NaOTF, and NaOTF in Diglyme electrolyte vacuum dried in the same manner that cycled electrodes are treated. Spectra in [b] include commercial $Na_2O_2$ collected on a 19.9 T NMR spectrometer, $Na_2O_2$ collected on a 11.7 T NMR spectrometer, synthesised $NaO_2$ collected on a 19.9 NMR spectrometer, and synthesised $NaO_2$ collected on a 11.7 T NMR spectrometer. The $NaO_2$ peak shifts between field strengths while the $Na_2O_2$ impurity resonance is static. ....	168
<b>Figure 4.11S.</b> [a] The first discharge capacity of NaOBs made with cathodes comprised of $Ti_4O_7$ on Ni foam, Bare Ni foam, and 90%- $Ti_4O_7$ on carbon paper. [b] The same plot of just the $Ti_4O_7$ on Ni foam and Bare Ni foam cells, zoomed in to the low-capacity region. The 90%- $Ti_4O_7$ cell is cycled with a current density of $0.1 \text{ mA cm}^{-2}$ , while the two Ni-foam cells were cycled with a current density of $0.01 \text{ mA cm}^{-2}$ . ....	169
<b>Figure 4.12S.</b> SEM and corresponding EDS images of [a] Pristine 0%- $Ti_4O_7$ , [b] Discharged 0%- $Ti_4O_7$ , [c] Pristine 90%- $Ti_4O_7$ , and [d] Discharged 90%- $Ti_4O_7$ . ....	170
<b>Figure 4.13S.</b> PXRD powder patterns of lifetime-cycled 0%- $Ti_4O_7$ and 90%- $Ti_4O_7$ cathodes. As well as relevant reference patterns. ....	171
<b>Figure 4.14S.</b> [a-b] $1D \text{ } ^{23}Na$ NMR spectra of the 0%- $Ti_4O_7$ and 90%- $Ti_4O_7$ cathodes with reference spectra. [c] $1D \text{ } 3QMAS$ spectra of both the 0%- $Ti_4O_7$ and 90%- $Ti_4O_7$ cathodes, as well as corresponding reference compounds. [d] $1D \text{ } ^{23}Na\{^1H\}$ DHMQC spectra of both the 0%- $Ti_4O_7$ and 90%- $Ti_4O_7$ cathodes as well as corresponding reference compounds. ....	172
<b>Figure 4.15S.</b> Reference [a] $^1H$ , [b] $^{23}Na$ , and [c] $^{23}Na\{^1H\}$ DHMQC spectra of $NaH_2PO_4$ . ....	173
<b>Figure 5.1.</b> [a] Ionic conductivity of LiTFSI in ADN solutions as a function of concentration. [b] Extrapolated phase diagram of LiTFSI in ADN measured by DSC. Circles and diamonds represent endothermic and exothermic transitions, respectively. [c] Overlay of the conductivity plot and phase diagram showing the distinct relationship between $C_{max}$ and $x\epsilon$ . ....	185
<b>Figure 5.2.</b> Variable temperature powder x-ray diffractogram of [a] 4.4 M LiTFSI in ADN electrolyte, corresponding to a 2 to 1 ADN:Li molar ratio, or 0.33 xLiTFSI, and [b] 0.1 M LiTFSI in ADN, corresponding to a 88 to 1 ADN:Li molar ratio, or 0.011 xLiTFSI. ....	187
<b>Figure 5.3.</b> [a] Diffusion coefficients of $Li^+$ , TFSI, and ADN measured by $7Li$ , $^{19}F$ , and $^1H$ PFG NMR respectively. [b] The quotient of diffusion coefficients as a function of temperature for (red) $Li^+$ over TFSI and (black) $Li^+$ over ADN. The red line represents a ratio of 1, where both species diffuse at the same rate. ....	191
<b>Figure 5.4.</b> Diffusion coefficient as a function of diffusion time ( $\Delta$ ) for each concentration of electrolyte for [a] TFSI and (b) $Li^+$ . (c) The ratio of zero-time diffusion ( $\Delta \rightarrow 0$ ) to bulk diffusion ( $\Delta = 500$ ), diffusion heterogeneity ( $hD$ ), for both $Li^+$ and TFSI. ....	194
<b>Figure 5.5.</b> CV of (a) 0.8 M ( $C_{max}$ ) and (b) 2.9 M (3 to 1 molar ratio) LiTFSI in ADN. Pt wire is used as both the counter and working electrodes, with a Li metal reference electrode. ....	199
<b>Figure 5.6.</b> Cyclic voltammetry of Li- $O_2$ coin cells in an $O_2$ atmosphere using (a) 0.8 M ( $C_{max}$ ) and (b) 2.9 M (3 to 1 molar ratio) LiTFSI in ADN electrolyte. Carbon cloth is used as the working electrode, and Li metal as the counter/reference in both cells. ....	200
<b>Figure 5.7S.</b> Copy of phase diagram seen in the main text. Data points here are labelled as DSC thermatogram peaks in the following figures. ....	206
<b>Figure 5.8S.</b> DSC plot of 0.1 M LiTFSI in ADN electrolyte, corresponding to a 88 to 1 ADN:Li molar ratio, or 0.011 xLiTFSI. ....	206
<b>Figure 5.9S.</b> DSC plot of 0.5 M LiTFSI in ADN electrolyte, corresponding to a 17.5 to 1 ADN:Li molar ratio, or 0.054 xLiTFSI. ....	207

<b>Figure 5.10S.</b> DSC plot of 1.0 M LiTFSI in ADN electrolyte, corresponding to a 8.8 to 1 ADN:Li molar ratio, or 0.10 xLiTFSI.....	207
<b>Figure 5.11S.</b> DSC plot of 1.8 M LiTFSI in ADN electrolyte, corresponding to a 5 to 1 ADN:Li molar ratio, or 0.17 xLiTFSI.....	208
<b>Figure 5.12S.</b> DSC plot of 2.9 M LiTFSI in ADN electrolyte, corresponding to a 3 to 1 ADN:Li molar ratio, or 0.25 xLiTFSI.....	208
<b>Figure 5.13S.</b> DSC plot of 3.5 M LiTFSI in ADN electrolyte, corresponding to a 2.5 to 1 ADN:Li molar ratio, or 0.28 xLiTFSI.....	209
<b>Figure 5.14S.</b> DSC plot of 4.4 M LiTFSI in ADN electrolyte, corresponding to a 2 to 1 ADN:Li molar ratio, or 0.33 xLiTFSI.....	209
<b>Figure 5.15S.</b> Variable temperature powder x-ray diffractogram of 0.1 M LiTFSI in ADN, corresponding to a 88 to 1 ADN:Li molar ratio, or 0.011 xLiTFSI.....	210
<b>Figure 5.16S.</b> Variable temperature powder x-ray diffractogram of 0.5 M LiTFSI in ADN, corresponding to a 17.5 to 1 ADN:Li molar ratio, or 0.054 xLiTFSI.....	210
<b>Figure 5.17S.</b> Variable temperature powder x-ray diffractogram of 1.0 M LiTFSI in ADN, corresponding to a 8.8 to 1 ADN:Li molar ratio, or 0.10 xLiTFSI.....	211
<b>Figure 5.18S.</b> Variable temperature powder x-ray diffractogram of 4.4 M LiTFSI in ADN electrolyte, corresponding to a 2 to 1 ADN:Li molar ratio, or 0.33 xLiTFSI.....	211
<b>Figure 5.19S.</b> RDF profile of dilute LiTFSI(ADN) <sub>11</sub> (0.8 M), the blue line corresponds to the partial RDF of Li - N <sub>(ADN)</sub> , and the orange line corresponds to Li - O <sub>(TFSI)</sub> .....	214
<b>Figure 5.20S.</b> RDF profile of highly concentrated LiTFSI(ADN) <sub>3</sub> (2.9 M), the blue line corresponds to the partial RDF of Li - N <sub>(ADN)</sub> , and the orange line corresponds to Li - O <sub>(TFSI)</sub> .....	215
<b>Figure 5.21S.</b> RDF profile of highly concentrated LiTFSI(ADN) <sub>2</sub> (4.4 M), the blue line corresponds to the partial RDF of Li - N <sub>(ADN)</sub> , and the orange line corresponds to Li - O <sub>(TFSI)</sub> .....	215
<b>Figure 6.1.</b> NaTFSI – ADN (a) Phase diagram measured by DSC and (b) Room temperature ionic conductivity isotherm measured by EIS. In the phase diagram legend: T <sub>melt</sub> stands for melting point, T <sub>eut</sub> is eutectic transition temperature, T <sub>g</sub> is glass transition temperature, and T <sub>dev</sub> is devitrification transition temperature.....	228
<b>Figure 6.2.</b> Calculated cumulative pCNs for (a) Na and N, (b) Na and O, and (c) Na and F in NaTFSI – ADN.....	231
<b>Figure 6.3.</b> Reactivity of NaTFSI – ADN electrolyte to Na metal at various concentrations.....	233
<b>Figure 6.4.</b> Cyclic voltammograms of (a) 1.0 M and (b) 2.9 M NaTFSI – ADN. (c – d) The same data sets zoomed into the Na deposition and dissolution region, showing the integrals of the reduction (deposition) and oxidation (dissolution) events, as well as the ratio of the two “E <sub>red/ox</sub> ”. (e) E <sub>red/ox</sub> shown as a function of concentration for NaTFSI – ADN electrolytes.....	235
<b>Figure 6.5.</b> Cyclic voltammograms of NaOB coin cells using (a) 1.0 M, (b) 2.2 M, (c) 2.9 M, and (d) 4.4 M NaTFSI – ADN electrolytes. Note: the 1.0 M cell is using different y-axis limits to show the large degradation peak.....	237
<b>Figure 6.6.</b> [a] LSV of Na    Al coin cells with a range of electrolyte concentrations from 3 to 4.3 V vs Na / Na <sup>+</sup> . [b] CA of the same Na    Al coin cells held at 4.3 V vs Na / Na <sup>+</sup> directly after LSV experiments. [c] CV of Na    Al coin cells of 1.0 M and 4.4 M coin cells.....	240
<b>Figure 6.7.</b> Galvanostatic cycling curves of Na    NVPF half cells employing [a] 1.0 M NaTFSI – ADN electrolyte and [b] 4.4 M NaTFSI – ADN electrolyte. The x-axis is stated in mAh g <sup>-1</sup> of NVPF.....	242
<b>Figure 6.8.</b> EIS spectra collected using a frequency range of 1 MHz to 0.01 Hz of Na    NVPF half-cells employing [a] 1.0 M NaTFSI – ADN electrolyte and [b] 4.4 M NaTFSI – ADN electrolyte. The entire frequency range is shown in both figures, and the inset in [a] zooms in on the uncycled 1.0 M cell to emphasize the initially low impedance.....	243
<b>Figure 6.9S.</b> DSC thermatograms for each of the NaTFSI – ADN concentrations tested. Each of the peaks in the thermatogram are labelled with the associated data point label used in the phase diagram.....	247

**Figure 6.10S.** [a] Diffusion coefficients of TFSI and ADN as measured by PFG  $^{19}\text{F}$  and  $^1\text{H}$  NMR respectively. [b – d]  $T_1$  and  $T_2$  values of [b] ADN, [c]  $\text{Na}^+$ , and [d] TFSI. ....249

**Figure 6.11S.** [a]  $^{23}\text{Na}$  MAS ssNMR spectra of cycled NVPF cathodes at different states of charge. [b] The same spectra zoomed into the NVPF region. [c] The relative integrals of each of the NVPF peaks in the cycled sample, normalized to the amount of active NVPF material in the cathode. ....250

**Figure 6.12S.** Full CV voltammograms of Pt vs Pt (Na Ref.) three electrode cells using each NaTFSI – ADN concentration. ....251

## List of Tables

**Table 1.1.** Summary of Li-ion cathode material intercalation voltages and achievable specific capacities.<sup>13, 14</sup> .....8

**Table 1.2.** Summary of select Na-ion cathode material intercalation voltages and achievable specific capacities. ....14

**Table 1.3.** Competing reaction pathways and resulting theoretical cell voltages, specific capacities, and energy densities for the NaOB. Table adapted from Hartmann et al. *Nature Materials*, 2013, 12, 228 – 232.<sup>40</sup> \*\*Specific capacity and energy density values are given in terms of mass of the formed product. .20

**Table 5.1S.** Physical parameters A and B for water, ACN and ADN obtained by fitting Equation S1 to their respective conductivity isotherms at room temperature. ....212

# List of Symbols and Abbreviations

## *Abbreviations (Alphabetical)*

3QMAS	triple quantum magic angle spinning
AC	alternating current
ACN	acetonitrile
ADN	adiponitrile
BETI	bis(perfluoroethylsulfonyl)imide
BOB	bis(oxalato)borate
BPP	bipolar pulse pairs
CA	chronoamperometry
CB	carbon black
CC	carbon cloth
CEI	cathode electrolyte interface
CIP	coordinated ion pair
CMC	carboxymethylcellulose
CN	coordination number
CNP	carbon nanotube paper
CPE	constant phase element
CSA	chemical shielding anisotropy
CT	central transition
CV	cyclic voltammetry
DAS	dynamic angle spinning
DC	direct current
DEC	diethyl carbonate
DEGDME	diethylene glycol dimethyl ether
DFOB	difluoro(oxalato)borate
DFT	density functional theory
DHMQC	dipolar heteronuclear multiple quantum correlation
DMC	dimethyl carbonate
DME	dimethyl ether
DMSO	dimethyl sulfoxide
DOR	double rotation
DOS	density of states
DSC	differential scanning calorimetry
EC	ethylene carbonate
EDS	energy dispersive x-ray spectroscopy

EEC	electrochemical equivalent circuit
EFG	electric field gradient
EIS	Electrochemical Impedance Spectroscopy
EMS	ethyl methane sulfonate
EV	electric vehicle
FEC	fluoroethylene carbonate
FID	free induction decay
FRA	frequency response analyzer
FSI	bis(fluorosulfonyl)imide
FT	Fourier transform
FTIR	Fourier transform infrared spectroscopy
GDL	gas diffusion layer
GN	glutaronitrile
Gr	graphite
GO	graphene oxide
HC	hard carbon
HSAB	hard-soft acid-base
LCO	$\text{LiCoO}_2$
LED	longitudinal eddy current delays
LFP	$\text{LiFePO}_4$
LIB	lithium-ion battery
LiOB	lithium-oxygen battery
LMNO	$\text{LiMn}_{1.5}\text{Ni}_{0.5}\text{O}_4$
LMO	$\text{LiMn}_2\text{O}_4$
LNP	$\text{LiNiPO}_4$
LSV	linear sweep voltammetry
LUMO	lowest unoccupied molecular orbital
MAS	magic angle spinning
MD	molecular dynamics
MEA	membrane electrode assemblies
MIB	metal-ion battery
MOB	metal-oxygen battery
MQ	multiple quantum
NaOB	sodium-oxygen battery
NASICON	sodium super ion conductor
NMC	$\text{Ni}_{1/3}\text{Mn}_{1/3}\text{Co}_{1/3}\text{O}_2$
$\beta$ -NMO	$\beta\text{-NaMnO}_2$
NMP	N-Methyl-2-pyrrolidone

NMR	nuclear magnetic resonance
NVP	$\text{Na}_3\text{V}_2(\text{PO}_4)_3$
NVPF	$\text{Na}_3\text{V}_2(\text{PO}_4)_2\text{F}_3$
OER	oxygen evolution reaction
ORR	oxygen reduction reaction
OTF	triflate
PAS	principle axis system
PC	propylene carbonate
pCN	partial coordination number
PEF	polyelectrolyte-fluoropolymer
PEMFC	polymer electrolyte membrane fuel cell
PFG	pulsed-field gradient
PGSTE	pulsed field gradient stimulated echo
PHEV	plug-in hybrid electric vehicle
PPTC	proton phase-transfer catalyst
PVDF	polyvinylidene fluoride
PXRD	powder x-ray diffraction
QC	quadrupolar coupling
RDF	radial distribution function
RF	radio frequency
RT	room temperature
SAED	selected area electron diffraction
SEI	solid electrolyte interface
SEM	scanning electron microscopy
SG	spoiler gradients
SI	supporting information
SIB	sodium-ion battery
SQ	single quantum
ssNMR	solid-state nuclear magnetic resonance
ST	satellite transition
TEGDME	tetraethylene glycol dimethyl ether
TEM	transmission electron microscopy
TEOS	tetraethyl orthosilicate
TFSI	bis(trifluoromethanesulfonyl)imide
VC	vinylene carbonate
XPS	x-ray photoelectron spectroscopy
XRD	x-ray diffraction

*Symbols (In Order of Appearance)*

$E_{cell}$	voltage of cell
$Q$	capacity
$U_{elec}$	stored electrical energy
$\Delta G$	change in Gibbs free energy
$I$	azimuthal spin quantum number
$\mu$	nuclear magnetic moment
$\gamma$	gyromagnetic ratio
$m_I$	magnetic spin quantum number
$\psi_{I,m}$	spin-state wavefunction of spin $I$ in state $m$
$ I, m\rangle$	Bra-Ket notation of spin-state wavefunction of spin $I$ in state $m$
$\hat{H}_{Ze}$	Zeeman Hamiltonian
$E_{I,m}$	energy of nuclear spin-state
$B_0$	applied external magnetic field
$\omega_0$	Larmor frequency
$\vec{M}$	net magnetization vector
$B_1$	magnetic field resulting from applied RF pulse
$T_1$	spin-lattice relaxation
$T_2$	spin-spin relaxation
$\sigma_{CS}$	chemical shielding tensor
$\sigma_{iso}$	chemical shielding isotropic value
$\Delta_{an}$	chemical shielding anisotropy
$\eta_{CS}$	chemical shielding asymmetry
$\omega_{CS}$	chemical shielding contribution to the Larmor frequency
$\theta$	polar angle of magnetic moment to $B_0$ in spherical coordinates
$U$	interaction energy of two magnetic moments
$\hat{H}_D$	dipolar interaction Hamiltonian
$c_D$	dipolar coupling constant
$\omega_{D,het}$	frequency contribution of dipolar heteronuclear coupling
$\Delta M$	nuclear transition coherence level
$\hat{H}_Q$	quadrupolar coupling Hamiltonian
$C_Q$	quadrupolar coupling constant
$\omega_Q$	quadrupolar contribution to Larmor frequency
$C_n^M$	constant for the $n^{\text{th}}$ -rank evolution of $M$ -quantum transition
$\eta$	quadrupolar asymmetry parameter
$\omega_{CT}^{(2)}$	2 <sup>nd</sup> order frequency correction of the quadrupolar central transition
$k$	isotropic echo ratio for the 3QMAS sequence
$g$	gradient pulse strength in PFG experiment

$\delta$	gradient pulse duration in PFG experiment
$\Delta$	diffusion time in PFG experiment
$D$	diffusion coefficient
$Z(\omega)$	measured complex impedance in EIS
$Z'$	real component of complex impedance, resistance
$Z''$	imaginary component of impedance, reactance
$R$	bulk resistance in EIS
$\kappa$	ionic conductivity
$T_m$	melting temperature
$C_{max}$	concentration of maximum ionic conductivity
$x_\epsilon$	eutectic composition
$h_D$	diffusion heterogeneity
$x_i / \chi_i$	molar composition of component $i$
$T_{eut}$	eutectic transition temperature
$T_g$	glass transition temperature
$T_{dev}$	devitrification transition temperature
$\mathcal{E}_{red/ox}$	ratio of reduction and oxidation current in CV

## Declaration of Academic Achievement

Zoe Reeve (Goward group, McMaster University) was the primary author of publication 1 in **Chapter 3**, and was responsible for ssNMR characterization of composite sodium-oxygen battery cathodes, and assisted in variable temperature characterization of NaO<sub>2</sub>. Hossein Yadegari (Sun group, Western University) was the primary author of publication 2 in **Chapter 3**, and provided electrochemical characterization of composite sodium-oxygen battery cathodes, synthesized surface-modified carbon cloth cathodes, and was responsible for scanning electron microscopy (SEM) and powder x-ray diffraction (PXRD) characterization of surface-modified carbon cloth cathodes. Jhoynner Martinez (Canadian Centre for Electron Microscopy, McMaster University) provided SEM characterization of Ti<sub>4</sub>O<sub>7</sub>-coated carbon paper cathodes. Chae-Ho Yim and Yaser Abu-Lebdeh (National Research Council of Canada) were responsible for all differential scanning calorimetry measurements, and, with Pamela Whitfield (National Research Council of Canada), collected the x-ray diffraction data on electrolyte samples. Fabian Årén, Mirna Alhanash, and Gustav Åvall (Johansson group, Chalmers University of Technology) were responsible for molecular dynamics simulations for radial distribution function and partial coordination number plots on electrolyte samples. All other synthesis, data acquisition, and interpretation were performed by Christopher J. Franko.

# 1 – Introduction

The degradative effects of burning fossil fuels on the Earth's climate has been brought to the forefront of public discourse in recent years, but scientific evidence for global warming by human-produced carbon dioxide (CO<sub>2</sub>) has been compiling since the early 1800's. In 1824, famed mathematician Joseph Fourier calculated that the Earth's surface should be substantially colder than it is, given its distance from the Sun.<sup>1</sup> In 1856, physicist Eunice Foote proved that the observed discrepancy in temperature was caused by atmospheric CO<sub>2</sub> and H<sub>2</sub>O, discovering what is now known as the greenhouse effect (becoming the first female to publish in the field of physics in the process!).<sup>2</sup> Later in 1896, Nobel laureate Svante Arrhenius extended the study of the greenhouse effect by showing that even minor variations of atmospheric CO<sub>2</sub> levels could have significant effects on surface temperature.<sup>3</sup> Finally, in 1938, Guy Callendar was able to show that recent increases in global surface temperature were a direct result of human-produced CO<sub>2</sub>, and could not be accounted for by natural increases in CO<sub>2</sub> levels,<sup>4</sup> concluding over one hundred years of scientific advancement.

Since Callendar's seminal report, the phenomenon of human-induced climate change has become irrefutable, and yet global CO<sub>2</sub> production has only continued to increase.<sup>5</sup> One of the main reasons for this is the relative ease of storing fossil fuels after extraction. When energy demands are low, excess coal, oil, or natural gas can simply be stockpiled, and subsequently used later when energy demands are higher. In contrast, renewable sources such as wind and solar produce electrical energy at the

point of extraction, and thus require the use of secondary energy storage technologies to be stockpiled.

Encouragingly, annual renewable power installations have still risen substantially in recent years, climbing from 160 GW in 2015, to 290 GW in 2020,<sup>5-7</sup> but if this trend is to continue, the global capacity for electrical energy storage must also increase. One of the most popular forms of energy storage today is the rechargeable electrochemical battery, which uses electrical energy to drive an unspontaneous chemical process to store energy as a chemical state, with the hope of mediating the reverse spontaneous process to recover said energy at a later time. The development of rechargeable battery technologies that can reliably store electrochemical energy is paramount to the continued development of renewable energy technology, and to the preservation of Earth's habitable climate.

## 1.1 – Rechargeable Batteries

The research presented in this thesis concerns the diagnosis and improvement of stability issues in multiple electrochemical energy storage systems, including Li-ion batteries (LIBs), Na-ion batteries (SIBs), Na-O<sub>2</sub> batteries (NaOBs), and very briefly, Li-O<sub>2</sub> batteries (LiOBs). The goal of this section is to introduce and compare the electrochemical processes of each of these battery systems, and to describe a curated selection of common degradation processes that relate these systems in the context of oxidative instability.

### 1.1.1 – The Li-ion Battery & Battery Fundamentals

Most people are familiar with the idea of a LIB. The name is ubiquitous with energy storage in today's world, as in modern society we are often surrounded by a

number of them on our person at any given time, whether that be in our cellphones, smart watches, tablets, laptops, or as of late, our cars. As such the LIB is a relatable model that can be used to introduce several electrochemical concepts that are important to the works described in this thesis. The research presented here on LIBs primarily concerns the liquid electrolyte, but an understanding of the basic principles of the anode, cathode, electrolyte, and how each of these cell components contributes to the whole, is useful for understanding the motivations behind the electrolyte investigations.

### *Li-Ion Fundamentals*

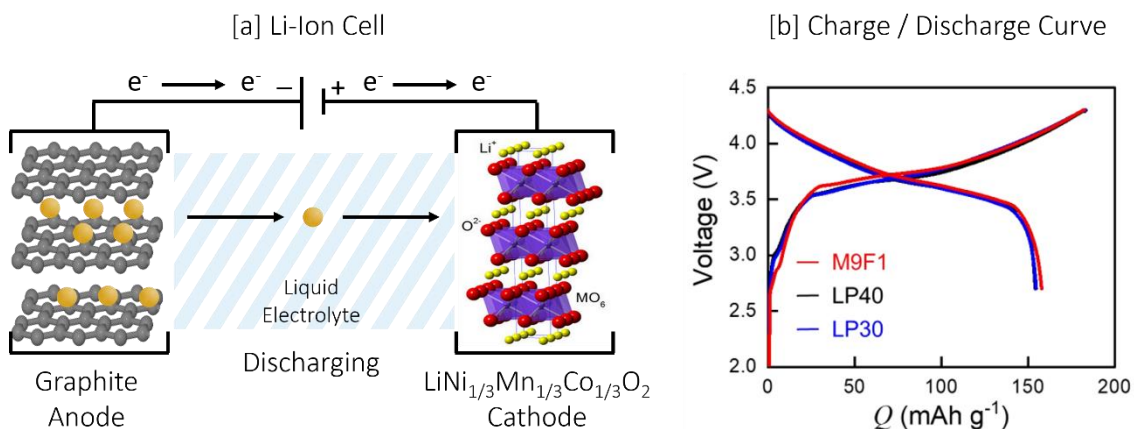


**Figure 1.1.** [a] General schematic of a typical Li-ion cell employing a graphite anode, a LiNMC cathode, and a liquid electrolyte. †[b] Representative galvanostatic charge / discharge curves of a Gr || NMC (Gr = graphite) full cell employing a variety of electrolyte systems. LP40 = 1 M LiPF<sub>6</sub> in EC / DEC, LP30 = 1 M LiPF<sub>6</sub> in EC / DMC, M9F1 = 1 M LiPF<sub>6</sub> in methyl propionate / fluoroethylene carbonate (FEC). †Reprinted with permission from ACS Energy Lett. 2021, 6, 5, 2016–2023 © 2021 American Chemical Society.<sup>8</sup>

**Fig. 1.1a** shows a typical LIB undergoing the discharge process. There are three major components to a Li-ion cell: the anode, the cathode, and the electrolyte. In a typical LIB, graphite is the anode, LiNi<sub>1/3</sub>Mn<sub>1/3</sub>Co<sub>1/3</sub>O<sub>2</sub> (LiNMC) is the cathode, and

a 1 M solution of lithium hexafluorophosphate ( $\text{LiPF}_6$ ) in a 1:1 mixture of ethylene carbonate (EC) and diethyl carbonate (DEC) is the liquid electrolyte.

Similar to the Zn || Cu galvanic cell (where A || B represents a cell with an “A” anode and a “C” cathode) that every introductory chemistry student has built at some point, electrons flow through the external circuit from the electrode with the less positive reduction voltage (negative electrode, anode) to the electrode with the more positive reduction voltage (positive electrode, cathode) during the spontaneous discharging process. At the same time, in the liquid electrolyte, cations are produced at the anode and consumed at the cathode, and there is a net positive ion flow toward the cathode to maintain charge neutrality. The discharging and charging process in intercalation-based LIBs are similar. During discharge, graphite intercalated with  $\text{Li}^+$  ions is oxidized to initiate  $\text{Li}^+$  dissolution into the electrolyte. In the electrolyte, there is a net flow  $\text{Li}^+$  flow from the graphite anode to the LiNMC cathode. At the cathode,  $\text{Li}^+$  is intercalated into the LiNMC structure.

The amount of energy we can extract from the Li-ion cell (eqn. 1.3) depends on the difference between the anode and cathode reduction voltages (eqn. 1.1), and the number of electrons transferred between them (eqn. 1.2).

$$E_{cell}(V) = E_{red,cat}(V) - E_{red,an}(V) \quad [1.1]$$

$$Q(mAh) = I(mA) * t(h) \quad [1.2]$$

$$U_{elec}(Wh) = Q(Ah) * E_{cell}(V) \quad [1.3]$$

Where “ $Q$ ” is the capacity of a cell run at a current of “ $I$ ” amperes for a time of “ $t$ ” hours, and “ $U_{elec}$ ” is the energy output of a cell with a capacity of “ $Q$ ” that operates at a working voltage of  $E_{cell}$ . When discussing Li-ion batteries, and other common

battery systems, these parameters are typically normalized by mass. Materials are often compared by their gravimetric specific capacities (instead of absolute capacity,  $Q$ ), in units of  $\text{mAh g}^{-1}$ , with their average operating voltages stated in V vs Li /  $\text{Li}^+$ . **Fig. 1.1b** shows how these terms come together to visualize the charge / discharge process in the form of a galvanostatic cycling curve. Cycling curves are presented often in this thesis, so it is worth the time to thoroughly understand what processes they depict. When cycling the battery, capacity is plotted on the x-axis in  $\text{mAh g}^{-1}$ , and voltage on y-axis in V vs Li /  $\text{Li}^+$ . Each cycle is plotted independently, with an initial capacity of 0. In the fully charged state, all of the  $\text{Li}^+$  is in the energetically unfavoured graphite anode, so cell voltage is at a maximum (4.25 V). As a constant current is produced by the cell, charge begins to be transferred, and the capacity value for that charge step begins to increase along to the x-axis. While charge is transferred,  $\text{Li}^+$  leaves graphite, travels through the electrolyte and enters the more energetically favourable LiNMC cathode, and thus cell voltage gradually drops. When the large majority of  $\text{Li}^+$  has left graphite and has entered LiNMC (approx.  $140 \text{ mAh g}^{-1}$  in **Fig. 1.1b**), the driving force for the discharging process diminishes, and cell voltage drops dramatically (toward 2.75 V). On the subsequent charging process, the capacity is plotted beginning again at 0 and counts up from there. On charge, the process is no longer spontaneous, and cell voltage increases as  $\text{Li}^+$  is moved from LiNMC to graphite. This cell managed a reversible capacity of approximately  $150 \text{ mAh g}^{-1}$ , with the majority of that charge transferred between 4.25 and 3.5 V.

Electrical energy ( $U_{elec}$ ) values tend to be reserved for when discussing a full battery system (instead of the individual electrodes) and tend to not be given for individual materials. This is due to the operating voltage of the cell being dependant

on the counter electrode, and the measured voltage of the material sometimes varying largely throughout the charge or discharge process (as seen in **Fib 1.1b**). When given, they tend to be stated in terms of specific energy density (as opposed to absolute energy,  $U_{elec}$ ) in units of Wh kg<sup>-1</sup>.

Nonetheless, it is clear that to increase the energy density of a battery, one needs to choose electrode materials with the largest voltage difference, and that can store the largest amount of charge per unit mass, or in terms of the Li-ion cell, the largest amount of Li<sup>+</sup> the material can store per unit mass. Also, it is equally important to consider the number of charge / discharge cycles the material can handle before significant degradation is observed. To use a practical example, an electric vehicle (EV) with an initial range of 500 km is much less impressive if a year later it is only able to drive 100 km on single charge.

### *Graphite Anode*

In modern Li-ion cells, the anode material is almost always graphitic carbon. Graphite operates at a low voltage of 0.01 to 0.3 V vs Li / Li<sup>+</sup>,<sup>9</sup> achieves a relatively high specific capacity of 370 mAh g<sup>-1</sup>,<sup>10</sup> and is able to retain over 90% of its capacity in Li-ion full cells after 4500 charge / discharge cycles. Graphite meets all of the criteria mentioned above for a high-quality electrode material. These excellent electrochemical considerations, along with the minimal toxicity, wide availability, and low cost of the material make graphite a relatively easy choice as the premier anode in LIBs.

Nonetheless, pure Li metal anodes have also garnered significant research attention, partially due to their slightly lower reduction voltage of 0 V vs Li / Li<sup>+</sup>, but mainly because of their much higher Li density and resultingly high specific capacity

of 3860 mAh g<sup>-1</sup>.<sup>11</sup> However, the reactivity of Li to other cell components, and the tendency of the anode to form large Li dendrites, which are sharp needle-like structures that form when Li is plated unevenly on the anode during charge (and can puncture the separator and cause a short circuit), give Li metal cells a comparatively low cycle-life. This is compounded by the obvious strains that working with Li would put on the battery manufacturing process. That being said, employing Li-metal anodes can still be useful in a research setting. It is a common practice to build “half-cells” when testing an electrode or electrolyte system. Half-cells utilize a Li-metal counter electrode opposite of a working electrode that is under investigation. The Li-metal counter electrode is used since it has a relatively infinite Li<sup>+</sup> supply and operates at 0 V vs Li / Li<sup>+</sup>. This way the observed cell voltage is (theoretically) solely dependant on the working electrode. For example, graphite is an anode material in LIBs, but in a Li-metal / graphite half cell (denoted as “Li<sub>(s)</sub> || Gr”), graphite acts as the cathode, but is still being examined for its properties as an anode material. In chapter 6 of this thesis, half cells are used to study the SIB cathode material, Na<sub>3</sub>V<sub>2</sub>(PO<sub>4</sub>)<sub>2</sub>F<sub>3</sub> (NVPF).

### *Choice of Cathode*

The cathode material is subject to more variability than the anode. Common cathode types include olivine structured polyanion phosphate materials such as LiFePO<sub>4</sub> (LFP), spinel structured materials such as LiMn<sub>2</sub>O<sub>4</sub> (LMO) or LiMn<sub>2/3</sub>Ni<sub>1/3</sub>O<sub>4</sub> (LMNO), and layered structured materials such as the LiCoO<sub>2</sub> (LCO), and LiNi<sub>1/3</sub>Mn<sub>1/3</sub>Co<sub>1/3</sub>O<sub>2</sub> (LiNMC).<sup>12-14</sup> The intercalation voltages and gravimetric capacities of each are summarized in **Table 1.1**.

**Table 1.1.** Summary of Li-ion cathode material intercalation voltages and achievable specific capacities.<sup>13, 14</sup>

Abbrev. Name	Molecular Formula	Average Voltage (V, vs Li / Li <sup>+</sup> )	Achievable Capacity (mAh g <sup>-1</sup> )
LFP	LiFePO <sub>4</sub>	3.45	170
LMO	LiMn <sub>2</sub> O <sub>4</sub>	4.1	148
LMNO	LiMn <sub>2/3</sub> Ni <sub>1/3</sub> O <sub>4</sub>	4.7	130
LCO	LiCoO <sub>2</sub>	3.9	140
LiNMC	LiNi <sub>1/3</sub> Mn <sub>1/3</sub> Co <sub>1/3</sub> O <sub>2</sub>	3.8	170

Each cathode material has unique advantages and disadvantages, like the safety and low cost of LFP due to the lack of precious metals in the compound,<sup>13</sup> or the high voltage and fast rate-capabilities of LMNO due to the 3D diffusion of Li<sup>+</sup> in its spinel structure.<sup>14</sup> Nonetheless, the most widely used of these materials is LiNMC due its high specific capacity, relatively high operating voltage, and good cycle-life.<sup>13</sup> The cycling curves shown in **Fig 1.1b** are of Gr || LiNMC full cells. Modern Gr || LiNMC LIBs can retain over 90% of their initial capacities after more than 4500 full charge / discharge cycles.<sup>15</sup>

### *Electrolyte Considerations for LIBs*

The third major component of the cell, and the main focus of the investigations on LIB and SIBs presented in this thesis, is the electrolyte. In **Fig. 1.1a**, graphite is shown as the anode, and LiNMC as the cathode, and the electrolyte appears as surrounding medium as if the cell is in a large vial. In practice, the anode and cathode materials are solid films deposited on copper and aluminum foils, respectively. The electrodes are then sandwiched together, only separated by a thin, permeable, electronically insulating separator (typically 25 μm thick, and composed of alternating polypropylene and polyethylene layers) that is wet with the liquid electrolyte.

The electrolyte has no *direct* effect on the standard voltage or charge storage capacity of the cell, as these are state functions of the electrodes. Instead, the electrolyte is the medium that facilitates stable  $\text{Li}^+$  transport between electrodes in the cell. The more stable, consistent, and rapid this transport process, the larger proportion of the cell's theoretical energy will be accessible for a larger number of cycles. As a result, the criteria of the ideal electrolyte focus on maintaining a long and stable cycle-life. The perfect electrolyte formulation should have a high thermal stability, high ionic conductivity, wide electrochemical stability window, and perhaps most importantly, the electrolyte needs to be able to form a stable solid electrolyte interface (SEI) on the electrodes. At the anode-electrolyte and cathode-electrolyte interfaces, the respective highly reductive and oxidative voltages cause significant electrolyte breakdown. The resulting insoluble electrolyte degradation products form a passivating layer on the electrode that are sufficiently electronically insulating to protect the electrolyte from further attack, but are still ionically conducting to  $\text{Li}^+$  to allow for rapid  $\text{Li}^+$  transport. It is important to note here although the term "SEI" can refer to passivating layer at both the anode and cathode, it is typically reserved for the anode-electrolyte interface, while the passivating layer at the cathode is typically referred to as the cathode-electrolyte interface (CEI). In this thesis "SEI" will refer to the interface at the anode, and CEI will refer to the interface at the cathode.

In LIBs, the electrolyte typically consists of an organic solvent and a Li-based salt. The current most commonly used liquid electrolyte is 1 M  $\text{LiPF}_6$  in an organic carbonate solvent, usually a 1:1 mixture by weight of EC / DEC (**Fig. 1.2**).

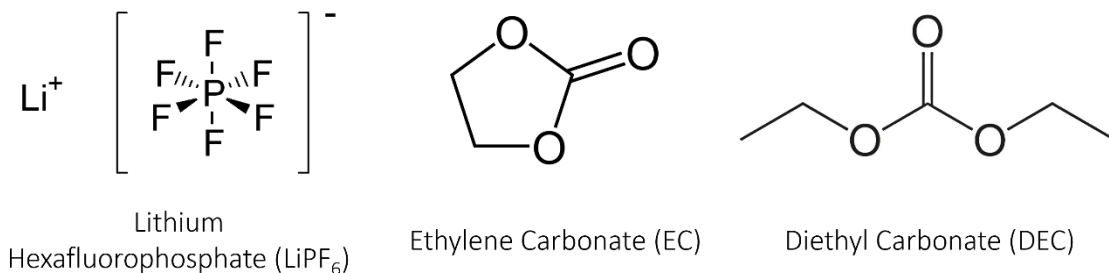


**Figure 1.2.** Molecular structures of LiPF<sub>6</sub>, EC, and DEC.

EC / DEC is an attractive choice for a high performance binary electrolyte. The high dielectric constant of EC contributes to high LiPF<sub>6</sub> solvation, while the low viscosity of DEC contributes to rapid Li<sup>+</sup> transport.<sup>16</sup> The 1:1 mixture exhibits a high ionic conductivity value of approximately 8 mS cm<sup>-1</sup> for the 1 M solution at room temperature.<sup>16</sup> The choice of PF<sub>6</sub><sup>-</sup> salt also contributes to the observed high ionic conductivity as the anion is relatively weakly coordinating, with the negative charge density distributed throughout the fluoride constituents, letting Li<sup>+</sup> move throughout the electrolyte relatively unhindered.<sup>17</sup> Perhaps the most appealing attribute of LiPF<sub>6</sub> – EC / DEC electrolytes is their ability to form stable SEI and CEI layers. The exact composition of the SEI and CEI are still the subject of multiple investigations,<sup>18</sup> but there is significant evidence to suggest that lithium carbonates resulting from EC degradation, and lithium fluoride (LiF) from LiPF<sub>6</sub> degradation, are key to an electronically passivating, but Li<sup>+</sup> conductive, SEI layer.<sup>19</sup>

However, this electrolyte formulation is not perfect. EC and DEC are both quite flammable, with DEC having a flash point of just 25 °C. Additionally, LiPF<sub>6</sub> is highly vulnerable to hydrolysis by any water (H<sub>2</sub>O) impurities in the cell, forming corrosive hydrofluoric acid (HF), which can degrade other cell components and pose significant environmental and safety risks.<sup>20</sup> Further, the electrolyte oxidizes readily above 4.5 V

vs Li / Li<sup>+</sup>.<sup>21, 22</sup> This imposes an upper voltage limit on the battery that is not an issue with the currently used LiNMC cathodes, but hinders the exploration of higher voltage, and thus possibly higher energy density, cathode materials.

Indeed, there are many factors to consider when choosing a suitable electrolyte for a battery system, and there is an abundance of research on different approaches to finding new and improved electrolyte systems. Section 1.3 discusses alternative electrolyte formulations for LIBs and SIBs, including the strategy of concentrating electrolytes close to their saturation point as a means of introducing favourable electrochemical properties. Chapter 5 of this thesis presents an investigation of the transport properties of highly concentrated lithium bis(trifluoromethyl sulfonyl)imide (LiTFSI) in adiponitrile (ADN) electrolytes, a possible candidate for a high voltage electrolyte system stable up to 6 V vs Li / Li<sup>+</sup>, while Chapter 6 presents an electrochemical study of the NaTFSI in ADN analogue. A more detailed examination of the advantages and disadvantages of alternative electrolyte formulations for LIBs is presented in section 1.3.

### 1.1.2 – From Li-Ion to Na-Ion Batteries

The above introduction to LIBs illustrates how the anode, cathode, and electrolyte need to work together in tandem to produce a high energy density, and long-life battery system. The following section will translate these concepts to the SIB, and discuss how they are different from, and similar to, LIBs, as it pertains to this thesis. Similar to the studies presented herein on LIBs, the research done in the context of SIBs also focuses on the electrolyte.

### *Hard Carbon Anodes*

The main operating principles of the SIB are identical to those of the LIB. Na<sup>+</sup> cations move from the anode to the cathode on discharge, through the liquid electrolyte. In practice however, there are a number of considerations that have held SIBs from reaching the popularity of the Li-ion cell. Firstly, current Na intercalation materials tend to have lower capacities and voltages than their Li counter parts.<sup>23</sup> The observed lower voltages are possibly due the weaker interaction from the comparatively “soft” nature of the Na<sup>+</sup> cation compared to Li<sup>+</sup>, making intercalation less favourable.<sup>24</sup> This effect is certainly present when attempting to use graphitic carbon anodes in SIBs. Na<sup>+</sup> intercalation into graphite is significantly less favourable than Li<sup>+</sup> intercalation due to insufficient interactions between Na<sup>+</sup> and the graphene layers.<sup>25</sup> This makes high density Na<sup>+</sup> intercalation less energetically favourable than simply plating Na metal on the graphite surface,<sup>26</sup> and as a result, standard graphite only reaches capacities of 35 mAh g<sup>-1</sup> in Na metal half-cells (compared to the 370 mAh g<sup>-1</sup> value for Li stated above).<sup>27</sup> To reiterate from earlier, an ideal anode material should have a low operating voltage, a high capacity, and a long cycle-life. The extremely low capacity of 35 mAh g<sup>-1</sup> for graphite in SIBs certainly does not qualify. For this reason, SIBs often employ “hard” carbonaceous materials instead of regular graphite. Hard carbon (HC) is synthesized by the high temperature pyrolysis of carbonaceous polymers such as cellulose and is comprised of a microstructure of disordered graphene layers arranged in a “house of cards” type structure, where graphene sheets are not stacked in a single dimension as they are for ordered graphite.<sup>26</sup> This disordered layering of graphene results in larger pore volumes, and a larger number of pore environments, that allows for favourable Na intercalation.<sup>26</sup>

The operating voltage of HC is in the range of 0.01 to 1 V, which is an unfavourable increase over the 0.01 to 0.3 V for graphite in LIBs. Nevertheless, modern HC materials can reach capacities of over 300 mAh g<sup>-1</sup>, and retain 93% of their initial capacity after 100 cycles.<sup>26, 28, 29</sup> HC is currently the best anode material for use in SIBs, and further improvements are expected as Na-based batteries garner more research attention going forward.

It should be noted here that, like with LIBs, Na metal anodes have also been thoroughly investigated for use in SIBs, but suffer the same drawbacks stemming from their highly reductive nature, and clear manufacturing difficulties that come with working with alkali metals. As such, they are not currently feasible for use in practical SIBs, but are still useful for testing individual anode or cathode materials in Na-ion half cells.

#### *Choice of Cathode*

The cathode choice in SIBs is notably more complicated than that of the anode. Similar to the LIB, the ideal SIB cathode needs to operate at a relatively high voltage and store a sufficiently high amount of Na<sup>+</sup> to achieve competitive energy densities and retain that energy density over a large number of cycles. However, unlike LiNMC materials in the LIB, no material clearly stands out as the cathode of choice. The Na analogue of LiNMC, NaNi<sub>1/3</sub>Mn<sub>1/3</sub>Co<sub>1/3</sub>O<sub>2</sub> (NaNMC) has been explored for use in SIBs, but shows a limited capacity of just 120 mAh g<sup>-1</sup> over an approximate average voltage of 2.8 V.<sup>30</sup> This is compared to the previously stated practical capacity of LiNMC of 170 mAh g<sup>-1</sup>, over an average voltage of 3.8 V.<sup>30</sup> The strikingly low operating voltage of the Na analogue is the result of the aforementioned reduced Na interactions with the layered oxide lattice due to the softer nature of the cation,

decreasing the energetic favourability of the intercalated structure.<sup>24</sup> Nonetheless, research has shown that this effect is most prominent in layered oxides, and other cathode classes can still offer competitive intercalation voltages. A summary of other notable SIBs cathodes is given in **Table 1.2**.

**Table 1.2.** Summary of select Na-ion cathode material intercalation voltages and achievable specific capacities.

Abbrev. Name	Molecular Formula	Average Voltage (V, vs Li / Li <sup>+</sup> )	Achievable Capacity (mAh g <sup>-1</sup> )
NaNMC	NaNi <sub>1/3</sub> Mn <sub>1/3</sub> Co <sub>1/3</sub> O <sub>2</sub>	2.8	170 <sup>30</sup>
β-NMO	β-NaMnO <sub>2</sub>	3.2	190 <sup>31</sup>
NVP	Na <sub>3</sub> V <sub>2</sub> (PO <sub>4</sub> ) <sub>3</sub>	3.4	120 <sup>32</sup>
NVPF	Na <sub>3</sub> V <sub>2</sub> (PO <sub>4</sub> ) <sub>2</sub> F <sub>3</sub>	3.85	120 <sup>33</sup>

A higher energy density alternative to NaNMC is β-NaMnO<sub>2</sub> (β-NMO), which was shown to be able to achieve an excellent initial capacity of 190 mAh g<sup>-1</sup> at an average voltage of 3.2 V, but retained a capacity of just 130 mAh g<sup>-1</sup> after 100 cycles.<sup>31</sup> 130 mAh g<sup>-1</sup> is still a reasonable capacity, but the steep trajectory of capacity decay implies significant material degradation that is not fit for long cycle-life SIBs. On the other side of this spectrum is Na<sub>3</sub>V<sub>2</sub>(PO<sub>4</sub>)<sub>3</sub> (NVP), which has been shown to achieve an excellent capacity retention of 86 % after 1000 cycles, albeit at a comparatively mediocre capacity of 120 mAh g<sup>-1</sup> and operating voltage of 3.4 V.<sup>32</sup> The multivalent nature of vanadium in the NVP cathode results in multiple distinct voltage plateaus upon cycling. The V<sup>2+</sup> / V<sup>3+</sup> couple is observed at 1.6 V and the V<sup>3+</sup> / V<sup>4+</sup> couple at 3.4 V. Unfortunately, only the higher voltage V<sup>3+</sup> / V<sup>4+</sup> couple has been accessed when the material is employed as a cathode, due to the 1.6 V couple being too close in voltage to the initial desodiation voltage of HC anodes.<sup>29, 32</sup> A higher voltage process for the

$V^{4+} / V^{5+}$  should also be viable, but was not attempted to be accessed in NVP cells, possibly due to voltage limitations of the electrolyte.

Similar to NVP,  $\text{Na}_3\text{V}_2(\text{PO}_4)_2\text{F}_3$  (NVPF) has also received attention as a possible SIB cathode material. The addition of fluorophosphates to the crystal structure significantly increases the operating voltage of the cell, with the  $V^{3+} / V^{4+}$  couple appearing as a two-tiered plateau with voltages of 3.6 and 4.1 V, respectively (**Fig. 1.3**).<sup>33, 34</sup> This two-tiered plateau for a single redox couple arises from there being two distinct, equally occupied  $\text{Na}^+$  sites in the NVPF crystal structure, with one site being more stable than the other. Focusing on the charging curve in **Fig. 1.3**,  $\text{Na}^+$  from the less stable site is extracted preferentially at 3.6 V to form  $\text{Na}_2\text{V}_2(\text{PO}_4)_2\text{F}$ , where half of the vanadium is oxidized to  $V^{4+}$ . At this point, extraction of the (originally) more stable Na site becomes preferential, and the deintercalation proceeds at the 4.1 V plateau to form  $\text{NaV}_2(\text{PO}_4)_2\text{F}$ , where all vanadium is now in the  $V^{4+}$  state.<sup>33</sup>

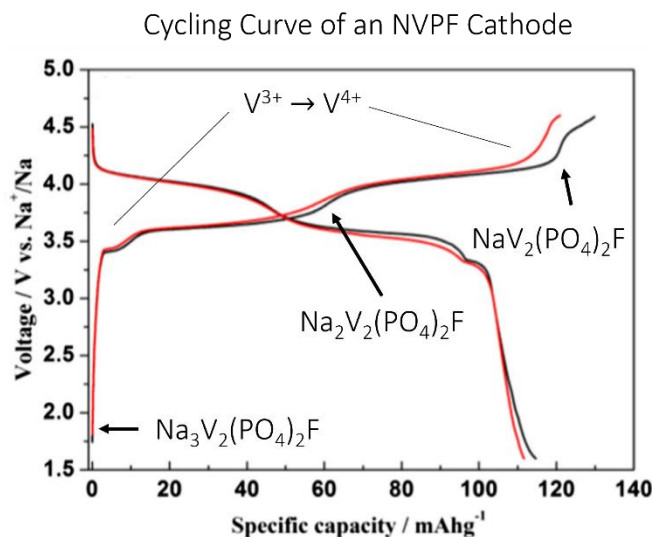


**Figure 1.3.** Cycling curve of an NVPF cathode, emphasizing the phase transformations during the charging process, where NVPF is deintercalated.<sup>33</sup>  
<sup>†</sup>Reprinted with permission from Journal of Power Sources 256 (2014) 258 – 263 © 2014 Elsevier.

If the cell is stopped at this point, a high average voltage of 3.85 V with a capacity of 120 mAh g<sup>-1</sup> is achieved.<sup>33</sup> The V<sup>4+</sup> / V<sup>5+</sup> redox couple is also accessible at 4.9 V, where full oxidation to the V<sub>2</sub>(PO<sub>4</sub>)<sub>2</sub>F phase is observed with a high capacity of 165 mAh g<sup>-1</sup>. Accessing this event significantly hinders the capacity retention of the cathode, possibly due to structural collapse as this extreme stage of cycling, but also due to significant electrolyte breakdown at this highly oxidizing voltage.<sup>34, 35</sup> Due to the good capacity, high voltage, reliability, and interesting chemistry of NVPF, all SIBs studied in this thesis utilize NVPF as the active cathode material.

### *Electrolyte Considerations for SIBs*

Electrolytes in SIBs play a similar role to the electrolytes of LIBs, except of course for the distinction of facilitating Na<sup>+</sup> transport rather than Li<sup>+</sup> transport. As a result, the needs of Na electrolytes for SIBs are equal to those of Li electrolytes for LIBs. They must exhibit a high ionic conductivity, high thermal stability, wide electrochemical stability window, and must be able to form stable, Na<sup>+</sup> conductive, SEIs and CEIs.

Na electrolytes tend to have higher ionic conductivities than their Li counterparts, again due to the relative softness of the Na<sup>+</sup> cation causing less cation – solvent interactions, allowing Na<sup>+</sup> to move more freely.<sup>36, 37</sup> Like the LIB, the most widely used SIB electrolyte is 1 M NaPF<sub>6</sub> in a solvent of 1:1 EC / DEC, with an equally high ionic conductivity of 8.5 mS cm<sup>-1</sup> for the 1 M solution at room temperature.<sup>38</sup> NaPF<sub>6</sub> in EC / DEC electrolytes offer the same stable SEI and CEI of the Li analogue, except of course with NaF in place of LiF as the main structural component.<sup>39</sup> Since the organic solvent is unchanged, the same thermal stability issues arising from the flammability of EC and DEC are still present, and the electrolyte is also limited by the same electrochemical stability window, with a 4.5 V upper limit.<sup>35</sup>

The research on SIBs presented in this thesis is found in Chapter 6, and is an investigation into the enhanced electrochemical stability of high voltage NaTFSI in ADN electrolytes at unusually high salt concentrations. A further review the electrochemical benefits of concentrating electrolytes far past the typical 1 M concentration is given in Chapter 6, and in section 1.3 of this introduction.

### 1.1.3 – Na-O<sub>2</sub> Batteries & Their (Many) Challenges

The transition from the LIB to the SIB is relatively simple. The transition from metal-ion batteries (MIBs) to metal-oxygen batteries (MOBs), such as the LiOB and the NaOB, is a bit more complex. The works of this thesis primarily focus on the NaOB (Chapters 3 and 4), with a brief examination of the LiOB in Chapter 6. The wide majority of LiOB chemistry relevant to this thesis can be directly translated from an understanding of the NaOB. As such, this introduction will concentrate on NaOBs alone.

#### *NaOB Fundamentals*

From a distance, the general electrochemical operating principles of NaOBs are identical to those of the SIBs. They are composed of an anode with a lower reduction potential, a cathode with a higher reduction potential, and a liquid electrolyte that facilitates ion transport. The main difference however, is that NaOBs do not produce energy through the an intercalation mechanism, instead the cell produces energy through the electrochemically-mediated exothermic synthesis reaction of Na metal and O<sub>2</sub> gas. **Fig. 1.4a** shows a general schematic of a NaOB undergoing the discharge process.

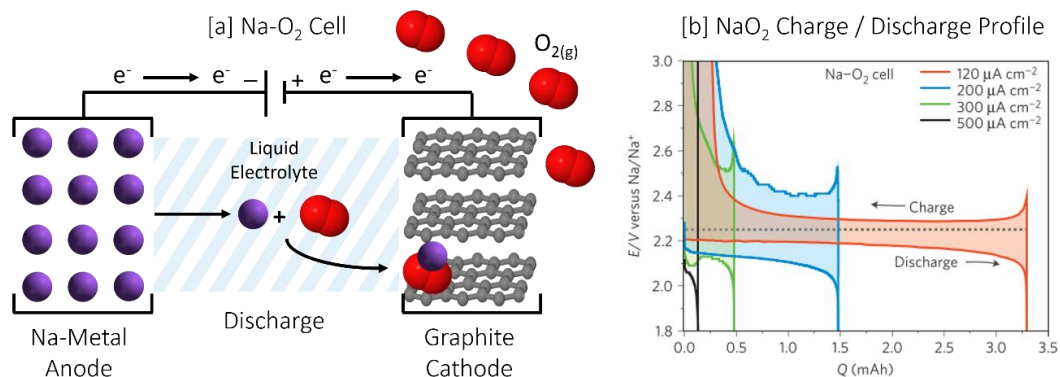


**Figure 1.4.** [a] General schematic of a typical Na-O<sub>2</sub> cell employing a Na-metal anode, a carbon cathode, and a liquid electrolyte. †[b] Representative galvanostatic discharge / charge curves of a NaO<sub>2</sub> producing NaOB cycled at varying current densities. †Reprinted with permission from Nature Mater 12, 228–232 (2013) © 2013 Nature Publishing Group.<sup>40</sup>

In a typical NaOB, Na metal is used as the anode, a carbon support is used as the cathode, sodium triflate (NaOTf) in diethylene glycol dimethyl ether (DEGDME) is used as the electrolyte, and the assembled cell is placed in a pure O<sub>2</sub> atmosphere. During discharge, Na metal is oxidized to form Na<sup>+</sup> cations in solution. Na<sup>+</sup> is then transported by the liquid electrolyte to the cathode. At the cathode, O<sub>2</sub> is dissolved into the liquid electrolyte, and the high surface area carbon support facilitates the reduction of O<sub>2</sub> to O<sub>2</sub><sup>-</sup> in what is called the oxygen reduction reaction (ORR). Under ideal circumstance, Na<sup>+</sup> and O<sub>2</sub><sup>-</sup> can then combine to form sodium superoxide (NaO<sub>2</sub>), which precipitates onto the carbon cathode in cubic crystallites.<sup>41</sup> On the reverse charging process, NaO<sub>2</sub> is solvated back into the Na<sup>+</sup> and O<sub>2</sub><sup>-</sup> substituents, where O<sub>2</sub><sup>-</sup> can be oxidized back into O<sub>2</sub> gas in the oxygen evolution reaction (OER), and Na<sup>+</sup> can be transported back to the Na anode to be reduced back to Na metal. A typical discharge / charge curve for a NaO<sub>2</sub> producing NaOB is given in **Fig.1.4b**. One of the large advantages of NaO<sub>2</sub> producing cells is the very low overpotential observed on charge, this due to the low dissolution energy of NaO<sub>2</sub>, and results in very high round

trip efficiencies in NaO<sub>2</sub>-based NaOBs. More insight on the morphology of crystallized NaO<sub>2</sub> is given below in **Fig. 1.5**.

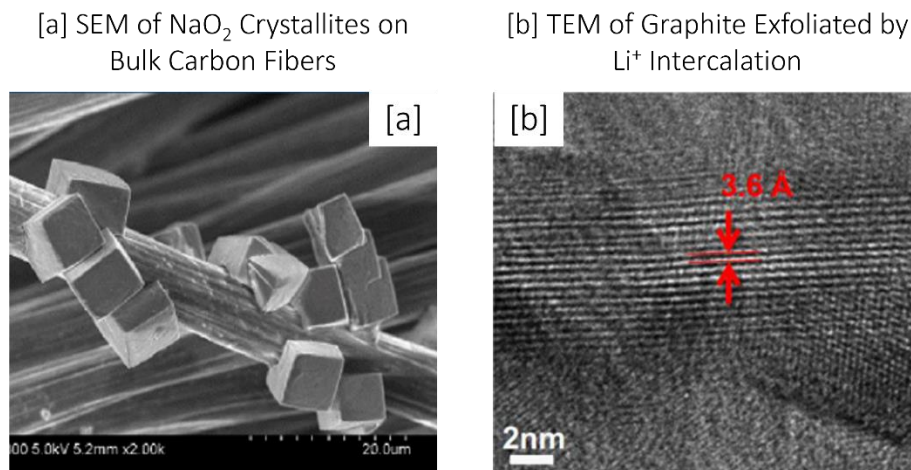


**Figure 1.5.** <sup>†</sup>[a] SEM image of NaO<sub>2</sub> crystallites that have deposited on the surface of the bulk carbon fibres of a carbon cloth NaOB cathode. <sup>††</sup>[b] TEM of exfoliated graphene layers of a LIB cathode after Li<sup>+</sup> intercalation. <sup>†</sup>Reprinted with permission from J. Phys. Chem. Lett. 2017, 8, 19, 4794–4800 © 2017 American Chemical Society.<sup>42</sup> <sup>††</sup>Reprinted with permission from Carbon 2012, 50, 10, 3836–3844 © 2012 Elsevier.<sup>43</sup>

**Fig. 1.5** highlights one of the main differences between MIBs and MOBs. **Fig 1.5b** shows an *in-situ* transmission electron microscopy (TEM) image of a charged LIB taken by Liu et al. The image characterizes the exfoliation of individual graphene layers in a graphite anode of a LIB during Li<sup>+</sup> intercalation. The addition of Li<sup>+</sup> to the graphite structure increases the layer spacing from approximately 3.4 to 3.6 Å.<sup>43</sup> In contrast, **Fib 1.5a** shows a scanning electron microscopy image (SEM) by Yadegari et al. of micrometer-scale cubic NaO<sub>2</sub> crystals that have precipitated from solution onto the bulk carbon fibres of a carbon cloth cathode during discharge.<sup>42</sup> This example highlights the significant differences between the electrochemical processes of LIBs and NaOBs.

As mentioned above, NaO<sub>2</sub> is produced exclusively in the ideal NaOB, and indeed studies indicate that NaO<sub>2</sub> is the most prominent electrochemical discharge product,<sup>41</sup> however, the formation of other sodium oxides is possible. To understand why NaO<sub>2</sub> is prominently observed, it helps to examine the competing discharge pathways. The change in Gibbs free energy ( $\Delta G$ ) for the synthesis reactions of NaO<sub>2</sub> and other competing electrochemical products are given in **Table 1.3**. The corresponding cell voltages are calculated using the standard thermodynamic relationship (**eqn. 1.4**):

$$\Delta G = -nFE_{cell} \quad [1.4]$$

Where “ $n$ ” is the number of electrons transferred in the formation process, and “ $F$ ” is the Faraday constant, 96485 C mol<sup>-1</sup>.

**Table 1.3.** Competing reaction pathways and resulting theoretical cell voltages, specific capacities, and energy densities for the NaOB. Table adapted from Hartmann et al. Nature Materials, 2013, 12, 228 – 232.<sup>40</sup> \*\*Specific capacity and energy density values are given in terms of mass of the formed product.

Reaction	$\Delta G$ (kJ mol <sup>-1</sup> )	$E_{cell}$ (V)	Theo. Specific Capacity** (mAh g <sup>-1</sup> )	Theo. Energy Density** (Wh kg <sup>-1</sup> )
$Na + O_2 \rightarrow NaO_2$	-219	2.27	488	1110
$2Na + O_2 \rightarrow Na_2O_2$	-450.	2.33	689	1610
$2Na + \frac{1}{2}O_2 \rightarrow Na_2O$	-415	1.95	867	1690

From a thermodynamic perspective, one may expect that Na<sub>2</sub>O<sub>2</sub> would be formed preferentially on discharge, however as stated above, NaO<sub>2</sub> is widely recognized as the major discharge product in NaOBs.<sup>41, 44-47</sup> This is due to NaO<sub>2</sub> being formed by a kinetically favoured single electron transfer process, whereas Na<sub>2</sub>O<sub>2</sub> is formed via a

thermodynamically favoured, but kinetically inhibited, two electron transfer process that requires the formation of the doubly reduced  $O_2^{2-}$  anion. The exact mechanism of electrochemical  $NaO_2$  formation in NaOBs is discussed below.

### *Solution-Based Discharge / Charge Mechanism*

The exact formation mechanism of  $NaO_2$  is a more complicated than what is shown in **Fig. 1.4**. A number of publications have shown that  $NaO_2$  formation occurs through a solution-based mechanism that is mediated by a proton phase-transfer catalyst (PPTC) (**Fig. 1.6**, **eqn. 1.5** and **1.6**).<sup>45, 47</sup>



As depicted in **Fig. 1.6**,  $O_2$  gas is dissolved into the liquid electrolyte and is reduced at the carbon cathode to form  $O_2^-$ .  $O_2^-$  is then able to diffuse within the electrolyte and be stabilized by the PPTC, forming  $HO_2$ .  $HO_2$  undergoes a substitution reaction with  $Na^+$  from the liquid electrolyte to form the final  $NaO_2$  product, which precipitates on the carbon cathode surface in cubic crystallites.<sup>41</sup> On the reverse charging process,  $NaO_2$  dissolution occurs to form  $Na^+$  and  $O_2^-$ . Once again the  $O_2^-$  anion is stabilized by the PPTC, before being oxidized at the carbon support to form  $O_{2(g)}$ .

The proton source in the solution-based mechanism can come from a number of different sources, including  $H_2O$  impurities in the liquid electrolyte or the supplied oxygen gas. Proton abstraction from the organic electrolyte is also a possibility, as  $O_2^-$  has been shown to be reactive toward carbonate, and some glyme, solvents.<sup>48-50</sup> A landmark study by Xia et al. goes as far to suggest that some form of  $H_2O$  impurity is necessary for  $NaO_2$  formation.<sup>45</sup>

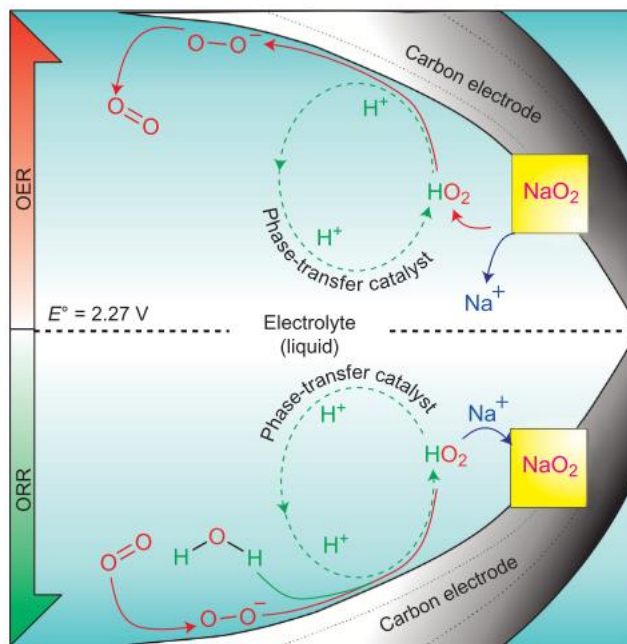
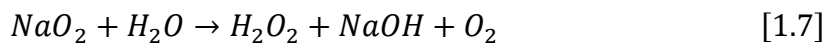


**Figure 1.6.** <sup>†</sup>[a] Solution-based formation and decomposition mechanism for NaO<sub>2</sub> showing the proton phase transfer catalyst. <sup>†</sup>Reprinted with permission from Nature Chemistry volume 7, pages 496–501 (2015) © 2013 Nature Publishing Group.<sup>45</sup>

The solution-based formation mechanism for NaO<sub>2</sub> has the benefit of inherently utilizing the entire cathode surface area, as the entire cathode should be thoroughly wet with liquid electrolyte that contains dissolved O<sub>2</sub>. However, the need for moisture also opens the door for a number of side reactions in the cell.

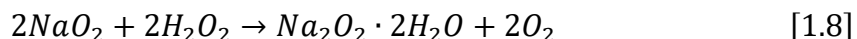
#### *NaO<sub>2</sub> & H<sub>2</sub>O: A Love / Hate Relationship*

As one may expect, NaO<sub>2</sub> is also moisture sensitive, reacting spontaneously to form hydrogen peroxide, sodium hydroxide, and oxygen gas (eqn. 1.7).<sup>51</sup>



The uncontrolled degradation of NaO<sub>2</sub> by moisture leads to a loss of the discharged capacity, as the formed NaOH is not rechargeable in the reverse process. This results in the need for strict controls on the amount of moisture in NaOBs, significantly more than those of LIB, which can be manufactured in simple dry-rooms.

Moisture present in the cell may also cause the formation of sodium peroxide dihydrate ( $\text{Na}_2\text{O}_2 \cdot 2\text{H}_2\text{O}$ ), another product that has been reported in NaOBs.<sup>48, 52, 53</sup> The exact formation mechanism for  $\text{Na}_2\text{O}_2 \cdot 2\text{H}_2\text{O}$  is less clear, but is thought to first involve the degradation of  $\text{NaO}_2$  by moisture to form  $\text{H}_2\text{O}_2$  as summarized above, followed by the attack of further  $\text{NaO}_2$  (eqn. 1.8).<sup>42</sup>



This mechanism is debatable, however, as multiple different reaction pathways have been discussed in literature, including the formation of  $\text{Na}_2\text{O}_2$  and simple absorption of  $\text{H}_2\text{O}$  from the electrolyte.<sup>48, 54</sup> Nonetheless, Some groups have reported reversible cycling when  $\text{Na}_2\text{O}_2 \cdot 2\text{H}_2\text{O}$  is the major discharge product.<sup>52, 55</sup> But unfortunately,  $\text{Na}_2\text{O}_2 \cdot 2\text{H}_2\text{O}$  production causes much higher overpotentials on charge, in the range of 1 to 2 V, which can irreversibly damage the cell overtime; and further,  $\text{Na}_2\text{O}_2 \cdot 2\text{H}_2\text{O}$  is unstable for long periods of time at room temperature, meaning a cell producing  $\text{Na}_2\text{O}_2 \cdot 2\text{H}_2\text{O}$  would lose capacity overtime as the dihydrate formed on discharge slowly decomposes.<sup>42, 56</sup>

### *NaO<sub>2</sub> & the Carbon Cathode*

Even if the moisture content of the cell is balanced perfectly to give preferable  $\text{NaO}_2$  formation,  $\text{NaO}_2$  has been shown to be inherently unstable to the carbon of the cathode support, oxidatively degrading the substrate to produce  $\text{Na}_2\text{CO}_3$  over time in a parasitic side-reaction.<sup>42, 50, 57</sup> The nature of the reactivity of  $\text{NaO}_2$  with the carbon support (and its initial direct observation) is the subject of the research conducted in Chapter 3 of this thesis, although the topic is worth mentioning here as it is important to understanding the direction of research in the NaOB community. Even before it was directly observed in the works presented herein, it had been previously expected

that NaO<sub>2</sub> degradation of the carbon cathode was present, due to the detection sodium carbonate (Na<sub>2</sub>CO<sub>3</sub>), and other carboxylate side products, in cycled Na-O<sub>2</sub> cells, as well as a similar degradation pathway being observed in LiOBs.<sup>44, 50</sup> Cathode degradation by NaO<sub>2</sub> results in a sudden increase in overpotentials upon charge, since the NaO<sub>2</sub>-carbon interface becomes passivated, and the resistance for charge transfer increases.<sup>50, 58, 59</sup> As mentioned previously, the observation of the reaction of NaO<sub>2</sub> with the carbon cathode, and the mitigation of this degradation process, are the subject of Chapters 3 and 4 of this thesis. A more extensive review of other attempts to stabilize the cathode of NaOBs is given in section 1.2 of this introduction.

### *Na Metal Anode*

The anode choice for NaOBs is relatively simple. Na metal is used in almost every study on NaOBs, as it is the only material currently capable of supplying enough Na<sup>+</sup> cations to facilitate the high capacities achieved at the carbon cathode. Using Na-metal in NaOB presents the same challenges of using Na-metal and Li-metal anodes for SIBs and LIBs, including the highly reductive nature of alkali metals, and their tendency to form destructive metallic dendrites on charge. The reactivity of Na is made worse when used in the O<sub>2</sub> atmosphere of the NaOB, where O<sub>2</sub><sup>-</sup> in the electrolyte can diffuse through the separator to react with Na metal and the organic electrolyte to form sodium carbonates on the Na metal surface, passivating the electrochemical activity of the anode.<sup>60</sup>

One study has attempted to use pre-sodiated carbon materials as the anode in place of Na metal.<sup>61</sup> The modified Na-O<sub>2</sub> cells did show a slight cycle-life improvement over Na-metal cells, but also at a significantly decreased capacity.<sup>61</sup> The idea of replacing the Na-anode with a more stable carbon anode is attractive, but

would eliminate the high energy density advantage of NaOBs. Na-metal will likely remain the only real candidate for NaOBs anodes in the near future.

### *Electrolyte Considerations for NaOBs*

The needs for NaOB electrolytes differ slightly from those of the SIB and LIB. The ideal NaOB electrolyte still has a high ionic conductivity, high thermal stability, and wide electrochemical stability window. The requirement for stable SEI production certainly still exists as well, but is less of a focus in NaOB research, as stabilizing the complex discharge chemistry at the cathode has taken priority. Stability to the  $O_2^-$  anion is also important, and is a consideration not needed in SIBs. Due to the open-top nature of Na- $O_2$  cells, the volatility of the electrolyte is a much larger consideration in NaOBs than in SIBs, and the  $O_2$  solubility of the electrolyte should also be considered due to the solution-based discharge mechanism discussed above.

The primary electrolyte used in NaOBs today is 0.5 M NaOTF in DEGDME (**Fig 1.7**). The relatively low concentration of 0.5 M used in NaOBs is due to  $O_2$  solubility considerations. Admittedly there has not been much research on this subject as of late, but in the early days of LiOB research, one study showed that 0.5 M  $LiPF_6$  in an organic carbonate solvent performed much better than the 1 M counterpart due to increased  $O_2$  solubility, with minimal loss of  $Li^+$  conductivity.<sup>62</sup> As a result the 0.5 M concentration persisted in LiOB and NaOB research, even throughout significantly different electrolyte formulations. DEGDME has a high boiling point of 162 °C, which suits the NaOB well, and is stable up to 4.5 V vs Na /  $Na^+$ .

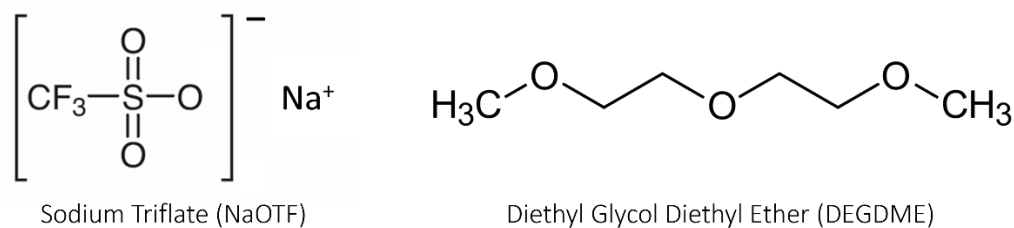


**Figure 1.7.** Molecular structures of NaOTF and DEGDME.

The primary reason for the use of an ether solvent, instead of the typically used carbonate solvents found in SIBs, is the resistance of the ether to superoxide attack. NaOBs discharged with both propylene carbonate (PC) and EC solvents were found to almost exclusively produce  $\text{Na}_2\text{CO}_3$  on discharge resulting from superoxide attack of PC and EC,<sup>48, 63</sup> a phenomenon that had been observed in LiOBs previously for multiple carbonate systems.<sup>64, 65</sup> In contrast, ether based electrolytes such as DEGDME, dimethyl ether (DME), and tetraethylene glycol dimethyl ether (TEGDME) have shown to be much more resilient to superoxide attack, and have all displayed excellent  $\text{NaO}_2$  formation on the initial discharge cycle.<sup>41, 63, 66</sup> The attack by superoxide on ether solvents is thought to involve proton abstraction from the solvent to form the aforementioned  $\text{HO}_2$  species,<sup>50</sup> and is expected to be a much slower process judging by the relative success of ether electrolytes in these battery systems. Each of the ether solvents mentioned are still used in NaOB research today, but DEGDME is thought to stabilize the  $\text{O}_2^-$  anion in solution to the greatest extent, and subsequently promote the most reversible ORR / OER process.<sup>67</sup> As a result DEGDME remains the most popular solvent for now.

NaOTF is used preferentially over  $\text{NaPF}_6$  in NaOBs results from early studies on LiOBs showing that  $\text{LiPF}_6$  was prone to degradation by  $\text{Li}_2\text{O}_2$ , forming large amounts of  $\text{LiF}$ .<sup>68</sup> The instability of  $\text{NaPF}_6^-$  in NaOB system was confirmed by Dilimon et al.,

who showed that NaPF<sub>6</sub> in dimethyl sulfoxide (DMSO) electrolytes do facilitate a reversible ORR. This was compared to NaOTF which showed excellent ORR reversibility in the same system.<sup>67</sup> The moisture instability of NaPF<sub>6</sub> is also an issue, the PF<sub>6</sub><sup>-</sup> anion is known to readily hydrolyze to produce HF, which is a significant issue in batteries that rely on H<sub>2</sub>O impurities in the electrolyte to cycle.

For these reasons, NaOTF in DEGDME remains the electrolyte of choice in NaOB systems. In the studies on NaOBs presented in this thesis, Na metal is used as the anode, and 0.5 M NaOTF in DEGDME is used as the electrolyte. The main purpose of the anode and electrolyte in these studies is to facilitate a consistent ORR and OER, so that the electrochemical processes happening at the cathode can be investigated.

## 1.2 – Cathode Choice in Na-O<sub>2</sub> Batteries

The challenge of finding a suitably stable cathode material for use in NaOBs is the main focus of the research presented in Chapters 3 and 4 of this thesis. As a result, it is necessary to have a basic knowledge of other cathode choices that have been studied in literature to understand the research direction chosen.

The cathode arguably plays the most important role in NaOBs, as it has the responsibility of providing a stable nucleation point for NaO<sub>2</sub> formed on discharge. Several different cathode materials have been implemented in the early stages of NaOB research, including both a variety of designer carbon allotrope materials, and precious metal catalyst-doped systems.

### 1.2.1 – Carbon Allotropes

In the most basic NaOB cells, cathodes are simple circular punch-outs of commercial carbon cloth or carbon paper gas diffusion layers (GDL). These cathodes

have the advantage of being porous, durable, lightweight, readily commercially available, and very easy to implement in research and commercial settings. The high porosity of carbon paper is advantageous as it allows  $O_2$  to homogeneously diffuse through the structure, and as a result, a high density of  $NaO_2$  cubic crystallites are observed in discharged carbon paper cells.<sup>41</sup> Ultimately though, the carbon paper is still susceptible to degradation by  $NaO_2$  and only a limited number of cycles are possible before significant decreases in capacity are observed.<sup>69</sup>

Jian et al. built expanded the use of carbon paper cathodes by synthesizing their own carbon nanotube paper (CNP) with the idea that the nanotube structure would provide a much higher surface area for  $NaO_2$  nucleation and be more active toward the ORR. The group was successful in this regard, observing very high discharge capacities of over  $7000 \text{ mAh g}^{-1}$ , and were able to achieve a stable discharge capacity of  $1000 \text{ mAh g}^{-1}$  over 7 discharge / charge cycles. However, the cell displayed significant irreversible capacities on the charging process, and the operating voltage on discharge decreased slowly with each cycle. Both of which the group attributed to the formation of irreversible side products during cycling.

Liu et al. attempted to move away from the standard paper style electrodes and instead implemented reduced graphene oxide (rGO) nanosheets cast directly onto a stainless-steel mesh current collector. They reported a mix of  $NaO_2$  and  $Na_2O_2 \cdot 2H_2O$  as the primary discharge products, and were able to cycle the rGO cathodes with an extremely high initial capacity of  $40,000 \text{ mAh g}^{-1}$ , corresponding to  $12 \text{ mAh cm}^{-2}$ . The group attributes this high capacity to the enhanced pore volume of the rGO electrode macrostructure compared to typical carbon materials, allowing  $NaO_2$  crystals grow to larger cube sizes before the electrode pores become blocked. The authors then showed

reversible cycling to a limited capacity of 3 mAh cm<sup>-2</sup> for 17 cycles before significant degradation was observed. Na<sub>2</sub>CO<sub>3</sub>, sodium formate (NaHCO<sub>2</sub>), and sodium acetate (NaCH<sub>3</sub>CO<sub>2</sub>) were all characterized as degradation products of the carbon cathode and DME electrolyte by a mix of <sup>23</sup>Na, <sup>1</sup>H, and <sup>13</sup>C solid-state NMR.<sup>58</sup>

One study reported Na<sub>2</sub>O<sub>2</sub> as the main discharge product on carbon cathodes instead of the commonly seen NaO<sub>2</sub>. Sun et al. used a diamond-like carbon thin films prepared by an r.f. sputtering technique.<sup>70</sup> Na<sub>2</sub>O<sub>2</sub> was identified by selected area electron diffraction (SAED), and further examination by Fourier Transform Infrared Spectroscopy (FTIR) identified the presence of Na<sub>2</sub>CO<sub>3</sub> as well. The production of Na<sub>2</sub>O<sub>2</sub> is interesting as the product is more stable than NaO<sub>2</sub>, so may lead to a longer-life battery, but unfortunately the group reported substantial capacity decay with every subsequent cycle due to the high overpotentials needed to oxidize Na<sub>2</sub>O<sub>2</sub> on charge, which caused electrolyte degradation.<sup>70</sup>

Changing the morphology of carbon can certainly have a positive impact on cell performance, as seen in the high capacities achieved in CNP and rGO cathode systems, and can even effect the identity of the discharge products. Nonetheless, cycle lifetime is still low and alternative strategies need to be examined to mitigate the oxidative instability of carbon within the cathode system.

### 1.2.2 – Catalysts in NaOBs

One popular approach to stabilizing the carbon cathode in NaOBs is to avoid the production of NaO<sub>2</sub> altogether by lowering the kinetic barrier for the formation of the more thermodynamically stable product, Na<sub>2</sub>O<sub>2</sub>. In order for this to work effectively, the catalyst should also catalyse the reverse OER to lower the overpotential of the reverse charging process, thus avoiding the degradative effects of electrolyte

decomposition on charge. Given the plethora of research on ORR / OER catalysts in the polymer electrolyte membrane fuel cell (PEMFC) community, it makes sense that a number of these would be applied to the NaOB.

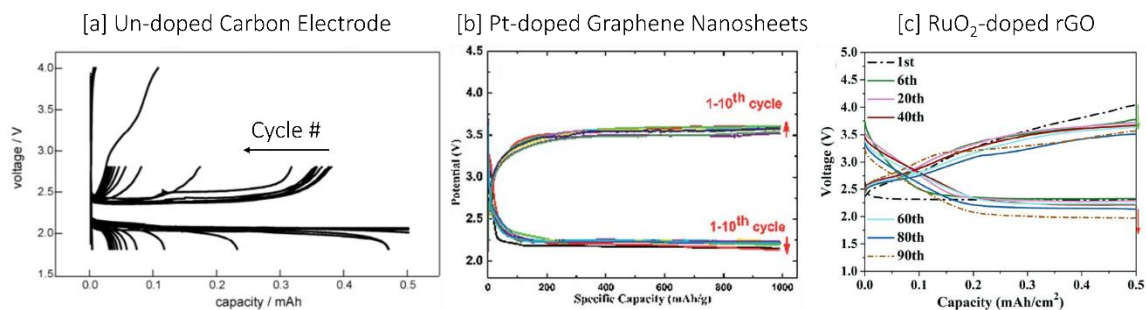


**Figure 1.8.** NaOB discharge / charge profiles utilizing <sup>†</sup>[a] un-doped carbon cathodes, <sup>††</sup>[b] Pt-doped graphene nanosheets cathodes, and <sup>#</sup>[c] RuO<sub>2</sub>-doped rGO cathodes. <sup>†</sup>Reprinted with permission from *J Phys Chem Lett.* 2016, 7, 23, 4841–4846 © 2016 American Chemical Society.<sup>58</sup> <sup>††</sup>Reprinted with permission from *J. Mater. Chem. A*, 2015, 3, 2568-2571 © 2016 Royal Society of Chemistry.<sup>71</sup> <sup>#</sup>Reprinted with permission from *Adv. Funct. Mater.* 2017, 27, 1700632 © 2017 John Wiley & Sons.<sup>72</sup>

Platinum (Pt) is the most widely used ORR catalyst in PEMFCs, and still receives a substantial amount of research attention in those systems.<sup>73</sup> Pt has only been utilized once in NaOBs to date, by Zhang et al. in 2015.<sup>71</sup> The authors doped graphene nanosheets with Pt nano particles, and observed discharge / charge curves that are consistent with Na<sub>2</sub>O<sub>2</sub> formation (shown in **Fig. 1.8b**). The cycling curves are compared with an undoped graphene cathode that was found to form NaO<sub>2</sub> (**Fig. 1.8a**), which illustrates the comparative stability of the Pt-doped cell, and the significantly higher overpotentials experienced when NaO<sub>2</sub> is not the primary discharge product. Even though the charge curves of the Pt-doped cell are consistent with Na<sub>2</sub>O<sub>2</sub> formation, the authors were only able to detect Na<sub>2</sub>CO<sub>3</sub> when examining discharged cathodes by FTIR. Interestingly, the Pt-doped cathode did not lower the charging overpotential when compared to an otherwise identical undoped cathode. Perhaps this should not be too surprising, as although Pt is clearly an excellent ORR

catalyst, it is not very efficient toward the OER due to the formation of Pt-oxides at high overpotentials.<sup>74, 75</sup> Pt is also known to catalyze the oxidation of the carbon surface, which only contributes to the instability issues of the cell.<sup>76</sup>

These results have sparked research into the use of metal oxide catalysts in NaOBs, which are known to be more selective to the OER, and are less likely to be further oxidized on the charging process.<sup>74</sup> Wu et al. published a study in which a ruthenium oxide ( $\text{RuO}_2$ ) catalyst was deposited on a boron doped rGO cathode (B-rGO), and the reversible formation of what they claim is a Na-deficient sodium peroxide ( $\text{Na}_{2-x}\text{O}_2$ ) was observed.<sup>72</sup> Impressively, the  $\text{RuO}_2$  on B-rGO cathode is able to reversibly cycle to a capacity of  $0.5 \text{ mAh cm}^{-2}$  for close to 90 cycles (**Fig. 1.8c**). In addition, the charging curves are a noticeable improvement over of the Pt-doped cathode, with significantly lower overpotentials in the initial stages of charge due to the activity of the oxide to the OER, but voltages still increase to  $> 3.5 \text{ V}$  throughout the charging period.

$\text{RuO}_2$  catalysts certainly offer attractive qualities to the NaOB system, and the general strategy of avoiding  $\text{NaO}_2$  production by the addition of ORR catalysts is a viable method of stabilizing the NaOB. However, the need for precious metals significantly hinders the viability of this strategy in the long term, and even with OER catalysis, the cell still struggles with issues of high overpotentials that are inherent to systems that produce  $\text{Na}_2\text{O}_2$ -like products on discharge. Alternative strategies need to be considered for the NaOB to become a practical cell chemistry in the future.

### 1.2.3 – Introduction to $\text{Ti}_4\text{O}_7$

Magneli-Phase  $\text{Ti}_4\text{O}_7$  is a reduced form of titanium dioxide ( $\text{TiO}_2$ ) that has gained significant attention for use as a stable electrode material in recent years.<sup>77</sup> Chapter 4

of this thesis introduces  $\text{Ti}_4\text{O}_7$  to NaOBs as a stabilizing coating for carbon paper cathodes. This alternative approach allows for the formation of  $\text{NaO}_2$  while significantly suppressing carbon degradation. The strategy of using  $\text{Ti}_4\text{O}_7$  in NaOBs was guided by a number of studies on the PEMFC and MOB communities that have reported on the desirable properties of  $\text{Ti}_4\text{O}_7$  as an electrode material.

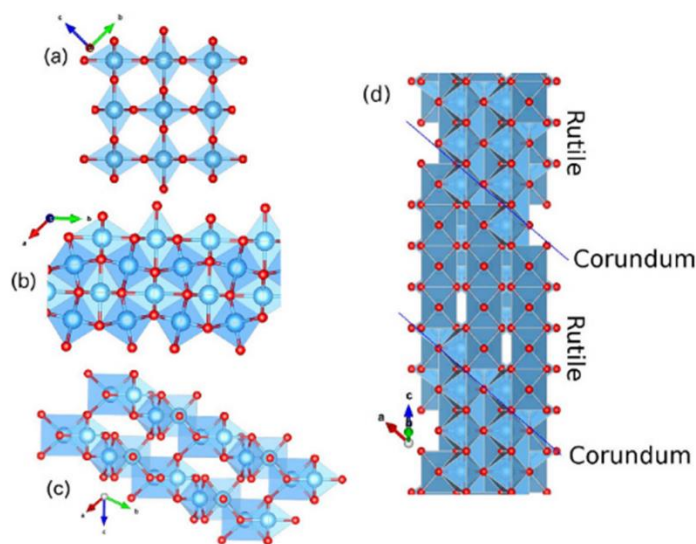


**Figure 1.9.** [a] Rutile  $\text{TiO}_2$ . [b / c] Corundum  $\text{Ti}_2\text{O}_3$  view along the c-axis, and parallel to the c-axis, respectively. [d] Magneli-phase  $\text{Ti}_4\text{O}_7$  structure, showing the rutile chains connected by face sharing shear planes. Reprinted with permission from Sci Rep 6, 28871 (2016) © 2016 Nature Publishing Group.<sup>78</sup>

$\text{Ti}_4\text{O}_7$  is typically produced by the high temperature reduction of  $\text{TiO}_2$  in a hydrogen atmosphere. The Magneli phases are classified by the formula  $\text{Ti}_n\text{O}_{2n-1}$ . For large values of “n” the oxygen vacancies can be seen as point defects, but as “n” approaches smaller values ( $n \leq 32$ ) the  $\text{Ti}_n\text{O}_{2n-1}$  structure arises as shown in **Fig. 1.9d**. Along the c-axis, chains of rutile  $\text{TiO}_2$  (**Fig. 1.9a**), composed of edge-sharing  $\text{TiO}_6$  octahedra of chain length “n”, are separated by shear planes of corundum  $\text{Ti}_2\text{O}_3$  (**Fig. 1.9b** and **1.9c**) with face-sharing octahedra.<sup>78</sup> The addition of face sharing shear planes lead to local O-deficient regions, and as “n” decreases the number of shear

planes increase. These O-deficient structures cause significant overlap in the d-orbital electrons of Ti, giving rise to the high electrical conductivity of  $\text{Ti}_4\text{O}_7$  (approx.  $1500 \text{ S cm}^{-1}$ ).<sup>79, 80</sup>

$\text{Ti}_4\text{O}_7$  first garnered attention in the fuel cell community when the material was investigated as a conductive substrate for the electrodeposition of metals, and was shown to withstand degradation under oxidative potentials in cyclic voltammetry (CV) experiments in the presence of 1 M sulfuric acid.<sup>81</sup> The material was subsequently tested for use in the PEMFC community, where membrane electrode assemblies (MEAs) of Pt/ $\text{Ti}_4\text{O}_7$  and Pt/C catalyst supports on Nafion™ membranes were made and tested under PEMFC operating conditions.<sup>77, 82</sup> The Pt/ $\text{Ti}_4\text{O}_7$  MEAs were shown to be stable at significantly more oxidative potentials than similarly made Pt/C MEAs. To confirm the long-term stability of the material, both MEAs were held at oxidizing potentials of 1.5 V at 80 °C in the presence of  $\text{O}_2$  gas for 1 h before CVs of the MEAs were taken in fuel cells environments (**Fig. 1.10**). Each sub-figure represents a unique cell assembly. In **Fig. 1.10a** and **1.10b**, CVs of Pt/C and Pt/ $\text{Ti}_4\text{O}_7$  MEAs using a carbon paper GDL were taken. The CV of the cell before the 1 h voltage hold is solid black, showing the ideal electrochemical behaviour of the PEMFC. After voltage holds at potentials of 1.4 and 1.5 V, the CV curve of the Pt/C MEA shows significant deviation from ideality, attributed to oxidation of the catalyst support. In contrast, the  $\text{Ti}_4\text{O}_7$  MEA only showed degradation at the 1.5 V hold. To eliminate the possible effect of carbon-GDL degradation, the same tests were performed with Ti mesh GDLs (**Fig. 1.10c** and **1.10d**). The Pt/C MEA showed the same substantial result, while the Pt/ $\text{Ti}_4\text{O}_7$  MEA experienced no noticeable degradation, confirming the excellent long-term stability of  $\text{Ti}_4\text{O}_7$  in highly oxidizing environments.<sup>77, 82</sup>

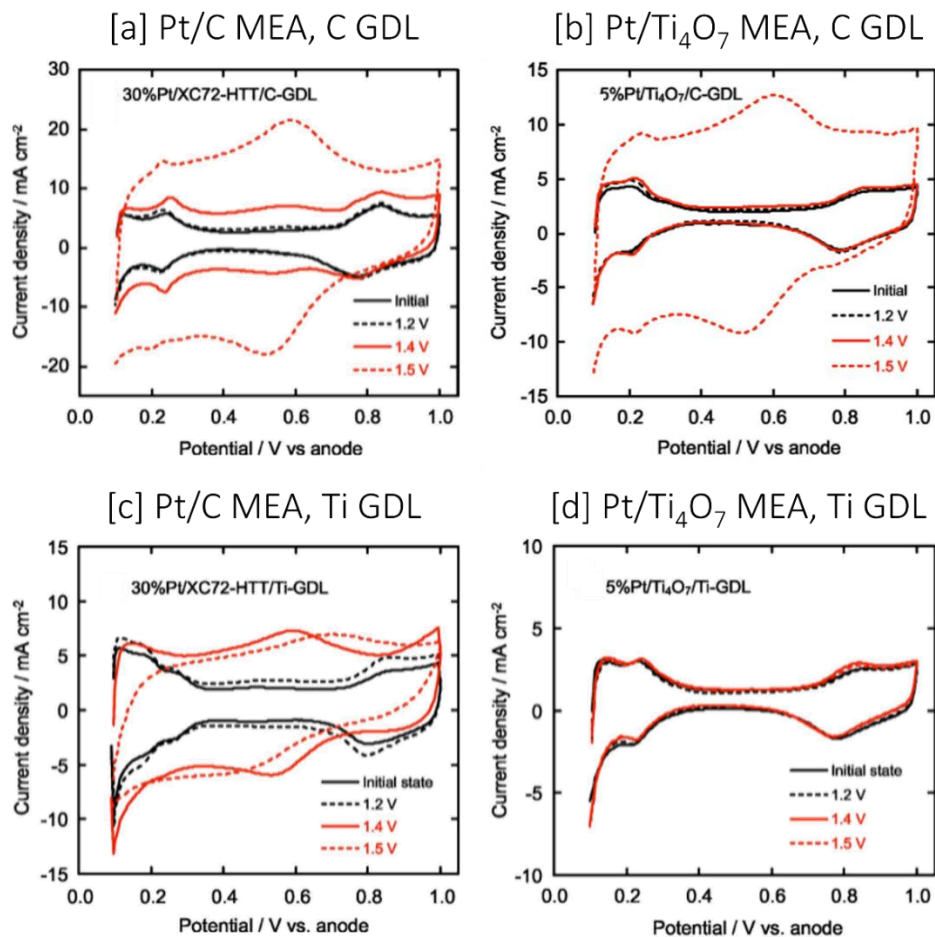


**Figure 1.10.** CVs of various MEAs in PEMFC fuel cells. [a] Pt/C MEA with a C GDL. [b] Pt/Ti<sub>4</sub>O<sub>7</sub> MEA with a C GDL. [c] Pt/C MEA with a Ti GDL. [d] Pt/Ti<sub>4</sub>O<sub>7</sub> MEA with a Ti GDL. In the original figure labels, “XC72-HTT” refers to the type of carbon used. Reprinted with permission from ECS Trans. 11 (2007) 1041 © 2007 The Electrochemical Society.<sup>82</sup>

Since these foundational studies, Ti<sub>4</sub>O<sub>7</sub> has been implemented as a stable support in a variety of catalyst systems, consistently showing improved stability to oxidation, without sacrificing catalytic activity to the ORR and OER.<sup>83</sup> The activity of Ti<sub>4</sub>O<sub>7</sub> toward the ORR and OER without the addition of catalysts was subsequently examined by Li et al. in the alkaline Zn-air battery system.<sup>84</sup> The authors conducted CV experiments in 6 M KOH<sub>(aq)</sub> electrolyte saturated with bubbled O<sub>2</sub> gas using a

glassy carbon electrode coated with a  $\text{Ti}_4\text{O}_7$  cast. They observed distinct, albeit weak, ORR and OER peaks in a CV curve that showed virtually no degradation after 5000 cycles (**Fig. 1.11a**). This showed that in addition to impressive oxidative stability,  $\text{Ti}_4\text{O}_7$  also has some inherent activity to the ORR and OER.<sup>84</sup>

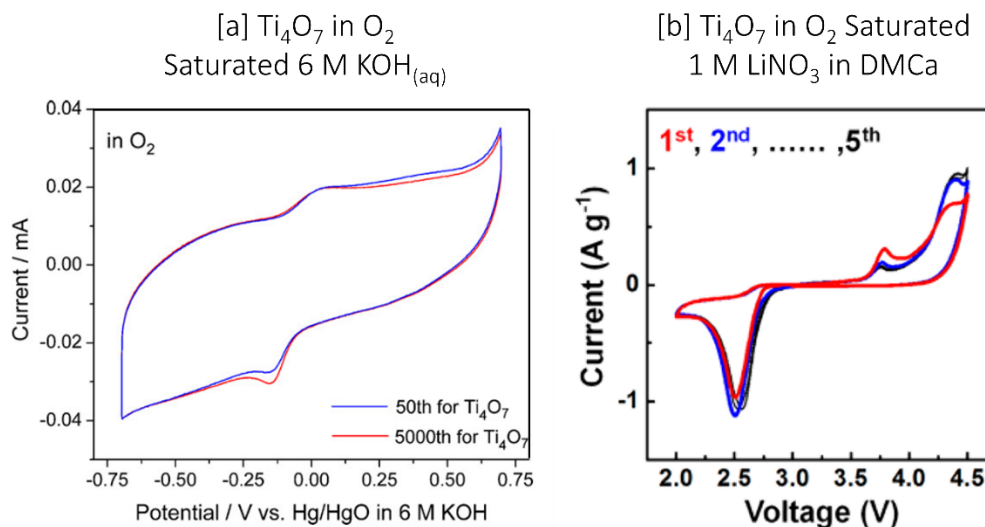


**Figure 1.11.** Cyclic voltammograms of [a] a  $\text{Ti}_4\text{O}_7$  on glassy carbon electrode in an  $\text{O}_2$  saturated 6 M  $\text{KOH}_{(\text{aq})}$  electrolyte for Zn-Air batteries, and [b] a nanosphere  $\text{Ti}_4\text{O}_7$  on Ni-foam electrode in a 1 M  $\text{LiNO}_3$  – DMC electrolyte for LiOBs. Reprinted with permission from *Electrochim Acta* 50, 20 (2010) 5891-5898 © 2010 Elsevier.<sup>84</sup> Reprinted with permission from *ACS Catal.* 2018, 8, 2601–2610 © 2018 American Chemical Society.<sup>85</sup>

These findings by Li et al. opened the door for  $\text{Ti}_4\text{O}_7$  to be explored further in the MOB community. Recently, Lee et al. synthesized a nanosphere  $\text{Ti}_4\text{O}_7$  material and fabricated both bare  $\text{Ti}_4\text{O}_7$  cathodes, and Ru nanoparticle on  $\text{Ti}_4\text{O}_7$  cathodes ( $\text{Ru}/\text{Ti}_4\text{O}_7$ ), for use in LiOBs.<sup>85</sup> The study showed significantly higher activity for  $\text{Ti}_4\text{O}_7$  in LiOBs in CV experiments than what was previously shown for  $\text{Ti}_4\text{O}_7$  Zn-Air batteries (**Fig. 1.11b**). LiOBs made with the bare  $\text{Ti}_4\text{O}_7$  nanosphere cathodes also showed highly reversible cycling for up to 50 cycles with little to no deterioration. This finding confirms that the observed stability of  $\text{Ti}_4\text{O}_7$  translates to the highly oxidizing

environments present in MOB. The increased activity in LiOBs (compared to what was observed in the Zn-Air system) is likely due to the high surface area of the nanosphere material compared to the bulk synthesis done by Li et al. in Zn-Air batteries. It is worth noting that although both battery systems function via the ORR and OER, it does not necessarily mean a given cathode should perform equally well in both systems, given the substantially different electrolyte environments, operating voltages, and ORR products being formed.

Although the LiOB and NaOB systems are certainly more similar than the LiOB and Zn-Air systems, they still have significant differences. In LiOBs,  $\text{LiO}_2$  is not observed as a discharge product, as  $\text{LiO}_2$  is substantially less stable than  $\text{NaO}_2$  (**Table 1.3**). Instead,  $\text{LiO}_2$  is formed as an intermediate, which is further reduced to  $\text{Li}_2\text{O}_2$  as the main discharge product (**eqn. 1.9** and **eqn. 1.10**).<sup>86, 87</sup> As a result, the charging process in LiOBs occurs via the two-electron transfer process (**eqn. 1.11**), and is surface mediated instead of occurring in solution.<sup>86, 87</sup> This results in charging voltages in the LiOB that are typically much higher than those of the NaOB.



This is in contrast to the single electron transfer processes observed in NaOBs. The  $\text{Li}_2\text{O}_2$  product is also significantly more thermodynamically stable than  $\text{NaO}_2$ , so achieving the level of reversibility observed by Lee et al. with  $\text{Ti}_4\text{O}_7$  will be difficult. Nonetheless, the success of  $\text{Ti}_4\text{O}_7$  in LiOBs bodes well for the application of  $\text{Ti}_4\text{O}_7$  in NaOB systems. The high oxidative stability of  $\text{Ti}_4\text{O}_7$ , observed in PEMFC fuel cells

and Zn-Air batteries, offers an attractive property to NaOBs given the tendency of  $\text{NaO}_2$  to oxidize the currently used carbon cathodes.

In Chapter 3 of this thesis,  $^{23}\text{Na}$  solid-state nuclear magnetic resonance (ssNMR) is used to directly detect  $\text{NaO}_2$  degrading the carbon cathode for the first time. The progression of this research is then focused toward to find a method of stabilizing this system, which is presented in Chapter 4. The reasoning for the strategies implemented in Chapter 4 can be understood by summarizing key points learned in this review of NaOB and  $\text{Ti}_4\text{O}_7$  cathode systems:

1.  $\text{NaO}_2$  is very unstable to carbon cathodes in NaOBs.
2. Carbon cathodes have a high activity toward the ORR and OER in NaOBs.
3. Avoiding  $\text{NaO}_2$  formation in favour of  $\text{Na}_2\text{O}_2$  formation requires expensive precious metal catalysts and results in high overpotentials on charge.
4.  $\text{Ti}_4\text{O}_7$  is extremely oxidatively stable as a stable active material support.

With this knowledge we employ a new strategy in Chapter 4 of using  $\text{Ti}_4\text{O}_7$ -coated carbon paper cathodes. The highly active carbon paper allows for preferential  $\text{NaO}_2$  formation, while the  $\text{Ti}_4\text{O}_7$  coating acts as a stable nucleation point for  $\text{NaO}_2$  formed in solution. Ultimately, this strategy is shown to lead to significantly improved cycle lifetimes in NaOBs.

### 1.3 – Concentrated Electrolytes in Li- and Na-Batteries

As discussed in the introduction, the choice of electrolyte can significantly affect the cycle-life of battery systems as it is responsible for facilitating stable ion transport throughout the lifetime of the cell. The original motivation for investigating electrolyte systems in this thesis arose from the quest to study materials that may be more

resilient to the oxidative environment of NaOBs. The first place to look was LIB literature, where a large number of electrolyte systems have been examined due to the high popularity of the battery system. This quickly turned into an examination of the interesting transport properties found at high concentration in one of the most oxidatively stable electrolyte systems ever characterized, LiTFSI in ADN. To understand the motivation of using highly concentrated electrolytes and the favourable properties they display, a brief review is presented herein of alternative electrolyte systems and the different mitigation strategies used to deal with issues such as reductive stability, Al corrosion, and SEI formation.

### 1.3.1 – High Voltage Adiponitrile Electrolytes

As discussed in section 1.1.1, the energy density of the cathode can be increased by either increasing the capacity or increasing the operating voltage of the active material. LiNMC is the most commonly used cathode material, and has an average operating voltage of 3.8 V vs Li / Li<sup>+</sup>.<sup>13</sup> Higher voltage cathode materials are the subject of numerous literature investigations.<sup>14, 88</sup> The most famous among these is LMNO due to the lack of expensive Co in its spinel structure, and high average voltage of 4.7 V vs Li / Li<sup>+</sup> with an achieved capacity of 130 mAh g<sup>-1</sup> (**Table 1.1**).<sup>14</sup> More recently, alternative high voltage polyanionic phosphate materials have also been explored in LIBs. Notably, LiNiPO<sub>4</sub> (LNP) operates at a very high voltage of 5.1 V vs Li / Li<sup>+</sup>, and can achieve gravimetric capacities between 140 and 167 mAh g<sup>-1</sup>.<sup>88, 89</sup> Both of these represent appreciable voltage gains over LiNMC, but also have much lower gravimetric capacities. One of the issues hindering further development of these high voltage materials is the low oxidative stability of the currently used LiPF<sub>6</sub> – EC / DEC electrolytes. **Fig. 1.12** overlays the intercalation voltage ranges of LiNMC,

LMNO, and LNP cathodes, with the upper voltage limit of LiPF<sub>6</sub> – EC / DEC electrolytes highlighted by a dotted line.<sup>89-91</sup>

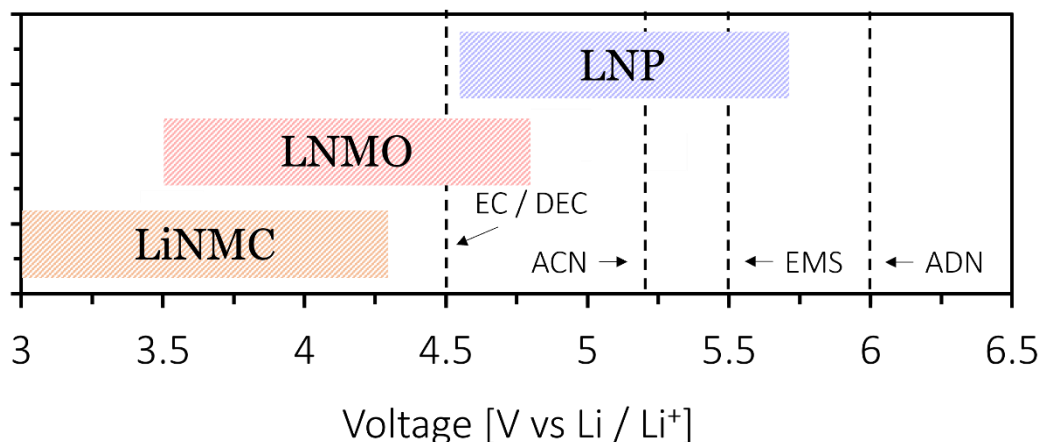


**Figure 1.12.** Intercalation voltage ranges of LiNMC (LiNi<sub>1/3</sub>Mn<sub>1/3</sub>Co<sub>1/3</sub>O<sub>2</sub>),<sup>91</sup> LMNO (LiNi<sub>0.5</sub>Mn<sub>1.5</sub>O<sub>4</sub>),<sup>90</sup> and LNP (LiNiPO<sub>4</sub>) cathodes,<sup>89</sup> With high voltage limits of various organic solvents varieties appearing as dotted lines.

Clearly, LiPF<sub>6</sub> – EC / DEC electrolytes are not suitable for high voltage cathode materials. This has been confirmed by studies that have used carbonate electrolytes directly with LMNO cells and found significant decomposition of EC and DEC to produce ethanol and diethyl ether.<sup>92</sup> The lack of a standardized high voltage electrolyte makes further research on high voltage materials difficult, as it is hard to control for the continuous oxidation of the carbonate solvent. This has prompted research into a number of oxidatively stable organic solvent varieties for their use in LIBs including sulfone, nitrile, and dinitrile solvents. To cover each of these in detail would surpass the scope of this review, but of common solvents tested for their oxidative stability in battery systems: ethyl methanesulfonate (EMS) paired with LiTFSI has been found to have the highest oxidative stability of for sulfone electrolyte systems, found to be stable until 5.5 V vs Li / Li<sup>+</sup>;<sup>93</sup> acetonitrile (ACN) with LiTFSI was found to be stable

until 5 V vs Li / Li<sup>+</sup> for nitrile solvents;<sup>94</sup> and ADN with LiTFSI is found to be stable until 6 V vs Li / Li<sup>+</sup> for dinitrile solvents.<sup>95</sup> To visualize the oxidative capabilities of each of these systems, the voltage limits quoted above are shown as dotted lines in **Fig. 1.12**. Focusing on ADN specifically, oxidative degradation of LiTFSI – ADN sits above the intercalation regions of each of the high voltage cathode materials presented,<sup>96</sup> and can be comfortably used with any system.

Although this high oxidative stability is certainly attractive, each of these electrolyte solvents do have a significant drawback. Sulfone, nitrile, and dinitrile systems are all unable to form stable SEI layers on the anode surface, instead they have been shown to be parasitically reduced throughout the cell lifetime.<sup>14</sup> Further, dinitriles such as ADN, the most appealing of the high voltage electrolytes, are not able to solvate LiPF<sub>6</sub> at concentrations high enough for LIBs. As a result, LiTFSI salt is typically used in dinitrile electrolytes.<sup>95</sup> LiTFSI is appealing because it is much more stable to hydrolysis than LiPF<sub>6</sub>, but unfortunately is also known to cause detrimental Al corrosion from the Al current collector used for the cathode.<sup>97</sup> A number of mitigating strategies to compensate for these issues have been investigated in order to make these high voltages electrolytes viable for use in modern LIBs. The most common of these involve the use of organic co-solvent and co-salt additives to facilitate the formation of stable SEIs and CEIs to prevent ADN reduction at the anode and Al corrosion by TFSI at the cathode, respectively.

Fluoroethylene carbonate (FEC) is one of the most common co-solvent additives used to promote SEI formation in LIBs.<sup>98</sup> FEC is preferentially reduced at the anode surface to form a thin, LiF-containing SEI that passivates the anode surface before the primary organic electrolyte can be sufficiently reduced.<sup>98</sup> FEC has been applied in

ADN-based cells, and has shown to be effective when paired with additional co-solvents such as dimethyl carbonate (DMC).<sup>99</sup> On the cathode side, co-salts such as LiBF<sub>4</sub> have been used to suppress Al corrosion in LiTFSI-based cells. Similar to FEC at the anode, the BF<sub>4</sub><sup>-</sup> anion is preferentially oxidized to form AlF<sub>3</sub> as a stable CEI, preventing parasitic Al corrosion by TFSI.<sup>100</sup> This was demonstrated by Song et al., who were able to stabilize a LiTFSI in EC / DMC electrolyte by adding a LiBF<sub>4</sub> co-salt in concentrations up to 0.5 M.<sup>100</sup>

The use of co-salts and co-solvents is certainly effective in mitigating Al corrosion and unstable SEI formation. However, the excessive use of co-salts and co-solvents can lead to quite complex electrolyte mixtures when the additives needed to stabilize both processes are considered. This is perhaps natural for LIBs given the advanced state of research the system is in, but is less attractive when trying to translate these electrolyte systems to SIBs and NaOBs where research is still in its infancy. More recently, concentrating simple electrolyte formulations far past the typical 1 M range has been explored as an alternative mitigating strategy for facilitating SEI formation, and suppressing Al corrosion.

### 1.3.2 – Ultraconcentrated Electrolytes

A more simplistic method of attacking both the SEI formation and Al-corrosion issues that has gained traction in research is the use of ultra-high concentration electrolytes. A number of recent publications have shown that electrolytes near their saturation limits exhibit widely altered electrochemical properties. Chapter 5 and 6 of this thesis explore this phenomenon in ultraconcentrated Li and NaTFSI in ADN solutions. This section gives a brief review of the studies that motivated these investigations.

### *Concentrated Electrolytes and The Anode*

The idea of concentrating electrolytes to bring about favourable electrochemical properties was first proposed by Jeong et al. in 2008, who showed suppressed Li dendrite formation on Li-metal anodes in highly concentrated (2.7 M) LiN(SO<sub>2</sub>C<sub>2</sub>F<sub>5</sub>)<sub>2</sub> (LiBETI) salt in PC electrolyte.<sup>101</sup> This led to more reversible Li deposition and dissolution in Li<sub>(s)</sub> || Ni<sub>(s)</sub> test cells when using concentrated 2.7 M electrolytes than much more typical 1.0 M electrolyte system. The group observed that the concentrated electrolyte facilitated a much thinner SEI layer, which likely led to the suppressed dendrite growth, but were unable to determine the mechanism behind this phenomenon.

Later in 2014, Yamada et al. shed light on a possible mechanism behind these phenomenon when they observed a similar result in highly concentrated LiTFSI in ACN electrolytes.<sup>94</sup> The authors observed that although 1 M LiTFSI in ACN reacted spontaneously with Li-metal, due to the known instability of nitrile solvents to reductive alkali metals, the highly concentrated 4.5 M LiTFSI in ACN electrolyte is stable when placed in contact with Li-metal for up to one week.<sup>94</sup> As a result, the electrolyte was able to intercalate graphite anodes reversibly in Li<sub>(s)</sub> || Gr half-cells for 25 cycles at various fast charging rates. The group also conducted a density functional theory-based molecular dynamics (DFT-MD) investigation to calculate the solution structure and projected density of states (pDOS) of the super concentrated and dilute electrolyte systems. They found that the lowest unoccupied molecular orbital (LUMO) in the dilute electrolyte system was on the carbon atom in free ACN (i.e. ACN not participating in TFSI solvation), and thus ACN is preferentially reduced. In the concentrated electrolyte system, the LUMO was instead on TFSI in heavily

coordinated Li–TFSI–ACN aggregate structures. This causes TFSI to be preferentially reduced at the anode instead of ACN, and as a result, a passivating TFSI-degradation-product layer is formed as a stable SEI.<sup>94</sup>

Similar phenomena have been observed in SIBs as well, where highly concentrated sodium bis(fluorosulfonyl)imide (NaFSI, not to be confused with NaTFSI) in EC / PC electrolytes exhibited significantly higher reversible HC intercalation in  $\text{Na}_{(s)} \parallel \text{HC}$  half cells.<sup>102</sup> The group attributes this to more stable SEI formation on the electrodes resulting from solvent-salt aggregate formation at high concentration, similar to what was observed by Yamada et al. It is certainly promising to see that the benefits of concentrated electrolytes translate to Na-based systems.

#### *Concentrated Electrolytes and Al Corrosion*

Concentrated electrolytes have also been found to be effective at suppressing Al corrosion. Matsumodo et al. first characterized this in 2013 when they observed significantly reduced Al corrosion in 1.8 M LiTFSI in EC / DEC electrolytes compared to the 1.0 M system.<sup>103</sup> Linear sweep voltammetry (LSV) was conducted on  $\text{Li}_{(s)} \parallel \text{Al}_{(s)}$  cells (**Fig. 1.13**). In LSV, the potential at the working electrode is linearly increased over time. As the potential increases, the dilute 0.8 M – 1.2 M electrolytes slowly experience a rise in current response that is characteristic of Al corrosion.<sup>95</sup> In the 1.8 M electrolyte, a slight onset of positive current is still observed, but is very weak compared to the more dilute samples.<sup>103</sup> The authors attribute this to the close proximity of  $\text{Li}^+$  and F of the TFSI at high concentrations, causing the formation of passivating LiF (observed by x-ray photoelectron spectroscopy (XPS)) on the Al surface when TFSI is oxidized.<sup>103</sup> A later investigation in 2014 that observed similar phenomenon in highly concentrated LiTFSI in EC claims that TFSI oxidation is not

involved in the stabilizing mechanism of the Al electrode.<sup>104</sup> Instead, the authors claim that the low concentration Al corrosion mechanism centres around simple  $\text{Al}^{3+}$  dissolution, and that at high concentrations, the prevalence of Li – TFSI – EC aggregates inhibit Al dissolution since no free solvent or TFSI is available to facilitate  $\text{Al}^{3+}$  dissolution.<sup>104</sup> No matter the exact mechanism, it is clear that concentrating LiTFSI electrolytes is a viable strategy to suppress Al corrosion.

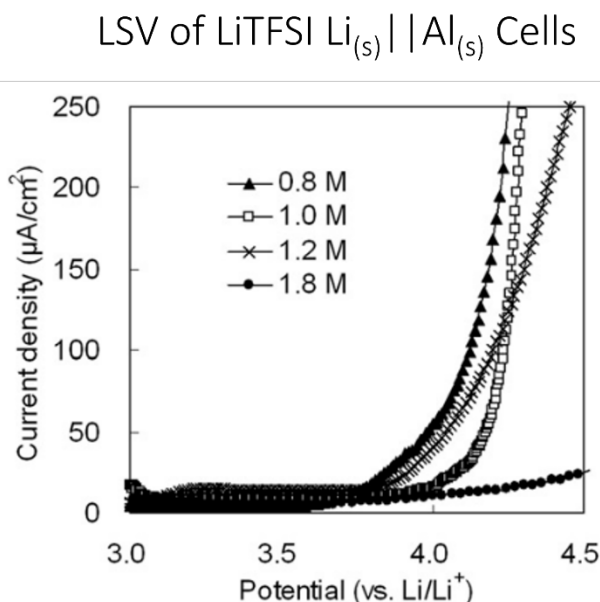


**Figure 1.13.** LSV of  $\text{Li}_{(s)} \parallel \text{Al}_{(s)}$  using different concentrations of LiTFSI in EC electrolytes.<sup>104</sup> Reprinted with permission from Journal of Power Sources 231 (2013) 234-238 © 2013 Elsevier.<sup>103</sup>

Concentrating electrolytes can be an effective two-for-one strategy at stabilizing both the anode and cathode in Li-systems. No such strategy for nitrile or dinitrile stabilization at the anode has been implemented in SIBs as of yet, nor for NaTFSI / Al stabilization at the cathode. Chapter 6 of this thesis presents an investigation of concentrated NaTFSI in ADN electrolytes centering around the alkali-metal stability and Al corrosion suppression phenomena observed in this review.

## 1.4 – Thesis Outline

This thesis describes the investigation of oxidatively stable cathode and electrolyte systems for various battery systems including the LIB, SIB, and NaOB. In order to accomplish this, modern analytic techniques such as ssNMR, pulsed field gradient (PFG) NMR, electrochemical impedance spectroscopy (EIS), and a variety of electrochemical experiments are used.

The preceding chapter (**Chapter 1**) summarizes the background knowledge needed to understand the phenomena under investigation in each study, and the motivation for choosing the particular electrolyte and cathode materials under investigation.

**Chapter 2** introduces the characterization methods used in this thesis, with an emphasis on ssNMR. The dipolar heteronuclear multiple quantum correlation (D-HMQC) and triple quantum magic angle spinning (3QMAS) experiments are described in detail, including the dipolar coupling and quadrupolar coupling interactions that underpin them. The general principals of PFG NMR and EIS are also described.

**Chapters 3 to 6** comprise the investigative section of this work. **Chapter 3** outlines two related studies on the use of the carbon cathodes in NaOBs.  $^{23}\text{Na}$  and  $^{19}\text{F}$  ssNMR experiments are used to identify the reactivity of  $\text{NaO}_2$  toward the carbon cathode.

In **Chapter 4**,  $\text{Ti}_4\text{O}_7$  is investigated by as a  $\text{NaO}_2$ -resistant coating for carbon paper cathodes in NaOBs. 1D  $^{23}\text{Na}$  and  $^1\text{H}$ , 2D  $^{23}\text{Na}$  3QMAS, and 2D  $^{23}\text{Na}\{^1\text{H}\}$  D-HMQC experiments are used to identify the mechanism by which  $\text{Ti}_4\text{O}_7$  elongates cell lifetime in NaOBs.

In **Chapter 5**, PFG NMR is used to investigate the transport properties, of LiTFSI in ADN electrolytes as a function of concentration. A novel variable diffusion time PFG experiment is used that probes the solution structure of the electrolyte.

**Chapter 6** presents an electrochemical study of concentrated NaTFSI in ADN. The concentrated system is shown to facilitate reversible Na deposition at the anode, and to suppress Al corrosion at the cathode, resulting in enhanced performance in  $\text{Na}_{(s)} || \text{NVPF}$  half-cells compared to the dilute system.

Lastly, **Chapter 7** gives a summary of the work, with the most important findings are echoed, and suggestions for subsequent investigations are given.

## 1.5 – References

1. Fleming, J. R., Joseph Fourier's Theory of Terrestrial Temperatures. In *Historical Perspectives on Climate Change*, Fleming, J. R., Ed. Oxford University Press: 1998; p 0.
2. Ortiz, J. D.; Jackson, R. *Notes and Records: the Royal Society Journal of the History of Science* **2022**, *76* (1), 67-84. DOI: 10.1098/rsnr.2020.0031
3. Arrhenius, S. *The London, Edinburgh, and Dublin Philosophical Magazine and Journal of Science* **1896**, *41* (251), 237-276. DOI: 10.1080/14786449608620846
4. Callendar, G. S. *Quarterly Journal of the Royal Meteorological Society* **1938**, *64* (275), 223-240. DOI: <https://doi.org/10.1002/qj.49706427503>
5. IEA *World Energy Outlook 2022*; IEA: Paris, 2022.
6. IEA, *World Energy Outlook 2016*. IEA, Ed. IEA: Paris, 2016.
7. IEA, *World Energy Outlook 2021*. IEA, Ed. IEA: Paris, 2021.
8. Cho, Y.-G.; Li, M.; Holoubek, J.; Li, W.; Yin, Y.; Meng, Y. S.; Chen, Z. *ACS Energy Letters* **2021**, *6* (5), 2016-2023. DOI: 10.1021/acsenergylett.1c00484
9. Cao, F.; Barsukov, I. V.; Bang, H. J.; Zaleski, P.; Prakash, J. *Journal of The Electrochemical Society* **2000**, *147* (10), 3579. DOI: 10.1149/1.1393942
10. Zhang, S. S. *Journal of The Electrochemical Society* **2020**, *167* (10), 100510. DOI: 10.1149/1945-7111/ab945e
11. Cheng, X.-B.; Zhang, R.; Zhao, C.-Z.; Zhang, Q. *Chemical Reviews* **2017**, *117* (15), 10403-10473. DOI: 10.1021/acs.chemrev.7b00115
12. Julien, C. M.; Mauger, A.; Zaghbi, K.; Groult, H. Comparative Issues of Cathode Materials for Li-Ion Batteries *Inorganics* [Online], 2014, p. 132-154.
13. Kam, K. C.; Doeff, M. M. *Material Matters* **2012**, *7* (4),
14. Kim, J. H.; Pieczonka, N. P.; Yang, L. *Chemphyschem* **2014**, *15* (10), 1940-54. DOI: 10.1002/cphc.201400052
15. Harlow, J. E.; Ma, X.; Li, J.; Logan, E.; Liu, Y.; Zhang, N.; Ma, L.; Glazier, S. L.; Cormier, M. M. E.; Genovese, M.; Buteau, S.; Cameron, A.; Stark, J. E.; Dahn, J. R. *Journal of The Electrochemical Society* **2019**, *166* (13), A3031-A3044. DOI: 10.1149/2.0981913jes
16. Lundgren, H.; Behm, M.; Lindbergh, G. *Journal of The Electrochemical Society* **2014**, *162* (3), A413-A420. DOI: 10.1149/2.0641503jes
17. Seo, D. M.; Borodin, O.; Han, S.-D.; Boyle, P. D.; Henderson, W. A. *Journal of The Electrochemical Society* **2012**, *159* (9), A1489-A1500. DOI: 10.1149/2.035209jes
18. Shan, X.; Zhong, Y.; Zhang, L.; Zhang, Y.; Xia, X.; Wang, X.; Tu, J. *The Journal of Physical Chemistry C* **2021**, *125* (35), 19060-19080. DOI: 10.1021/acs.jpcc.1c06277
19. Nie, M.; Chalasani, D.; Abraham, D. P.; Chen, Y.; Bose, A.; Lucht, B. L. *The Journal of Physical Chemistry C* **2013**, *117* (3), 1257-1267. DOI: 10.1021/jp3118055
20. Liu, M.; Vratamanu, J.; Chen, X.; Xing, L.; Xu, K.; Li, W. *ACS Energy Letters* **2021**, *6* (6), 2096-2102. DOI: 10.1021/acsenergylett.1c00707
21. Nelson, K. J.; d'Eon, G. L.; Wright, A. T. B.; Ma, L.; Xia, J.; Dahn, J. R. *Journal of The Electrochemical Society* **2015**, *162* (6), A1046-A1054. DOI: 10.1149/2.0831506jes
22. Xia, J.; Nie, M.; Ma, L.; Dahn, J. R. *Journal of Power Sources* **2016**, *306*, 233-240. DOI: 10.1016/j.jpowsour.2015.12.013

23. Xiao, J.; Li, X.; Tang, K.; Wang, D.; Long, M.; Gao, H.; Chen, W.; Liu, C.; Liu, H.; Wang, G. *Materials Chemistry Frontiers* **2021**, *5* (10), 3735-3764. DOI: 10.1039/d1qm00179e
24. Ong, S. P.; Chevrier, V. L.; Hautier, G.; Jain, A.; Moore, C.; Kim, S.; Ma, X.; Ceder, G. *Energy & Environmental Science* **2011**, *4* (9), 3680-3688. DOI: 10.1039/C1EE01782A
25. DiVincenzo, D. P.; Mele, E. J. *Physical Review B* **1985**, *32* (4), 2538-2553. DOI: 10.1103/PhysRevB.32.2538
26. Stevens, D. A.; Dahn, J. R. *Journal of The Electrochemical Society* **2001**, *148* (8), A803. DOI: 10.1149/1.1379565
27. Ge, P.; Foulletier, M. *Solid State Ionics* **1988**, *28-30*, 1172-1175. DOI: [https://doi.org/10.1016/0167-2738\(88\)90351-7](https://doi.org/10.1016/0167-2738(88)90351-7)
28. Irisarri, E.; Ponrouch, A.; Palacin, M. R. *Journal of The Electrochemical Society* **2015**, *162* (14), A2476-A2482. DOI: 10.1149/2.0091514jes
29. Li, Y.; Xu, S.; Wu, X.; Yu, J.; Wang, Y.; Hu, Y.-S.; Li, H.; Chen, L.; Huang, X. *Journal of Materials Chemistry A* **2015**, *3* (1), 71-77. DOI: 10.1039/C4TA05451B
30. Sathiya, M.; Hemalatha, K.; Ramesha, K.; Tarascon, J. M.; Prakash, A. S. *Chemistry of Materials* **2012**, *24* (10), 1846-1853. DOI: 10.1021/cm300466b
31. Billaud, J.; Clément, R. J.; Armstrong, A. R.; Canales-Vázquez, J.; Rozier, P.; Grey, C. P.; Bruce, P. G. *Journal of the American Chemical Society* **2014**, *136* (49), 17243-17248. DOI: 10.1021/ja509704t
32. Saravanan, K.; Mason, C. W.; Rudola, A.; Wong, K. H.; Balaya, P. *Advanced Energy Materials* **2013**, *3* (4), 444-450. DOI: <https://doi.org/10.1002/aenm.201200803>
33. Song, W.; Ji, X.; Wu, Z.; Yang, Y.; Zhou, Z.; Li, F.; Chen, Q.; Banks, C. E. *Journal of Power Sources* **2014**, *256*, 258-263. DOI: 10.1016/j.jpowsour.2014.01.025
34. Gover, R. K. B.; Bryan, A.; Burns, P.; Barker, J. *Solid State Ionics* **2006**, *177* (17), 1495-1500. DOI: <https://doi.org/10.1016/j.ssi.2006.07.028>
35. Feng, J.; An, Y.; Ci, L.; Xiong, S. *Journal of Materials Chemistry A* **2015**, *3* (28), 14539-14544. DOI: 10.1039/C5TA03548A
36. Kuratani, K.; Uemura, N.; Senoh, H.; Takeshita, H. T.; Kiyobayashi, T. *Journal of Power Sources* **2013**, *223*, 175-182. DOI: <https://doi.org/10.1016/j.jpowsour.2012.09.039>
37. Okoshi, M.; Yamada, Y.; Yamada, A.; Nakai, H. *Journal of The Electrochemical Society* **2013**, *160* (11), A2160-A2165. DOI: 10.1149/2.074311jes
38. Landesfeind, J.; Hosaka, T.; Graf, M.; Kubota, K.; Komaba, S.; Gasteiger, H. A. *Journal of The Electrochemical Society* **2021**, *168* (4), 040538. DOI: 10.1149/1945-7111/abf8d9
39. Pan, Y.; Zhang, Y.; Parimalam, B. S.; Nguyen, C. C.; Wang, G.; Lucht, B. L. *Journal of Electroanalytical Chemistry* **2017**, *799*, 181-186. DOI: <https://doi.org/10.1016/j.jelechem.2017.06.002>
40. Hartmann, P.; Bender, C. L.; Vracar, M.; Durr, A. K.; Garsuch, A.; Janek, J.; Adelhelm, P. *Nature Materials* **2013**, *12* (3), 228-232. DOI: 10.1038/nmat3486
41. Hartmann, P.; Bender, C. L.; Sann, J.; Durr, A. K.; Jansen, M.; Janek, J.; Adelhelm, P. *Phys. Chem. Chem. Phys.* **2013**, *15* (28), 11661-11672. DOI: 10.1039/c3cp50930c
42. Yadegari, H.; Franko, C. J.; Banis, M. N.; Sun, Q.; Li, R.; Goward, G. R.; Sun, X. *J. Phys. Chem. Lett.* **2017**, *8* (19), 4794-4800. DOI: 10.1021/acs.jpcllett.7b02227

43. Liu, X. H.; Wang, J. W.; Liu, Y.; Zheng, H.; Kushima, A.; Huang, S.; Zhu, T.; Mao, S. X.; Li, J.; Zhang, S.; Lu, W.; Tour, J. M.; Huang, J. Y. *Carbon* **2012**, *50* (10), 3836-3844. DOI: <https://doi.org/10.1016/j.carbon.2012.04.025>
44. Zhao, N.; Li, C.; Guo, X. *Phys. Chem. Chem. Phys.* **2014**, *16* (29), 15646-15652. DOI: 10.1039/c4cp01961j
45. Xia, C.; Black, R.; Fernandes, R.; Adams, B.; Nazar, L. F. *Nat. Chem.* **2015**, *7* (6), 496-501. DOI: 10.1038/nchem.2260
46. Ortiz-Vitoriano, N.; Batcho, T. P.; Kwabi, D. G.; Han, B.; Pour, N.; Yao, K. P.; Thompson, C. V.; Shao-Horn, Y. *J Phys Chem Lett* **2015**, *6* (13), 2636-43. DOI: 10.1021/acs.jpcclett.5b00919
47. Xia, C.; Fernandes, R.; Cho, F. H.; Sudhakar, N.; Buonacorsi, B.; Walker, S.; Xu, M.; Baugh, J.; Nazar, L. F. *J. Am. Chem. Soc.* **2016**, *138* (35), 11219-11226. DOI: 10.1021/jacs.6b05382
48. Kim, J.; Lim, H. D.; Gwon, H.; Kang, K. *Phys. Chem. Chem. Phys.* **2013**, *15* (10), 3623-3629. DOI: 10.1039/c3cp43225d
49. Schwenke, K. U.; Meini, S.; Wu, X.; Gasteiger, H. A.; Piana, M. *Phys. Chem. Chem. Phys.* **2013**, *15* (28), 11830-9. DOI: 10.1039/c3cp51531a
50. Black, R.; Shyamsunder, A.; Adeli, P.; Kundu, D.; Murphy, G. K.; Nazar, L. F. *ChemSusChem* **2016**, *9* (14), 1795-1803. DOI: 10.1002/cssc.201600034
51. Gilles, P. W.; Margrave, J. L. *J. Phys. Chem.* **1956**, *60*, 1333-1335. DOI: 10.1021/j150543a045
52. Hossein Yadegari; Yongliang Lia; Mohammad Norouzi Banisa; Xifei Lia; Biqiong Wang; Qian Suna; Ruying Lia; Tsun-Kong Shamb; Xiaoyu Cuic; Xueliang Suna *Energy & Environmental Science* **2014**, *7* (11),
53. Bi, X.; Wang, R.; Ma, L.; Zhang, D.; Amine, K.; Lu, J. *Small Methods* **2017**, *1* (7), DOI: 10.1002/smtd.201700102
54. Yadegari, H.; Li, Y.; Banis, M. N.; Li, X.; Wang, B.; Sun, Q.; Li, R.; Sham, T.-K.; Cui, X.; Sun, X. *Energy Environ. Sci.* **2014**, *7* (11), 3747-3757. DOI: 10.1039/c4ee01654h
55. Bi, X.; Wang, R.; Yuan, Y.; Zhang, D.; Zhang, T.; Ma, L.; Wu, T.; Shahbazian-Yassar, R.; Amine, K.; Lu, J. *Nano Lett* **2020**, *20* (6), 4681-4686. DOI: 10.1021/acs.nanolett.0c01670
56. Vannerberg, N.-G., Peroxides, Superoxides, and Ozonides of the Metals of Groups Ia, IIa, and IIb. In *Prog. Inorg. Chem.*, John Wiley & Sons: 1962; Vol. 4, pp 125-197.
57. Reeve, Z. E.; Franko, C. J.; Harris, K. J.; Yadegari, H.; Sun, X.; Goward, G. R. *J. Am. Chem. Soc.* **2017**, *139* (2), 595-598. DOI: 10.1021/jacs.6b11333
58. Liu, T.; Kim, G.; Casford, M. T.; Grey, C. P. *J. Phys. Chem. Lett.* **2016**, *7* (23), 4841-4846. DOI: 10.1021/acs.jpcclett.6b02267
59. Knudsen, K. B.; Nichols, J. E.; Vegge, T.; Luntz, A. C.; McCloskey, B. D.; Hjelm, J. *The Journal of Physical Chemistry C* **2016**, *120* (20), 10799-10805. DOI: 10.1021/acs.jpcc.6b02788
60. Lin, X.; Sun, Q.; Yadegari, H.; Yang, X.; Zhao, Y.; Wang, C.; Liang, J.; Koo, A.; Li, R.; Sun, X. *Advanced Functional Materials* **2018**, *28* (35), 1801904. DOI: <https://doi.org/10.1002/adfm.201801904>
61. Bender, C. L.; Jache, B.; Adelhelm, P.; Janek, J. *Journal of Materials Chemistry A* **2015**, *3* (41), 20633-20641. DOI: 10.1039/c5ta06640a
62. Read, J.; Mutolo, K.; Ervin, M.; Behl, W.; Wolfenstine, J.; Driedger, A.; Foster, D. *Journal of The Electrochemical Society* **2003**, *150* (10), A1351. DOI: 10.1149/1.1606454
63. Zhao, N.; Guo, X. *The Journal of Physical Chemistry C* **2015**, *119* (45), 25319-25326. DOI: 10.1021/acs.jpcc.5b09187

64. Reeve, Z. E. M.; Goward, G. R.; Bain, A. D. *Canadian Journal of Chemistry* **2015**, *93* (9), 976-982. DOI: 10.1139/cjc-2014-0577
65. Freunberger, S. A.; Chen, Y.; Peng, Z.; Griffin, J. M.; Hardwick, L. J.; Bardé, F.; Novák, P.; Bruce, P. G. *Journal of the American Chemical Society* **2011**, *133* (20), 8040-8047. DOI: 10.1021/ja2021747
66. Lutz, L.; Alves Dalla Corte, D.; Tang, M.; Salager, E.; Deschamps, M.; Grimaud, A.; Johnson, L.; Bruce, P. G.; Tarascon, J.-M. *Chemistry of Materials* **2017**, *29* (14), 6066-6075. DOI: 10.1021/acs.chemmater.7b01953
67. Dilimon, V. S.; Hwang, C.; Cho, Y.-G.; Yang, J.; Lim, H.-D.; Kang, K.; Kang, S. J.; Song, H.-K. *Scientific Reports* **2017**, *7* (1), 17635. DOI: 10.1038/s41598-017-17745-9
68. Oswald, S.; Mikhailova, D.; Scheiba, F.; Reichel, P.; Fiedler, A.; Ehrenberg, H. *Analytical and Bioanalytical Chemistry* **2011**, *400* (3), 691-696. DOI: 10.1007/s00216-010-4646-z
69. Bender, C. L.; Hartmann, P.; Vračar, M.; Adelhelm, P.; Janek, J. *Advanced Energy Materials* **2014**, *4* (12), 1301863. DOI: 10.1002/aenm.201301863
70. Sun, Q.; Yang, Y.; Fu, Z.-W. *Electrochemistry Communications* **2012**, *16* (1), 22-25. DOI: 10.1016/j.elecom.2011.12.019
71. Zhang, S.; Wen, Z.; Rui, K.; Shen, C.; Lu, Y.; Yang, J. *Journal of Materials Chemistry A* **2015**, *3* (6), 2568-2571. DOI: 10.1039/c4ta05427j
72. Wu, F.; Xing, Y.; Lai, J.; Zhang, X.; Ye, Y.; Qian, J.; Li, L.; Chen, R. *Advanced Functional Materials* **2017**, *27* (30), 1700632. DOI: <https://doi.org/10.1002/adfm.201700632>
73. Zhu, E.; Wu, M.; Xu, H.; Peng, B.; Liu, Z.; Huang, Y.; Li, Y. *Advanced Functional Materials* **2022**, *32* (30), 2203883. DOI: <https://doi.org/10.1002/adfm.202203883>
74. Huang, Z.-F.; Wang, J.; Peng, Y.; Jung, C.-Y.; Fisher, A.; Wang, X. *Advanced Energy Materials* **2017**, *7* (23), 1700544. DOI: 10.1002/aenm.201700544
75. Sadhasivam, T.; Palanisamy, G.; Roh, S.-H.; Kurkuri, M. D.; Kim, S. C.; Jung, H.-Y. *International Journal of Hydrogen Energy* **2018**, *43* (39), 18169-18184. DOI: <https://doi.org/10.1016/j.ijhydene.2018.08.035>
76. Lazaridis, T.; Gasteiger, H. A. *Journal of The Electrochemical Society* **2021**, *168* (11), 114517. DOI: 10.1149/1945-7111/ac35ff
77. Ioroi, T.; Siroma, Z.; Fujiwara, N.; Yamazaki, S.-i.; Yasuda, K. *Electrochemistry Communications* **2005**, *7* (2), 183-188. DOI: <https://doi.org/10.1016/j.elecom.2004.12.007>
78. Padilha, A. C.; Raebiger, H.; Rocha, A. R.; Dalpian, G. M. *Sci Rep* **2016**, *6*, 28871. DOI: 10.1038/srep28871
79. Szot, K.; Rogala, M.; Speier, W.; Klusek, Z.; Besmehn, A.; Waser, R. *Nanotechnology* **2011**, *22* (25), 254001. DOI: 10.1088/0957-4484/22/25/254001
80. Houlihan, J. F.; Danley, W. J.; Mulay, L. N. *Journal of Solid State Chemistry* **1975**, *12* (3), 265-269. DOI: [https://doi.org/10.1016/0022-4596\(75\)90317-5](https://doi.org/10.1016/0022-4596(75)90317-5)
81. Graves, J. E.; Pletcher, D.; Clarke, R. L.; Walsh, F. C. *Journal of Applied Electrochemistry* **1991**, *21* (10), 848-857. DOI: 10.1007/BF01042450
82. Ioroi, T.; Senoh, H.; Yamazaki, S.-i.; Siroma, Z.; Fujiwara, N.; Yasuda, K. *J. Electrochem. Soc.* **2008**, *155* (4), B321-B326. DOI: 10.1149/1.2833310
83. Won, J.-E.; Kwak, D.-H.; Han, S.-B.; Park, H.-S.; Park, J.-Y.; Ma, K.-B.; Kim, D.-H.; Park, K.-W. *Journal of Catalysis* **2018**, *358*, 287-294. DOI: <https://doi.org/10.1016/j.jcat.2017.12.013>

84. Li, X.; Zhu, A. L.; Qu, W.; Wang, H.; Hui, R.; Zhang, L.; Zhang, J. *Electrochimica Acta* **2010**, *55* (20), 5891-5898. DOI: 10.1016/j.electacta.2010.05.041
85. Lee, S.; Lee, G.-H.; Kim, J.-C.; Kim, D.-W. *ACS Catalysis* **2018**, *8* (3), 2601-2610. DOI: 10.1021/acscatal.7b03741
86. Laoire, C. O.; Mukerjee, S.; Abraham, K. M. *J. Phys. Chem. C* **2009**, *113* (46), 20127–20134. DOI: 10.1021/jp908090s
87. Cao, R.; Walter, E. D.; Xu, W.; Nasybulin, E. N.; Bhattacharya, P.; Bowden, M. E.; Engelhard, M. H.; Zhang, J. G. *ChemSusChem* **2014**, *7* (9), 2436-40. DOI: 10.1002/cssc.201402315
88. Ling, J.; Karupiah, C.; Krishnan, S. G.; Reddy, M. V.; Misnon, I. I.; Ab Rahim, M. H.; Yang, C.-C.; Jose, R. *Energy & Fuels* **2021**, *35* (13), 10428-10450. DOI: 10.1021/acs.energyfuels.1c01102
89. Nasir, M. H.; Janjua, N. K.; Santoki, J. *Journal of The Electrochemical Society* **2020**, *167* (13), 130526. DOI: 10.1149/1945-7111/abb83d
90. Monaco, S.; De Giorgio, F.; Da Col, L.; Riché, M.; Arbizzani, C.; Mastragostino, M. *Journal of Power Sources* **2015**, *278*, 733-740. DOI: <https://doi.org/10.1016/j.jpowsour.2014.12.099>
91. Coban, A.; Gungor, H. *Arabian Journal for Science and Engineering* **2022**, *47* (6), 7147-7155. DOI: 10.1007/s13369-022-06725-5
92. Pieczonka, N. P. W.; Liu, Z.; Lu, P.; Olson, K. L.; Moote, J.; Powell, B. R.; Kim, J.-H. *The Journal of Physical Chemistry C* **2013**, *117* (31), 15947-15957. DOI: 10.1021/jp405158m
93. Abouimrane, A.; Belharouak, I.; Amine, K. *Electrochemistry Communications* **2009**, *11* (5), 1073-1076. DOI: <https://doi.org/10.1016/j.elecom.2009.03.020>
94. Yamada, Y.; Furukawa, K.; Sodeyama, K.; Kikuchi, K.; Yaegashi, M.; Tateyama, Y.; Yamada, A. *J Am Chem Soc* **2014**, *136* (13), 5039-46. DOI: 10.1021/ja412807w
95. Abu-Lebdeh, Y.; Davidson, I. *Journal of The Electrochemical Society* **2009**, *156* (1), A60-A65. DOI: 10.1149/1.3023084
96. Franko, C. J.; Yim, C.-H.; Årén, F.; Åvall, G.; Whitfield, P. S.; Johansson, P.; Abu-Lebdeh, Y. A.; Goward, G. R. *Journal of The Electrochemical Society* **2020**, *167* (16), 160532. DOI: 10.1149/1945-7111/abcf17
97. Yang, H.; Kwon, K.; Devine, T. M.; Evans, J. W. *Journal of The Electrochemical Society* **2000**, *147* (12), 4399-4407.
98. Heine, J.; Hilbig, P.; Qi, X.; Niehoff, P.; Winter, M.; Bieker, P. *Journal of The Electrochemical Society* **2015**, *162* (6), A1094-A1101. DOI: 10.1149/2.0011507jes
99. Ehteshami, N.; Ibing, L.; Stolz, L.; Winter, M.; Paillard, E. *Journal of Power Sources* **2020**, *451*, DOI: 10.1016/j.jpowsour.2020.227804
100. Song, S.-W.; Richardson, T. J.; Zhuang, G. V.; Devine, T. M.; Evans, J. W. *Electrochimica Acta* **2004**, *49* (9-10), 1483-1490. DOI: 10.1016/s0013-4686(03)00930-7
101. Jeong, S.-K.; Seo, H.-Y.; Kim, D.-H.; Han, H.-K.; Kim, J.-G.; Lee, Y. B.; Iriyama, Y.; Abe, T.; Ogumi, Z. *Electrochemistry Communications* **2008**, *10* (4), 635-638. DOI: 10.1016/j.elecom.2008.02.006
102. Patra, J.; Huang, H.-T.; Xue, W.; Wang, C.; Helal, A. S.; Li, J.; Chang, J.-K. *Energy Storage Materials* **2019**, *16*, 146-154. DOI: <https://doi.org/10.1016/j.ensm.2018.04.022>

103. Matsumoto, K.; Inoue, K.; Nakahara, K.; Yuge, R.; Noguchi, T.; Utsugi, K. *Journal of Power Sources* **2013**, *231*, 234-238. DOI: <https://doi.org/10.1016/j.jpowsour.2012.12.028>
104. McOwen, D. W.; Seo, D. M.; Borodin, O.; Vatamanu, J.; Boyle, P. D.; Henderson, W. A. *Energy & Environmental Science* **2014**, *7*(1), 416-426. DOI: 10.1039/C3EE42351D

## 2 – Methods

This chapter will describe the analytical techniques that are used in this thesis to characterize the chemical processes in battery systems. Magic angle spinning (MAS) solid-state nuclear magnetic resonance (ssNMR) and pulsed field gradient (PFG) diffusional NMR are the main focus of this chapter, as they are the primary techniques used in these studies. Electrochemical impedance spectroscopy (EIS) is also described in relative detail. The methods for setting up specific experiments on individual samples are presented in the experimental sections of each chapter.

### 2.1 – Solid-State NMR Spectroscopy

Solution-state NMR spectroscopy is a common technique that has found application in nearly every field of chemistry and materials science. ssNMR spectroscopy is less common than the solution-state analogue, but enjoys much of the same resolution and characterization range benefits of the solution technique when MAS is employed. This section presents the basic theoretical background of ssNMR spectroscopy, including the origin of the NMR signal, relevant nuclear interactions, MAS, and the pulse sequences used in this work.

#### 2.1.1 – The Zeeman Effect & The Origin of NMR Signal

The technique of NMR spectroscopy revolves around the manipulation of nuclear spin-states to excited energy levels in order to observe the energy given off during their subsequent relaxation back to the ground state. Understanding the origin of nuclear spin-states and their energy levels is helpful when analysing the NMR spectroscopic data in this thesis.

### Nuclear Spin

Spin angular momentum is an intrinsic property of elementary particles, similar to mass or charge. The quarks that constitute nucleons have this fundamental property, and when they combine to form composite protons and neutrons, the result is a particle with an intrinsic spin of magnitude  $\frac{1}{2}$ . When protons and neutrons then combine to form the atomic nucleus, the product has a spin angular momentum as well, which can easily be referred to by the nuclear spin quantum number, “ $I$ ”. The ground-state of nuclear spin of an atom is not easily predicted and can take on a variety of values as the make-up of its constituent nucleons change.<sup>1</sup> There is, however, a quick method for classifying nuclei into one of three nuclear spin categories:<sup>1</sup>

1. If the number of neutrons and number of protons in the nucleus are both even, then  $I = 0$ , the nucleus has no overall nuclear spin, and is NMR-inactive. Examples of this are seen in the  $^{12}\text{C}$  and  $^{16}\text{O}$  nuclei.
2. If both the number of neutrons and number of protons in the nucleus are odd, then  $I = n$ , the nucleus will have an overall integer spin. Some examples of this are the  $^{14}\text{N}$  ( $I = 1$ ), and  $^2\text{H}$  ( $I = 1$ ) nuclei.
3. If one of the number of neutrons or the number of protons is odd, while the other is even, then  $I = \frac{n}{2}$ , the nucleus will have an overall half-integer spin (such as  $I = \frac{1}{2}$ ). This category includes  $^1\text{H}$  ( $I = \frac{1}{2}$ ),  $^7\text{Li}$  ( $I = \frac{3}{2}$ ), and  $^{23}\text{Na}$  ( $I = \frac{3}{2}$ ) nuclei.

Nuclei of spin  $I = 0$  are NMR inactive, and cannot be studied by the technique. Conversely, all nuclei with  $I \neq 0$  are NMR active and can be characterized. For the

purposes of this thesis, no nuclei of integer spin are characterized. There is an important difference between nuclei with exactly  $I = \frac{1}{2}$  and with  $I > \frac{1}{2}$ . Nuclei with  $I = \frac{1}{2}$  are spherical in nature and are not “quadrupolar”, while nuclei with  $I > \frac{1}{2}$  are not spherical and are quadrupolar. Non-quadrupolar nuclei studied in this thesis include  $^1\text{H}$  and  $^{19}\text{F}$ , while quadrupolar nuclei include  $^{23}\text{Na}$  and  $^7\text{Li}$ . The interesting properties that quadrupolar nuclei bring to NMR analysis is discussed further in section 2.2.3.

### *Zeeman Splitting*

Analogous to rotational angular momentum, the spin angular momentum of the positively charged nucleus results in the production of a net magnetic field. The nucleus then has an intrinsic magnetic moment,  $\mu$ , which is related to the nuclear spin by eqn. 2.01.<sup>1,2</sup>

$$\hat{\mu}_I = \gamma \hbar \hat{I} \quad [2.01]$$

Where  $\hbar$  is the reduced Planck’s constant, and  $\gamma$  is the gyromagnetic ratio of the nucleus.  $\gamma$  is an intrinsic parameter that relates the spin angular momentum of a nucleus to the strength of the magnetic dipole moment. Each of the NMR active nuclei discussed above have unique values of  $\gamma$ .

In the absence of an external magnetic field, a bulk collection of many nuclei has no appreciable net magnetization, as the magnetic moments of each nucleus have no energetically preferred orientation. If an external magnetic field is applied to the sample, the magnetization vectors of the nuclei will precess around the applied magnetic field in one of multiple stable orientations referred to as spin-states.<sup>1</sup> This splits the previously degenerate energy levels of the nuclear spin ground-state into a number of non-degenerate quantized spin-states. For a given nuclear spin, there are

$2I + 1$  stable spin-states, taking on values of  $m_I = -I, -I + 1, \dots, I$ .<sup>1, 2</sup> These spin-states can be modelled both as vectors and as quantum states, and elements of both descriptions are useful for understanding magnetic phenomena in NMR spectroscopy. The quantum spin-states are each described by a corresponding wavefunction,  $\psi$ , denoted simply by:

$$\psi_{I,m} = |I, m\rangle \quad [2.02]$$

Where  $|I, m\rangle$  describes the nuclear spin  $I$  with a magnetic moment in spin-state  $m$ . It is helpful to know that  $|I, m\rangle$  is an eigenfunction to the  $\hat{l}_z$  operator, which represents the z-component of the  $|I, m\rangle$  spin-state.<sup>2</sup> Applying  $\hat{l}_z$  to the eigenfunction  $|I, m\rangle$  gives the  $m_I$  value of the individual spin-state as its eigenvalue.<sup>2</sup>

$$\hat{l}_z |I, m\rangle = m |I, m\rangle \quad [2.03]$$

The splitting of spin-states into separate non-degenerate energy levels is known as Zeeman splitting. The energy levels of the spin-states resulting from Zeeman splitting can be obtained by applying the Zeeman Hamiltonian ( $\hat{H}_{Ze}$ ) on the nuclear spin wavefunction ( $|I, m\rangle$ ). It can be shown that  $|I, m\rangle$  is also an eigenfunction of  $\hat{H}_{Ze}$ , giving the eigenvalue  $E_{I,m}$ :<sup>2</sup>

$$\hat{H}_{Ze} |I, m\rangle = E_{I,m} |I, m\rangle \quad [2.04]$$

$$\hat{H}_{Ze} = -\gamma \hbar \hat{l}_z B_0 \quad [2.05]$$

Where  $B_0$  is the strength of the external magnetic field. Combining these with **eqn. 2.03** gives:

$$\hat{H}_{Ze} |I, m\rangle = -\gamma \hbar \hat{l}_z B_0 |I, m\rangle = -\gamma \hbar B_0 \hat{l}_z |I, m\rangle = -\gamma \hbar B_0 m |I, m\rangle$$

$$\therefore E_{I,m} = -\gamma\hbar B_0 m \quad [2.06]$$

Where  $E_{I,m}$  is the energy of spin-state  $m$  from the nuclear spin  $I$ . Generally, the energy difference between two spin-states is:

$$\Delta E = -\hbar\gamma B_0 \Delta m \quad [2.07]$$

Where  $B_0$  is the strength of the externally applied magnetic field. A visualization of the resulting energy levels for spin-states after Zeeman splitting is given in **Fig. 2.1**.

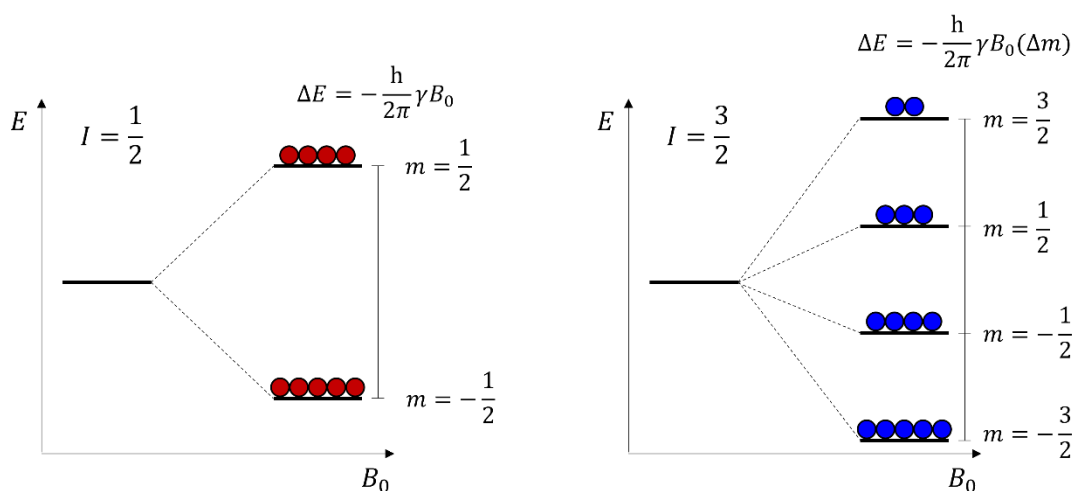


**Figure 2.1.** Zeeman splitting of a  $I = \frac{1}{2}$  and a  $I = \frac{3}{2}$  nuclear spin into non-degenerate spin-states in the presence of an external magnetic field,  $B_0$ .<sup>1,2</sup>

**Fig. 2.1** visualizes Zeeman splitting of the ground state nuclear spin energy levels for both  $I = \frac{1}{2}$  and  $I = \frac{3}{2}$  nuclei. In the  $I = \frac{1}{2}$  nuclei, there is only one transition of  $\Delta m = 1$  stemming from the  $m = \frac{1}{2}$  and  $m = -\frac{1}{2}$  spin-states. In the  $I = \frac{3}{2}$  nuclei, there are six possible transitions from four values of  $m$ , with resulting  $\Delta m$  values of 1, 2, and 3. A general selection rule in NMR spectroscopy states that only transitions of  $\Delta m = \pm 1$  are observable.<sup>1,2</sup> These are called *in-phase single quantum coherences*. A nucleus of

spin  $I$  will produce  $2 \cdot I \Delta m = \pm 1$  transitions.<sup>1</sup> The manipulation of multiple quantum coherences with  $\Delta m > 1$  are important in advanced NMR pulse sequences, but the magnetization must always be in a  $\Delta m = 1 \pm$  coherence during acquisition. As a result of this selection rule, the observable energy can be calculated by **eqn. 2.08** regardless of  $I$  (where  $\Delta m = 1$ ).

$$\Delta E = -\hbar\gamma B_0 \quad [2.8]$$

**Eqn. 2.08** states that nuclei with an intrinsically larger  $\gamma$  will have a larger  $\Delta E$ . A larger  $\Delta E$  results in a larger equilibrium population difference between spin-states, which yields greater signal in the NMR experiment. The  $^1\text{H}$  nucleus has the largest  $\gamma$  out of all NMR active nuclei and gives the greatest sensitivity as a result. Of course, nuclei choice is relatively limited by the sample under characterization. The high  $\gamma$  of  $^1\text{H}$  is not helpful when trying to characterize  $\text{NaO}_2$ , for example. The majority of NMR experiments presented in this thesis are done on the  $^{23}\text{Na}$  nucleus, with  $\gamma = 11.3 \text{ MHz T}^{-1}$ , while other nuclei include  $^7\text{Li}$  with  $\gamma = 16.5 \text{ MHz T}^{-1}$ ,  $^{19}\text{F}$  with  $\gamma = 40.1 \text{ MHz T}^{-1}$ , and  $^1\text{H}$  with  $\gamma = 42.6 \text{ MHz T}^{-1}$ . A second method of increasing  $\Delta E$  (and thus signal) from **Eqn. 2.08** is using a stronger applied magnetic field,  $B_0$ . The majority of NMR experiments done in this work are at a field strength of 11.7 T, with a few experiments at 7 T and 19.9 T as well. In general, the nuclei studied herein, and the field strengths used, give more than adequate sensitivity for characterization.

### Larmor Frequency

Spin-state transitions have been discussed in units of energy so far. In the context of NMR spectroscopy, these transitions are often discussed in terms of frequency.

Simply taking the relationship  $E = h\omega$  and **eqn. 2.06**:

$$\omega_0 = -\frac{\gamma B_0}{2\pi} \quad [2.09]$$

Where  $\omega_0$  corresponds to the Larmor frequency, the frequency of the Zeeman energy transition. In the vector model, this can also be described as the frequency at which the magnetization vector,  $\vec{\mu}$ , of the nucleus precesses around the axis of the applied magnetic field ( $B_0$ ), which is typically taken as the z-axis. In the bulk sample, this results in a net magnetisation vector,  $\vec{M}$ , that is a geometric average of all  $\vec{\mu}$  in the sample.

In NMR experiments, every chemically unique nucleus of a chemical species has a unique  $\omega_0$ . In the classic NMR spectrum,  $\omega_0$  is plotted on the x-axis, and the intensity of the signal on the y-axis. The next section will describe how the basic NMR experiment is able to produce this spectrum.

#### 2.1.2 – The Basic NMR Experiment

In order to properly understand the evolution of magnetization during an NMR experiment, it helps to use a combination of concepts from the vector and quantum mechanical descriptions of nuclear spin. This is often called product operator formulism (PrOF).<sup>3</sup> In PrOF, the Hamiltonian describing the energy of a spin-state is tracked as it evolves throughout the various interactions of a pulse-sequence.

### From Spin to Spectrum

To observe the relaxation of nuclear spins from higher to lower energy spin-states, the nuclei are first excited into the higher state. This is done by the application of a radio frequency (RF) electromagnetic pulse. The RF pulse is produced by applying an electrical current through a coil that surrounds the sample. This creates an additional magnetic field,  $B_1$ , that is perpendicular to the external magnetic field,  $B_0$ . If  $B_0$  is taken to be along the z-axis, then the application of  $B_1$  applies a torque to tip the bulk magnetization vector,  $\vec{M}$ , into the x – y plane. This is often referred to as a  $90^\circ$ , or  $\frac{\pi}{2}$  pulse (Fig. 2.2).

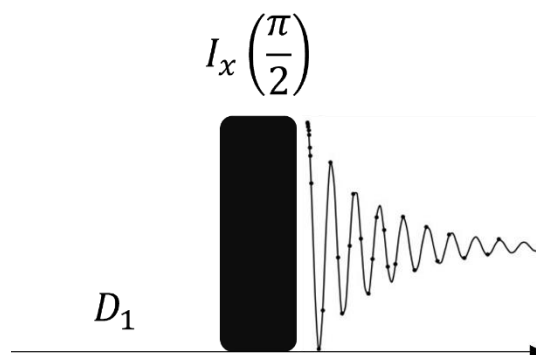


**Figure 2.2.** Simple “onepulse” pulse sequence showing a  $\frac{\pi}{2}$  pulse on nucleus  $I$  with a phase of x. The resulting free-induction decay is shown as  $I$  precesses in the x – y plane.  $D_1$  is the delay time parameter, and is the time allowed for magnetization to relax before each scan.

Consider a nuclear spin along the z-axis, the Hamiltonian describing this spin is  $\hat{H} = \omega_I \hat{I}_z$ . Where  $\omega_I$  is the Larmor frequency specific to spin  $I$ , and  $\hat{I}_z$  specifies that  $\hat{H}$  is describing the precession of  $I$  around the z-axis. Throughout the NMR pulse sequence, the Hamiltonian evolves as the magnetization is affected by RF pulses and various nuclear interactions. A “onepulse” pulse sequence is shown in Fig. 2.2, where

a single RF pulse is applied to spin  $I$ . The operator for the RF pulse is in the same form as the spin Hamiltonian above:  $\omega_{B_1} \hat{I}_x$  (the “hat” denoting  $I$  as an operator is assumed from here). This denotes a pulse applied to the  $I$  nucleus along the x-axis (or with a *phase* of “x”) with a rotational frequency,  $\omega_{B_1}$ , that corresponds to the strength of the applied  $B_1$  field. When an operator is applied to the Hamiltonian, the result is a combination of the original state and a new state weighted by the  $\cos()$  and  $\sin()$  functions, similar to describing the components of a vector in a 2D plane. This takes the form:

$$I_z \xrightarrow{\omega_{B_1} I_x} I_z \cos(\omega_{B_1} t) - I_y \sin(\omega_{B_1} t)$$

The new state,  $-I_y$ , is determined by the cyclic commutative properties of the spin operators, specifically:  $[I_z, I_x] = -I_y$ ,  $[I_z, I_y] = I_x$ , and  $[I_x, I_y] = I_z$ . Conceptually, the magnetization simply rotates with respect to the direction of the applied field following the right-hand rule. The resulting  $I_z$  and  $I_y$  components are weighted by the tip-angle  $\omega_{B_1} t$ . Since both  $\omega_{B_1}$  and  $t$  are set in the pulse-sequence, they can be chosen appropriately to give a desired tip-angle of  $\frac{\pi}{2}$ , i.e.  $t = \frac{\pi}{2\omega_{B_1}}$ . This gives:

$$I_z \xrightarrow{\omega_{B_1} I_x} I_z \cos\left(\frac{\pi}{2}\right) - I_y \sin\left(\frac{\pi}{2}\right) = -I_y$$

Therefore, the  $\frac{\pi}{2}$  pulse on nucleus  $I$  rotates the magnetization from z onto the y-axis. For completion the entire process was shown, but in practice it is easier to name RF pulse operators just by the chosen tip angle and phase needed to reach the final state directly:

$$I_z \xrightarrow{I_x(\frac{\pi}{2})} -I_y$$

The magnetization in the x – y plane still undergoes Larmor precession about  $B_0$  at the nuclei specific frequency,  $\omega_I$ . This is shown by applying the original precession operator  $\omega_I I_z$ , where the same commutative properties apply:

$$-I_y \xrightarrow{\omega_I I_z} -I_y \cos(\omega_I t) + I_x \sin(\omega_I t)$$

Instead of resulting in a distinct final state, the magnetization is undergoing Larmor precession in the x – y plane with the x and y components oscillating at  $\omega_I$  as time increases. The oscillating  $I_x$  state represents the *in-phase single quantum coherence* of  $\Delta m = \pm 1$ , and is therefore observable.<sup>3</sup>

The oscillating magnetic field produced by  $I$  produces an oscillating current in the same coil that was used to create the original RF pulse. The receiver used to detect this current response also has a distinct phase that the spectroscopist can choose. In this example the receiver can be set with a phase of y. Since the y-component of the magnetization is governed by “ $I_y \cos(\omega_I t)$ ”, the y-component of the induced current will oscillate sinusoidally with a frequency  $\omega_I$ . This results in a decaying sinusoidal signal known as a free induction decay (FID), and is shown as the decaying signal after the RF pulse in **Fig. 2.2**. To better interpret the FID, a signal processing tool called a Fourier transform (FT) is used. In short, the time-domain FID is analysed computationally to identify the frequencies and amplitudes of the constituent sine waves that compose it. This data is plotted with frequency on the x-axis and intensity on the y-axis, in what is the final NMR spectrum.

The use of PrOF to describe a simple one-pulse experiment is excessive. Nonetheless, introducing the general concepts of PrOF here are helpful to understand more advanced experiments described later.

### *T<sub>1</sub> and T<sub>2</sub> Relaxation*

As shown in **Fig 2.2**, the observed signal in the FID decays spontaneously over time. This decay primarily occurs via two phenomena called spin-lattice and spin-spin relaxation, which are denoted by nuclei specific time-constants  $T_1$  and  $T_2$ , respectively. Spin-lattice relaxation,  $T_1$ , is the rate that the longitudinal component of the excited magnetization relaxes back to equilibrium along the z-axis. Physically this can be thought of as the magnetization of excited nuclei relaxing to lower energy states via the rapid sampling of adjacent states by thermal motion.<sup>1</sup> In order to have full relaxation of the magnetization to equilibrium, the delay time between scans of an NMR experiment,  $D_1$  (**Fig. 2.2**), is typically set to  $5 * T_1$ .

Spin-spin relaxation,  $T_2$ , is the rate that the transverse (x – y) component of the excited magnetization relaxes to equilibrium. In a bulk sample, immediately after the RF pulse, all of the excited nuclei in the x – y plane have an equal phase, i.e. all their magnetization vectors are directly overlapping. As they evolve in the transverse plane, each nuclei will precess at a slightly different rate due to small local inhomogeneities in the magnetic field. Thus, each nuclei will accumulate slightly varying phases throughout time, and will no longer constructively interfere. This dephasing causes an exponential loss of NMR signal.<sup>1</sup>

Both of these interactions are present for the nuclei described by PrOF in the one-pulse experiment described above, and are the reason for the decay of the FID during signal acquisition. In general, samples with low  $T_1$  are amiable to work with, since

many scans can be acquired in a short time when  $D_1$  is small. However, in almost all cases  $T_2 > T_1$ , and if  $T_2$  is very small, the signal can dephase completely before the magnetization is appropriately sampled. This results in a low-resolution FID, and broad peak widths upon FT. This is especially a problem in complex experiments that require the magnetization to evolve for extended periods of time before acquisition.

$T_2$  relaxation is not the only phenomenon that can cause significant peak broadening in the final spectrum. In a real chemical sample, a large number of heterogenous nuclei are in close proximities to each other, and can interact in a variety of ways that can have adverse effects on their observable magnetization. The most relevant of these interactions are examined in detail in the following section.

## 2.2 – Nuclear Spin Interactions

The energetic transitions of nuclear spins are sensitive to a number of additional interactions that can perturb the Zeeman spin-states. As a result, nuclear spin interactions have a pronounced affect on the observed frequencies in the final NMR spectrum. These interactions include chemical shielding ( $\omega_{CS}$ ), dipolar coupling ( $\omega_D$ ), quadrupolar coupling ( $\omega_Q$ ), scalar coupling ( $\omega_J$ ), the paramagnetic interaction ( $\omega_P$ ), and the Knight shift ( $\omega_K$ ).  $\omega_{CS}$ ,  $\omega_D$ , and  $\omega_Q$  are covered in detail in this section, as they are the primary interactions needed to understand the NMR spectra and techniques presented in this thesis.

### 2.2.1 – Chemical Shielding

When an external magnetic field ( $B_0$ ) is applied to a chemical species, a current is induced in the electron cloud surrounding the nucleus. The induced current creates a small magnetic field ( $B_{ind}$ ) that opposes  $B_0$ .<sup>2</sup> This is where the term chemical shielding arises, as the induced field “shields” the nucleus from  $B_0$ .  $B_{ind}$  perturbs  $B_0$  additively to create an effective local magnetic field,  $B_{eff}$ :<sup>1</sup>

$$B_{eff} = B_0 + B_{ind} \quad [2.10]$$

The electron density of a molecule is highly spatially sensitive, so  $B_{ind}$  can vary widely within a single chemical species. Therefore, the  $B_{eff}$  felt by a given atomic nucleus is highly dependant on the immediate chemical environment. Rewriting **eqn. 2.09** (for the Larmor frequency of a nucleus), in terms of  $B_{eff}$ :

$$\omega_0 = -\frac{\gamma\hbar B_{eff}}{2\pi} \quad [2.11]$$

**Eqn. 2.11** shows how otherwise identical nuclei can have variable precession frequencies based on the local electronic environment.

The spatial orientation of the chemical species within a sample will also have a large effect on  $B_{eff}$ , as the orientation of the electron cloud changes. The orientation dependence of  $B_{eff}$  is described by:<sup>2</sup>

$$B_{eff} = B_0(1 - \sigma_{CS}) \quad [2.12]$$

Where  $\sigma_{CS}$  is a matrix tensor describing the spatial orientation of chemical shielding based on the orientation of the electron cloud:<sup>2</sup>

$$\sigma_{CS} = \begin{bmatrix} \sigma_{xx} & \sigma_{xy} & \sigma_{xz} \\ \sigma_{yx} & \sigma_{yy} & \sigma_{yz} \\ \sigma_{zx} & \sigma_{zy} & \sigma_{zz} \end{bmatrix} \quad [2.13]$$

$\sigma_{CS}$  can be simplified to just the diagonal contributions by choosing a frame of reference specific to the distribution of electron density in a given the chemical species.<sup>1, 2</sup> This frame of reference is called the principal axis system (PAS):

$$\sigma_{CS}^{PAS} = \begin{bmatrix} \sigma_{XX} & 0 & 0 \\ 0 & \sigma_{YY} & 0 \\ 0 & 0 & \sigma_{ZZ} \end{bmatrix} \quad [2.14]$$

Where  $\sigma_{XX}$ ,  $\sigma_{YY}$ , and  $\sigma_{ZZ}$  are called the principal values of the tensor. The orientation dependence of chemical shielding for a nucleus can be simplified into three parameters that measure the amount of deviation in the principal values: the isotropic value ( $\sigma_{iso}$ ), the chemical shielding anisotropy ( $\Delta$ ), and the shielding asymmetry parameter ( $\eta_{CS}$ ).<sup>1, 2</sup>

$\sigma_{iso}$  for a particular nucleus is simply the average of x, y, and z principal values.<sup>2</sup> The chemical shielding is said to be truly isotropic only if each of the three principal values are equal. Otherwise,  $\sigma_{iso}$  is just an average of the inhomogeneous shielding.

$$\sigma_{iso} = \frac{1}{3}(\delta_{XX} + \delta_{YY} + \delta_{ZZ}) \quad [2.15]$$

$\Delta_{an}$  is the measurement of the magnitude of the orientation dependence of chemical shielding, the anisotropy.<sup>2</sup> It is quantified by the largest difference of a principal value from the mean, which is typically assigned to the  $\sigma_{ZZ}$  value.

$$\Delta_{an} = \sigma_{ZZ} - \sigma_{iso} \quad [2.16]$$

$\eta_{CS}$  represents the asymmetry of the orientation dependence and is defined as the difference between the remaining two principal values normalized by  $\Delta$ .<sup>2</sup>  $\sigma_{YY}$  is typically taken as the larger of the two principal values, therefore  $0 < \eta_{CS} < 1$ .

$$\eta_{CS} = \frac{\sigma_{YY} - \sigma_{XX}}{\Delta_{an}} \quad [2.17]$$

Each of these parameters contribute to the chemical shielding contribution to the observed Larmor frequency ( $\omega_{CS}$ ) through the equation:<sup>2</sup>

$$\omega_{CS}(\theta, \phi) = \omega_0 \sigma_{iso} - \frac{1}{2} \omega_0 \Delta_{an} [3 \cos^2(\theta) - 1 + \eta_{CS} \sin^2(\theta) \cos(2\phi)] \quad [2.18]$$

Where  $\omega_0$  is the Larmor precession frequency of the nucleus with no electron cloud, and angles  $\theta$  and  $\phi$  describe the orientation, in spherical coordinates, of the principal axis of the chemical species with respect to  $B_0$ .

**Eqn. 2.18** shows how the orientation of a nucleus in a non-spherical chemical environment can have a significant effect on the resulting observed frequency. In solution state NMR spectroscopy, species undergo rapid molecular motion at rates that are orders of magnitude larger than the frequency of the chemical shielding anisotropy interactions. This causes the directional dependence of  $\omega_{CS}(\theta, \phi)$  to be averaged to the isotropic value, and thus only a single frequency is observed.<sup>1</sup> In a solid powder sample,  $\omega_{CS}(\theta, \phi)$  is not averaged, and every orientation of  $\theta$  and  $\phi$  are present. The expected powder pattern can be gained by integrating  $\omega_{CS}(\theta, \phi)$  over the spherical coordinate space. An example simulated spectrum for a static solid sample with only chemical shielding anisotropy (CSA) contributions is shown in **Fig. 2.3**. To better coincide with the spectra presented in this thesis, the shift-referenced “ $\delta$ ”

analogues of the “ $\sigma$ ” shielding parameters discussed above are used, which correspond to the same phenomena.<sup>1</sup>

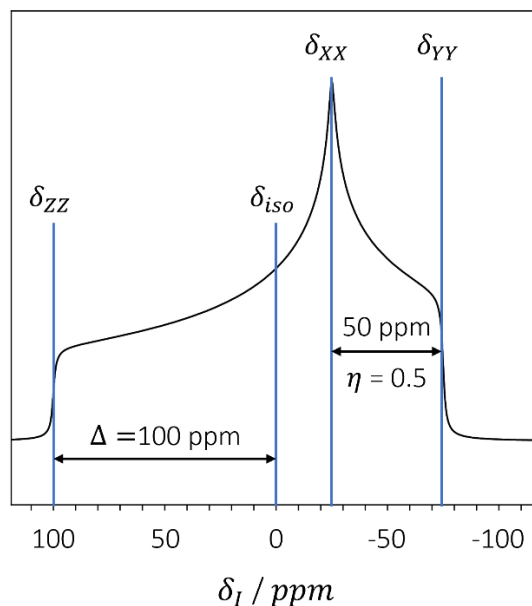


**Figure 2.3.** Simulated powder pattern with CSA contributions with  $\delta_{iso} = 0$  ppm,  $\Delta = 100$  ppm, and  $\eta = 0.5$ . Each of the contributions from the z, x, and y primary axis are highlighted. Simulated in ssNake V1.3.<sup>4</sup>

It is clear from **Fig. 2.3** that many frequencies are detected outside of the averaged isotropic shift,  $\delta_{iso}$ , at 0 ppm. Each of the individual nuclei contribute a sharp single-frequency resonance to the overall pattern. Nuclei oriented along the z principal axis have the largest deviation from the mean, appearing at  $\delta_{zz} = 100$  ppm, giving a  $\Delta$  of 100 ppm. Nuclei oriented along the x and y principal axis appear at  $\delta_{xx} = -25$  ppm and  $\delta_{yy} = -75$  ppm, respectively, giving an  $\eta_{CS}$  value of 0.5. Each of the measured frequencies between these states represent orientations that are linear combinations of the z, x, and y principal axis. In section 2.2.4, a technique for powder samples that mimics the rotational averaging seen in liquid samples called magic angle spinning

(MAS) is introduced. This technique allows each of the individual frequencies making up the powder pattern to coalesce toward  $\delta_{iso}$ , and has similar benefits for other nuclear interactions discussed below.

### 2.2.2 – Dipolar Coupling

In a given molecule there can be multiple nuclei in close proximity, each with their own magnetic moments that can interact with each other through space. The interaction energy,  $U$ , of two magnetic moments,  $\mu_i$ , separated in space by a distance,  $r$ , is given by **eqn. 2.19**.<sup>2</sup>

$$U = \frac{\rho_0}{4\pi} \left[ \frac{\mu_I \cdot \mu_S}{r^3} - \frac{3(\mu_I \cdot \vec{r})(\mu_S \cdot \vec{r})}{r^5} \right] \quad [2.19]$$

$\rho_0$  is the vacuum permeability, and  $\vec{r}$  is the vector between  $\mu_I$  and  $\mu_S$ . Recall **Eqn. 2.01**, which relates the magnetic moment operator of a nucleus to the nuclear spin operator. By combining **eqn. 2.01** with **eqn. 2.19**, the Hamiltonian for the dipolar interaction can be obtained:<sup>2</sup>

$$\hat{H}_D = \left[ \frac{\rho_0}{4\pi} \right] \gamma_I \gamma_S \hbar^2 \left[ \frac{\hat{I} \cdot \hat{S}}{r^3} - \frac{3(\hat{I} \cdot \vec{r})(\hat{S} \cdot \vec{r})}{r^5} \right] \quad [2.20]$$

Where  $\hat{I}$  and  $\hat{S}$  are nuclear spins with gyromagnetic ratios of  $\gamma_I$  and  $\gamma_S$ , respectively. This equation can be modified further by expressing the vectors in spherical coordinates (similar to  $\omega_{CS}(\theta, \phi)$ ), which results in the following simplified expression:<sup>2</sup>

$$\hat{H}_D = - \left[ \frac{\rho_0}{4\pi} \right] \left[ \frac{\gamma_I \gamma_S \hbar^2}{r^3} \right] [A + B + C + D + E + F] \quad [2.21]$$

With corresponding terms:

$$A = \hat{I}_z \hat{S}_z [3 \cos^2 \theta - 1] \quad [2.22]$$

$$B = -\frac{1}{4} [\hat{I}_+ \hat{S}_- + \hat{I}_- \hat{S}_+] [3 \cos^2 \theta - 1]$$

$$C = -\frac{3}{2} [\hat{I}_z \hat{S}_+ + \hat{I}_+ \hat{S}_z] \sin \theta \cos \theta e^{-i\phi}$$

$$D = -\frac{3}{2} [\hat{I}_z \hat{S}_- + \hat{I}_- \hat{S}_z] \sin \theta \cos \theta e^{+i\phi}$$

$$E = -\frac{3}{4} [\hat{I}_+ \hat{S}_+] \sin^2 \theta e^{-2i\phi}$$

$$F = -\frac{3}{4} [\hat{I}_- \hat{S}_-] \sin^2 \theta e^{+2i\phi}$$

$\hat{I}_\pm$  and  $\hat{S}_\pm$  are the ladder operators for the  $I$  and  $S$  nuclear spins, while  $\hat{I}_z$  and  $\hat{S}_z$  are the operators for the z-component of their respective magnetization. The Hamiltonian appears quite complex, but further analysis proves that each of the  $C$ ,  $D$ ,  $E$ , and  $F$  terms have no significant effect on the energy levels of the spin system, so  $\hat{H}_D$  can be truncated.<sup>2</sup> The leading term of  $\hat{H}_D$  contains the dipolar coupling constant,  $c_D$ :

$$c_D = \left[ \frac{\rho_0}{4\pi} \right] \left[ \frac{\gamma_I \gamma_S \hbar}{2\pi r^3} \right] \quad [2.23]$$

$c_D$  determines the strength of the dipolar interaction between the  $I$  and  $S$  nuclei. Even though the dipolar Hamiltonian is orientation dependant, as can be seen from the terms in **eqn. 2.22**,  $c_D$  is orientation independent and is a system specific parameter. The constant is very sensitive to the internuclear distance between  $I$  and  $S$ , and as a result, measurement of  $c_D$  between nuclei can help determine atomic distances and is important to fields such as NMR crystallography.<sup>5</sup>

In general, dipolar coupling can be separated into homonuclear and heteronuclear interactions, where  $I$  and  $S$  are equivalent and separate nuclei, respectively. The Hamiltonians for the homonuclear ( $\hat{H}_D^{hom}$ ) and heteronuclear ( $\hat{H}_D^{het}$ ) dipolar interactions are shown below in eqn 2.24 and eqn. 2.25.<sup>2</sup>

$$\hat{H}_D^{hom} = -c_D h [3 \cos^2 \theta - 1] \left[ \hat{I}_z \hat{S}_z - \frac{1}{2} [\hat{I}_x \hat{S}_x + \hat{I}_y \hat{S}_y] \right] \quad [2.24]$$

$$\hat{H}_D^{het} = -c_D h [3 \cos^2 \theta - 1] \hat{I}_z \hat{S}_z \quad [2.24]$$

The  $\hat{I}_\pm$  and  $\hat{S}_\pm$  ladder operators have been evaluated to their Cartesian forms and the  $C$ ,  $D$ ,  $E$ , and  $F$  terms have been truncated.  $\hat{H}_D^{hom}$  and  $\hat{H}_D^{het}$  differ only by the exclusion of the  $B$  term in  $\hat{H}_D^{het}$ . This is because the  $\hat{I}_x \hat{S}_x$  and  $\hat{I}_y \hat{S}_y$  operators seen in  $\hat{H}_D^{hom}$  are only significant if  $I$  and  $S$  have similar  $\omega_0$ ,<sup>2</sup> which is only the case if they are equivalent nuclei. Therefore, in  $\hat{H}_D^{het}$  the transverse terms can be ignored. The outcome of this is that the spin wavefunction under heteronuclear dipolar coupling ( $\psi_{I,m_I} \psi_{S,m_S}$ ) is a simple product of the original, uncoupled, spin-states:<sup>2</sup>

$$\psi_{I,m_I} = |I, m_I\rangle$$

$$\psi_{S,m_S} = |S, m_S\rangle$$

$$\psi_{I,m_I} \psi_{S,m_S} = |I, m_I \cdot S, m_S\rangle \quad [2.25]$$

The Hamiltonian can be applied in the same fashion as in eqn. 2.04 to find the dipolar contribution to the Zeeman energy transitions:<sup>2</sup>

$$-c_D h [3 \cos^2 \theta - 1] \hat{I}_z \hat{S}_z |I, m_I \cdot S, m_S\rangle = -c_D h [3 \cos^2 \theta - 1] m_I m_S |I, m_I \cdot S, m_S\rangle$$

$$E_D^{het} = c_D h [3 \cos^2 \theta - 1] m_I m_S \quad [2.26]$$

$$\Delta E_D^{het} = c_D h [3 \cos^2 \theta - 1] [m_{I,\beta} m_{S,\beta} - m_{I,\alpha} m_{S,\alpha}] \quad [2.27]$$

Recall the selection rule described in section 2.1.1, where only coherences of  $\Delta m_I = \pm 1$  can be observed. In a multi-spin system, this translates to the sum of coherences between spins  $I$  and  $S$ ,  $\Delta M = \Delta m_I + \Delta m_S$ , must also be equal to  $\pm 1$ . Therefore, if  $I$  magnetization is to be observed as  $\Delta m_I = \pm 1$ ,  $\Delta m_S$  must be 0, and as a result:

$$m_{I,\beta} m_{S,\beta} - m_{I,\alpha} m_{S,\alpha} = \pm \frac{1}{2} \quad [2.28]$$

$$\therefore \Delta E_D^{het} = \pm \frac{1}{2} c_D h [3 \cos^2 \theta - 1] \quad [2.29]$$

The observed frequency of spin  $I$  under heteronuclear dipolar coupling can then be found by directly translating the energetic contribution to frequency terms:

$$\omega_{D,het}^I = \omega_0^I \pm \frac{1}{2} c_D [3 \cos^2 \theta - 1] \quad [2.30]$$

Where  $\omega_0^I$  is the precession frequency of  $I$  in the absence of dipolar coupling.

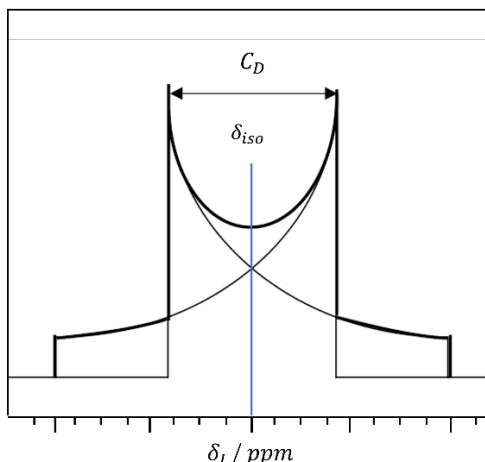


**Figure 2.4.** Simulated dipolar coupling powder pattern, showing the manifestation of  $C_D$  in the spectrum.<sup>2</sup> Reprinted with permission from *Solid State NMR Spectroscopy: Principles and Applications*. John Wiley & Sons: Cambridge, 2001 © 2001 John Wiley & Sons.<sup>2</sup>

**Fig. 2.4** shows the resulting powder pattern for nucleus  $I$ . The  $\pm \frac{1}{2}$  term arising from **eqn. 2.28** results in there being two distinct transitions with  $-[3 \cos^2 \theta - 1]$  and  $+ [3 \cos^2 \theta - 1]$  orientational dependencies. This results in the powder pattern of each transition being the mirror image of the other, with equal values of  $\delta_{iso}$ . Similar to what was seen for chemical shift anisotropy, the orientational dependence of the dipolar coupling powder pattern can be effectively averaged to  $\delta_{iso}$  by MAS, when the frequency of sample rotation is sufficiently large as compared to the strength of the dipolar couplings in the material of interest.

In section 2.3.2, a pulse sequence called dipolar heteronuclear multiple quantum correlation (D-HMQC) is described where the heteronuclear dipolar interaction is taken advantage of to gain chemical information on NaOB electrochemical products. As mentioned above, only the in-phase single quantum  $\Delta M = \pm 1$  coherences can be directly observed, but the D-HMQC experiment will take advantage of the unobservable multiple quantum ( $\Delta M > 1$ ) coherences to gain structural information about a sample.

### 2.2.3 – Quadrupolar Coupling

In **Fig. 2.1**, the Zeeman splitting for both  $I = \frac{1}{2}$  and  $I = \frac{3}{2}$  nuclei were shown. In the  $I = \frac{3}{2}$  diagram, the Zeeman energy levels of each  $m$  spin-state were equally spaced, resulting in a single observable frequency from three separate  $\Delta m = \pm 1$  transitions. In reality, the energy levels of quadrupolar nuclei undergo further perturbation from the ideal Zeeman splitting due to the quadrupolar coupling (QC) interaction.<sup>2, 6</sup> The

QC interaction results from  $I > \frac{1}{2}$  nuclei possessing an electric quadrupole moment in addition to the magnetic dipole moment of  $I = \frac{1}{2}$  nuclei.<sup>2</sup> The electric quadrupole moment interacts with any electric field gradient (EFG) in the immediate environment of the nucleus.<sup>2</sup> The Hamiltonian resulting from this interaction is a complex multiterm expansion of the EFG tensor ( $\mathbf{eq}$ ) that describes the spatial orientation of the EFG around the nucleus. A simplified Hamiltonian with an unexpanded EFG tensor is given in **eqn. 2.31**:<sup>2</sup>

$$\hat{H}_Q = \frac{eQ}{6I(2I-1)\hbar} [I \cdot \mathbf{eq} \cdot I] \quad [2.31]$$

Where  $Q$  is the nuclear quadrupole moment,  $e$  is the proton charge, and  $\mathbf{eq}$  is the EFG tensor. From this, the quadrupolar coupling constant ( $C_Q$ ) and quadrupolar frequency ( $\omega_Q$ ) are defined in **eqn. 2.32** and **eqn. 2.33**.<sup>2</sup>  $C_Q$  describes the strength of the QC interaction for a given nucleus, while  $\omega_Q$  is the base quadrupolar contribution to the transition frequency:<sup>2,7</sup>

$$C_Q = \frac{e^2 q Q}{\hbar} \quad [2.32]$$

$$\omega_Q = \frac{C_Q}{2I(2I-1)} \quad [2.33]$$

The effect of the expanded QC Hamiltonian on the Zeeman energy levels is typically computed via perturbation theory, rather than directly from the expanded Hamiltonian, and is quite complex.<sup>2</sup> The qualitative effect of the first and second order perturbative QC interactions on the Zeeman energy levels for an  $I = \frac{3}{2}$  nucleus is visualized in **Fig. 2.5**.<sup>6</sup>

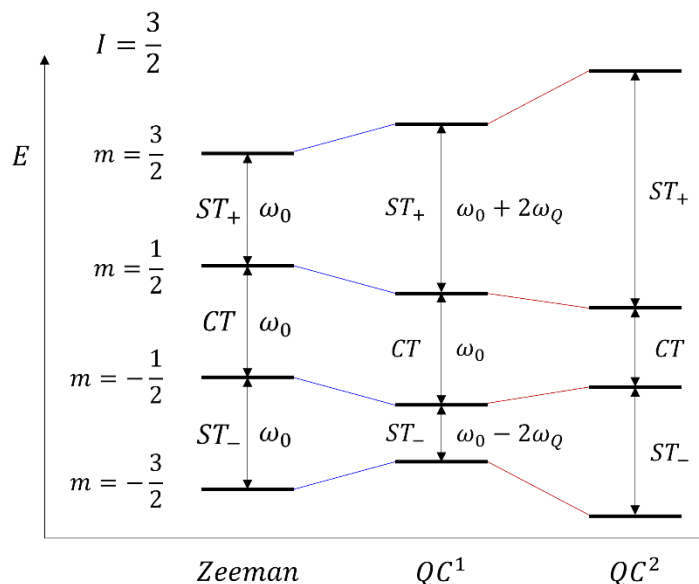


**Figure 2.5.** The perturbation of  $I = \frac{3}{2}$  Zeeman energy states by QC interactions of the first order ( $QC^1$ ) and second order ( $QC^2$ ).

As mentioned above, each of the three possible  $\Delta m = \pm 1$  transitions are of the same frequency,  $\omega_0$ , under Zeeman splitting alone. The subsequent first order perturbation ( $QC^1$ ) shifts all energy levels by the quadrupolar frequency,  $\omega_Q$ , and results in the transition having the familiar “ $3 \cos^2 \theta - 1$ ” orientation dependence that was seen for the chemical shielding and dipolar coupling interactions.<sup>6, 8</sup> The  $\omega_Q$  shift results in an asymmetric effect on the  $m = -\frac{1}{2} \rightarrow -\frac{3}{2}$  and  $m = \frac{3}{2} \rightarrow \frac{1}{2}$  satellite transitions (ST), while leaving the  $m = \frac{1}{2} \rightarrow -\frac{1}{2}$  central transition (CT) unaffected.<sup>2, 6</sup> In the case of a nucleus with a small  $C_Q$ ,  $QC^1$  is sufficient to describe the system.<sup>2, 6, 8</sup> An example of this is seen in **Fig. 2.6a**, which shows a simulated powder pattern of a  $I = \frac{3}{2}$  nuclei with a  $C_Q$  of 0.337 MHz and an  $\eta$  value of 0 (these values correspond to

those of the  $^{23}\text{Na}$  nucleus in  $\text{Na}(\text{NO}_3)$ , a common reference material in  $^{23}\text{Na}$  NMR).<sup>8</sup> The sharp CT is unaffected by the first order interaction, and experiences no anisotropic broadening or frequency shift. Both STs are observed on either side of the CT, spaced by  $2\omega_Q$ , and are heavily anisotropically broadened by the  $3 \cos^2 \theta - 1$  dependency.<sup>8</sup>

If  $C_Q$  is appreciable, the effect of the second order perturbation (QC<sup>2</sup>) must be considered. Unlike what was seen with QC<sup>1</sup>, QC<sup>2</sup> does not shift each energy level uniformly, and has a second orientation dependency of “ $35 \cos^4 \theta - 30 \cos^2 \theta + 3$ ” in addition to the original  $3 \cos^2 \theta - 1$  dependence.<sup>2, 6</sup> As a result, the QC<sup>2</sup> correction further distorts the STs, but also affects the CT frequency, causing significant anisotropic broadening. A simplified version of the QC<sup>2</sup> contribution to the frequency of a given transition,  $\omega_Q^M$ , is given in eqn. 2.34.<sup>6</sup>

$$\omega_Q^M(\theta) = \frac{\omega_Q}{\omega_0} [C_0^M + C_2^M [3 \cos^2 \theta - 1] + C_4^M [35 \cos^4 \theta - 30 \cos^2 \theta + 3]] \quad [2.34]$$

Where  $C_0^M$ ,  $C_2^M$ , and  $C_4^M$  are coefficients that depends on the magnitude ( $M$ ) of the transition being excited. The result of the anisotropic interactions on the CT ( $M = 1$ ) are shown in **Fig. 2.6b** and **2.6c**, which display the simulated spectra of a  $C_Q = 2.48$  MHz,  $I = \frac{3}{2}$  nucleus over broad, and enhanced frequency ranges. The ST of high  $C_Q$  nuclei are often unobservable, as the anisotropic broadening becomes very large and the transition frequencies are shifted substantially from  $\omega_0$ , as shown by the disappearance of the ST in **Fig. 2.6b**.<sup>2, 8</sup> In the expanded **Fig. 2.6c**, the effect of CT broadening is apparent, and the powder pattern has a distinct quadrupolar lineshape.

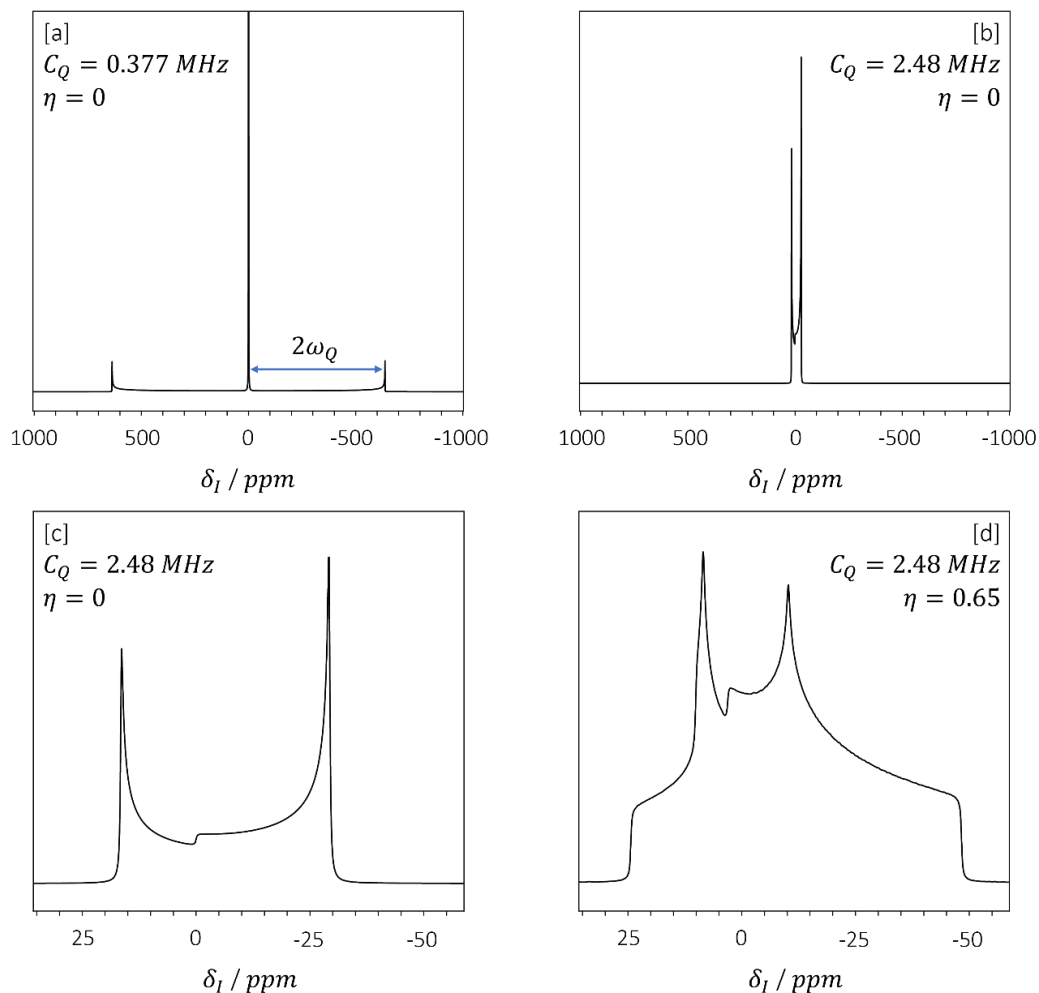


**Figure 2.6.** Simulated quadrupolar lineshapes with various parameter sets. [a]  $C_Q = 0.377 \text{ MHz}$ ,  $\eta = 0$  nucleus. [b]  $C_Q = 2.48 \text{ MHz}$ ,  $\eta = 0$  nucleus with a broad spectral width. [c]  $C_Q = 2.48 \text{ MHz}$ ,  $\eta = 0$  nucleus with an enhanced spectral width. [d]  $C_Q = 2.48 \text{ MHz}$ ,  $\eta = 0.65$  nucleus. Simulated in ssNake V1.3.<sup>4</sup>

The breadth of the CT lineshape is primarily dependant on  $C_Q$ , while the symmetry of the lineshape is primarily dependant on the quadrupolar asymmetry parameter,  $\eta$ .  $\eta$  is defined similarly to  $\eta_{CS}$  (for the chemical shielding interaction):<sup>2</sup>

$$\eta = \frac{q_{YY}^{PAS} - q_{XX}^{PAS}}{q_{ZZ}^{PAS}} \quad [2.35]$$

Where  $q_{ZZ}^{PAS}$ ,  $q_{XX}^{PAS}$ , and  $q_{YY}^{PAS}$  are the x, and y components of the EFG tensor ( $\mathbf{eq}$ ) in the PAS. **Fig. 2.6d** shows the same simulated nucleus with the  $\eta$  value increased from 0 to 0.65. The symmetry of the lineshape is significantly changed from the **Fig. 2.6c**, where  $\eta = 0$ . The  $C_Q = 2.48$  MHz,  $\eta = 0.65$  parameter set corresponds to that of one of the  $^{23}\text{Na}$  crystallographic sites of  $\text{Na}_2\text{CO}_3$ , a species commonly characterized in this thesis.<sup>9</sup>

It is evident that QC can have substantial effects on solid-state lineshapes, with the extent of lineshape distortion being dependant on the  $C_Q$  of the nucleus.  $C_Q$  itself is highly dependant on the structural symmetry of the chemical species being examined, since it is a function of the EFG tensor. Therefore, if the EFG tensor for a given nucleus is highly symmetrical,  $C_Q$  will be negligible, and the QC interaction has little to no effect on the final spectrum. This is observed for  $\text{NaO}_2$ , a species often seen in NMR spectra presented in this thesis, which is part of the cubic crystal system and has a  $C_Q$  of 0 for its single  $^{23}\text{Na}$  nucleus.

When  $C_Q$  is large, MAS can help partially mediate the QC anisotropic broadening, but unlike the dipolar and chemical shielding interactions, the effect is not completely averaged due to the additional “ $35 \cos^4 \theta - 30 \cos^2 \theta + 3$ ” orientational dependence presented by QC.<sup>2</sup> This can result in convoluted, overlapping spectra when multiple quadrupolar nuclei are present in a sample.

However, the strong QC interaction can also have benefits to sample characterisation. For one,  $\omega_Q^M(\theta)$  also has an isotropic contribution that is proportional to the  $C_Q$  of the nucleus (eqn. 2.34), similar to what was seen for  $\omega_{CS}$  (eqn. 2.18). Thus, the isotropic frequency of a quadrupolar nucleus contains both chemical shielding and quadrupolar additions to the original Zeeman frequency.

Secondly, the quadrupolar lineshape is very sensitive to  $C_Q$  and  $\eta$ , as seen in Fig. 2.6, resulting in different nucleic environments being distinguishable based on their anisotropic lineshape. This is one of the main reasons for the focus on NaOBs instead of LiOBs in this thesis.  $^7\text{Li}$  nuclei tend to have substantially lower  $C_Q$  values than  $^{23}\text{Na}$  nuclei, resulting in many of the  $^7\text{Li}$  nucleic environments seen in LiOB discharge products having very similar observed frequencies in NMR spectra, with broad, homogenous, overlapping lineshapes.<sup>10</sup> In contrast,  $^{23}\text{Na}$  nuclei appear over a wider frequency range, and have a larger variety of observable lineshapes. This has resulted in greater success in characterizing discharge products in NaOBs compared to the LiOB system.<sup>9</sup>

Lastly, the acquisition of high-resolution solid-state spectra of quadrupolar nuclei can still be obtained by a technique called *triple quantum magic angle spinning spectroscopy* (3QMAS). The details of the 3QMAS experiment, and what information it can provide, are given in section 2.3.3.

#### 2.2.4 – Magic Angle Spinning

The preceding three sections have described various nuclear interactions that can have adverse effects on the final observed NMR spectrum. Spectra with multiple nucleic environments quickly become difficult to interpret when every resonance is

anisotropically broadened by various orientational dependencies. The contributions from each nuclear interaction can be written in simplified forms as follows:<sup>2</sup>

$$\omega_{CS}(\theta) \propto \omega_0 \sigma_{iso} + [3 \cos^2 \theta - 1] \quad [2.36]$$

$$\omega_D^{het}(\theta) \propto [3 \cos^2 \theta - 1] \quad [2.37]$$

$$\omega_{CT}^{(2)}(\theta) \propto \frac{C_Q}{\omega_0} + [3 \cos^2 \theta - 1] + [35 \cos^4 \theta - 30 \cos^2 \theta + 3] \quad [2.38]$$

As mentioned in section 2.2.1, solution-state samples undergo rapid tumbling at rates that are many orders of larger than the broadening frequencies of each of these nuclear interactions, thus the orientational dependencies are completely averaged, and spectral peaks remain narrow. In ssNMR, MAS is used to reduce these anisotropic contributions.

Solid samples are packed into small cylindrical sample holders referred to as *rotors*. ssNMR rotors have small fins on one of the capped ends of the cylinder that have pressurized gas passed over them to induce spinning along the cylindrical longitudinal axis. The axis of rotation is specifically chosen to be at an angle of 54.74° to the z-axis of the  $B_0$  field ( $\theta$ ), the so-called “magic angle”. At  $\theta = 54.74^\circ$ , the  $3 \cos^2(\theta) - 1$  term in the above orientational dependencies becomes 0 (because  $\cos^2(54.74^\circ) = \frac{1}{3}$ ). This has the effect of completely averaging the anisotropic contributions of  $\omega_{CS}(\theta)$  and  $\omega_D^{het}(\theta)$  to 0. Importantly, the “ $\omega_0 \sigma_{iso}$ ” term of  $\omega_{CS}(\theta)$  is unaffected, as it has no orientational dependence. This is what allows for the separation of chemically different species in an NMR spectrum. In contrast,  $\omega_D^{het}(\theta)$  has no isotropic component, and the interaction is completely removed in MAS and solution-state spectra. This effect is shown in **Fig. 2.7a** to **2.7d** which contain the

simulated spectra of an  $I = \frac{3}{2}$  nucleus broadened by chemical shielding anisotropy at different MAS frequencies.

As the MAS frequency increases from 0 kHz (**Fig. 2.7a**) to 1 kHz (**Fig. 2.7b**) the continuous anisotropic lineshape is broken into many individual resonances surrounding the isotropic peak. These peaks are referred to as *spinning side bands* and are separated by the MAS frequency. During signal acquisition, the spinning rotor causes a periodic oscillation in the time-domain signal due to the orientation dependent anisotropic interaction. When the periodic signal undergoes FT, the result is a periodic distribution of peaks spaced by the MAS frequency. As the MAS frequency increases, the spacing between the spinning side bands also increases, and a greater proportion of the overall signal focuses into fewer sidebands, and ultimately into the isotropic peak.

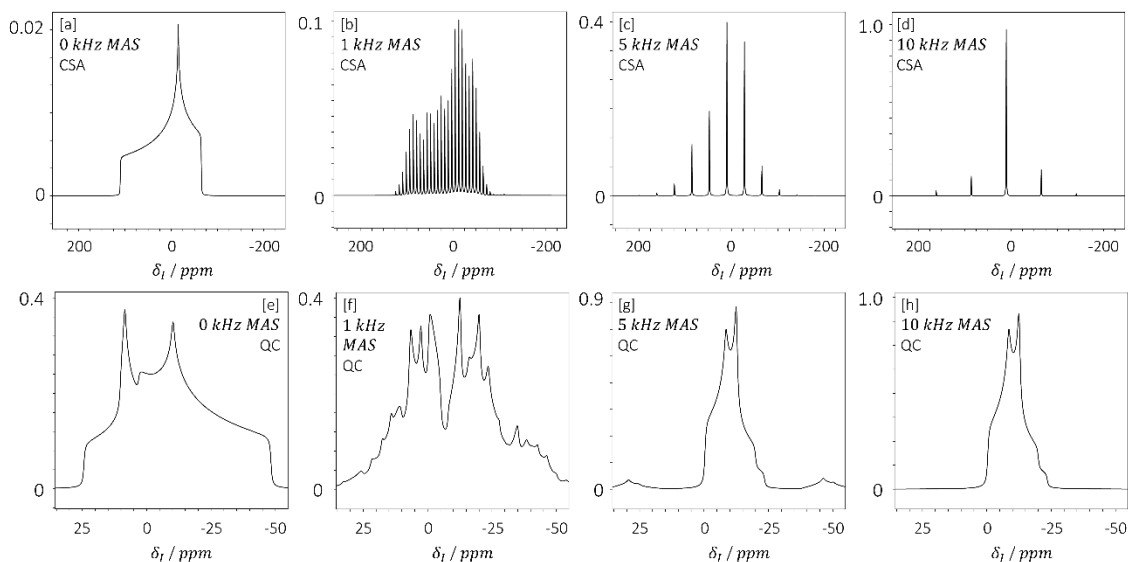


**Figure 2.7.** Simulated solid-state MAS spectra of an  $I = \frac{3}{2}$  nucleus under primarily [a – d] chemical shielding anisotropy and [e – h] quadrupolar coupling. Simulated in ssNake V1.3.<sup>4</sup>

In contrast to the dipolar and chemical shielding interactions, the quadrupolar anisotropic contribution to the CT frequency,  $\omega_{CT}(\theta)$ , is not completely averaged by MAS. The second rank “ $3 \cos^2 \theta - 1$ ” term still equals 0 under sufficiently fast MAS, but the fourth rank “ $35 \cos^4 \theta - 30 \cos^2 \theta + 3$ ” term is not completely eliminated. Instead, the fourth rank term is averaged to 0 at  $\theta = 30.56^\circ$ , and the resulting observed CT of quadrupolar nuclei retains significant anisotropic broadening even at high MAS rates. This is shown in **Fig. 2.7e** to **2.7h**, which contain the simulated spectra of the same  $I = \frac{3}{2}$  nucleus seen in **Fig. 2.6d**. As the MAS frequency is increased, the CT is significantly narrowed, but the broad anisotropic lineshape remains.

The double angular dependence of  $\omega_{CT}(\theta)$  can result in spectra with unresolved, overlapping peaks when multiple quadrupolar nuclei are present. A number of techniques have been developed to collect high resolution isotropic spectra on quadrupolar nuclei with appreciable  $C_Q$  values. Two prominent techniques include double rotation spinning (DOR) and dynamic angle spinning (DAS), which involve spinning the solid-state rotor at multiple  $\theta$  angles, either simultaneously or sequentially, to average both the second- and fourth-rank terms of  $\omega_{CT}(\theta)$  to 0.<sup>2, 11, 12</sup> Both of these techniques are certainly useful, but are impractical to implement with standard ssNMR hardware. An alternative approach is to average the anisotropic interactions by manipulating the magnetization using an appropriate pulse sequence. This is done by the 3QMAS experiment, and is described in the following section.

## 2.3 – Pulse Sequences

The goal of an NMR pulse sequence is to manipulate the magnetization of a sample in such a way as to provide the spectroscopist with the desired chemical information. An extensive number of pulse sequences exist, which can provide a large variety of information including sample identity, reaction kinetics, chemical structure via nuclear correlations established through J-coupling or dipolar coupling interactions, ion dynamics, and more.<sup>5, 9, 13, 14</sup> The pulse sequences most frequently used in this thesis are described in this section.

### 2.3.1 – The Spin Echo

The one-pulse experiment described in section 2.1.2 is shown in **Fig. 2.8a** along with the pulse sequence of the Hahn-echo experiment in **Fig. 2.8b**. The one-pulse experiment is often adequate for the characterisation of electrochemical products in battery systems, but a challenge of the experiment is the use of the same RF coil to apply a high-power pulse immediately before recording the resulting FID. This can result in the first few points of the FID containing residual ringing current from the excitatory RF pulse, obscuring the valuable initial data points of the signal. The Hahn-echo pulse sequence avoids this through a simple, but clever, manipulation of nuclear spin-states.<sup>15</sup>

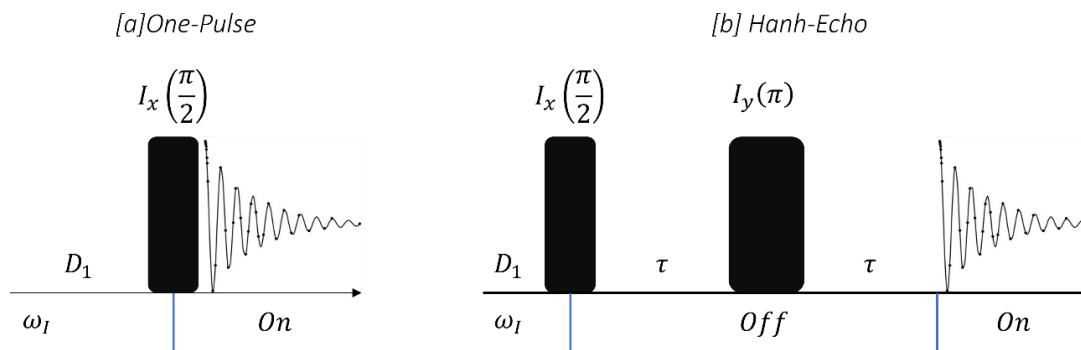


**Figure 2.8.** [a] One-pulse and [b] Hahn-echo pulse sequences. The pulse sequence “blocks” where magnetization evolution is effectively “on” or “off” are identified below each sequence.

The initial RF pulse of the Hahn-echo is identical to that of the one-pulse experiment, and the magnetization is excited into the  $x - y$  plane. Recalling the PrOF described in section 2.1.2:

$$I_z \xrightarrow{I_x(\frac{\pi}{2})} -I_y$$

The transverse magnetization is then allowed to evolve under Larmor precession for a specified time,  $\tau$ :

$$-I_y \xrightarrow{\omega_I I_z} -I_y \cos(\omega_I \tau) + I_x \sin(\omega_I \tau)$$

This results in the magnetization vector being at some angle “ $\omega_I \tau$ ” to the  $y$ -axis in the transverse plane. A  $\pi$  ( $180^\circ$ ) pulse is then applied along the  $y$ -axis, which has the effect of inverting the magnetization with respect to the  $y$ -axis:

$$-I_y \cos(\omega_I \tau) + I_x \sin(\omega_I \tau) \xrightarrow{I_y(\pi)} -I_y \cos(\omega_I \tau) - I_x \sin(\omega_I \tau)$$

In the vector model, this can be thought of as moving the magnetization vector from the  $[x, -y]$  quadrant of the transverse plane to the  $[-x, -y]$  quadrant. The magnetization is now allowed to evolve under Larmor precession for an additional period,  $\tau$ . This

results in the entire  $-I_y \cos(\omega_I \tau) - I_x \sin(\omega_I \tau)$  spin-state being acted upon by the Larmor precession operator, resulting in a linear combination of spin-states that can be stated as:

$$-I_y \cos(\omega_I \tau) - I_x \sin(\omega_I \tau) \xrightarrow{\omega_I I_z} \begin{cases} [-I_y \cos(\omega_I \tau) - I_x \sin(\omega_I \tau)] \cos(\omega_I \tau) \\ [I_x \cos(\omega_I \tau) - I_y \sin(\omega_I \tau)] \sin(\omega_I \tau) \end{cases}$$

Where the bracket operator simply implies the sum of the initial (upper) and resulting (lower) spin-states. Recalling the identity “ $\cos^2(x) + \sin^2(x) = 1$ ”, this state is evaluated as:

$$\begin{aligned} & [-I_y \cos(\omega_I \tau) - I_x \sin(\omega_I \tau)] \cos(\omega_I \tau) + [-I_y \cos(\omega_I \tau) - I_x \sin(\omega_I \tau)] \sin(\omega_I \tau) \\ &= -I_y \cos^2(\omega_I \tau) - I_x \sin(\omega_I \tau) \cos(\omega_I \tau) + I_x \cos(\omega_I \tau) \sin(\omega_I \tau) - I_y \sin^2(\omega_I \tau) \\ &= -I_y \cos^2(\omega_I \tau) - I_y \sin^2(\omega_I \tau) \\ &= -I_y [\cos^2(\omega_I \tau) + \sin^2(\omega_I \tau)] \\ &= -I_y \end{aligned}$$

This admittedly excessive treatment proves that the Hahn-echo pulse sequence develops pure  $-I_y$  magnetization after the second  $\tau$  period. The result is magnetization of full intensity at the moment acquisition begins, with a time delay of  $\tau$  since the last RF pulse to minimize any residual current in the RF coil. This pulse sequence also has the property of refocusing any bulk dephasing that occurred due to spin-spin ( $T_2$ ) relaxation. This can be easily understood by imagining the above PrOF result for a real sample composed of many individual spins, each with a slightly different Larmor precession frequency,  $\omega_I$ . Since the treatment is not dependant on the absolute value of  $\omega_I$ , every individual spin that dephases during the initial  $\tau$  period,

will refocus during the second  $\tau$  period to reach  $-I_y$  precisely at the moment of acquisition. Thus, the dephasing effect of  $T_2$  is removed, and the signal is guaranteed to be fully in-phase at the start of the FID.

### 2.3.2 – Dipolar Heteronuclear Multiple Quantum Correlation (D-HMQC)

As discussed in section 2.2.2, the dipolar interaction couples the magnetic fields of excited spin-states through physical space. The two-dimensional D-HMQC pulse sequence is used to map the dipolar interaction of coupled heterogenous nuclei in a sample. In this thesis, the sequence is used to deconvolute complex  $^{23}\text{Na}$  spectra by identifying chemical species that contain both  $^1\text{H}$  and  $^{23}\text{Na}$  nuclei.

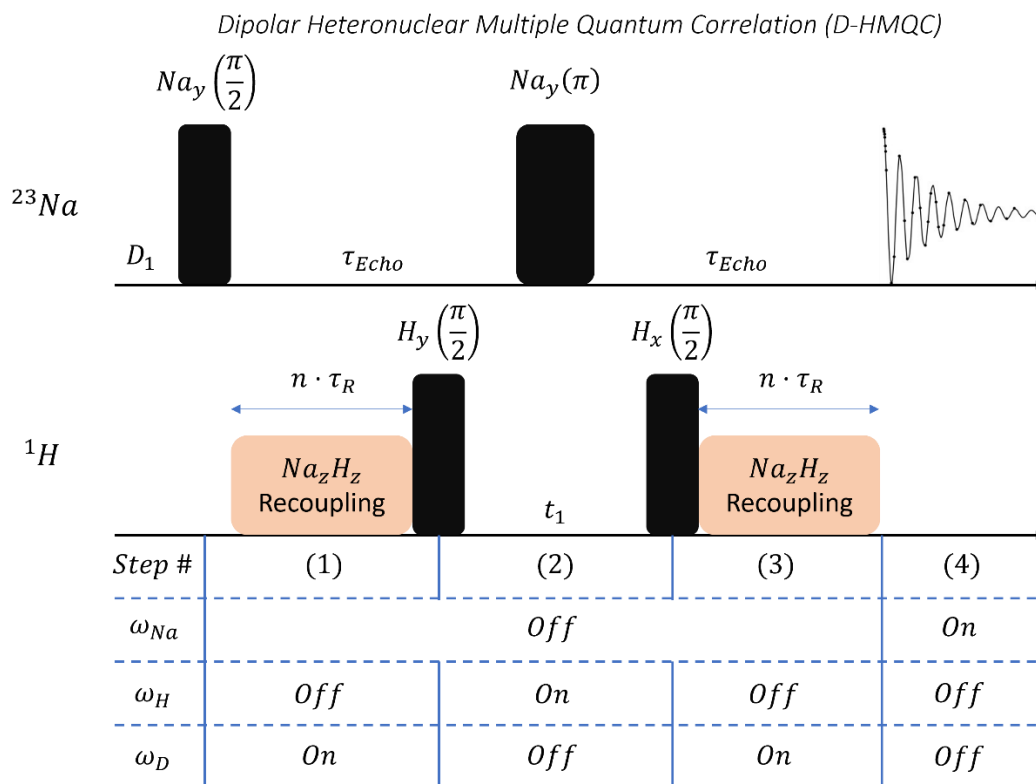


**Figure 2.9.** Pulse sequence of the  $^{23}\text{Na}\{^1\text{H}\}$  D-HMQC experiment used in this thesis.<sup>16</sup>

The two-dimensional  $^{23}\text{Na}\{^1\text{H}\}$  D-HMQC pulse sequence (**Fig. 2.9**) achieves this through four distinct pulse sequence stages:

- (1) a  $^{23}\text{Na} / ^1\text{H}$  correlation is created via the dipolar interaction.
- (2) the  $^1\text{H}$  component of the coherence evolves over a variable time,  $t_1$ .
- (3) the coherence is uncoupled to give pure  $^{23}\text{Na}$  magnetization.
- (4)  $^{23}\text{Na}$  Larmor precession is observed.

The result of this is observable  $^{23}\text{Na}$  magnetization that has been imprinted with  $^1\text{H}$  magnetization from the evolution period in step (2). However, in order to couple and decouple the  $^1\text{H}$  and  $^{23}\text{Na}$  nuclei in steps (1) and (3), the dipolar interaction must be reintroduced to the system due to the effective cancelling out of dipolar coupling by MAS (as described in section 2.2.2). This is achieved using predetermined dipolar *recoupling* blocks within the D-HMQC pulse sequence (shown in orange). In short, recoupling blocks in MAS experiments reintroduce the dipolar interaction by applying  $\pi$  pulses at defined intervals throughout a single rotor rotation period, inverting the magnetization at regular intervals to make the sinusoidal MAS averaging constructive instead of destructive.

To make the PrOF treatment of the  $^{23}\text{Na}\{^1\text{H}\}$  D-HMQC pulse sequence simpler, notice that the pulse arrangement of the  $^{23}\text{Na}$  channel is identical to that of the Hahn-echo sequence described above. Therefore, after the initial  $^{23}\text{Na}$  excitation pulse, no Larmor evolution of  $^{23}\text{Na}$  ( $\omega_{Na}$ ) occurs. This is shown under the pulse sequence by describing  $\omega_{Na}$  as “*Off*” until acquisition. Similar treatments can be done on each of the  $\omega_H$  and  $^{23}\text{Na} / ^1\text{H}$  dipolar ( $\omega_D$ ) evolution to determine when each interaction is

present in the experiment. For simplicity, only the “*On*” interactions will be tracked in this treatment.

Initially the  $^{23}\text{Na}$  spin is excited by the  $\frac{\pi}{2}_y$  pulse:

$$Na_z \xrightarrow{Na_y\left(\frac{\pi}{2}\right)} Na_x$$

During the recoupling period, the dipolar interaction is refocused. The dipolar coupling operator is  $\omega_D Na_z H_z$ , representing the  $^{23}\text{Na} / ^1\text{H}$  coupled magnetization which evolves at the frequency,  $\omega_D$ , for a chosen time,  $n\tau_R$ , that is an integer multiple of a rotor period:

$$Na_x \xrightarrow{\omega_D Na_z H_z} Na_x \cos(\omega_D n\tau_R) + Na_y H_z \sin(\omega_D n\tau_R)$$

When setting up the  $^{23}\text{Na}\{^1\text{H}\}$  D-HMQC pulse sequence,  $n\tau_R$  is optimized to be equal to be  $\frac{\pi}{2\omega_D}$ , which gives:

$$Na_x \cos\left(\omega_D \frac{\pi}{2\omega_D}\right) + Na_y H_z \sin\left(\omega_D \frac{\pi}{2\omega_D}\right) = Na_y H_z$$

Therefore, by the end of step (1) only the dipolar-coupled antiphase SQ coherence,  $Na_y H_z$ , is present. In step (2) a  $\frac{\pi}{2}$  pulse is applied on the  $^1\text{H}$  channel to excite the  $^1\text{H}$  component into the transverse plane, creating the multiple quantum (MQ) coherence ( $|\Delta M| > 1$ ):

$$Na_y H_z \xrightarrow{H_y\left(\frac{\pi}{2}\right)} Na_y H_x$$

In step (2) of the pulse sequence, the  $^1\text{H}$  component of the MQ coherence is allowed to evolve unperturbed for a time,  $t_1$ , imprinting the magnetization with pure  $^1\text{H}$  evolution:

$$Na_y H_x \xrightarrow{\omega_H H_z} Na_y H_x \cos(\omega_H t_1) + Na_y H_y \sin(\omega_H t_1)$$

In a more thorough treatment, it can be shown that only the resultant  $Na_y H_y \sin(\omega_H t_1)$  state will produce observable magnetization during acquisition. Therefore, the  $Na_y H_x \cos(\omega_H t_1)$  term is ignored. The  $^1\text{H}$  evolution is ended by the subsequent  $H_x \left(\frac{\pi}{2}\right)$  pulse:

$$\sin(\omega_H t_1) Na_y H_y \xrightarrow{H_x \left(\frac{\pi}{2}\right)} \sin(\omega_H t_1) Na_y H_z$$

In step (3), the dipolar coupling is now allowed to evolve again for a time  $\frac{\pi}{2\omega_D}$  to create pure a  $^{23}\text{Na}$  in-phase SQ coherence:

$$\sin(\omega_H t_1) Na_y H_z \xrightarrow{\omega_D Na_z H_z \left(\frac{\pi}{2\omega_D}\right)} -\sin(\omega_H t_1) Na_x$$

Finally, in step (4) the in-phase SQ  $Na_x$  magnetization (imprinted with  $\omega_H$ ) can evolve throughout acquisition at  $\omega_{Na}$ :

$$-\sin(\omega_H t_1) Na_x \xrightarrow{\omega_{Na} Na_z} -\sin(\omega_H t_1) Na_y \sin(\omega_{Na} t_{aq})$$

The final result is an oscillating observable  $^{23}\text{Na}$  magnetization that is weighted by the imprinted constant “ $\sin(\omega_H t_1)$ ”. Therefore, if many 1D spectrum are acquired while varying the  $^1\text{H}$  evolution time,  $t_1$ , the intensity of coupled  $^{23}\text{Na}$  peaks will sinusoidally oscillate with a frequency of  $\omega_H$ , as the argument of the  $\sin$  function,  $\omega_H t_1$ , increases.

Thus a second FT can be implemented in the  $t_1$  dimension that results in an indirectly obtained  $^1\text{H}$  spectrum where each  $^1\text{H}$  frequency,  $\omega_H$ , is correlated to a  $^{23}\text{Na}$  frequency,  $\omega_{\text{Na}}$ .

In practice, a 2D spectrum is constructed with the directly observed  $^{23}\text{Na}$  spectrum along the x-axis, and the indirectly observed  $^1\text{H}$  spectrum along the y-axis, with cross peaks appearing in the correlated contour plot. A practical example of this is shown in **Fig. 2.10**, where the 1D  $^{23}\text{Na}$  (**Fig. 2.10a**), 1D  $^1\text{H}$  (**Fig. 2.10b**), and 2D  $^{23}\text{Na}\{^1\text{H}\}$  D-HMQC (**Fig. 2.10c**) spectra of  $\text{NaH}_2\text{PO}_4$  are shown.

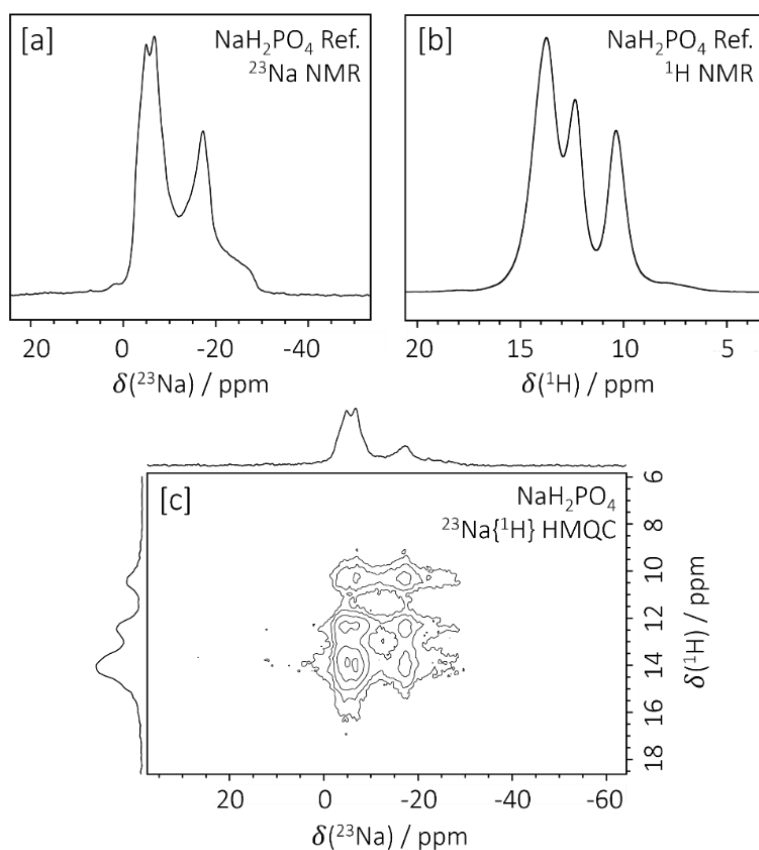


**Figure 2.10.** [a] 1D  $^{23}\text{Na}$ , [b] 1D  $^1\text{H}$ , and [c] 2D  $^{23}\text{Na}\{^1\text{H}\}$  D-HMQC spectrum of  $\text{NaH}_2\text{PO}_4$ . Each spectrum was collected at a field of 11.7 T at a spinning rate of 30 kHz MAS.

The compound has two distinct quadrupolar  $^{23}\text{Na}$  resonances resulting from two unique  $^{23}\text{Na}$  crystallographic sites, and three resolved  $^1\text{H}$  peaks from four unique  $^1\text{H}$  environments (with two overlapping resonances forming the single peak at -14 ppm). The 2D spectrum shows the dipolar correlation between each of the  $^{23}\text{Na}$  and  $^1\text{H}$  environments as cross peaks in the contour plot, suggesting that every  $^{23}\text{Na}$  nucleus is within an appropriate distance of each  $^1\text{H}$  nucleus to be dipolar coupled. In a complex electrochemical spectrum with  $^{23}\text{Na} / ^1\text{H}$

### 2.3.3 – Triple Quantum Magic Angle Spinning Spectroscopy (3QMAS)

Similar to  $^{23}\text{Na}\{^1\text{H}\}$  D-HMQC, which leverages the dipolar coupling interaction to separate  $^1\text{H}$ -correlated  $^{23}\text{Na}$  resonances by their corresponding  $^1\text{H}$  shifts, the 3QMAS pulse sequence leverages the QC interaction to separate anisotropic  $^{23}\text{Na}$  resonances by their isotropic CT shifts.<sup>17, 18</sup> Recall **eqn 2.34**, which gave a simplified analysis of the isotropic, second-rank anisotropic, and fourth-rank anisotropic contributions of QC to the observed CT frequency. The equation states that the contribution of the quadrupolar interaction to the Larmor frequency is dependant on the magnitude of the transition being excited ( $M$ ). For example, the energy level diagram of the  $I = \frac{3}{2}$  nucleus (**Fig. 2.5**) has two symmetric transitions of  $\frac{3}{2} \rightarrow -\frac{3}{2}$  and  $\frac{1}{2} \rightarrow -\frac{1}{2}$ , corresponding to the triple quantum ( $M = 3$ ) and single quantum ( $M = 1$ ) transition, respectively. The QC contributions of magnetization evolving under these transitions are shown below, with the second-rank anisotropic term omitted since it is averaged to 0 by MAS:<sup>6</sup>

$$\omega_Q^{1Q}(\theta) = \frac{C_Q}{\omega_0} [C_{1Q}^0 + C_{1Q}^4(35 \cos^4 \theta - 30 \cos^2 \theta + 3)] \quad [2.39]$$

$$\omega_Q^{3Q}(\theta) = \frac{C_Q}{\omega_0} [C_{3Q}^0 + C_{3Q}^4(35 \cos^4 \theta - 30 \cos^2 \theta + 3)] \quad [2.40]$$

A pulse sequence can be imagined where the 3Q transition is first excited and allowed to evolve for some time  $t_1$ , and the 1Q transition is subsequently excited and evolved for some time  $t_2$ . The total fourth-rank anisotropic contribution ( $An_Q^4$ ) would be:<sup>6</sup>

$$An_Q^4 = t_1 C_{3Q}^4 + t_2 C_{1Q}^4 (35 \cos^4 \theta - 30 \cos^2 \theta + 3)$$

To completely remove  $An_Q^4$ :

$$t_1 C_{3Q}^4 + t_2 C_{1Q}^4 = 0$$

$$t_2 = -\frac{C_{3Q}^4}{C_{1Q}^4} t_1 = k t_1 \quad [2.41]$$

$$k = -\frac{C_{3Q}^4}{C_{1Q}^4} \quad [2.42]$$

Therefore, it is possible to observe completely isotropic quadrupolar resonances if the 3Q and 1Q transitions are excited in a controlled manner.<sup>2, 6</sup> The ratio  $k$  is constant for a given nuclear spin value,  $I$ . For spin  $I = \frac{3}{2}$  nuclei,  $k = -\frac{7}{9}$ , and thus an isotropic echo is at  $t_2 = -\frac{7}{9} t_1$ .<sup>2, 6</sup> The 3QMAS pulse sequence takes advantage of this phenomenon to create 2D spectra of quadrupolar nuclei separated in the indirect dimension by their isotropic frequencies.

There are multiple versions of the basic 3QMAS pulse sequence.<sup>2</sup> However, only the three-pulse z-filtered sequence is used in the work presented in thesis and is presented in **Fig. 2.11**. **Fig. 2.11** also includes a plot of the coherence pathway

traversed by the magnetization throughout the course of the sequence. Initially, a high-power pulse excites the high energy  $\pm 3Q$  coherence, and the magnetization is allowed to evolve for a time  $t_1$ . The magnetization is then refocused to the  $0Q$  state in a process known as z-storage. After a short delay,  $\tau$ , the central transition is selectively excited by a relatively weak RF pulse, resulting in a  $1Q$  coherence. The magnetization then evolves in the  $1Q$  state while the signal is acquired. When the  $kt_1$  refocusing time described by eqn. 2.42 is reached, the anisotropic interaction is refocused, and an isotropic echo is observed.

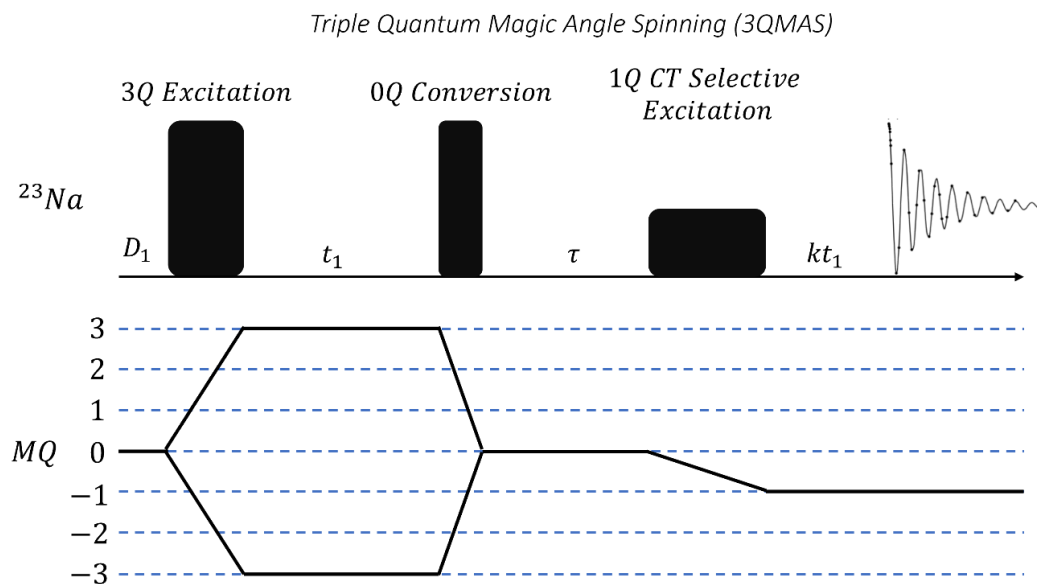


**Figure 2.11.** Pulse sequence of the z-filtered 3QMAS experiment, with the coherence order of the magnetization over the course of the pulse sequence plotted below.<sup>2, 6</sup>

In the 2D experiment, each subsequent 1D slice is collected with increasing  $t_1$ .<sup>6</sup> This results in longer  $3Q$  evolution, and therefore the isotropic echo is pushed further into the acquisition period, as  $kt_1$  increases as well. After applying a FT in the  $t_2$  and  $t_1$  dimensions, a 2D spectrum is generated with the isotropic axis tilted at a slope of  $k$

with respect to the anisotropic dimension. Applying a shearing transformation then yields gives an aligned 2D spectrum with the quadrupolar anisotropic lineshapes on the direct (x) axis, and the pure isotropic lineshapes on the indirect (y) axis.<sup>18</sup>

Practically, this allows for separation of broad, overlapping, quadrupolar lineshapes based on their isotropic frequency. The fully processed 2D 3QMAS spectrum of  $\text{Na}_2\text{CO}_3$ , a common material characterized in NaOBs, is shown in **Fig. 2.12b**. The simple 1D one-pulse spectrum is shown in **Fig. 2.12a** for comparison. The  $\text{Na}_A$  and  $\text{Na}_B$  sites that are overlapping in the 1D experiment are separated in the indirect dimension in the 3QMAS spectrum due to their significantly different isotropic frequencies. The vertical and horizontal projections of the 2D spectrum, representing the anisotropic and isotropic lineshapes, are shown in **Fig. 2.12c** and **Fig. 2.12d**. In the direct projection, the typical quadrupolar powder patterns are observed and resemble those of the 1D experiment in **Fig. 2.12a**. In the indirect projection, the broad anisotropic pattern of  $\text{Na}_C$  is no longer observed. Instead, the resonance appears as an isotropic gaussian, albeit with significant intensity loss.

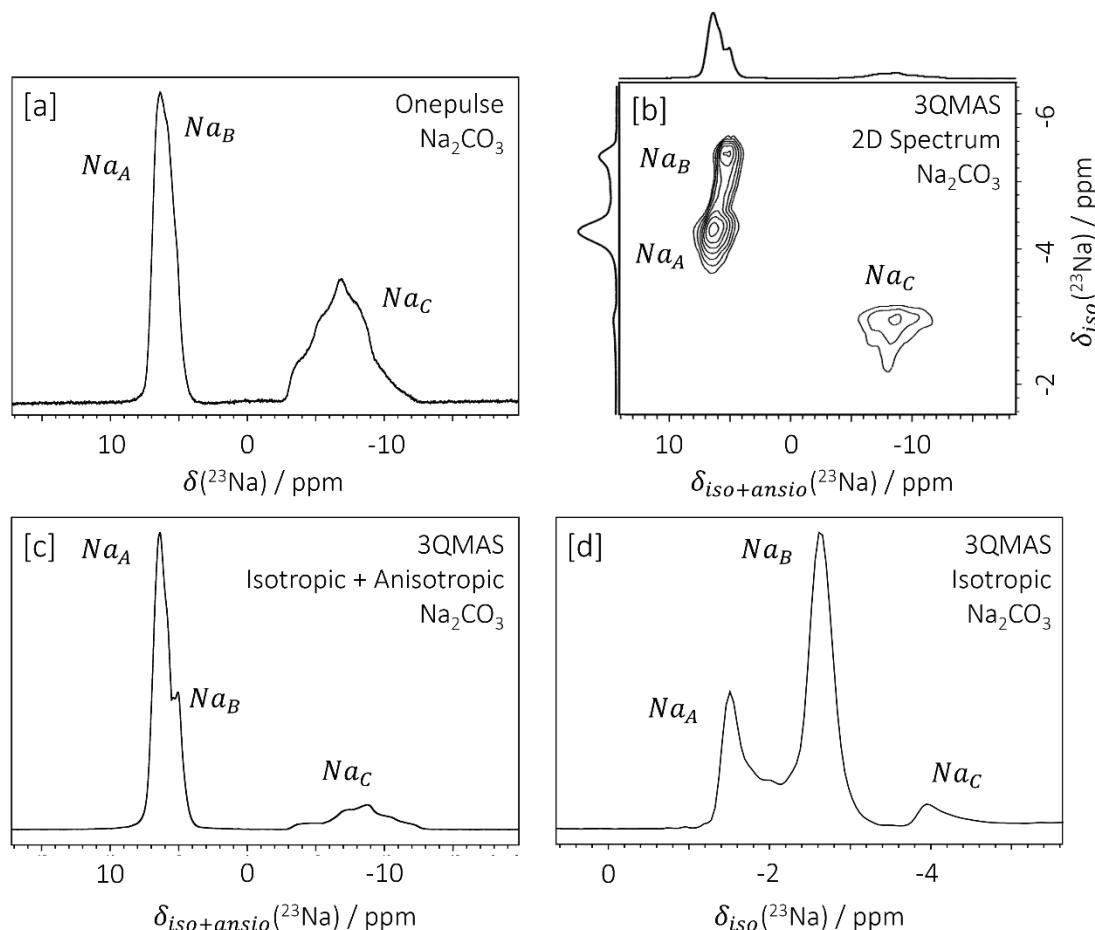


**Figure 2.12.** [a] 1D onepulse spectrum of  $\text{Na}_2\text{CO}_3$  [b] 2D 3QMAS spectrum of  $\text{Na}_2\text{CO}_3$ . [c] Projection of the direct dimension giving the 1D  $\text{Na}_2\text{CO}_3$  spectrum with isotropic and anisotropic contributions. [d] Projection of the indirect dimension giving the 1D pure isotropic  $\text{Na}_2\text{CO}_3$  spectrum. This spectrum was collected at a magnetic field of 19.9 T at a MAS spinning rate of 30 kHz.

Different variations of the 3QMAS pulse sequence from the one showed here exist, and each arrive at the same chemical information.<sup>18</sup> The z-filter analogue was chosen for use in this thesis since it offers the largest tolerance toward ranging nucleic environments in the sample. In the z-filter sequence, the  $M = -3$  and  $M = 3$  coherences both get converted to  $M = 0$  by the 0Q conversion pulse, before being excited to  $M = -1$  for acquisition. Both of the  $M = \pm 3 \rightarrow 0$  transitions have equal

amplitudes of  $\Delta M = 3$ , and are effectively completed by a single pulse. Other sequences that omit the z-filter step instead have to convert both the  $M = -3$  and  $M = 3$  coherences simultaneously to  $M = -1$  for acquisition, which have unequal transition amplitudes of  $\Delta M = 2$  and  $\Delta M = 4$  respectively. The efficiencies of these transitions are substantially different, and result in significant distortions of the final FID.<sup>2</sup> The z-filter sequence does not experience these spectral distortions. The one downside of choosing the z-filter sequence is that a significant portion of the bulk magnetization is lost during the z-storage period.

Nonetheless, the  $^{23}\text{Na}$  z-filter 3QMAS sequence is used in this thesis to effectively characterize the electrochemical products of the NaOB. Pairing this technique with simple 1D experiments, and the 2D  $^{23}\text{Na}\{^1\text{H}\}$  D-HMQC allows for a wealth of information to be gained on electrochemical samples.

#### 2.3.4 – ssNMR Practical Challenges

The carbon-based NaOB cathodes studied in this thesis have a substantial bulk electrical conductivity, which is needed to facilitate rapid electron transfer within the cell. However, this presents a challenge to characterisation by ssNMR. When electrically conductive materials are forced to spin at rapid rates in the large  $B_0$  field of an NMR spectrometer, a large eddy current can be produced within the electrically conductive rotating material that produces its own magnetic field that opposes  $B_0$ .<sup>19</sup> This opposing magnetic field resists spinning, and higher gas pressures are needed to achieve appreciable MAS frequencies. This results in less stable spinning rates, and may lead to a rotor crash, damaging the NMR probe.

This effect is lessened at lower  $B_0$  fields, and is the main reason for use of the 11.7 T magnet (over the 19.9 T magnet) for the characterisation of cycled NaOB cathodes in this thesis. The effect is also mitigated by packing a lower amount of conductive material into the spinning rotor and mixing the conductive sample with an electrically insulating (and chemically stable) additive to break up any long-range conduction. This strategy was also implemented here, using  $\text{TiO}_2$  as the co-packing material for NaOB cathodes. In general, even with the adverse phenomenon described above, the materials studied by ssNMR in this thesis were relatively amiable.

### 2.3 – Pulsed Field Gradient NMR Spectroscopy

In each of the NMR experiments described above, the strength of the external magnetic field,  $B_0$ , has been assumed to be static through the spatial coordinates of the sample. In fact, this assumption is imperative to ensuring narrow lineshapes are observed in the NMR spectrum. This is due to the dependence of the Larmor frequency on  $B_0$ , described by [eqn. 2.09](#). If the  $B_0$  field was instead spatially dependent, a range of frequencies would be observed as equivalent, but spatially separated, nuclei would experience different values of  $B_0$ :<sup>1</sup>

$$\omega_0(\mathbf{r}) = -\gamma B_0(\mathbf{r}) \quad [2.43]$$

Where  $\mathbf{r}$  is a vector describing the spins location in space.  $B_0(\mathbf{r})$  can be made spatially dependent in a controlled manner by applying a separate magnetic field gradient over the sample,  $\mathbf{G}$ . This is typically achieved through the use of specially designed gradient RF coils that create a gradient magnetic field that adds to the existing homogenous  $B_0$  field. In the work described in this thesis, the created gradient field is always

unidirectional along the  $z$ -axis. The resulting dependence of  $\omega_0$  to an applied gradient field is then:<sup>1</sup>

$$B_0(\mathbf{z}) = B_0 + \mathbf{zG} \quad [2.44]$$

$$\omega_0(\mathbf{z}) = -\gamma[B_0 + \mathbf{zG}] \quad [2.45]$$

Where  $\mathbf{z}$  is the positional vector describing the spins position along the  $z$ -axis. The ability to create magnetic field gradients via RF pulses allows for the design of pulse sequences that encode spatial information. This type of NMR spectroscopy is referred to as pulsed-field gradient (PFG) NMR.

PFG NMR is used in this thesis to measure diffusion coefficients of liquid electrolytes. There are multiple variations of PFG pulse sequences that can accomplish this, but the general principles by which PFG experiments measure diffusion coefficients are best understood by analysing the basic stimulated echo sequence (PGSTE) (**Fig. 2.13**).<sup>20</sup>

### 2.3.1 – The Pulsed Field Gradient Stimulated Echo Experiment (PGSTE)

The PGSTE pulse sequence is outlined in **Fig. 2.13a**, with the accumulated phase of the nucleus during the experiment illustrated in **Fig. 2.13b**. Just examining channel  $I$ , the sequence is similar to the Hahn-echo experiment described in section 2.3.1, except the inverting  $\pi$  pulse is split into two separate  $\frac{\pi}{2}$  pulses to allow for a  $z$ -storage delay. Thus, the PGSTE experiment is simply a refocusing echo with phase encoding gradient pulses.

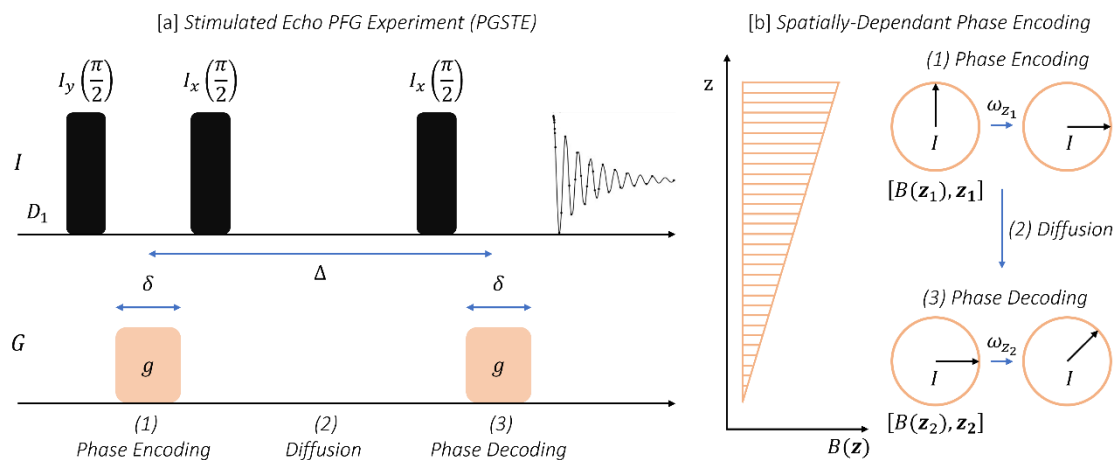


**Figure 2.13.** [a] PGSTE pulse sequence.<sup>20</sup> The  $I$  channel represent typical RF pulses, while the  $G$  channel represents gradient pulses. [b] Illustration of spatially-dependant phase encoding during the PGSTE sequence.

In step (1) of the sequence, transverse magnetization is created by the initial  $\frac{\pi}{2}$ , and almost immediately a gradient pulse of strength,  $g$ , and of relatively short duration,  $\delta$ , is applied to encode a spatially dependant phase. This leaves the magnetization with some phase  $\omega_{z_1} \delta$ . Where  $\omega_{z_1}$  is the Larmor frequency of a spin located at position  $z_1$  along the  $z$ -axis. This is shown by the clockwise rotation of the magnetization vector in step (1) of **Fig. 2.13b**.

In step (2) of the sequence, immediately after the first gradient pulse, a second  $\frac{\pi}{2}$  pulse is used to longitudinally store the magnetization while nuclei undergo translational diffusion. The total diffusion time is represented by  $\Delta$  and is typically of tens to hundreds of milliseconds. The  $z$ -storage component of the PGSTE sequence is notable since it allows for the elimination of dephasing by  $T_2$  relaxation while nuclei

diffuse. This increases the allowable timescale of  $\Delta$  from being under  $T_2$  control to  $T_1$  control, which is typically preferable.

In step (3), after the diffusion period, a second  $\frac{\pi}{2}$  pulse is applied, making the total contribution of the two  $\frac{\pi}{2}$  pulses equivalent to the single  $\pi$  pulse seen in the Hahn-echo experiment. The transverse magnetization then undergoes a *refocusing* period where the phase accumulated in the initial Larmor precession period is refocused by Larmor precession of the inverted state at its new position along  $z$  after translation diffusion. This is shown by the counter-clockwise rotation of the magnetization vector in step (3) of **Fig. 2.13b**. Notice that since the strength of the effective magnetic field is lower at position  $\mathbf{z}_2$ , the phase is only partially refocused.

The phase accumulated during the refocusing period is  $\omega_{\mathbf{z}_2} \delta$ , making the total accumulated phase during the sequence equal to  $\omega_{\mathbf{z}_1} \delta - \omega_{\mathbf{z}_2} \delta$ . Therefore, the phase of the magnetization at acquisition is dependant on the difference in the position of the nucleus during the encoding and decoding periods. If no diffusion occurs (i.e.  $\mathbf{z}_1 = \mathbf{z}_2$ ), then  $\omega_{\mathbf{z}_1} = \omega_{\mathbf{z}_2}$  and the pulse sequence reduces to a simple echo. If diffusion is present, then the situation described by **Fig. 2.13b** occurs and the signal will be attenuated due to a net dephasing. The amount of signal attenuation in a PFG experiment can be modelled by **eqn. 2.46**.<sup>21</sup>

$$I(\delta, g, \Delta) = I_0 e^{-D \cdot \gamma^2 g^2 \delta^2 \left[ \Delta - \frac{\delta}{3} \right]} \quad [2.46]$$

Where  $I_0$  and  $I(\delta, g, \Delta)$  represents the signal intensity without and with attenuation, and  $D$  is the diffusion coefficient. In order to accurately measure  $D$ , a series of

individual PGSTE experiments are acquired with varying the gradient strength,  $g$ . As  $g$  increases, the net dephasing of the bulk magnetization,  $\omega_{z_1}\delta - \omega_{z_2}\delta$ , will increase as well, resulting in greater signal attenuation according to **eqn. 2.46**. The measured signal can be plotted as a function of  $g$  to give a gaussian decay curve like that seen in **Fig. 2.14**.

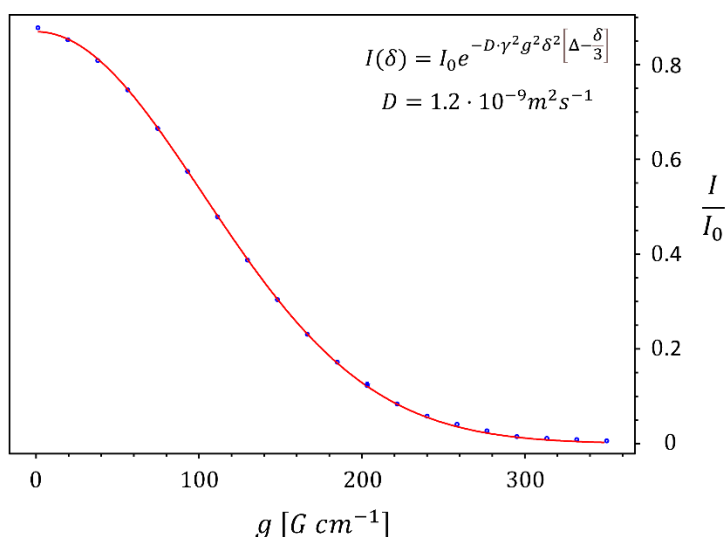


**Figure 2.14.** Diffusional decay curve of 1 M  $\text{NaCl}_{(\text{aq})}$ . Measured datapoints are in blue and are each the result of an individual PGSTE experiment using a gradient strength  $g$ . The computed gaussian decay model fit to extract  $D$  is in red.

Each of the data points in **Fig. 2.14** are the result of individual PGSTE experiments where an attenuated echo was collected with a gradient strength of  $g$ , resulting in a signal decay of  $\frac{I}{I_0}$ . The decay curve is then modelled to **eqn. 2.46** to extract the diffusion coefficient of the nuclei involved.

### 2.3.2 – PFG Pulse Sequence Additions

The PGSTE sequence is an adequate sequence for measuring accurate diffusion coefficients in a wide variety of samples. However, when large gradient strengths,  $g$ , and short diffusion times,  $\Delta$ , are used, the resulting magnetic fields can induce significant eddy currents within the probe circuitry that can distort the observed signal. A number of additions to the pulse sequence can be made to mitigate this issue, including bipolar gradient pulse pairs (BPP),<sup>22</sup> longitudinal eddy current delays (LED),<sup>23</sup> and spoiler gradients (SG).<sup>24</sup> A modified PGSTE sequence with each of these additions is shown in **Fig. 2.15**.

This sequence appears significantly more complex than the standard PGSTE sequence in **Fig. 2.13**, but the general form of phase encoding, diffusion, and phase decoding steps is unchanged. During phase encoding and decoding, the original gradient pulses of length  $\delta$  are each split into two oppositely signed gradient pulses of length  $\frac{\delta}{2}$ , separated by a  $\pi$  pulse on the  $I$  channel. Since the magnetization is inverted between the two opposing gradient pulses, the cumulative effect on phase encoding is the same as a single gradient pulse of length  $\delta$ . However, since the induced eddy currents are not affected by the  $\pi$  pulse, they are generated with opposing sign and are significantly cancelled, resulting in less spectral distortion.<sup>22</sup>

The bipolar sequence can be modified further by the SG addition. When SGs are implemented, the BPPs are set slightly different in their magnitudes, with the SG pulse making up the difference immediately after the transverse magnetization is stored along the z-axis (seen in **Fig. 2.15** as the smaller, “hallow”, gradient pulse). The SG addition allows for better compensation of induced eddy currents, and has the

secondary effect of dephasing any unwanted, left-over, transverse magnetization during the z-storage period.<sup>24</sup>

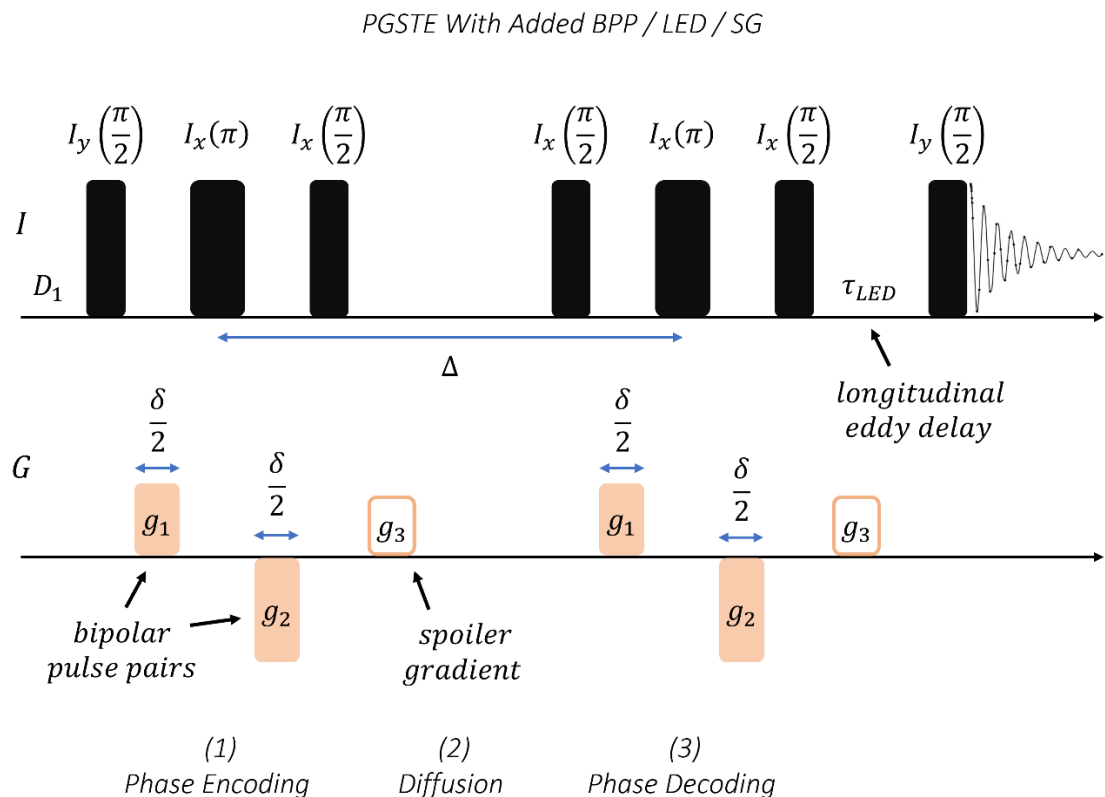


**Figure 2.15.** PGSTE experiment implementing bipolar pulse pairs, spoiler gradient pulses, and a longitudinal eddy delay.<sup>22-24</sup>

Lastly, the LED sequence adds a second z-storage delay period immediately after the phase decoding period. The LED z-storage delay is typically much shorter than the z-storage delay during the diffusion period, and allows for the dissipation of eddy currents caused by the refocusing gradients. This ensures no unwanted current is present in the coil during acquisition.<sup>23</sup>

These three additions to the standard PGSTE sequence allow for robust and accurate diffusion coefficient measurement. The sequence shown in **Fig. 2.15** is used

for the diffusion coefficients measurement in LiTFSI – ADN electrolytes in chapter 5 of this thesis.

### 2.3.3 – Practical Challenges

As mentioned above, the PGSTE with BPP, SG, and LED additions are used to successfully measure the  $^7\text{Li}$ ,  $^{19}\text{F}$ , and  $^1\text{H}$  diffusion coefficients of LiTFSI – ADN electrolytes in chapter 5 of this thesis. The result in an interesting study on the diffusional behaviour of the electrolyte as a function of concentration, and as a function of diffusion time,  $\Delta$ . A comparative study on  $^{23}\text{Na}$ ,  $^{19}\text{F}$ , and  $^1\text{H}$  diffusion coefficients of NaTFSI – ADN electrolytes was planned and was the inspiration for the work presented in chapter 6 of this thesis. Unfortunately, it was found that the  $T_1$  and  $T_2$  relaxation times of the  $^{23}\text{Na}$  nuclei in NaTFSI are on the order of hundreds of micro-seconds. This resulted in negligible signal in PFG experiments at reasonable  $\Delta$  values. Z-storage was applied in an attempt to mitigate the issue of short  $T_2$  values, but was found to be futile as  $T_1$  is only marginally longer. This resulted in the more electrochemically-focused study of NaTFSI – ADN electrolytes presented herein.

## 2.4 – Electrochemical Impedance Spectroscopy (EIS)

Electrochemical Impedance Spectroscopy (EIS) is an excellent technique for studying macroscopic transport properties of materials due to its high sensitivity, non-destructive nature, and ease of use with both bulk and *in-situ* samples. The technique is used in battery research to study a range of phenomena such as electrolyte conductivity,<sup>25</sup> SEI layer formation,<sup>26</sup> and cell degradation.<sup>27</sup> In Chapter 5 and Chapter 6 of this thesis, EIS is used to measure the ionic conductivity of liquid

electrolyte samples, and further in Chapter 6 to characterize electrolyte degradation in SIB half-cells. The basic principles needed to understand these plots and they data they contain is summarized in this section.

At its core, EIS data is obtained by applying a sinusoidal voltage of some magnitude,  $V_0$ , and frequency,  $\omega$ , over an electrochemical cell and analyzing the resulting sinusoidal current response. The current response will have some magnitude,  $I_0$ , and phase shift,  $\phi$ , relative to the applied voltage that defines the impedance of the cell. The applied voltage ( $V(t)$ ), current response ( $I(t)$ ), and impedance ( $Z(\omega)$ ) are defined as:<sup>28, 29</sup>

$$V(t) = V_0 \sin(\omega t) \quad [2.47]$$

$$I(t) = I_0 \sin(\omega t + \phi) \quad [2.48]$$

$$Z(\omega) = \frac{V_0 \sin(\omega t)}{I_0 \sin(\omega t + \phi)} = Z_0 \frac{\sin(\omega t)}{\sin(\omega t + \phi)} \quad [2.49]$$

which, represented in the complex plane, corresponds to:

$$Z(\omega) = Z_0(\cos\phi + i\sin\phi) \quad [2.50]$$

Where the real ( $Z'$ ) component of impedance is the resistance of the cell, and imaginary ( $Z''$ ) component is the reactance of the cell:

$$Z' = Z_0 \cos\phi \quad [2.51]$$

$$Z'' = Z_0 i\sin\phi \quad [2.52]$$

In a typical EIS experiment, the impedance of the cell is measured multiple times with a varying  $\omega$ , which is typically scanned from the MHz to mHz range. The measured impedance is then plotted with  $Z'$  on the x-axis and  $-Z''$  on the y-axis,

forming the familiar Nyquist plot. Example Nyquist plots of a typical liquid ion conductor, and a typical solid ion conductor are given in **Fig. 2.15a** and **Fig. 2.15b**.

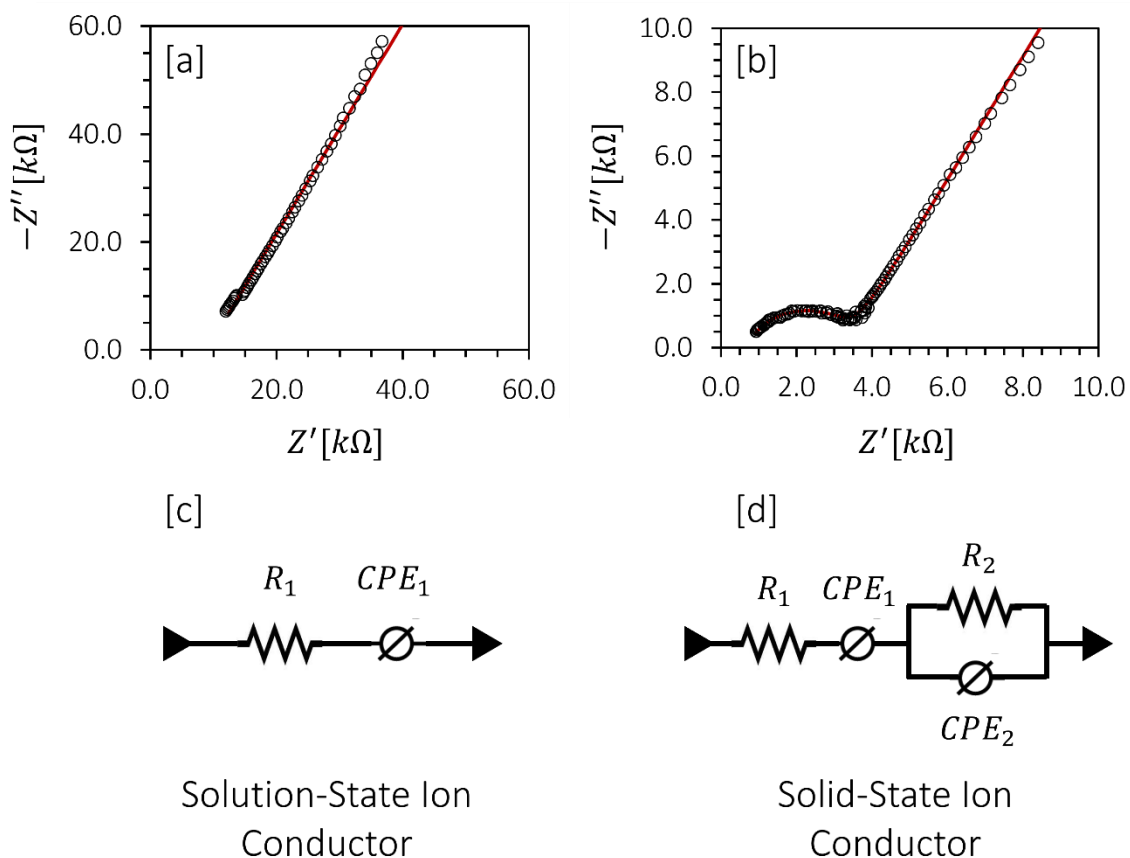


**Figure 2.16.** [a] Nyquist plot and [c] EEC model for a solution-state ion conductor. [b] Nyquist plot and [d] EEC model for a solid-state ion conductor.<sup>29-31</sup>

The observed lineshape in the Nyquist plot is the result of individual circuit elements, such as resistors and capacitors, that contribute to  $Z(\omega)$ , and thus  $Z'$  and  $Z''$ . The contributions of resistors ( $Z_R$ ) and capacitors ( $Z_C$ ) to cell impedance are:

$$Z_R = R \quad [2.53]$$

$$Z_C(\omega) = \frac{1}{(i\omega)^\alpha C} \quad [2.54]$$

Where  $R$  is the resistance of the resistor,  $C$  is the capacitance of the capacitor, and  $\alpha$  is a factor describing the ideality of the capacitor (where for an ideal capacitor  $\alpha = 1$ ).<sup>29</sup> It can be seen from **eqn. 2.53** that a pure resistor has no dependence on  $\omega$  and offers no  $Z''$  component to cell impedance. In contrast, **eqn. 2.54** shows that a pure capacitor (when  $\alpha = 1$ ) is  $\omega$  dependant, and only contributes to  $Z''$ . However, when  $\alpha < 1$ , which is often observed in real systems, the capacitor is unideal and contributes to both  $Z'$  and  $Z''$ . In the unideal case the capacitor is referred to as a constant phase element (CPE).

Therefore, in the Nyquist plot, the pure resistance of the cell is identified when  $Z'' = 0$ . To find this value analytically, an electrochemical equivalent circuit (EEC) model is built from the above circuit elements that should be a reasonably realistic representation the cell under investigation. Typical EEC models for liquid- and solid-state ion conductors are shown below the corresponding Nyquist plots in **Fig. 2.16c** and **Fig. 2.16d**, respectively. For the purposes of this thesis, it is enough to understand that each EEC model has a corresponding complex mathematical function for  $Z(\omega)$ , resulting from the series and parallel combinations of  $Z_R$  and  $Z_C(\omega)$  elements. This function is perturbatively fit to the EIS data to extract the corresponding  $R$ ,  $C$ , and  $\alpha$  parameters of each element.

Examining the liquid electrolyte EIS data (**Fig. 2.16a**) and EEC model (**Fig. 2.16c**), only a single  $R$  value will be obtained that corresponds to the bulk ionic resistance ( $R_{tot}$ ) of the electrolyte. The ionic conductivity ( $\kappa$ ) of the sample can then be calculated by:

$$\kappa = R_{tot} \cdot \frac{L}{A} \quad [2.55]$$

Where  $L$  is the length of the conducting medium between electrodes, and  $A$  is the cross-sectional area of the conducting medium that is in contact with the electrodes. This process was used frequently in this thesis to measure  $\kappa$  of LiTFSI – ADN and NaTFSI – ADN electrolytes as a function of concentration.

In the case of the solid-state ion conductor, a semi-circular lineshape is observed in the EIS spectrum (**Fig. 2.16b**). This behaviour is modelled by the parallel resistor and CPE elements in the EEC model (**Fig. 2.16d**).<sup>32</sup> This results in multiple areas where the EIS lineshape approaches the  $Z''$  axis, and thus multiple  $R$  values. The exact electrochemical interpretation of each  $R$  value is the subject of significant debate,<sup>33</sup> but it is common practice in a pure solid-ion conductor to take the sum of both values as the bulk resistance.<sup>31, 34</sup> From here the ionic-conductivity value of the conductor can be calculated by **eqn. 2.55**.

Real SIBs are composed of at least two solid-ion conducting components (in the intercalation electrodes) and at least one solution-state ion conductor (in the liquid electrolyte). These numbers only grow larger as the SEI and CEI layers are considered, as well as the differing ion transport in bulk electrolyte compared to electrolyte in the porous electrodes. This makes quantitative analysis of SIB EIS spectra quite complex. For this reason, in the EIS experiments performed in this thesis on SIBs, only semi-quantitative analysis is made by comparing the overall breadth of semi-circles in the Nyquist plots. In this way, the evolution of the bulk resistivity of the cell is observed as a means of tracking cell degradation during cycling.

## 2.4 – References

1. Levitt, M. H., *Spin Dynamics: Basics of NMR Spectroscopy*. 2 ed.; John Wiley & Sons: England, 2008.
2. Duer, M. J., *Solid State NMR Spectroscopy: Principles and Applications*. John Wiley & Sons: Cambridge, 2001.
3. Brown, L. R.; Bremer, J. *Journal of Magnetic Resonance (1969)* **1986**, *68* (2), 217-231. DOI: [https://doi.org/10.1016/0022-2364\(86\)90239-8](https://doi.org/10.1016/0022-2364(86)90239-8)
4. van Meerten, S. G. J.; Franssen, W. M. J.; Kentgens, A. P. M. *Journal of Magnetic Resonance* **2019**, *301*, 56-66. DOI: <https://doi.org/10.1016/j.jmr.2019.02.006>
5. Brouwer, D. H.; Darton, R. J.; Morris, R. E.; Levitt, M. H. *Journal of the American Chemical Society* **2005**, *127* (29), 10365-10370. DOI: 10.1021/ja052306h
6. Ashbrook, S. E. *Physical Chemistry Chemical Physics* **2009**, *11* (32), 6892-6905. DOI: 10.1039/B907183K
7. Charpentier, T. Résonance magnétique nucléaire haute-résolution sur les noyaux quadropolaires dans les solides. Université Paris Sud - Paris XI, 1998.
8. Kentgens, A. P. M. *Geoderma* **1997**, *80* (3), 271-306. DOI: [https://doi.org/10.1016/S0016-7061\(97\)00056-6](https://doi.org/10.1016/S0016-7061(97)00056-6)
9. Reeve, Z. E.; Franko, C. J.; Harris, K. J.; Yadegari, H.; Sun, X.; Goward, G. R. *J. Am. Chem. Soc.* **2017**, *139* (2), 595-598. DOI: 10.1021/jacs.6b11333
10. Reeve, Z. E. M.; Goward, G. R.; Bain, A. D. *Canadian Journal of Chemistry* **2015**, *93* (9), 976-982. DOI: 10.1139/cjc-2014-0577
11. Wu, Y.; Sun, B. Q.; Pines, A.; Samoson, A.; Lippmaa, E. *Journal of Magnetic Resonance (1969)* **1990**, *89* (2), 297-309. DOI: [https://doi.org/10.1016/0022-2364\(90\)90236-3](https://doi.org/10.1016/0022-2364(90)90236-3)
12. Grandinetti, P. J.; Baltisberger, J. H.; Llor, A.; Lee, Y. K.; Werner, U.; Eastman, M. A.; Pines, A. *Journal of Magnetic Resonance, Series A* **1993**, *103* (1), 72-81. DOI: <https://doi.org/10.1006/jmra.1993.1132>
13. Pereira, T. L. E.; Sanders, K. J.; Smiley, D. L.; Britten, J. F.; Goward, G. R. *Chemistry of Materials* **2022**, *34* (19), 8551-8560. DOI: 10.1021/acs.chemmater.2c01357
14. Yan, Z. B.; Brouwer, D. H.; Goward, G. R. *Macromolecules* **2016**, *49* (19), 7331-7339. DOI: 10.1021/acs.macromol.6b01291
15. Hahn, E. L. *Physical Review* **1950**, *80* (4), 580-594. DOI: 10.1103/PhysRev.80.580
16. Amoureux, J. P.; Trebosc, J.; Wiench, J.; Pruski, M. *Journal of Magnetic Resonance* **2007**, *184* (1), 1-14. DOI: <https://doi.org/10.1016/j.jmr.2006.09.009>
17. Frydman, L.; Harwood, J. S. *J. Am. Chem. Soc.* **1995**, *117* (19), 5367-5368. DOI: 10.1021/ja00124a023
18. Frydman, L., Fundamentals of Multiple-Quantum Magic-Angle Spinning NMR on Half-Integer Quadrupolar Nuclei. In *Encyclopedia of Nuclear Magnetic Resonance*, Grant, D. M.; Harris, R. K., Eds. John Wiley & Sons: Chichester, 2002; Vol. 9, pp 262-274.
19. Gadian, D. G.; Robinson, F. N. H. *Journal of Magnetic Resonance (1969)* **1979**, *34* (2), 449-455. DOI: [https://doi.org/10.1016/0022-2364\(79\)90023-4](https://doi.org/10.1016/0022-2364(79)90023-4)
20. Cotts, R. M.; Hoch, M. J. R.; Sun, T.; Markert, J. T. *Journal of Magnetic Resonance (1969)* **1989**, *83* (2), 252-266. DOI: [https://doi.org/10.1016/0022-2364\(89\)90189-3](https://doi.org/10.1016/0022-2364(89)90189-3)

21. Price, W. S. *Concepts in Magnetic Resonance* **1997**, 9 (5), 299-336. DOI: [https://doi.org/10.1002/\(SICI\)1099-0534\(1997\)9:5<299::AID-CMR2>3.0.CO;2-U](https://doi.org/10.1002/(SICI)1099-0534(1997)9:5<299::AID-CMR2>3.0.CO;2-U)
22. Wu, D. H.; Chen, A. D.; Johnson, C. S. *Journal of Magnetic Resonance, Series A* **1995**, 115 (2), 260-264. DOI: <https://doi.org/10.1006/jmra.1995.1176>
23. Gibbs, S. J.; Johnson, C. S. *Journal of Magnetic Resonance (1969)* **1991**, 93 (2), 395-402. DOI: [https://doi.org/10.1016/0022-2364\(91\)90014-K](https://doi.org/10.1016/0022-2364(91)90014-K)
24. Pelta, M. D.; Morris, G. A.; Stchedroff, M. J.; Hammond, S. J. *Magnetic Resonance in Chemistry* **2002**, 40 (13), S147-S152. DOI: <https://doi.org/10.1002/mrc.1107>
25. Franko, C. J.; Yim, C.-H.; Áren, F.; Ávall, G.; Whitfield, P. S.; Johansson, P.; Abu-Lebdeh, Y. A.; Goward, G. R. *Journal of The Electrochemical Society* **2020**, 167 (16), 160532. DOI: 10.1149/1945-7111/abcf17
26. Zhang, S. S.; Xu, K.; Jow, T. R. *Electrochimica Acta* **2006**, 51 (8), 1636-1640. DOI: <https://doi.org/10.1016/j.electacta.2005.02.137>
27. Mingant, R.; Bernard, J.; Sauvant Moynot, V.; Delaille, A.; Mailley, S.; Hognon, J.-L.; Huet, F. *ECS Transactions* **2011**, 33 (39), 41. DOI: 10.1149/1.3589920
28. Magar, H. S.; Hassan, R. Y. A.; Mulchandani, A. *Electrochemical Impedance Spectroscopy (EIS): Principles, Construction, and Biosensing Applications Sensors* [Online], 2021.
29. Gamry. *Basics of Electrochemical Impedance Spectroscopy* 2016. <https://www.gamry.com/application-notes/EIS/basics-of-electrochemical-impedance-spectroscopy/>.
30. Li, Y.; Deng, Z.; Peng, J.; Chen, E.; Yu, Y.; Li, X.; Luo, J.; Huang, Y.; Zhu, J.; Fang, C.; Li, Q.; Han, J.; Huang, Y. *Chemistry* **2018**, 24 (5), 1057-1061. DOI: 10.1002/chem.201705466
31. Deng, Z.; Gu, J.; Li, Y.; Li, S.; Peng, J.; Li, X.; Luo, J.; Huang, Y.; Fang, C.; Li, Q.; Han, J.; Huang, Y.; Zhao, Y. *Electrochimica Acta* **2019**, 298, 121-126. DOI: 10.1016/j.electacta.2018.12.092
32. Smaha, R. W.; Roudebush, J. H.; Herb, J. T.; Seibel, E. M.; Krizan, J. W.; Fox, G. M.; Huang, Q.; Arnold, C. B.; Cava, R. J. *Inorg Chem* **2015**, 54 (16), 7985-91. DOI: 10.1021/acs.inorgchem.5b01186
33. Mei, B.-A.; Lau, J.; Lin, T.; Tolbert, S. H.; Dunn, B. S.; Pilon, L. *The Journal of Physical Chemistry C* **2018**, 122 (43), 24499-24511. DOI: 10.1021/acs.jpcc.8b05241
34. Li, Y.; Deng, Z.; Peng, J.; Gu, J.; Chen, E.; Yu, Y.; Wu, J.; Li, X.; Luo, J.; Huang, Y.; Xu, Y.; Gao, Z.; Fang, C.; Zhu, J.; Li, Q.; Han, J.; Huang, Y. *ACS Appl Mater Interfaces* **2018**, 10 (18), 15760-15766. DOI: 10.1021/acsami.8b03938

## 3 – Characterising Carbon Cathode Decay in Sodium-Oxygen Batteries by Solid-State NMR Spectroscopy

This chapter is an amalgamation of two previously published articles in which the author was the second author. The corresponding articles with their rights and permissions are given below. Both publications study the behaviour of graphitic carbon cathodes in (sodium-oxygen batteries) NaOBs:

1. “Detection of Electrochemical Reaction Products from the Sodium-Oxygen Cell with Solid-State  $^{23}\text{Na}$  NMR Spectroscopy” Adapted with permission from the Journal of the American Chemical Society © 2016 American Chemical Society (Reeve Z. E., Franko C. J., Harris K. J., Yadegari H., Sun X., Goward G. R., *J. Am. Chem. Soc.* **2017**, 139(2), 595-598).<sup>1</sup>
2. “How to Control the Discharge Products in Na-O<sub>2</sub> Cells: Direct Evidence toward the Role of Functional Groups at the Air Electrode Surface” Adapted with permission from the Journal of Physical Chemistry Lett © 2017 American Chemical Society (Yadegari H., Franko C. J., Banis M. N., Sun Q., Li R., Goward G. R., Sun X., *J. Phys. Chem. Lett.* **2017**, 8(19), 4794-4800).<sup>2</sup>

The former publication introduces the use of (magic-angle spinning) MAS (solid-state nuclear magnetic resonance) ssNMR as a method of characterizing the electrochemical discharge products formed on the carbon cathode. Composite NaOB carbon cathodes, composed of carbon black (CB) and polyvinylidene fluoride (PVDF), are discharged and examined by  $^{23}\text{Na}$  ssNMR. Sodium peroxide ( $\text{Na}_2\text{O}_2$ ), sodium fluoride (NaF), and sodium carbonate ( $\text{Na}_2\text{CO}_3$ ) are identified as the main components of the electrochemical slurry after discharge. To identify the origin of NaF

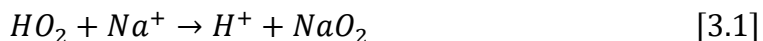
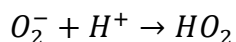
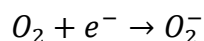
and  $\text{Na}_2\text{CO}_3$  in the discharge slurry, sodium superoxide ( $\text{NaO}_2$ ) is synthesized and separately ground with the CB and PVDF components of the cathode, and the resulting products are characterized by  $^{23}\text{Na}$  and  $^{19}\text{F}$  ssNMR.  $\text{NaO}_2$  is found to oxidize CB to form  $\text{Na}_2\text{CO}_3$ , and is also found to react with PVDF to form NaF and further  $\text{Na}_2\text{CO}_3$ . It is concluded that  $\text{NaO}_2$  is formed upon discharge in NaOBs, but subsequently reacts with the CB and PVDF of the cathode to form the observed NaF and  $\text{Na}_2\text{CO}_3$  products. This study proves the utility of ssNMR in dissecting the chemistry of the NaOB. The author was responsible for the synthesis and characterization of  $\text{NaO}_2$ ,  $^{23}\text{Na}$  and  $^{19}\text{F}$  ssNMR characterization of the  $\text{NaO}_2$  reactivity,, and assisted in preparation of the manuscript.

The latter publication applies  $^{23}\text{Na}$  ssNMR (along with a number of other characterization methods) to study how surface modification of carbon cathodes affects the discharge slurry. Binder-free carbon-cloth (CC) cathodes are made into *hydrophobic* and *hydrophilic* analogues by  $\text{H}_2$  reduction and potassium permanganate ( $\text{KMnO}_4$ ) oxidation, respectively. The electrochemical discharge behaviours of each cathode are examined, and the discharge products are characterized by scanning electron microscopy (SEM), powder x-ray diffraction (PXRD), and  $^{23}\text{Na}$  ssNMR. Hydrophilic cathodes are found to discharge via a surface-mediated mechanism, producing mainly the  $\text{Na}_2\text{CO}_3$  degradation product. While hydrophobic cathodes are found to discharge via a solution-mediated mechanism that produces mainly  $\text{NaO}_2$ .  $^{23}\text{Na}$  ssNMR experiments on the hydrophobic cathode show that  $\text{NaO}_2$  degrades the binder-free CC cathode to produce  $\text{Na}_2\text{CO}_3$ . This study illustrates the difference in competing discharge pathways in NaOBs, highlights the advantages of using PXRD and ssNMR in tandem for characterizing complex

electrochemical product mixtures, and adds additional evidence for the instability of  $\text{NaO}_2$  toward carbon cathode systems. The author was responsible for  $^1\text{H}$  ssNMR characterization of hydrophobic and hydrophilic cathodes,  $^{23}\text{Na}$  ssNMR characterization of discharged cathodes, and assisted in preparation of the manuscript.

### 3.1 – Introduction

The sodium-oxygen battery (NaOB) is a promising energy storage technology that has attracted significant attention in literature as an alternative to the more popular lithium-oxygen battery (LiOB). One of the major advantages of the NaOB over the LiOB is the increased stability of sodium superoxide ( $\text{NaO}_2$ ) compared to lithium superoxide ( $\text{LiO}_2$ ), resulting in  $\text{NaO}_2$  being the primary discharge product in non-aqueous NaOBs. The superoxide is formed in a solution mediated single electron transfer process outlined by (eqn. 3.1) below.<sup>3,4</sup>



Dissolved  $\text{O}_2$  gas in the electrolyte is reduced to  $\text{O}_2^-$  at the carbon cathode, and is stabilized in solution by  $\text{H}^+$  to form  $\text{HO}_2$ .  $\text{HO}_2$  can then undergo substitution with  $\text{Na}^+$  to form insoluble  $\text{NaO}_2$ , which precipitates on the cathode.<sup>4</sup> In contrast,  $\text{LiO}_2$  is only formed as an intermediate in the LiOB, being further reduced to lithium peroxide ( $\text{Li}_2\text{O}_2$ ) in a two-electron transfer discharge process.<sup>5</sup> The production of superoxide on discharge allows for much smaller charging overpotentials in NaOBs compared to

those observed in LiOBs ( $\leq 0.5$  V compared to  $\geq 1.5$  V, respectively).<sup>2, 3</sup> This is due to the significantly higher electrical conductivities, and lower dissolution energies, of the superoxide products compared to the peroxides.<sup>6</sup>

Even though  $\text{NaO}_2$  is expected to be the primary species formed, the exact identity and relative proportion of discharge products vary widely throughout literature. Sodium peroxide ( $\text{Na}_2\text{O}_2$ ) and sodium peroxide dihydrate ( $\text{Na}_2\text{O}_2 \cdot 2\text{H}_2\text{O}$ ) have both been detected as primary discharge products instead of  $\text{NaO}_2$  in some studies.<sup>7, 8</sup> In addition, a number of compounds resulting from parasitic side-reactions have also been observed, including sodium carbonate ( $\text{Na}_2\text{CO}_3$ ) and sodium fluoride ( $\text{NaF}$ ), but the exact degradation mechanisms that produce them have not been identified.<sup>3, 9, 10</sup> In the LiOB, lithium carbonate ( $\text{Li}_2\text{CO}_3$ ) is primarily produced via the oxidation of the organic carbonate electrolyte solvent by the  $\text{LiO}_2$  intermediate.<sup>11</sup> However, in the NaOB, the superoxide is expected to be stabilized in solution by  $\text{HO}_2$  (as outlined by **eqn. 3.1**), and ether electrolyte solvents are used in place of carbonates, which are significantly more stable to superoxide attack.<sup>12</sup>  $\text{NaF}$  has been proposed to be formed by degradation of the electrolyte salt, sodium triflate ( $\text{NaOTf}$ ), but the species has only been occasionally observed, and there is no direct evidence for  $\text{NaOTf}$  degradation.<sup>3</sup> It is clear that more research needs to be done to deconvolute the degradation pathways of  $\text{NaO}_2$  in NaOBs.

As of the time of these publications, solid-state nuclear magnetic resonance (ssNMR) has not yet been utilized as a diagnostic tool for examining the discharge chemistry of the NaOB. ssNMR is an ideal technique for the characterization of complex electrochemical products as it is not restricted by the degree of crystallinity of the product slurry, and is very sensitive to minute differences in chemical

environments. Herein,  $^{23}\text{Na}$  MAS ssNMR is used to identify the origin of  $\text{Na}_2\text{CO}_3$  and NaF degradation products in discharged NaOBs.

## 3.2 – Experimental

### 3.2.1 – $\text{NaO}_2$ Synthesis

[Adapted from Reeve et al. *J. Am. Chem. Soc.* 2017, 139, 2, 595]<sup>1</sup> Sodium superoxide was chemically synthesized under an argon atmosphere in a modified version of a previously published procedure.<sup>13</sup> Ammonia ( $\text{NH}_3$ ) was condensed in a round-bottom flask over a dry-ice/acetone bath under a flowing Ar atmosphere.  $\text{O}_2$  gas was rapidly bubbled through the solution, and Na metal was then added to the solution slowly to keep Na the limiting reagent. The solution gradually gains a deep blue colour as Na is dissolved, which dissipates gradually as  $\text{NaO}_2$  is formed. We observed that if Na is dissolved in  $\text{NH}_3$  before  $\text{O}_2$  is added (as the referenced literature suggests),<sup>13</sup>  $\text{Na}_2\text{O}_2$  is formed preferentially over  $\text{NaO}_2$ . After the reaction is complete, the dry ice is removed and  $\text{NH}_3$  is allowed to evaporate. The remaining  $\text{NaO}_2$  product was then dried under vacuum and is stored in the Ar glovebox. The  $\text{NaO}_2$  has a pale yellow colour, while  $\text{Na}_2\text{O}_2$  is a much more vibrant yellow.

### 3.2.2 – Preparation and Electrochemical Characterization of Composite CB / PVDF Cathodes

[Adapted from Reeve et al.]<sup>1</sup> Gas diffusion electrodes were prepared by casting a mixture of commercial carbon black (N330) and Polyvinylidene fluoride (PVDF, Alfa Aesar) with a weight ratio of 9:1 on a separator (Celgard 3500). The electrodes were 3/8 inch in diameter with a loading of ~0.25 mg.

Swagelok type cells comprised of sodium foil anode, Celgard 3500 separator, gas diffusion electrode and a stainless-steel mesh as current collector were used to prepare the discharge product. Sodium foil was prepared from sodium metal blocks (Sigma Aldrich), with the aid of a homemade stainless steel press machine using, inside the argon filled glove box. The electrolyte was a 0.5 M solution of sodium triflate ( $\text{NaSO}_3\text{CF}_3$  98%, Aldrich) dissolved in diethylene glycol dimethyl ether (DEGDME reagent grade  $\geq 98\%$ , Aldrich). The sodium triflate electrolyte salt was dried at 80 °C under vacuum for 48 hours and the water content of diethylene glycol dimethyl ether solvent was removed using molecular sieves for at least 10 days. The assembled Na- $\text{O}_2$  cells were sealed into a specially designed testing chamber and then taken out of the glove box. A moderate vacuum was applied to remove the argon, and subsequently the chamber was back-filled with pure oxygen (purity 99.993%). The oxygen pressure was brought to 1.0 atm and maintained under static conditions throughout the discharge cycle. The Na- $\text{O}_2$  cells were discharged at a current density of 75 mA g<sup>-1</sup> and stopped at the specific capacities of interest along the discharge curve. Following electrochemical cycling the Na- $\text{O}_2$  cells were disassembled in the glovebox and packed in an NMR rotor without further modification.

### 3.2.3 – Preparation and Electrochemical Characterization of Surface-Modified CC Cathodes

[Adapted from Yadegari et al.]<sup>2</sup> Plain Carbon Cloth (AvCarb Material Solutions) was used as starting electrode materials. The carbon cloth samples were treated under Ar/ $\text{H}_2$  (10:1) atmosphere at 750°C for 2 hours to obtain hydrophobic air electrodes. To prepare hydrophilic air electrodes, carbon cloth samples were oxidized in  $\text{KMnO}_4$  (1 mg/ml) and  $\text{H}_2\text{SO}_4$  (5%) solution at 50°C for 1 hour. The electrodes were then

transferred to hydrogen peroxide and HCl solutions to remove the residual manganese oxide. Afterward, the hydrophilic electrodes were thoroughly washed with water and ethanol and dried in vacuum oven at 110°C.

Swagelok-type cells composed of sodium foil anode, glass fiber separator (1/2 in. in diameter), different air electrode, and a stainless-steel mesh as current collector were used to carry out electrochemical measurements. The air electrodes were cut into circular pieces (3/8 in. in diameter) with the geometric surface area of 0.71 cm<sup>2</sup>. A fresh sodium foil (3/8 in. in diameter) was used as negative electrode material. The electrolyte used in this study was 0.5 M sodium triflate (NaSO<sub>3</sub>CF<sub>3</sub>, Aldrich) dissolved in diethylene glycol diethyl ether (DEGDME, Anhydrous ≥ 99.5%, Aldrich). Sodium triflate electrolyte salt was dried at 80 °C under vacuum for 48 h, and the water content of DEGDME solvent was removed using molecular sieves (3Å) for at least 10 days. The amount of electrolyte in the cell was ~200 μL. The assembled Na-O<sub>2</sub> cells were placed into custom fitted airtight chambers inside the glovebox and then transferred to the testing room. The argon content of testing box was moderately vacuumed out and then pure oxygen (purity 5.0) was purged into the box. The pressure of the testing box was kept at 1.0 atm during the electrochemical tests. Discharge/charge characteristics were performed using an Arbin BT-2000 battery station at RT (25°C).

### 3.2.4 – Physical Characterizations

[Adapted from Reeve et al and Yadegari et al.]<sup>1, 2</sup> X-ray diffractograms were obtained using a Bruker D8 Advance (Cu-Kα source, 40 kV, 40 mA). For the X-ray diffraction (XRD) measurements, the Na-O<sub>2</sub> cells were disassembled in an Ar-filled glovebox following electrochemical cycling, and the positive electrode materials were

placed into an air-sensitive XRD sample holder. Morphological studies were performed by Hitachi S-4800 field-emission scanning electron microscope (SEM).

All  $^{23}\text{Na}$  NMR spectra were acquired on a Bruker Avance I spectrometer ( $B_0 = 11.7\text{ T}$ ) using a custom-built double-resonance probe supporting 1.8 mm rotors capable of magic angle spinning (MAS) frequencies from 20 kHz up to 45 kHz. The spectra were referenced to a 1 M NaCl solution at 0 ppm. All 1D spectra were collected via single pulse experiments using a hard 90 pulse at an RF field of 125 kHz, and signal averaging over eight scans. The delay times used for the synthesized  $\text{NaO}_2$ , pristine  $\text{Na}_2\text{O}_2$ , pristine  $\text{Na}_2\text{CO}_3$  and sodium triflate were 1 s, 30 s, 5 s, and 5 s respectively. A 1 s delay time was used for the cycled cathodes. Variable temperature  $^{23}\text{Na}$  MAS experiments were performed for  $\text{NaO}_2$  between 300 – 350 K.  $^{19}\text{F}$  experiments were collected on the same instrument with the same probe. All  $^{19}\text{F}$  spectra were referenced to  $\text{CFCl}_3$  at 0 ppm. Spectra of PVDF,  $\text{NaO}_2$  with PVDF, and NaF were collected using a D1 of 30 s over 32 scans.  $^1\text{H}$  spectra of the pristine surface-modified CC cathodes were collected on a Bruker Avance III 850HD spectrometer ( $B_0 = 19.9\text{ T}$ ) using a Bruker 1.9 mm probe with a MAS frequency of 34 kHz.

## 3.3 – Results & Discussion

### 3.3.1 – $\text{NaO}_2$ Synthesis & Characterization

In order to thoroughly evaluate the discharge products of NaOBs by MAS ssNMR,  $\text{NaO}_2$  was synthesized to provide an adequate reference spectrum. In short,  $\text{O}_2$  gas was rapidly bubbled through liquid  $\text{NH}_3$  while slowly adding small pieces of polished Na metal to solution. As Na is dissolved to  $\text{Na}^+$  in the  $\text{NH}_3$  solvent,  $\text{O}_2$  is rapidly reduced to  $\text{O}_2^-$  by the free electron and combines with  $\text{Na}^+$  to form  $\text{NaO}_2$ . The

powder x-ray diffraction (PXRD) pattern of the product is given in **Fig. 3.1a**, along with a reference pattern from literature (ICSD 87176).  $\text{NaO}_2$  is the major product, with only minor impurity reflections appearing.

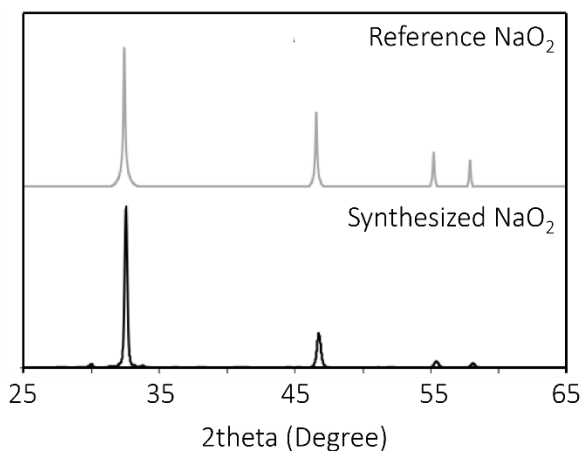


**Figure 3.1.** PXRD diffractogram of synthesized  $\text{NaO}_2$ , along with a calculated reference pattern (ICSD 87176). Adapted with permission from the Journal of the American Chemical Society 2017, 139, 2, 595–598 © 2016 American Chemical Society.<sup>1</sup>

$\text{NaO}_2$  was then characterized by  $^{23}\text{Na}$  MAS ssNMR (**Fig. 3.2a**).  $\text{NaO}_2$  appears as a single sharp peak at approximately -23 ppm. In the NMR spectrum, a significant  $\text{NaOH}$  impurity is observed as the higher frequency broad resonance centered at 0 ppm. Even though  $^{23}\text{Na}$  is a quadrupolar nucleus, the lineshape of  $\text{NaO}_2$  is that of an isotropic Gaussian, this is due to the cubic symmetry of the molecule resulting in a quadrupolar coupling constant ( $C_Q$ ) of 0 for the  $^{23}\text{Na}$  nucleus in  $\text{NaO}_2$ .  $\text{NaO}_2$  is also expected to experience the paramagnetic interaction, due to the single unpaired electron of  $\text{O}_2^-$ . To visualize this, the  $^{23}\text{Na}$  spectrum of  $\text{NaO}_2$  was collected with increasing temperature (**Fig. 3.2b**). As sample temperature is increased from 330 K to 350 K, a distinct shift of the paramagnetic  $\text{NaO}_2$  resonance to lower frequencies is observed. This is inline with the predicted trend from Curie's Law, which states that

the magnetic susceptibility of a paramagnetic material is inversely proportional to temperature.<sup>14</sup> This results in weaker magnetic moments as temperature increases, and thus lower spin-state transition frequencies. A counterexample to this behaviour shown by the diamagnetic impurity in the NaO<sub>2</sub> sample (highlighted in purple), which does not experience a frequency shift with temperature. Each of the other expected electrochemical discharge and degradation products (Na<sub>2</sub>O<sub>2</sub>, NaF, and Na<sub>2</sub>CO<sub>3</sub>) were also characterized by <sup>23</sup>Na MAS ssNMR, and their spectra are shown with that of NaO<sub>2</sub> in **Fig. 3.3** in the following section.

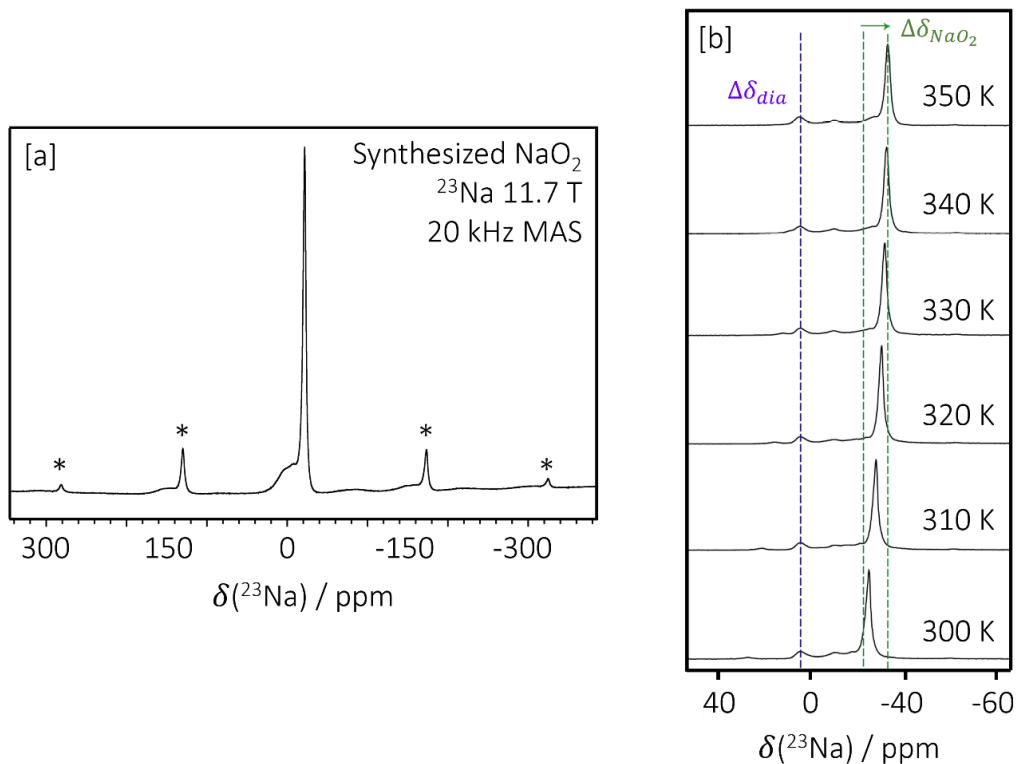


**Figure 3.2.** [a] <sup>23</sup>Na NMR spectrum of synthesized NaO<sub>2</sub>. The NaO<sub>2</sub> Asterisk symbols in the NMR spectrum denote spinning side bands. [b] NaO<sub>2</sub> <sup>23</sup>Na NMR spectra at varying temperatures from 300 K to 350 K.  $\Delta\delta_{dia}$  represents the unchanging shift of a diamagnetic impurity in the sample. Adapted with permission from the Journal of the American Chemical Society 2017, 139, 2, 595–598 © 2016 American Chemical Society.<sup>1</sup>

### 3.3.2 – $^{23}\text{Na}$ NMR of Discharged NaOB Composite Cathodes

In order to study the degradation mechanisms of NaOB discharge products, NaOB cathodes were discharged to capacities of 100 and 750 mAh g<sup>-1</sup>. A representative discharge profile for each cell is shown in **Fig. 3.3a**.

Each cell initially discharges at a flat voltage plateau of approximately 2.2 V, which is characteristic of NaO<sub>2</sub> production.<sup>3, 4</sup> The voltage eventually drops as the cathode becomes saturated with product and the ORR becomes unfavourable. After discharge, each cathode was extracted from the cell and examined by  $^{23}\text{Na}$  MAS ssNMR spectroscopy. The  $^{23}\text{Na}$  spectrum of each discharged cathode is shown in **Fig. 3.3b**, and the  $^{23}\text{Na}$  NMR spectra of the expected electrochemical discharge and degradation products (NaO<sub>2</sub>, Na<sub>2</sub>O<sub>2</sub>, NaF, and Na<sub>2</sub>CO<sub>3</sub>) are shown in **Fig. 3.3c** and **3.3d** (NaF is included separately in **Fig. 3.3d** as it was not part of the original publication).

The frequency ranges of the characterized reference compounds are highlighted in the spectra of the discharged cathodes. NaF and Na<sub>2</sub>CO<sub>3</sub> are the primarily observed species, with a smaller amount of Na<sub>2</sub>O<sub>2</sub> being formed as well. The relative proportion of Na<sub>2</sub>CO<sub>3</sub> grows larger as the cathode is cycled to higher capacity, while the proportion of Na<sub>2</sub>O<sub>2</sub> does not appear to significantly change. As discussed above, Na<sub>2</sub>CO<sub>3</sub> is expected to form from parasitic side reactions involving NaO<sub>2</sub>, which is not identified as a major electrochemical discharge product in either sample. It may be the case that NaO<sub>2</sub> is being formed throughout discharge, as suggested by the electrochemical discharge profile, but is consumed immediately to form Na<sub>2</sub>CO<sub>3</sub> and NaF. However, the origin of these degradation products is not clear from examining the discharged cathode alone.

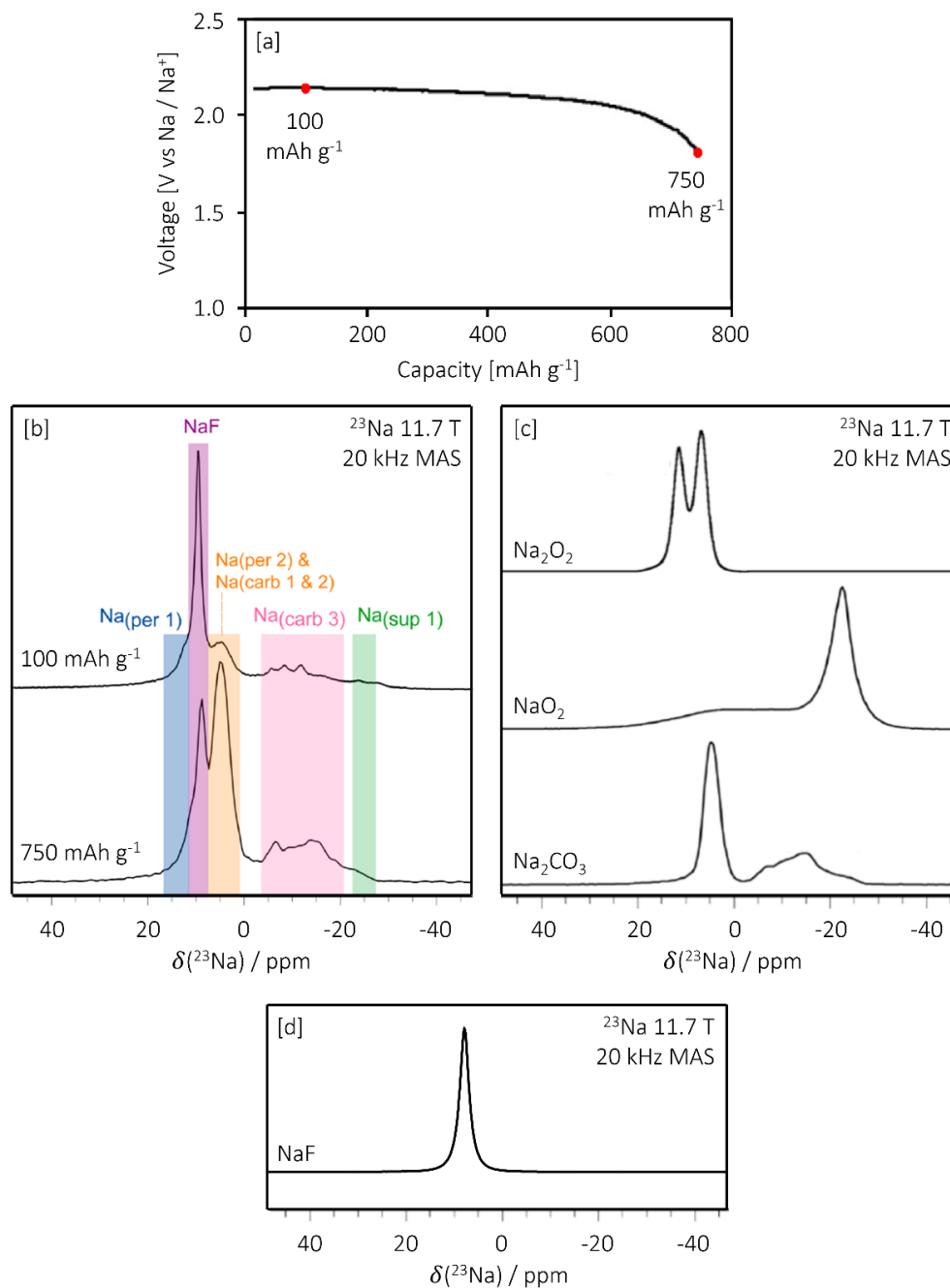


**Figure 3.3.** [a] Representative galvanostatic discharge curve of NaOBs studied by <sup>23</sup>Na NMR discharged at a current density of 75 mAh g<sup>-1</sup>. The 100 mAh g<sup>-1</sup> and 750 mAh g<sup>-1</sup> points are marked. [b] <sup>23</sup>Na MAS ssNMR spectra of the NaOB cathodes discharged to a capacity of 100 and 750 mAh g<sup>-1</sup>. [c] and [d] <sup>23</sup>Na MAS ssNMR spectra of expected electrochemical discharge products in NaOBs. Adapted with permission from the Journal of the American Chemical Society 2017, 139, 2, 595–598 © 2016 American Chemical Society.<sup>1</sup>

### 3.3.3 – Reactivity of NaO<sub>2</sub> to Composite Cathodes

In order to further probe how Na<sub>2</sub>CO<sub>3</sub> and NaF are formed in the NaOB, synthesized NaO<sub>2</sub> was ground separately with the each of the free-standing cathode components, CB and PVDF, and the resulting reaction mixtures were analysed by ssNMR (**Fig. 3.4** and **Fig. 3.5**, respectively).

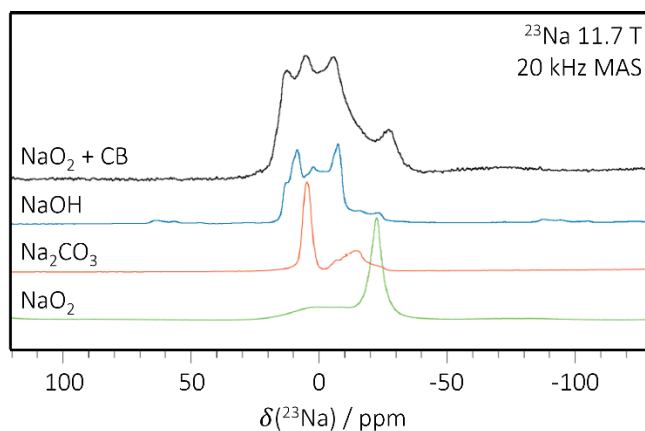


**Figure 3.4.** <sup>23</sup>Na NMR spectrum of NaO<sub>2</sub> ground with CB, and spectra of relevant reference compounds. Adapted with permission from the Journal of the American Chemical Society 2017, 139, 2, 595–598 © 2016 American Chemical Society.<sup>1</sup>

**Fig. 3.4** shows the <sup>23</sup>Na NMR spectrum of the NaO<sub>2</sub> / CB reaction mixture one week after grinding, along with the reference spectra of NaO<sub>2</sub>, Na<sub>2</sub>CO<sub>3</sub>, and NaOH. The NaO<sub>2</sub> resonance has almost entirely deteriorated, and Na<sub>2</sub>CO<sub>3</sub> has been produced as a result. A significant amount of NaOH is also observed, however this is assumed to a by-product of the NaO<sub>2</sub> synthesis. This suggests that when NaO<sub>2</sub> is formed during the discharge process in NaOBs, it can immediately oxidize the carbon support to form parasitic Na<sub>2</sub>CO<sub>3</sub>. A similar process has been observed in LiOBs, where Li<sub>2</sub>O<sub>2</sub> has been shown to react with the carbon cathode to produce Li<sub>2</sub>CO<sub>3</sub>.<sup>15</sup> The sodium products are generally expected to be more stable than their lithium counterparts,<sup>16, 17</sup> but this result proves their stability does not extend to the carbon cathode.

**Fig. 3.5a** shows the  $^{23}\text{Na}$  NMR spectra of the  $\text{NaO}_2$  / PVDF reaction mixture. The lineshape of the reaction products is very similar to what was observed for the  $\text{NaO}_2$  / CB mixture, with  $\text{NaO}_2$  being completely degraded and significant amounts of  $\text{Na}_2\text{CO}_3$  being formed. Notably,  $\text{NaF}$  is not directly observed in the  $^{23}\text{Na}$  spectrum, but may be hidden under the broad  $\text{NaOH}$  and  $\text{Na}_2\text{CO}_3$  lineshapes. To better probe for  $\text{NaF}$  formation, the reaction mixture was also analyzed by  $^{19}\text{F}$  ssNMR.

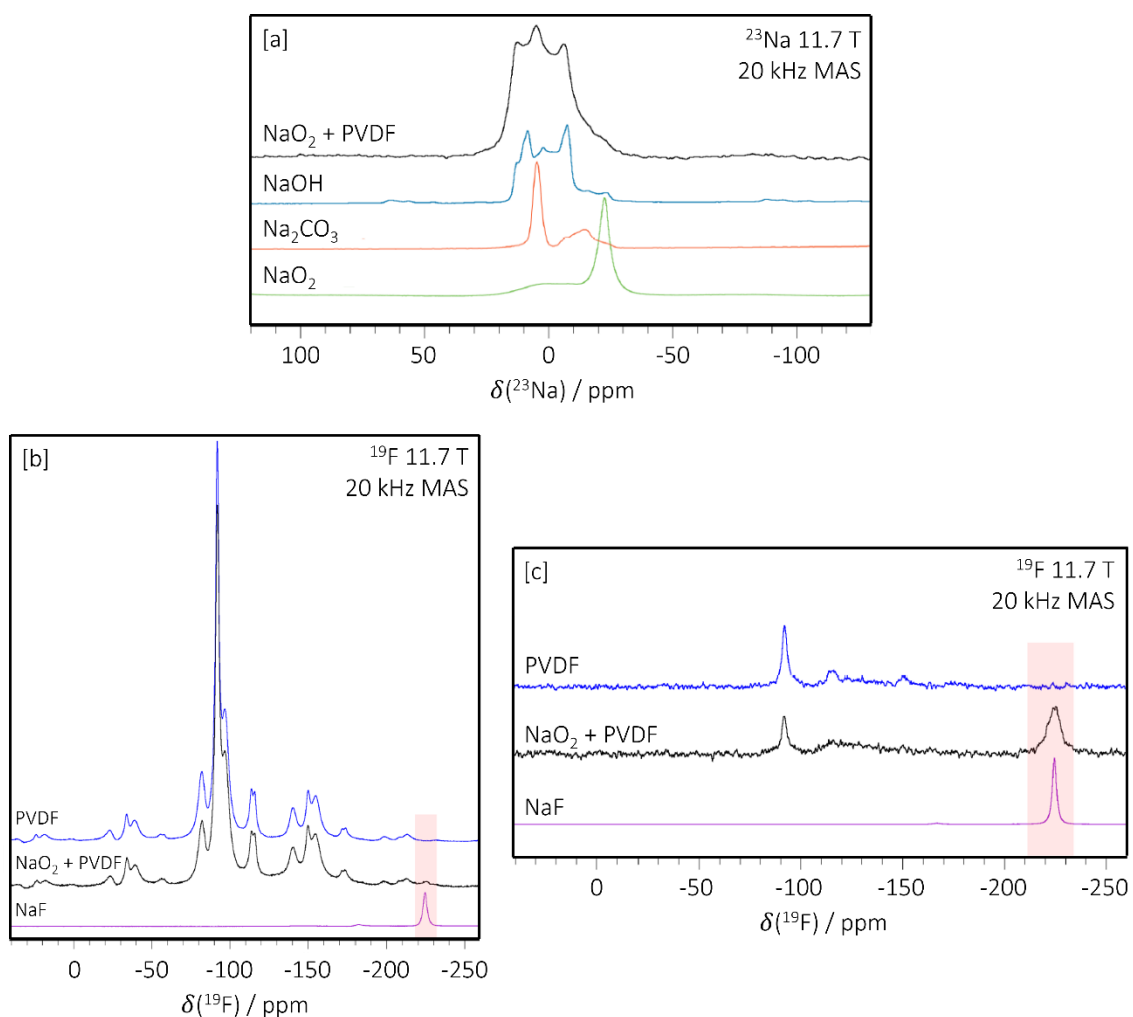


**Figure 3.5.** [a]  $^{23}\text{Na}$  NMR [b]  $^{19}\text{F}$  NMR, and [c]  $^{19}\text{F}$  SelSat NMR spectrum of  $\text{NaO}_2$  ground with PVDF, and spectra of relevant reference compounds. Adapted with permission from the Journal of the American Chemical Society 2017, 139, 2, 595–598 © 2016 American Chemical Society.<sup>1</sup>

The simple one-pulse  $^{19}\text{F}$  ssNMR spectrum of the mixture is given in **Fig. 3.5b**, along with the spectrum of pure PVDF and NaF. There is a small signal in the spectrum of the  $\text{NaO}_2$  / PVDF mixture that overlaps with the lone NaF peak, suggesting that  $\text{NaO}_2$  may be reacting with the PVDF binder. A similar reaction has been observed with transient  $\text{LiO}_2$  and PVDF in LiOBs.<sup>18</sup> Even so, the PVDF spectrum is quite complex and includes a broad spinning side-band manifold that makes assignment of the NaF peak tenuous. To better resolve the NaF region, a selective-saturation pulse sequence (SelSat) was implemented in **Fig. 3.5c**. In the SelSat sequence, a series of pulses with a narrow excitation bandwidth are used to selectively saturate the PVDF central transition, before a second broad-band pulse is applied to entire frequency range, and data is acquired. This results in the selectively saturated transition being effectively filtered out of the NMR spectrum. The effect is apparent in both the pure PVDF and  $\text{NaO}_2$  / PVDF spectra in **Fig. 3.5c**, where the central PVDF lineshape has been significantly reduced, and the spinning side-band manifold is completely removed. Specifically in the  $\text{NaO}_2$  / PVDF spectra, the peak in the NaF region is now clearly resolved, and can be confidently assigned to NaF.

The dual phenomenon of CB and PVDF degradation by  $\text{NaO}_2$  explains the prominence of  $\text{Na}_2\text{CO}_3$  and NaF, as well as the absence of  $\text{NaO}_2$ , in the discharged NaOB cathodes. Electrochemically formed  $\text{NaO}_2$  can nucleate out of solution on the composite cathode during discharge and react with both CB and PVDF to form  $\text{Na}_2\text{CO}_3$  and NaF, thus poisoning the reversible capacity of the cell. This is the first direct evidence of cathode decay by  $\text{NaO}_2$  in NaOBs, and proves the utility of ssNMR for deconvoluting the complex chemistry of the system.

### 3.3.4 – Surface-Modified Binder-Free Carbon-Cloth Cathodes

To further probe the reactivity of NaO<sub>2</sub> to carbon cathode systems, modified binder-free carbon-cloth (CC) cathodes were studied for their use in NaOBs. Two sets of CC analogues were produced with varying surface chemistries. *Hydrophobic* cathodes were made by heat treating CC under a flowing Ar / H<sub>2</sub> atmosphere at 750 °C for 2 hours to purge the CC surface of any oxygen containing functional groups. *Hydrophilic* cathodes were made by treating fresh CC with a modified Hummer's method to add oxygen containing carboxyl and carbonyl functional groups to the carbon surface.<sup>19</sup> The <sup>1</sup>H MAS ssNMR of each cathode is given in **Fig. 3.6**. The hydrophobic cathode has a single resonance that is assigned to the edge protons around the graphite sheets, while the hydrophilic analogue has a second higher frequency resonance that is assigned to the additional hydroxyl groups added in the oxidative treatment.

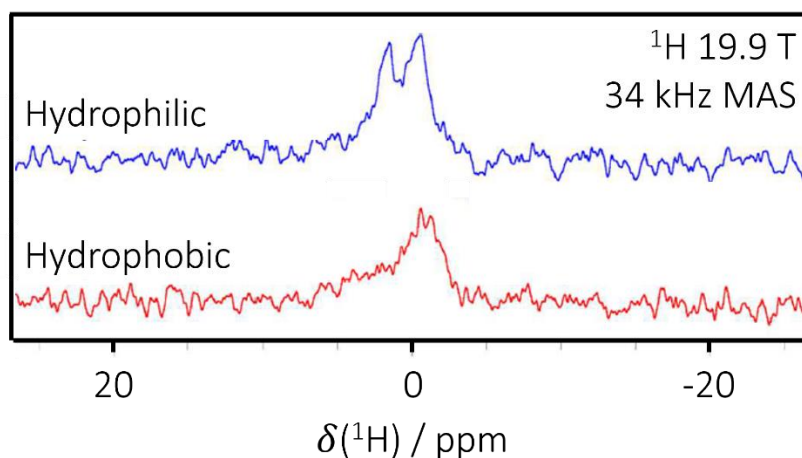


**Figure 3.6.** <sup>1</sup>H MAS ssNMR spectra of hydrophilic and hydrophobic CC cathodes. Adapted with permission from the Journal of Physical Chemistry Lett 2017, 8, 19, 4794–4800 © 2017 American Chemical Society.<sup>2</sup>

To explore the effects of functionalization on the discharge chemistry of the NaOB, the modified CC cathodes were put into full NaOB cells and subjected to one

full discharge / charge cycle. The resulting galvanostatic curves are shown in **Fig. 3.7a**. The hydrophobic cathode achieves a high capacity of  $1.2 \text{ mAh cm}^{-2}$ , and exhibits both the plateaued discharge and low overpotential charge profiles that are characteristic of  $\text{NaO}_2$  production.<sup>20</sup> Conversely, the hydrophilic cathode achieves a comparatively small capacity of  $0.2 \text{ mAh cm}^{-2}$  in a sloping discharge profile, and exhibits a large overpotential on charge, which is similar to that observed for  $\text{Li}_2\text{O}_2$  production in LiOBs.<sup>20</sup>

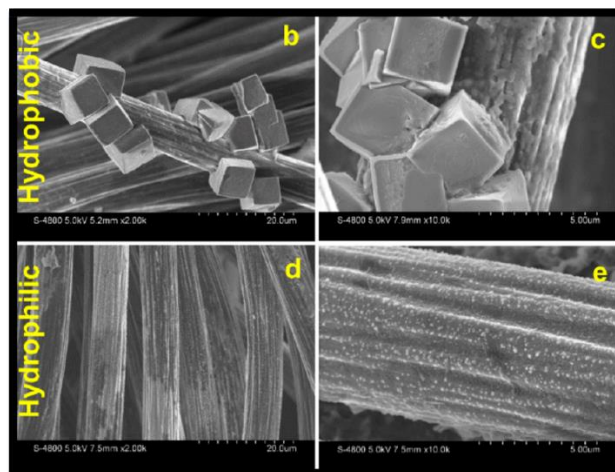
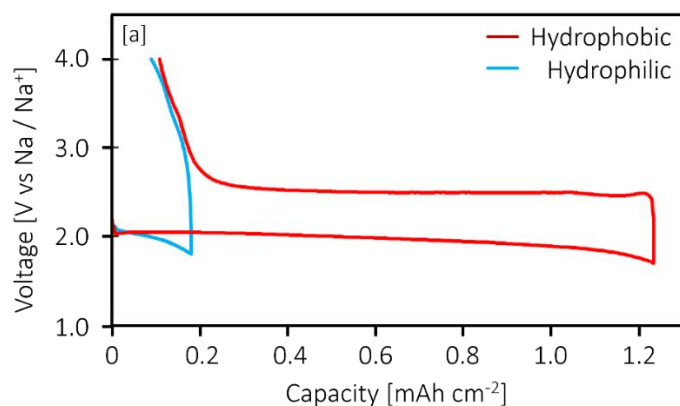


**Figure 3.7.** [a] Galvanostatic cycling curves for a single cycle of hydrophobic and hydrophilic cathodes in NaOBs. [b - e] SEM micrographs of the [b / c] hydrophobic cathode and the [d / e] hydrophilic cathode at varying resolutions. Adapted with permission from the Journal of Physical Chemistry Lett 2017, 8, 19, 4794–4800 © 2017 American Chemical Society.<sup>2</sup>

To better understand the morphological differences between each system, SEM was used to characterize cathodes in the fully discharged state (**Fig. 3.7b** to **3.7e**). As expected from the voltage profile, the SEM micrographs of the hydrophobic cathode (**Fig 3.7b** and **3.7c**) shows the formation of crystalline cubic discharge products that are characteristic of  $\text{NaO}_2$  formed via the solution-mediated mechanism.<sup>3, 4, 21</sup> In contrast, the micrographs of the hydrophilic cathode (**Fig 3.7d** and **3.7e**) show the formation of a conformal film of discharge products. The production of a film in metal- $\text{O}_2$  batteries suggests a surface-mediated formation mechanism for the hydrophilic cathodes, rather than the solution-mediated mechanism observed for the hydrophobic analogue.<sup>21</sup> The surface-mediated discharge mechanism is hypothesized to be the result of  $\text{O}_2$  absorption, and subsequent ORR catalysis, by the additional oxygen-containing functional groups on the hydrophilic cathode surface, as oxidized carbon surfaces have been reported to have inherent ORR catalytic activity.<sup>22</sup> This process appears to have detrimental effects on the discharge process. To better understand why, the identities of the discharge products formed on each cathode were investigated by PXRD (**Fig. 3.8a**).

The PXRD diffraction pattern of the hydrophobic cathode shows  $\text{NaO}_2$  as the only major electrochemical product, while that of the hydrophilic cathode shows no discernable reflections. The lack of reflections in the hydrophilic sample is consistent with the amorphous film of product that was seen by SEM. A much greater thickness is likely necessary to be properly characterized by typical PXRD measurements. In order to overcome this limitation, freshly discharged cathodes were also examined by  $^{23}\text{Na}$  MAS ssNMR. **Fig. 3.8b** and **3.8c** show the ssNMR spectra of discharged hydrophobic and hydrophilic cathodes, as well as reference  $\text{NaO}_2$  and  $\text{Na}_2\text{CO}_3$ .

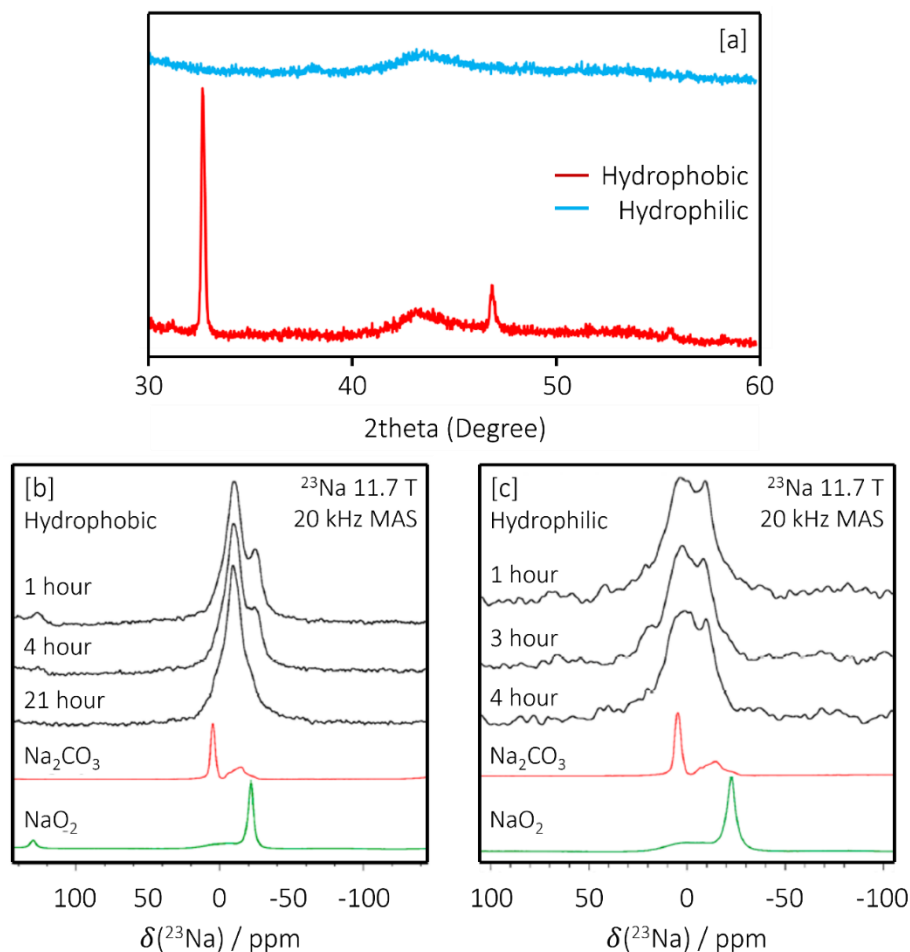


**Figure 3.8.** [a] PXRd diffraction patterns of discharged hydrophobic and hydrophilic cathodes. [b - c]  $^{23}\text{Na}$  ssNMR spectra of discharged [b] hydrophobic and [c] hydrophilic cathodes through time as the reaction mixture aged after discharging. Adapted with permission from the Journal of Physical Chemistry Lett 2017, 8, 19, 4794–4800 © 2017 American Chemical Society.<sup>2</sup>

In both spectra, the large resonance at -10 ppm corresponds to the NaOTF electrolyte salt. Focusing on the hydrophobic cathode spectrum (**Fig. 3.8b**),  $\text{NaO}_2$  is observed as the primary discharge product. This represents the first time in literature that  $\text{NaO}_2$  is directly observed in NaOBs by ssNMR. As the cathode sits in the NMR magnet,  $\text{NaO}_2$  is observed to decay overtime to form  $\text{Na}_2\text{CO}_3$ , representing the degradative oxidation of the carbon surface that was characterized above in **Fig. 3.4**.

In contrast to the composite cathodes studied above, NaF is not observed here as no PVDF binder is present in the CC cathodes.

In the  $^{23}\text{Na}$  spectrum of the hydrophilic cathode (**Fig. 3.8c**), no  $\text{NaO}_2$  is present, which is consistent with the sloping discharge profile and high overpotentials seen in the hydrophilic cycling data. Instead, there is a single broad peak that is primarily composed of  $\text{Na}_2\text{CO}_3$ , and no time evolution of the resonances is observed. NaOB utilizing carbon cathodes with other ORR catalysing species, such as Pt, have also reported homogenous deposition of  $\text{Na}_2\text{CO}_3$ , and observed similar overpotentials to those seen here.<sup>23</sup> This is consistent with reports that  $\text{O}_2^-$  needs to be stabilized in solution as  $\text{HO}_2$  for consistent  $\text{NaO}_2$  formation (**eqn. 3.1**).<sup>4</sup> The  $\text{O}_2^-$  formed in a surface-mediated pathway in hydrophilic cells would have no opportunity to be stabilized by  $\text{H}^+$ , and therefore immediately oxidizes the carbon surface to form  $\text{Na}_2\text{CO}_3$ . This passivates the cathode throughout the course of the discharge process, impeding charge-transfer resistance, and causing the observed sloping discharge profiles. The observations made here suggest that the discharge pathway of the NaOB can be controlled by modification of the cathode, but ultimately, the instability of  $\text{O}_2^-$  to the carbon surface still results in parasitic degradation of the cathode.

### 3.4 – Conclusions

ssNMR was shown to be a sensitive probe for studying the complex discharge chemistry of the NaOB. In  $^{23}\text{Na}$  ssNMR experiments,  $\text{Na}_2\text{CO}_3$  and NaF were found to be the dominant degradation products in discharged CB / PVDF composite cathodes.  $^{23}\text{Na}$  and  $^{19}\text{F}$  ssNMR showed that  $\text{Na}_2\text{CO}_3$  is formed by  $\text{NaO}_2$  oxidation of

both CB and PVDF from the composite cathode, while NaF is formed by NaO<sub>2</sub> oxidation of PVDF.

Surface-modified binder-free CC cathodes were employed to further explore the role of NaO<sub>2</sub> in the NaOB. Hydrophobic cathodes devoid of surface groups were found to facilitate the solution-mediated NaO<sub>2</sub> formation mechanism. NaO<sub>2</sub> was observed directly by <sup>23</sup>Na ssNMR for the first time in the discharged hydrophobic cathode, but was still found to degrade oxidative to form Na<sub>2</sub>CO<sub>3</sub> over time. Hydrophilic cathodes were found to promote a surface-mediated discharge mechanism, which resulted in further Na<sub>2</sub>CO<sub>3</sub> production. These results prove the instability of NaO<sub>2</sub> to the carbon cathode surface and provide a foundation for the use of ssNMR in studying the chemistry of NaOBs in the future.

### 3.5 – References

1. Reeve, Z. E.; Franko, C. J.; Harris, K. J.; Yadegari, H.; Sun, X.; Goward, G. R. *J. Am. Chem. Soc.* **2017**, *139* (2), 595-598. DOI: 10.1021/jacs.6b11333
2. Yadegari, H.; Franko, C. J.; Banis, M. N.; Sun, Q.; Li, R.; Goward, G. R.; Sun, X. *J. Phys. Chem. Lett.* **2017**, *8* (19), 4794-4800. DOI: 10.1021/acs.jpcllett.7b02227
3. Hartmann, P.; Bender, C. L.; Sann, J.; Durr, A. K.; Jansen, M.; Janek, J.; Adelhelm, P. *Phys. Chem. Chem. Phys.* **2013**, *15* (28), 11661-11672. DOI: 10.1039/c3cp50930c
4. Xia, C.; Black, R.; Fernandes, R.; Adams, B.; Nazar, L. F. *Nat. Chem.* **2015**, *7* (6), 496-501. DOI: 10.1038/nchem.2260
5. Cao, R.; Walter, E. D.; Xu, W.; Nasybulin, E. N.; Bhattacharya, P.; Bowden, M. E.; Engelhard, M. H.; Zhang, J. G. *ChemSusChem* **2014**, *7* (9), 2436-40. DOI: 10.1002/cssc.201402315
6. Lee, B.; Kim, J.; Yoon, G.; Lim, H.-D.; Choi, I.-S.; Kang, K. *Chemistry of Materials* **2015**, *27* (24), 8406-8413. DOI: 10.1021/acs.chemmater.5b03877
7. Liu, W.; Sun, Q.; Yang, Y.; Xie, J. Y.; Fu, Z. W. *Chem Commun (Camb)* **2013**, *49* (19), 1951-3. DOI: 10.1039/c3cc00085k
8. Kim, J.; Lim, H. D.; Gwon, H.; Kang, K. *Phys. Chem. Chem. Phys.* **2013**, *15* (10), 3623-3629. DOI: 10.1039/c3cp43225d
9. Liu, T.; Kim, G.; Casford, M. T.; Grey, C. P. *J. Phys. Chem. Lett.* **2016**, *7* (23), 4841-4846. DOI: 10.1021/acs.jpcllett.6b02267
10. Black, R.; Shyamsunder, A.; Adeli, P.; Kundu, D.; Murphy, G. K.; Nazar, L. F. *ChemSusChem* **2016**, *9* (14), 1795-1803. DOI: 10.1002/cssc.201600034
11. Reeve, Z. E. M.; Paurić, A. D.; Harris, K. J.; Goward, G. R. *The Journal of Physical Chemistry C* **2015**, *119* (48), 26840-26848. DOI: 10.1021/acs.jpcc.5b08488
12. Schwenke, K. U.; Meini, S.; Wu, X.; Gasteiger, H. A.; Piana, M. *Phys. Chem. Chem. Phys.* **2013**, *15* (28), 11830-9. DOI: 10.1039/c3cp51531a
13. Schechter, W. H.; Sisler, H. H.; Kleinberg, J. *Journal of the American Chemical Society* **1948**, *70* (1), 267-269. DOI: 10.1021/ja01181a083
14. Parigi, G.; Ravera, E.; Luchinat, C. *Progress in Nuclear Magnetic Resonance Spectroscopy* **2019**, *114-115*, 211-236. DOI: <https://doi.org/10.1016/j.pnmrs.2019.06.003>
15. Ottakam Thotiyl, M. M.; Freunberger, S. A.; Peng, Z.; Bruce, P. G. *Journal of the American Chemical Society* **2013**, *135* (1), 494-500. DOI: 10.1021/ja310258x
16. McCloskey, B. D.; Scheffler, R.; Speidel, A.; Girishkumar, G.; Luntz, A. C. *The Journal of Physical Chemistry C* **2012**, *116* (45), 23897-23905. DOI: 10.1021/jp306680f
17. Kang, S.; Mo, Y.; Ong, S. P.; Ceder, G. *Nano Letters* **2014**, *14* (2), 1016-1020. DOI: 10.1021/nl404557w
18. Black, R.; Oh, S. H.; Lee, J. H.; Yim, T.; Adams, B.; Nazar, L. F. *J. Am. Chem. Soc.* **2012**, *134* (6), 2902-2905. DOI: 10.1021/ja2111543
19. Marcano, D. C.; Kosynkin, D. V.; Berlin, J. M.; Sinitskii, A.; Sun, Z.; Slesarev, A.; Alemany, L. B.; Lu, W.; Tour, J. M. *ACS Nano* **2010**, *4* (8), 4806-4814. DOI: 10.1021/nn1006368
20. Hartmann, P.; Bender, C. L.; Vracar, M.; Durr, A. K.; Garsuch, A.; Janek, J.; Adelhelm, P. *Nature Materials* **2013**, *12* (3), 228-232. DOI: 10.1038/nmat3486
21. Aetukuri, N. B.; McCloskey, B. D.; García, J. M.; Krupp, L. E.; Viswanathan, V.; Luntz, A. C. *Nat. Chem.* **2015**, *7* (1), 50-56. DOI: 10.1038/nchem.2132

22. Ruiz-Camacho, B.; Palafox-Segoviano, J. A.; Pérez-Díaz, P. J.; Medina-Ramírez, A. *International Journal of Hydrogen Energy* **2021**, *46* (51), 26027-26039. DOI: <https://doi.org/10.1016/j.ijhydene.2021.03.143>
23. Zhang, S.; Wen, Z.; Rui, K.; Shen, C.; Lu, Y.; Yang, J. *Journal of Materials Chemistry A* **2015**, *3* (6), 2568-2571. DOI: 10.1039/c4ta05427j

## 4 – Ti<sub>4</sub>O<sub>7</sub>-Enhanced Carbon Supports to Stabilize NaO<sub>2</sub> in Sodium-Oxygen Batteries

This chapter is a reformatted version of an article that has been accepted for publication in *Journal of Physical Chemistry C*. The co-authors are Zoya Sadighi, and Gillian R. Goward. The author was responsible for all experiments described below, except for scanning electron microscopy (SEM), which was carried out by Jhoynner Martinez of the Canadian Centre for Electron Microscopy.

This study continues the work presented in Chapter 3 by implementing a novel strategy of coating carbon-paper cathodes with Magnéli-phase Ti<sub>4</sub>O<sub>7</sub> to stabilize NaO<sub>2</sub> in NaOBs. Herein, Ti<sub>4</sub>O<sub>7</sub> is shown to be stable toward NaO<sub>2</sub> attack via <sup>23</sup>Na magic angle spinning (MAS) solid state nuclear magnetic resonance (ssNMR). Subsequently, NaOB coin cells are constructed with cathodes made from slurries of various Ti<sub>4</sub>O<sub>7</sub> wt. % cast onto carbon paper substrates. It is found that cycle-life increases dramatically with Ti<sub>4</sub>O<sub>7</sub> content. Characterization of the discharged cathodes by <sup>23</sup>Na ssNMR shows that NaO<sub>2</sub> is the main electrochemical product in both pure carbon and Ti<sub>4</sub>O<sub>7</sub>-coated systems, although the degradation of NaO<sub>2</sub> is significantly hindered in Ti<sub>4</sub>O<sub>7</sub> containing cells. Scanning electron microscopy (SEM) data acquired for the discharged cathodes demonstrates that NaO<sub>2</sub> is indeed formed electrochemically on the Ti<sub>4</sub>O<sub>7</sub> surface, confirming that the stability of Ti<sub>4</sub>O<sub>7</sub> is able to contribute to the observed extended cell lifetime. A discharge/charge model is proposed where NaO<sub>2</sub> precipitates and reversibly dissociates on the Ti<sub>4</sub>O<sub>7</sub> surface through the previously reported solution-based formation and decomposition mechanisms. Characterization of lifetime-cycled cathodes using the two-dimensional

$^{23}\text{Na}$ - $^1\text{H}$  dipolar heteronuclear multiple quantum correlation ( $^{23}\text{Na}\{^1\text{H}\}$  D-HMQC) and  $^{23}\text{Na}$  triple quantum magic angle spinning (3QMAS) experiments show that eventual cell death is caused by the build up of carbonaceous  $\text{NaO}_2$  degradation products such as sodium carbonate ( $\text{Na}_2\text{CO}_3$ ) and sodium formate ( $\text{NaHCO}_2$ , NaFormate), but is delayed in  $\text{Ti}_4\text{O}_7$  systems as a higher proportion of  $\text{NaO}_2$  is formed on the stable  $\text{Ti}_4\text{O}_7$  surface, which agrees with the proposed formation-decomposition mechanism.

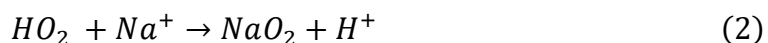
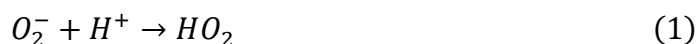
## 4.1 – Introduction

In recent years, the world has seen a major increase in demand for energy storage devices. From 2015 to 2020, global electric vehicle (EV) and plug-in hybrid electric vehicle (PHEV) sales rose from approximately 550,000 to 3.2 million units annually.<sup>1, 2</sup> This is reflected by a parallel increase in new installations of renewable energy production methods, which rose from 160 GW of annual new installs globally to 290 GW over the same timeframe.<sup>3, 4</sup> This rapid rise in demand for energy storage has prompted interest in alternative battery systems that can out-perform the currently used Li-ion battery.

In particular, sodium-oxygen batteries (NaOB) are an interesting candidate for reversible energy storage, with a theoretical energy density double that of the Li-ion battery (1105 Wh  $\text{kg}^{-1}$  to 548 Wh  $\text{kg}^{-1}$ ,  $\text{NaO}_2$  to  $\text{LiCoO}_2$  respectively).<sup>5</sup> In addition to this, the price of sodium carbonate ( $\text{Na}_2\text{CO}_3$ ) is nearly just 1% that of lithium carbonate ( $\text{Li}_2\text{CO}_3$ ) (\$150 vs \$13,000 per tonne; 2019), leading to significant decreases in the cost of battery material production in Na-based cells.<sup>6</sup> However, these benefits do come at a cost. The NaOB does not operate through an intercalation

mechanism such as that seen in classic Li- or Na-ion cells, instead the cell discharges via the solution-mediated exothermic synthesis reaction between Na and O<sub>2</sub>. This comparatively complex chemistry leads to a larger host of possible side reactions, and electrochemical discharge products. The most commonly reported discharge products include: sodium superoxide (NaO<sub>2</sub>), sodium peroxide (Na<sub>2</sub>O<sub>2</sub>), and sodium peroxide dihydrate (Na<sub>2</sub>O<sub>2</sub>·2H<sub>2</sub>O); as well as a number of degradation products including sodium hydroxide (NaOH), Na<sub>2</sub>CO<sub>3</sub>, and sodium fluoride (NaF).<sup>7-10</sup>

The formation of NaO<sub>2</sub> is advantageous due to a low overpotential in the reverse degradation reaction upon cell charging but is complicated due to the instability of the superoxide anion, and the solution-based mechanism by which it forms. In short, O<sub>2</sub> gas is dissolved into the electrolyte and reduced at the carbon cathode to form O<sub>2</sub><sup>-</sup>, which then combines with a H<sup>+</sup> phase-transfer catalyst, supplied by trace H<sub>2</sub>O impurities in the electrolyte or O<sub>2</sub> gas,<sup>11, 12</sup> to stabilize the superoxide anion, before undergoing substitution with Na<sup>+</sup> to form NaO<sub>2</sub> (eqns. 1, 2).<sup>8, 12</sup>



Although NaO<sub>2</sub> formation is kinetically favorable, the superoxide has the major drawback of being inherently unstable, and has been shown to oxidatively degrade the carbon substrate of the cathode over time, producing Na<sub>2</sub>CO<sub>3</sub> through the life of the cell.<sup>7</sup> This parasitic side reaction adds to the irreversible capacity of the cell and causes a significant increase in charge transfer resistance at the carbon surface.<sup>7, 8, 13, 14</sup> This phenomenon has been seen with a variety of carbon morphologies. For example: Zhao et al. employed high surface area vertically aligned carbon nanotubes, Reeve et al. used free-standing carbon black electrodes, Liu et al. employed reduced-

graphene oxide cast onto stainless steel mesh, and Yadegari et al. used both bare and functionalized carbon cloth diffusion layers; all of whom observed  $\text{Na}_2\text{CO}_3$  formation attributed to the reaction of superoxide with the carbon substrate.<sup>7, 8, 15, 16</sup>

Indeed, many research groups have published on the frustrating instability of  $\text{NaO}_2$ . An approach to stabilizing the NaOB is to add oxygen reduction reaction (ORR) catalysts to the carbon cathode to increase the kinetic favourability of the more thermodynamically stable  $\text{Na}_2\text{O}_2$  product.<sup>17-19</sup> These cells have significant success in achieving more homogenous and stable electrochemistry, however it does come at a cost. One notable downside is that the overpotential for  $\text{Na}_2\text{O}_2$  charging is significantly higher than that of the ideal  $\text{NaO}_2$  chemistry (usually in the range of 1.2 V for  $\text{Na}_2\text{O}_2$  vs 0.2 V for  $\text{NaO}_2$ ).<sup>5, 18</sup> Additionally the employed electrocatalysts typically include expensive precious metal nanoparticles such as Pt or Ru,<sup>17, 18</sup> and are susceptible to the similar high cost, large catalyst loading, and catalyst poisoning issues that burden proton exchange membrane fuel cells (PEMFC).<sup>20, 21</sup>

An alternative approach to stabilizing the NaOB, while keeping the low overpotentials and kinetic benefits that  $\text{NaO}_2$  offers, is to search for a cathode support that is more stable toward  $\text{NaO}_2$  than the currently used carbon-based materials. Similar strategies have been explored in the PEMFC community, where the carbon substrate used as a catalyst support is also susceptible to oxidative degradation overtime.<sup>20</sup> One promising material that has been explored is the Magneli-phase reduced titanium dioxide ( $\text{TiO}_2$ ):  $\text{Ti}_4\text{O}_7$ . The oxygen vacancies created in  $\text{TiO}_2$  reduction give the  $\text{Ti}_4\text{O}_7$  phase a high electrical conductivity, while keeping the excellent oxidative stability of the  $\text{TiO}_2$  parent phase.<sup>20, 22, 23</sup>

Ioroi et al. demonstrated the applicability of this to energy storage devices using  $\text{Ti}_4\text{O}_7$  in place of carbon as the Pt-support in PEMFCs. The  $\text{Ti}_4\text{O}_7$ -based electrode showed significantly increased stability to highly oxidizing voltages in an  $\text{O}_2$  atmosphere.<sup>20</sup> Li et al. built on this by studying  $\text{Ti}_4\text{O}_7$  in the context of zinc-air batteries.<sup>24</sup> The authors coated  $\text{Ti}_4\text{O}_7$  on glossy carbon electrodes and used them in cyclic voltammetry (CV) experiments in  $\text{O}_2$ -saturated  $\text{KOH}_{(\text{aq})}$  electrolyte. The CV showed limited, but distinct, oxygen reduction and oxidation events, confirming the material is possibly receptive to the ORR and oxygen evolution reaction (OER).<sup>24</sup>

More recently, Lee et al. produced high surface area, carbon-free,  $\text{Ti}_4\text{O}_7$  electrodes for use in Li- $\text{O}_2$  batteries (LiOBs).<sup>25</sup> They did this by casting synthesised  $\text{Ti}_4\text{O}_7$  nanospheres with a deposited ruthenium dioxide ( $\text{RuO}_2$ ) catalyst onto Ni-foam. The authors demonstrated impressive cycling stability with reversible lithium peroxide ( $\text{Li}_2\text{O}_2$ ) formation on  $\text{Ti}_4\text{O}_7$  electrodes with and without the added  $\text{RuO}_2$  catalysts, albeit with more favourable overpotentials when  $\text{RuO}_2$  was used. CV of the bare  $\text{Ti}_4\text{O}_7$  electrodes also showed significantly higher ORR and OER activity than what was seen by Li et al. for  $\text{Ti}_4\text{O}_7$  on glossy carbon, perhaps due to the high surface area of the synthesised nanospheres. This raises the question of whether  $\text{Ti}_4\text{O}_7$  made from commercially available  $\text{TiO}_2$  may be generally viable as a metal- $\text{O}_2$  battery cathode support material, or if the more synthetically intensive high surface area nanospheres are necessary.

$\text{Ti}_4\text{O}_7$  has yet to be applied to NaOBs, but the success of  $\text{Ti}_4\text{O}_7$  in LiOBs leads to the proposal that these materials may also be of use in the Na analogue. The cell chemistries of the two battery systems are similar, with both cells relying on reversible oxygen reduction and evolution, but one notable difference is the transient stability of

the lithium superoxide ( $\text{LiO}_2$ ) relative to  $\text{NaO}_2$ . This results in the disproportionation of  $\text{LiO}_2$  into the  $\text{Li}_2\text{O}_2$  in LiOBs,<sup>26-28</sup> a process that is not observed for  $\text{NaO}_2$ . Thus, the same electrochemical behaviour is not necessarily expected for  $\text{Ti}_4\text{O}_7$  in NaOBs, and the long-term stability of  $\text{Ti}_4\text{O}_7$  to the superoxide anion is still in question.

This study aims to expand on the work already completed on  $\text{Ti}_4\text{O}_7$  by studying the material for use in NaOB systems. Here we implement  $\text{Ti}_4\text{O}_7$  synthesised from commercial  $\text{TiO}_2$  nanoparticles as a stabilizing additive for simple carbon paper cathodes to limit  $\text{NaO}_2$  degradation in NaOBs. We observe that  $\text{Ti}_4\text{O}_7$  acts as a stable nucleation point for  $\text{NaO}_2$  formed in solution on discharge, and as a result significantly extends cell lifetimes without directly catalyzing the ORR. We propose that the high surface area, light weight, and simplicity of carbon paper are still advantageous to NaOB cells when it is used as the main cathode support, and the addition of  $\text{Ti}_4\text{O}_7$  as a cathode-stabilizing additive allows the system to keep these favourable properties while enhancing cathode stability to  $\text{NaO}_2$ .

$^{23}\text{Na}$  magic angle spinning (MAS) solid state nuclear magnetic resonance (ssNMR) is used to characterize the formation and degradation of  $\text{NaO}_2$  in discharged NaOB cells, identifying significantly reduced degradation in  $\text{Ti}_4\text{O}_7$ -additive cathodes. This in turn leads to longer cycle-lives as less  $\text{NaO}_2$  is reacting with the carbon substrate over the lifetime of the cell. Through more advanced 2D-ssNMR techniques, such as the triple quantum magic angle spinning (3QMAS) and  $^{23}\text{Na}$  observe 2D  $^1\text{H}$  to  $^{23}\text{Na}$  dipolar heteronuclear multiple quantum correlation ( $^{23}\text{Na}\{^1\text{H}\}$  D-HMQC),<sup>29-32</sup> we show that degradative  $\text{Na}_2\text{CO}_3$  and sodium formate ( $\text{NaHCO}_2$ , NaFormate) production is still ultimately responsible for cell death.

## 4.2 – Experimental

### 4.2.1 – Ti<sub>4</sub>O<sub>7</sub> Synthesis

Ti<sub>4</sub>O<sub>7</sub> was synthesised by first coating commercial anatase TiO<sub>2</sub> nanoparticles (Millipore Sigma, 99.7%) with silicon dioxide (SiO<sub>2</sub>) in a solgel process. 0.5 g of TiO<sub>2</sub> was added to a centrifuge tube with 30 mL of ethanol and 5 mL of distilled water. The solution was sonicated for 1 hour before 1.5 mL of 25% ammonia solution (Millipore Sigma) was added. The solution was then stirred rapidly as 4.5 mL of tetraethyl orthosilicate (TEOS, Millipore Sigma, 99%) was added dropwise over the course of 20 minutes. The solution was then allowed to stir overnight. The resulting dispersed SiO<sub>2</sub>-coated TiO<sub>2</sub> product was repeatedly sonicated, decanted, and rinsed with distilled water until the decant was a neutral pH.

SiO<sub>2</sub>-coated TiO<sub>2</sub> was then reduced in a H<sub>2</sub> atmosphere in a tube furnace at 1050 °C for 4 hr. The heating rate used was 120 °C hr<sup>-1</sup> and the cooling rate after reduction was 150 °C hr<sup>-1</sup>. The resulting SiO<sub>2</sub>-coated Ti<sub>4</sub>O<sub>7</sub> product was collected and added to a 0.25 M NaOH<sub>(aq)</sub> solution and left to reflux at 90 °C under a condenser for 8 hr to remove the SiO<sub>2</sub> coating. The resulting Ti<sub>4</sub>O<sub>7</sub> solution was once again repeatedly sonicated, decanted, and rinsed with distilled water until the decant was a neutral pH. The final nanoparticle Ti<sub>4</sub>O<sub>7</sub> product was dried overnight.

### 4.2.2 – Cathode Preparation

Cathode slurries were prepared by stirring the appropriate amounts of Ti<sub>4</sub>O<sub>7</sub>, polyvinylidene fluoride (PVDF, Atofina, Kynar 741, >99 %), and Super P carbon (Alfa Aesar, >99 %) in acetone for 24 hr. The relative ratios of each component followed the formula X / 90 – X / 10 corresponding to the weight percentages (wt. %) of Ti<sub>4</sub>O<sub>7</sub> / SuperP / PVDF respectively. After the casts were thoroughly mixed, they were each

drop-cast on 3/8 in (0.375 in, 0.953 cm) carbon paper punches. The carbon paper punches each weighed 3.0 mg, while the weight of the Ti<sub>4</sub>O<sub>7</sub> / SuperP / PVDF cast on each cathode ranged from 0.7 to 0.9 mg from 0%-Ti<sub>4</sub>O<sub>7</sub> to 90%-Ti<sub>4</sub>O<sub>7</sub>, as the Ti<sub>4</sub>O<sub>7</sub> material is denser than SuperP carbon. The cathodes were then dried in a vacuum oven overnight at 125 °C before being brought into the Ar-filled glovebox (MBraun).

#### 4.2.3 – Electrochemical Characterization

All materials used for battery preparation were stored in an Ar-filled glovebox. Na-O<sub>2</sub> cells were prepared in both coin-cell and Swagelok geometries. Coin cells were of the 2032 format and the tops of cells were modified to have holes for O<sub>2</sub> gas diffusion. Swagelok cell casings were made of Teflon with two stainless steel plungers for current distribution. The plunger on the cathodic side of the cell is hollow to allow for gas diffusion. The same batch of 0.5 M sodium triflate (NaOTF, Solvionic, 99.5 %) in diethylene glycol dimethyl ether (DEGDME, Millipore Sigma, anhydrous, 99.5 %) electrolyte was used for all cells. DEGDME was degassed via the freeze pump thaw method before being dried over 3Å molecular sieves. After dissolving the NaOTF salt, the completed electrolyte was stored under 3Å molecular sieves to ensure minimal water content.

For all cells, pure Na metal pressed onto a stainless-steel spacer was used as the anode and two punches of Celgard 2325 were used as the separator. Na-O<sub>2</sub> cells were constructed in the order: Na metal anode, 40 µL electrolyte, Celgard separator, 20 µL electrolyte, Celgard separator, 40 µL electrolyte, carbon paper-based cathode, and stainless-steel gas diffusion layer as the current collector. The fabricated cells were sealed in air-tight chambers before being brought out of the glove box and getting

repeatedly vacuumed and subsequently charged with O<sub>2</sub> (Linde, 4.5, 99.995 %) in triplicate to ensure an ample supply of O<sub>2</sub> gas.

The final O<sub>2</sub>-charged cells were tested on an Arbin BT-2000 battery tester. Cells were cycled within a voltage window of 1.8 to 4.3 V at a current density of 0.1 mA cm<sup>-2</sup> (19.3 mA g<sup>-1</sup> to 18.3 mA g<sup>-1</sup> for 0%-Ti<sub>4</sub>O<sub>7</sub> to 90%-Ti<sub>4</sub>O<sub>7</sub> cathodes, respectively) to an upper limit areal capacity of 0.28 mAh cm<sup>-2</sup>. Single discharged cells were discharged to a capacity of 1 mAh cm<sup>-2</sup> for powder x-ray diffraction (PXRD) and NMR

#### 4.2.4 – Cathode Characterization

For electrochemical product characterization, cells were brought into the Ar-filled glovebox immediately after cycling and the cathode was then extracted and dried at room temperature under vacuum for approximately 30 minutes. For NMR spectroscopy, the cathode was then packed into an airtight 2.5 mm diameter solid state NMR rotor. All spectra of battery cathodes were collected on a Bruker Avance I 11.7 T spectrometer using a Bruker 2.5 mm broadband probe. Spectra were collected under MAS conditions at a spinning speed of 30 kHz. Samples were spun under N<sub>2</sub> gas to ensure an inert atmosphere, and were also stored in the Ar glovebox when not under direct characterization. All <sup>23</sup>Na and <sup>1</sup>H spectra are referenced to 1 M NaCl<sub>(aq)</sub> at 0 ppm, and to solid Adamantane at 1.85 ppm, respectively. Parameters for 3QMAS and D-HMQC pulse sequences are provided in section 3.5.

For PXRD, dried cathodes were placed in a stainless steel PXRD sample holder and sealed with Kapton tape. Measurements were taken on a PANalytical X'Pert PRO diffractometer equipped with the Ge monochromator using Cu k α<sub>1</sub> radiation.

SEM images were taken with a JEOL JSM-7000F microscope equipped with an Integrated Oxford Instruments X-Maxn 50 mm<sup>2</sup> energy dispersive x-ray

spectroscopy (EDS) detector. All cathode samples were coated with 7 nm of Pt before characterization.

## 4.3 – Results and Discussion

### 4.3.1 – Ti<sub>4</sub>O<sub>7</sub> Synthesis & Stability

The synthesis of Ti<sub>4</sub>O<sub>7</sub> from commercial TiO<sub>2</sub> is described in detail in the experimental section. In short, anatase TiO<sub>2</sub> nanoparticles are first coated with SiO<sub>2</sub> to produce SiO<sub>2</sub>-coated TiO<sub>2</sub> in a sol-gel process. The SiO<sub>2</sub>-coated TiO<sub>2</sub> particles are then reduced to Ti<sub>4</sub>O<sub>7</sub> at 1050 °C under H<sub>2</sub> flow. Finally, the SiO<sub>2</sub> is stripped in aqueous NaOH at 90 °C to give the final Ti<sub>4</sub>O<sub>7</sub> product. The technique of coating TiO<sub>2</sub> with SiO<sub>2</sub> via the sol-gel process has been reported previously, and has been shown to keep TiO<sub>2</sub> surface area high after heat treatment.<sup>33-37</sup> Lee et al. extended this process to the high temperature H<sub>2</sub>-reduction synthesis needed to form Ti<sub>4</sub>O<sub>7</sub>, and showed that the growth of TiO<sub>2</sub> particles during reduction is minimized when the particles are pre-coated with silica.<sup>25</sup> PXRD of our SiO<sub>2</sub>-coated Ti<sub>4</sub>O<sub>7</sub> and the final SiO<sub>2</sub>-stripped Ti<sub>4</sub>O<sub>7</sub> product show that the Ti<sub>4</sub>O<sub>7</sub> phase is homogenous, with only the reflections of Ti<sub>4</sub>O<sub>7</sub> present, except for the amorphous silica in the SiO<sub>2</sub>-coated sample (**Fig. 4.1a**).

In order to test the stability of Ti<sub>4</sub>O<sub>7</sub> in NaOB-like environments, reference NaO<sub>2</sub> was synthesised as described in the supporting information (section 4.5). The <sup>23</sup>Na NMR signature of NaO<sub>2</sub> collected at both 19.9 and 11.7 T field strengths are shown in **Fig. 4.10S** (section 4.5, supporting information). Due to the mildly paramagnetic nature of NaO<sub>2</sub>, the resonance of the <sup>23</sup>Na nuclei is slightly shifted at each of the two field strengths, appearing at -23 ppm at 19.9 T and at -31 ppm at 11.7 T. This is

highlighted by the constant peak position of the non-paramagnetic  $\text{Na}_2\text{O}_2$  impurity in the  $\text{NaO}_2$  spectra, centered at -9 ppm.

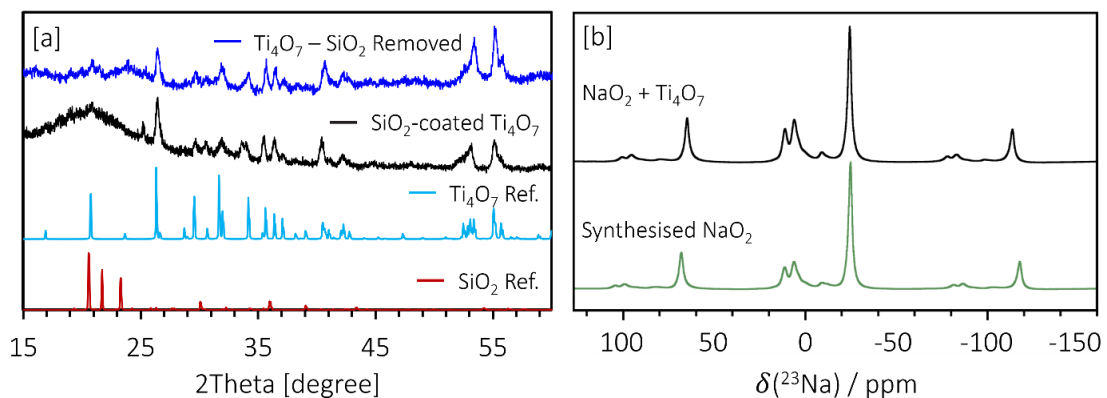


**Figure 4.1.** [a] PXRD diffractograms of the  $\text{Ti}_4\text{O}_7$  synthesis products. [b]  $^{23}\text{Na}$  NMR spectrum of  $\text{Ti}_4\text{O}_7$  ground with  $\text{NaO}_2$ .

The stability of the synthesised  $\text{Ti}_4\text{O}_7$  product was tested by grinding the material with synthesised  $\text{NaO}_2$  under argon, packing the mixture into a solid-state NMR rotor, and monitoring the  $^{23}\text{Na}$  NMR signal over time. **Fig. 4.1b** shows the  $^{23}\text{Na}$  NMR spectra of the pristine  $\text{NaO}_2$  and the  $\text{NaO}_2$ - $\text{Ti}_4\text{O}_7$  mixture 24 hr after grinding. No change in the  $^{23}\text{Na}$  resonances occur, indicating that  $\text{NaO}_2$  is very stable toward the synthesised  $\text{Ti}_4\text{O}_7$ . This is in stark contrast to previous reports of the instability of  $\text{NaO}_2$  toward commonly used carbon materials, where significant amounts of  $\text{Na}_2\text{CO}_3$  are formed over time as the carbon powder is oxidized.<sup>7, 8</sup> The high stability of  $\text{Ti}_4\text{O}_7$  is thought to be due to a thin  $\text{TiO}_2$  passivation layer formed on the surface of the particles when exposed to ambient atmosphere after synthesis, preventing the bulk  $\text{Ti}_4\text{O}_7$  from further oxidation.<sup>24</sup> This result confirms that the oxidative stability of  $\text{Ti}_4\text{O}_7$  extends to the highly unstable  $\text{NaO}_2$ .

### 4.3.2 – NaOB Long-Term Cycle-Life

As discussed in the introduction, when Lee et al. used  $\text{Ti}_4\text{O}_7$  as the primary active material cast on Ni-foam in LiOBs, a very high capacity of  $3,200 \text{ mAh g}^{-1}$  was observed.<sup>25</sup> This implies  $\text{Ti}_4\text{O}_7$  itself has significant activity toward to the ORR and OER. However, when we employed  $\text{Ti}_4\text{O}_7$  cast on Ni-foam in NaOBs, the first discharge areal capacity was comparable of that to bare Ni-foam (**Fig. 4.11S**), reaching  $0.029$  and  $0.033 \text{ mAh cm}^{-2}$  respectively ( $A = 0.712 \text{ cm}^{-2}$ ). It is possible that the NaOB chemistry is not suitable for pure  $\text{Ti}_4\text{O}_7$ , as the ORR activity of the material is not consistent across metal- $\text{O}_2$  battery systems.<sup>24, 25</sup> It may also be the case that this difference in activity may instead be the result of differing  $\text{Ti}_4\text{O}_7$  particle sizes, and surface areas, between studies. While Li et al. observed limited activity in  $\text{Ti}_4\text{O}_7$  made from commercial  $\text{TiO}_2$  in Zn- $\text{O}_2$  cells, the high capacity and activity seen by Lee et al. in LiOBs was achieved from  $\text{Ti}_4\text{O}_7$  made from a more complex, sol-gel synthesised,  $\text{TiO}_2$  nanosphere material.<sup>24, 25</sup>

As previously described, the current study uses  $\text{Ti}_4\text{O}_7$  synthesised from commercial  $\text{TiO}_2$  nanoparticles in an effort to keep the cathode fabrication process as simple as possible. This may explain the limited ORR activity observed. To test whether the observed stability of  $\text{Ti}_4\text{O}_7$  toward  $\text{NaO}_2$  can still have a positive effect on NaOB electrochemical capacity and reversibility, even with the materials limited ORR activity, cathode slurries prepared with varying amounts of  $\text{Ti}_4\text{O}_7$  and SuperP carbon black (referred to as “SuperP”) were made and cast onto carbon paper substrates. Each cathode will be referenced by the  $\text{Ti}_4\text{O}_7$  composition alone, for example a 40 wt. %  $\text{Ti}_4\text{O}_7$ , 10 wt. % PVDF, and 50 wt. % SuperP cathode will be referred to as “40%- $\text{Ti}_4\text{O}_7$ ”.  $\text{Ti}_4\text{O}_7$  was able to mix in the acetone-based slurries in a smooth, ink-like, consistency. The slurries were deep blue in colour, with the blue tone being more

apparent as a larger proportion of  $\text{Ti}_4\text{O}_7$  was included. NaOBs assembled with cathodes consisting of 0%- $\text{Ti}_4\text{O}_7$  (only SuperP and PVDF), 40%- $\text{Ti}_4\text{O}_7$ , 60%- $\text{Ti}_4\text{O}_7$ , 80%- $\text{Ti}_4\text{O}_7$ , and 90%- $\text{Ti}_4\text{O}_7$  (only  $\text{Ti}_4\text{O}_7$  and PVDF) slurries were continuously cycled with a limited discharge voltage of  $0.28 \text{ mAh cm}^{-2}$  (0.2 mAh), a current density of  $0.1 \text{ mA cm}^{-2}$ , and upper and lower voltage limits 4.3 and 1.8 V, respectively. The discharge capacity of each cell as a function of cycle number is shown in **Fig. 4.2a**, and the galvanostatic discharge/charge curves for each cell are shown in **Fig. 4.2b-f**.

Each cell initially is able to discharge to the full  $0.28 \text{ mAh cm}^{-2}$  capacity limit until at some point the lower cut-off voltage of 1.8 V is reached before the cell can fully discharge, signalling cell deterioration. The cell assembled with the 0%- $\text{Ti}_4\text{O}_7$  cathode (only SuperP and PVDF) has the shortest lifetime, discharging to the full capacity for 10 cycles before the capacity drops rapidly. This sudden deterioration is common in NaOBs. Side reactions involving  $\text{NaO}_2$  or other electrochemical discharge products passivate the electrochemically active surface area of the cathode over time, until the ORR and OER become unfavourable and capacity plummets.<sup>15</sup> The mechanism of cell death by cathode degradation, instead of electrolyte breakdown, is supported by reports that DEGDME-based electrolytes are stable toward superoxide attack.<sup>38</sup>

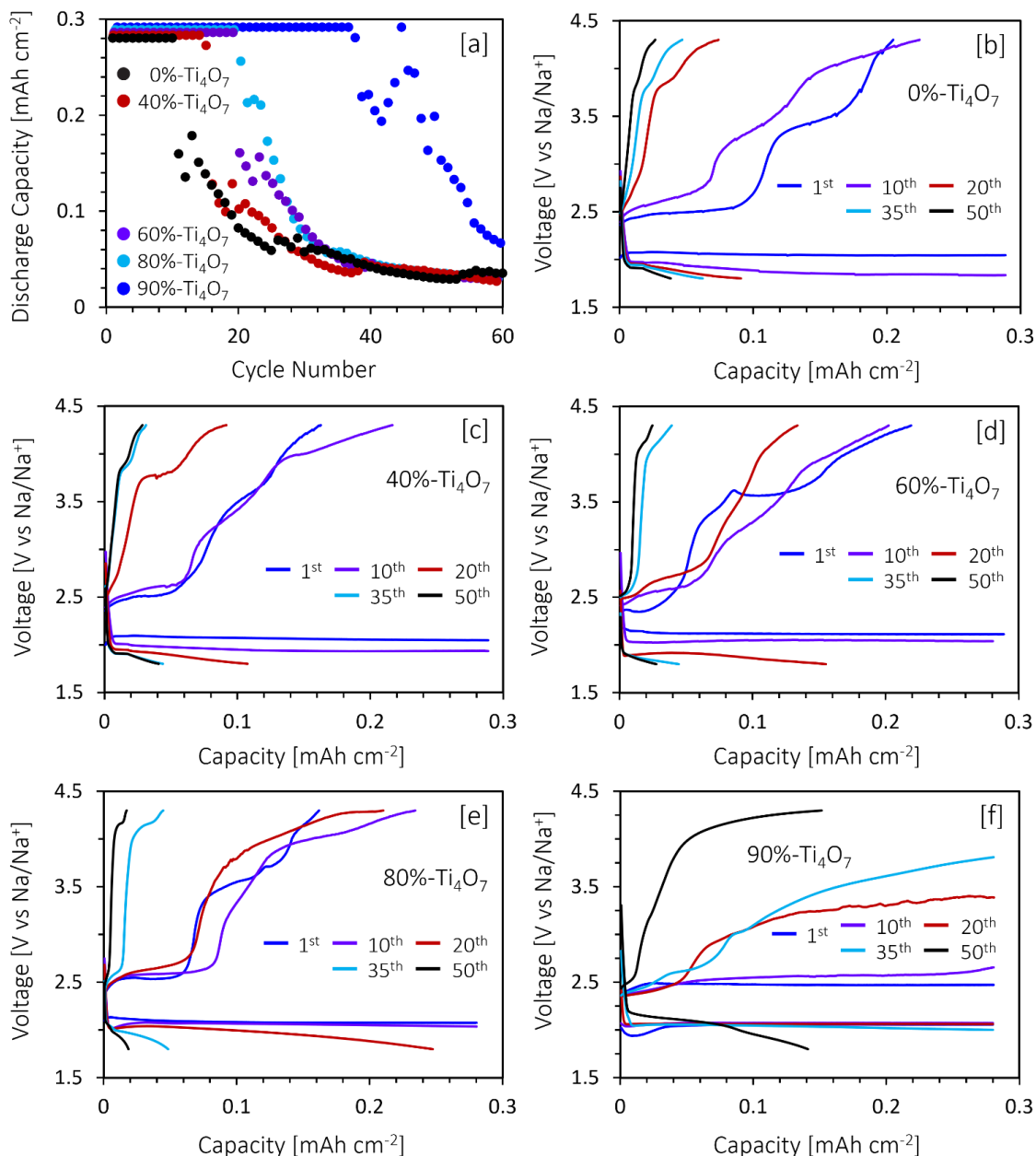


**Figure 4.2.** [a] Discharge capacity achieved as a function of cycle number for NaOB assembled with cathodes of varying  $\text{Ti}_4\text{O}_7$  weight percentage. All cells are limited to a discharge capacity of  $0.28 \text{ mAh cm}^{-2}$  and are cycled at a current density of  $0.1 \text{ mA cm}^{-2}$ . Data points are offset with each series for visibility. [b-f] Galvanostatic discharge/charge curves for NaOB assembled with cathodes of varying  $\text{Ti}_4\text{O}_7$  weight percentage. [b] 0%- $\text{Ti}_4\text{O}_7$ , [c] 40%- $\text{Ti}_4\text{O}_7$ , [d] 60%- $\text{Ti}_4\text{O}_7$ , [e] 80%- $\text{Ti}_4\text{O}_7$ , [f] 90%- $\text{Ti}_4\text{O}_7$ .

As  $\text{Ti}_4\text{O}_7$  is added to the cathode slurry in the 40%- $\text{Ti}_4\text{O}_7$  sample, cell lifetime is elongated to 15 cycles before significant degradation is observed. This number is further extended to 19 and 20 cycles for the 60%- $\text{Ti}_4\text{O}_7$  and 80%- $\text{Ti}_4\text{O}_7$  cells respectively, before being extended significantly to 37 cycles in the 90%- $\text{Ti}_4\text{O}_7$  system. There is a clear trend formed here between cycle-lifetime and  $\text{Ti}_4\text{O}_7$  weight percentage, supporting the hypothesis that  $\text{Ti}_4\text{O}_7$  is able to have a positive effect on the stability of the cathode to  $\text{NaO}_2$ , without having a high ORR activity.

Examining the galvanostatic discharge curves of each cathode (**Fig. 4.2b-f**), each of the 0%- $\text{Ti}_4\text{O}_7$  to 80%- $\text{Ti}_4\text{O}_7$  cells shows a distinct drop in discharge voltage from cycle 1 (blue) to cycle 10 (purple) and further to cycle 20 (red), signaling an increase in interfacial resistance on the cathode. This voltage drop is less significant as  $\text{Ti}_4\text{O}_7$  is added to the cell, and in the 90%- $\text{Ti}_4\text{O}_7$  sample there is no significant voltage deterioration over the first 20 cycles. At this point in cycling, each cell except the one utilizing the 90%- $\text{Ti}_4\text{O}_7$  cathode experiences some capacity fade, with the level of capacity fading also being inversely related to  $\text{Ti}_4\text{O}_7$  wt. %. By cycle 35 the 90%- $\text{Ti}_4\text{O}_7$  cell begins to experience noticeable voltage deterioration, and by cycle 50 roughly half of the discharge capacity is lost.

The charging voltage in NaOBs is highly dependant on the presence of degradation products on the carbon surface.<sup>39</sup> Even though  $\text{NaO}_2$  is suspected to be formed homogenously on discharge, many publications have shown that parasitic  $\text{NaO}_2$  degradation occurs to produce carboxylate degradation products that impede reversible  $\text{NaO}_2$  oxidation on charge, leading to charging curves that are highly variant from cell to cell.<sup>15, 39-41</sup> The low voltage plateau at approximately 2.5 V is attributed to electrochemical  $\text{NaO}_2$  oxidation with minimal interfacial resistance.<sup>5, 39</sup>

In each of the 0%- to 80%-Ti<sub>4</sub>O<sub>7</sub> cells, some amount of NaO<sub>2</sub> is being oxidized at this voltage, before transitioning toward medium and high voltage sloping regions from approximately 3.0 – 3.5 and 4 – 4.5 V, respectively (**Fig. 4.2b-e**). This two-tiered region is characteristic of the production of carboxylate containing degradation products such as Na<sub>2</sub>CO<sub>3</sub> or NaFormate, which passivate the cathode surface at the NaO<sub>2</sub> interface, and increase the voltage necessary for NaO<sub>2</sub> oxidation.<sup>39</sup> In contrast, the 90%-Ti<sub>4</sub>O<sub>7</sub> cell is able to exclusively charge in the low voltage region (**Fig. 4.2f**). This suggests that all produced NaO<sub>2</sub> is reversibly oxidized, and no carboxylate degradation products are formed. This is likely due to the majority of NaO<sub>2</sub> being deposited on the stable, homogeneously coated, Ti<sub>4</sub>O<sub>7</sub> cast (investigated by SEM below). It is also worth noting that it is possible the added Ti<sub>4</sub>O<sub>7</sub> is catalyzing the OER without having a significant effect on the ORR. Metal oxides have been shown to be some of the most effective OER catalysts,<sup>42</sup> and Ti<sub>4</sub>O<sub>7</sub> has been shown to catalyze the OER in metal-oxygen cells before, as discussed in the introduction.<sup>24, 25</sup>

It is of note that each of the 0%- (**Fig. 4.2b**), 40%- (**Fig. 4.2c**), 60%- (**Fig. 4.2d**), and 80%-Ti<sub>4</sub>O<sub>7</sub> (**Fig. 4.2e**) cells do not reach full capacity on the first charging process before reaching the cut-off voltage of 4.3 V, indicating that on the first cycle there is a larger amount of initial carboxylate formation, that is overcome in later cycles. This phenomenon has been observed in other NaOBs employing limited discharge capacity cycling,<sup>14, 43-45</sup> and is a result of the irreversible capacity on charge not being a direct measure of “lost” capacity in NaOBs. There is a large excess of O<sub>2</sub> in the cathode environment, so the cell can “lose” a significant portion of discharged O<sub>2</sub> to irreversible products such as Na<sub>2</sub>CO<sub>3</sub> or NaFormate, and still reach the full discharge capacity cut-off on subsequent cycles. It is only when the cumulative amount of

formed irreversible products cause interfacial resistance increases to the point where the ORR and OER become extremely unfavourable that discharge capacity is hindered. A clear trend for influence of this on the charging process is not observed when examining individual charging curve profiles, but the cumulative effect of parasitic carboxylate production on cell lifetime is clearly seen in **Fig. 4.2a**.

#### 4.3.3 – Characterization of Discharge Products

To confirm  $\text{NaO}_2$  as the main electrochemical product in  $\text{Ti}_4\text{O}_7$  containing NaOBs, both 0%- $\text{Ti}_4\text{O}_7$  and 90%- $\text{Ti}_4\text{O}_7$  cathodes were examined after the initial discharge by PXRD (**Fig. 4.3**).

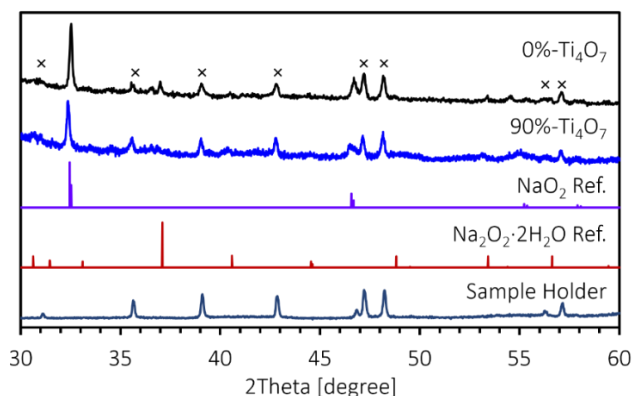


**Figure 4.3.** PXRD diffractograms of single-discharge 0%- $\text{Ti}_4\text{O}_7$  and 90%- $\text{Ti}_4\text{O}_7$  cathodes. The reference patterns of  $\text{NaO}_2$  and  $\text{Na}_2\text{O}_2 \cdot 2\text{H}_2\text{O}$  are shown below, as well as the pattern of the empty air-free sample holder used for discharged cathode data collection. The reflections of the sample holder are also marked by “x” symbols in the discharged cathode diffractograms.

It is clear from the PXRD experiments that both cathodes produce  $\text{NaO}_2$  as the main electrochemical discharge product. The diffractogram of the 0%- $\text{Ti}_4\text{O}_7$  cell also shows a weak reflection at  $37^\circ$  which is characteristic of  $\text{Na}_2\text{O}_2 \cdot 2\text{H}_2\text{O}$ , but none of the other expected peaks are present and thus the assignment is not confirmed.  $\text{Na}_2\text{O}_2 \cdot 2\text{H}_2\text{O}$  has been reported in carbon-cathode NaOBs previously, but requires a large amount

H<sub>2</sub>O impurities to form, which is not expected in the anhydrous conditions employed here.<sup>40, 46</sup> The lack of any Na<sub>2</sub>O<sub>2</sub>·2H<sub>2</sub>O reflections in the 90%-Ti<sub>4</sub>O<sub>7</sub> diffractogram confirms that hydrate formation is likely not present in these cells.

To better understand the evolution of the discharge products as a function of time, <sup>23</sup>Na MAS ssNMR was used to characterize the sodium-containing electrochemical discharge species in single-discharge 0%-Ti<sub>4</sub>O<sub>7</sub> and 90%-Ti<sub>4</sub>O<sub>7</sub> cathodes. **Fig. 4.4a** and **4.4b** show the <sup>23</sup>Na spectra 2.66 hours (blue) and 1 month (black) after discharging was terminated of the 0%-Ti<sub>4</sub>O<sub>7</sub> and 90%-Ti<sub>4</sub>O<sub>7</sub> cells respectively. Each spectrum shows two major resonances at -12 and -33 ppm assigned to the NaOTF electrolyte and NaO<sub>2</sub>, respectively. The reference spectrum of each is included. The reference NaOTF lineshape is that of the used NaOTF in DEGDME electrolyte that has been vacuumed dried for approximately 1 hour. A comparison of this with the dry electrolyte is shown in **Fig. 4.10S**, along with other species commonly found in NaOBs. Both the NaO<sub>2</sub> and NaOTF resonances are significantly broader in the electrochemical discharge slurry than in the reference spectra. This is due to the observed species being formed on conductive substrates like carbon or Ti<sub>4</sub>O<sub>7</sub>, as well as the largely amorphous nature of electrochemically formed products, and the possibility of smaller amounts of unassigned side-reactions products given the unstable nature of these cells. It is also of note that the NaO<sub>2</sub> peaks in the 90%-Ti<sub>4</sub>O<sub>7</sub> spectra are broader than those in the 0%-Ti<sub>4</sub>O<sub>7</sub> analogue. This is likely due to the majority of NaO<sub>2</sub> being formed on the Ti<sub>4</sub>O<sub>7</sub> surface, which contains a portion of paramagnetic Ti<sup>3+</sup>.

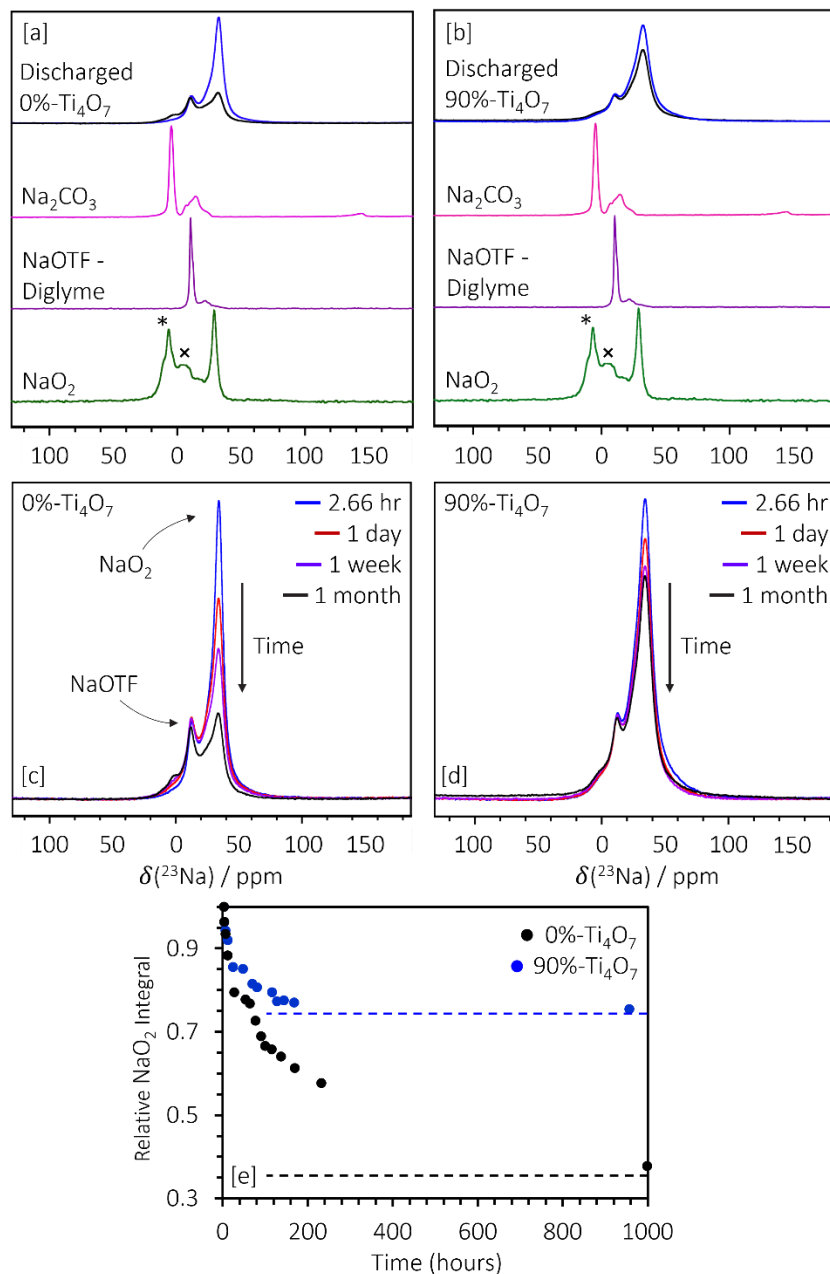


**Figure 4.4.**  $^{23}\text{Na}$  ssNMR spectra of discharged [a] 0%- $\text{Ti}_4\text{O}_7$  and [b] 90%- $\text{Ti}_4\text{O}_7$  cathodes (blue is 2.66 hours after discharge, black is 1 month). Each includes the reference spectra of  $\text{Na}_2\text{CO}_3$  (pink), NaOTF that has been wet with DEGDME (purple), and synthesised  $\text{NaO}_2$  (green). [c-d] Time dependant  $^{23}\text{Na}$  ssNMR spectrum showing the decay of  $\text{NaO}_2$  in the discharged [c] 0%- $\text{Ti}_4\text{O}_7$  and [d] 90%- $\text{Ti}_4\text{O}_7$  cathodes. [e] The  $\text{NaO}_2$  integral taken from the  $^{23}\text{Na}$  spectra of the discharged NaOB cathodes plotted over time.

In both cells  $\text{NaO}_2$  is identified as the only major electrochemical species formed, which is in good agreement with the PXRD experiments. **Fig. 4.4c** and **4.4d** track the evolution of the  $^{23}\text{Na}$  resonances over time for the 0%- $\text{Ti}_4\text{O}_7$  and 90%- $\text{Ti}_4\text{O}_7$  cells, respectively. Spectra are shown 2.66 hours, 1 day, 1 week, and 1 month after discharge. The spontaneous degradation of  $\text{NaO}_2$  can be seen as time increases, while the  $\text{NaOTF}$  resonance remains unchanged throughout the entire time period, confirming the stability of the electrolyte salt. The degradation of  $\text{NaO}_2$  in the 0%- $\text{Ti}_4\text{O}_7$  cell is clearly much greater than that of the 90%- $\text{Ti}_4\text{O}_7$  analogue. A shoulder is seen to form as time increases at approximately 4 ppm in the 0%- $\text{Ti}_4\text{O}_7$  cell, which corresponds to the shift of the main peak of  $\text{Na}_2\text{CO}_3$  (**Fig. 4.4a**). There is also some mass in the 4 ppm region of the 90%- $\text{Ti}_4\text{O}_7$  cell, but the evolution is much less pronounced.

To track the degradation of  $\text{NaO}_2$  more effectively, the integral of the  $\text{NaO}_2$  peak is plotted as a function of time since terminating discharge in **Fig. 4.4e**. In each case, the initial degradation of  $\text{NaO}_2$  over the first several hours happens at a similar rate. However, by the 1 week point, the 90%- $\text{Ti}_4\text{O}_7$  cathode retained 77% of the  $\text{NaO}_2$  signal and degradation has noticeably leveled off. While the 0%- $\text{Ti}_4\text{O}_7$  cathode has retained only 61% of the  $\text{NaO}_2$  signal and degradation is not slowing. These samples were then kept in the air-tight NMR rotors in the Ar glovebox for an additional three weeks before analysing again to find that the  $\text{NaO}_2$  decay had almost halted in the 90%- $\text{Ti}_4\text{O}_7$  sample, with the  $\text{NaO}_2$  signal dropping just 2 percentage points in the additional 33 days to 75% of the initial value. Conversely the 0%- $\text{Ti}_4\text{O}_7$   $\text{NaO}_2$  signal has continued deteriorating to 38% of the initial value over a similar time frame.

This behaviour is explained by the hypothesis that the  $\text{Ti}_4\text{O}_7$  is acting as a stable nucleation point for  $\text{NaO}_2$  in  $\text{Ti}_4\text{O}_7$ -additive cathodes. In both cells,  $\text{NaO}_2$  is formed on the prepared electrode slurry, and on the residual carbon paper substrate.  $\text{NaO}_2$  that is formed in direct contact with carbon begins to decay immediately, producing similar initial degradation rates. In the 0%- $\text{Ti}_4\text{O}_7$  cathode, this decay continues until all the  $\text{NaO}_2$  on the electrode surface is passivated, after which the decay rate finally decreases. However in the 90%- $\text{Ti}_4\text{O}_7$  cathode the  $\text{NaO}_2$  in contact with carbon paper is quickly depleted and decay tails off much sooner as the majority of remaining  $\text{NaO}_2$  is on the stable  $\text{Ti}_4\text{O}_7$  surface. By this mechanism, a significantly smaller portion of the cathode is passivated with each cycle, leading to longer cell lifetimes as  $\text{Ti}_4\text{O}_7$  is added to the cell.

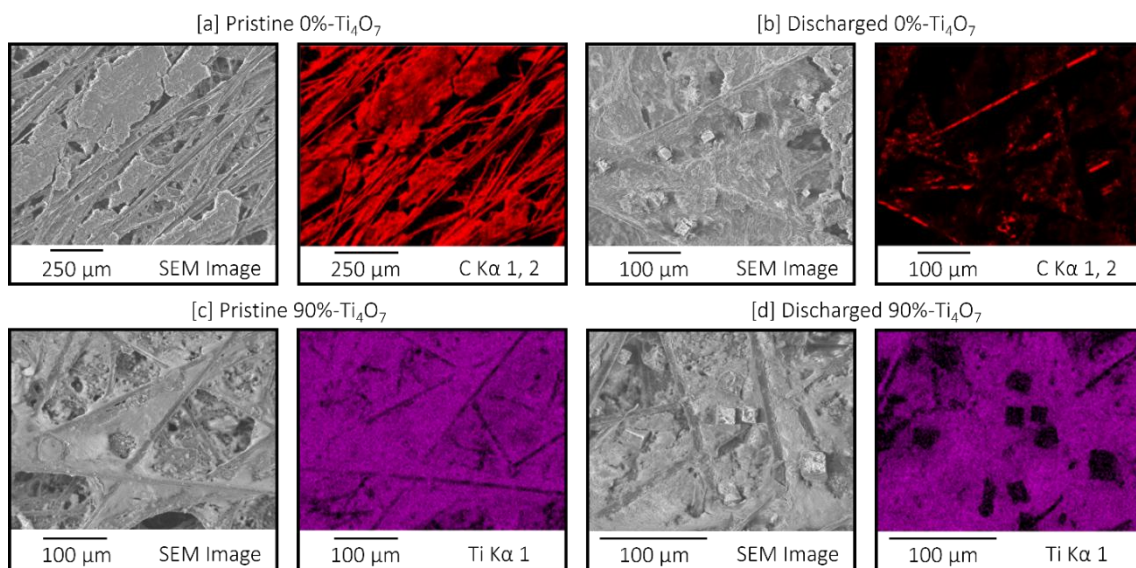


**Figure 4.5.** SEM and EDS characterization of pristine and discharged NaOB cathodes. [a] SEM and C K $\alpha$ 1, 2 EDS of a Pristine 0%- $\text{Ti}_4\text{O}_7$  cathode. [b] SEM and C K $\alpha$ 1, 2 EDS of a Discharged 0%- $\text{Ti}_4\text{O}_7$  cathode. [c] SEM and Ti K $\alpha$ 1 EDS of a Pristine 90%- $\text{Ti}_4\text{O}_7$  cathode. [d] SEM and Ti K $\alpha$ 1 EDS of a Discharged 90%- $\text{Ti}_4\text{O}_7$  cathode.

In order to confirm the hypothesis that  $\text{NaO}_2$  is being formed directly on the  $\text{Ti}_4\text{O}_7$  surface, scanning electron microscopy (SEM) paired with energy dispersive spectroscopy (EDS) was used to image the surface of pristine and discharged 90%  $\text{Ti}_4\text{O}_7$  and 0%  $\text{Ti}_4\text{O}_7$  NaOB cathodes (**Fig. 4.5**). The SEM image of the pristine 0%  $\text{Ti}_4\text{O}_7$  cathode (**Fig. 4.5a**) shows the individual carbon fibres of the carbon paper substrate as well as the SuperP and PVDF cast matrix surrounding said carbon paper fibres. Likewise, in the pristine 90%  $\text{Ti}_4\text{O}_7$  cell (**Fig. 4.5c**), the  $\text{Ti}_4\text{O}_7$  matrix can be seen interweaving the carbon fibres, with the EDS image showing Ti homogeneously deposited throughout the cathode. In both the discharged 0%  $\text{Ti}_4\text{O}_7$  (**Fig. 4.5b**) and the discharged 90%  $\text{Ti}_4\text{O}_7$  (**Fig. 4.5d**) cathodes, cubic  $\text{NaO}_2$  crystallites can be seen in the cast matrix between the carbon fibres themselves. Specifically in the Ti  $\text{K}\alpha 1$  EDS image of the discharged 90%  $\text{Ti}_4\text{O}_7$  cathode (**Fig. 4.5d**), the  $\text{NaO}_2$  is highlighted as distinct black cubes among the purple Ti cast matrix.  $\text{NaO}_2$  nucleating out of solution in characteristic cubic crystallites has been thoroughly reported in NaOB systems.<sup>5, 8, 9, 15, 43</sup> It is interesting to find the crystallites nucleating directly on the cast matrix rather than on the carbon fibres alone. This confirms that the  $\text{Ti}_4\text{O}_7$  cast does participate as a  $\text{NaO}_2$  nucleation point to have  $\text{NaO}_2$  form directly on  $\text{Ti}_4\text{O}_7$ , even if it is not highly active toward the ORR in this system. These  $\text{NaO}_2$  crystallites can remain stable on the  $\text{Ti}_4\text{O}_7$  for extended periods of time, as proven by the  $\text{NaO}_2$  /  $\text{Ti}_4\text{O}_7$  stability test (**Fig. 4.1b**) and the observed longer  $\text{NaO}_2$  lifetime in discharged 90%  $\text{Ti}_4\text{O}_7$  cells (**Fig. 4.4e**), subsequently extending the lifetime of the cell.

#### 4.3.4 – Characterization of Cell Death

The experiments above prove that cell lifetime is significantly extended by the addition of  $\text{Ti}_4\text{O}_7$  as a stable nucleation point for  $\text{NaO}_2$ , but it is still expected that any

NaO<sub>2</sub> forming on the carbon paper surface will rapidly degrade, as evidenced by the initial degradation of the NaO<sub>2</sub> NMR signal in **Fig. 4.4e**. Over many discharge / charge cycles, this will result in the accumulation of degradation products that will contribute to cell death. In order to confirm this model, the spent cathodes of the lifetime-cycled 0%-Ti<sub>4</sub>O<sub>7</sub> and 90%-Ti<sub>4</sub>O<sub>7</sub> cells were examined by PXRD and ssNMR spectroscopy. The PXRD diffractograms of both cycled cathodes are shown in **Fig. 4.13S**, along with the reference powder patterns of relevant electrochemical species and the air-free sample holder. Notably, the only discernable peaks in the x-ray diffractograms of both cells are those of the sample holder. This is not surprising given that the cathode is not expected to contain crystalline electrochemical discharge products by the end of the lifecycle of the cell. Instead, the majority of material in the cathode is likely to be degradation products that produce an amorphous insulating film over the electrochemically active surface. In contrast, NMR spectroscopy is not limited by the crystalline nature of the electrochemical products. **Fig. 4.6a** shows the <sup>23</sup>Na NMR spectrum of the lifetime-cycled 0%-Ti<sub>4</sub>O<sub>7</sub> and 90%-Ti<sub>4</sub>O<sub>7</sub> cathodes, along with relevant reference spectra.

Each cathode spectrum has significant contributions from the NaOTF electrolyte at approximately -11 ppm, as well as the Na<sub>2</sub>CO<sub>3</sub> degradation product at approximately 4 ppm. The appearance of Na<sub>2</sub>CO<sub>3</sub> is consistent with previous reports that have observed little to no Na<sub>2</sub>CO<sub>3</sub> via PXRD on cycled NaOB cathodes, but see significant production of the side product when examining the same cathodes by <sup>23</sup>Na ssNMR.<sup>8</sup> Each of the cycled cathodes also appear to have a third peak between the NaOTF and Na<sub>2</sub>CO<sub>3</sub> resonances at approximately -5.5 ppm, and the 0%-Ti<sub>4</sub>O<sub>7</sub> in particular has an additional shoulder on the right of the Na<sub>2</sub>CO<sub>3</sub> peak at 1 ppm. The

$^{23}\text{Na}$  chemical shift of the -5.5 ppm peak suggests it is the resonance of sodium bicarbonate ( $\text{NaHCO}_3$ , NaBicarbonate), and the 1 ppm resonance is consistent with NaFormate.<sup>15, 47</sup>

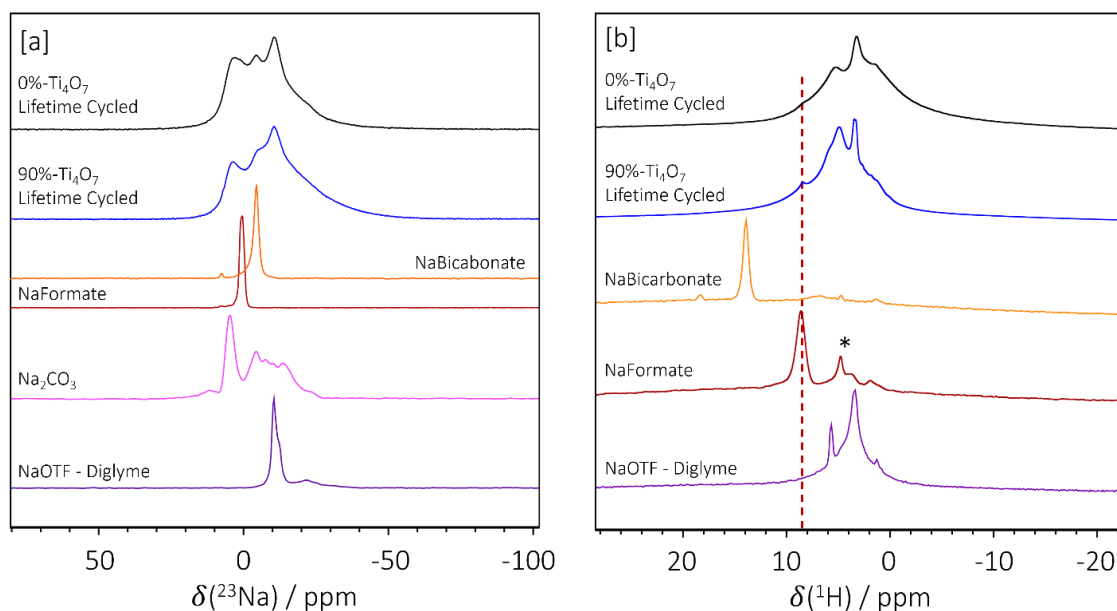


**Figure 4.6.** [a] 1D  $^{23}\text{Na}$  and [b] 1D  $^1\text{H}$  ssNMR spectra of lifetime-cycled 0%- $\text{Ti}_4\text{O}_7$  and 90%- $\text{Ti}_4\text{O}_7$  cathodes. The asterisk in the NaFormate spectrum marks an impurity in the sample.

In order to further test these assignments  $^1\text{H}$  NMR was also collected on the cathode samples (**Fig. 4.6b**). The  $^1\text{H}$  resonance of reference NaBicarbonate appears at approximately 14 ppm, however there is no distinct peak in the  $^1\text{H}$  spectrum of either cathode in this area, suggesting a different identity for the -5.5 ppm resonance in the  $^{23}\text{Na}$  spectra. The  $^1\text{H}$  shift of NaFormate appears at 8.4 ppm, where each cathode spectrum has a distinct peak. The simultaneous confirmation of NaFormate and rejection of NaBicarbonate as electrochemical species is consistent with previous reports, as NaFormate has been identified as a degradation product in  $\text{NaO}_2$ -based

NaOBs previously, while there is little support in literature for NaBicarbonate formation.<sup>15, 39, 48, 49</sup>

Although the 1D  $^{23}\text{Na}$  and  $^1\text{H}$  NMR experiments are useful, the broad, amorphous nature of resonances from electrochemical degradation species make direct assignment difficult. In order to help separate these overlapping resonances and further confirm the assignments made above, 2D  $^{23}\text{Na}\{^1\text{H}\}$  D-HMQC was implemented on the cycled NaOB cathodes. The 2D spectra of both the 0%- $\text{Ti}_4\text{O}_7$  and 90%- $\text{Ti}_4\text{O}_7$  samples are shown in **Fig. 4.7a** and **4.7b** respectively, along with the combined spectra of each the NaFormate, NaBicarbonate, and NaOTF in DEGDM reference materials in **Fig. 4.7c**. Each spectrum displays the same four areas of significant  $^{23}\text{Na}\{^1\text{H}\}$  correlated intensity. With the peaks of the 90%- $\text{Ti}_4\text{O}_7$  spectrum appearing less resolved than those of the 0%- $\text{Ti}_4\text{O}_7$  analogue. This is due to the intimate mixture of the observed products with the paramagnetic  $\text{Ti}_4\text{O}_7$  material, causing significantly faster relaxation of the produced magnetization. Even so, each contribution is still clearly observed.

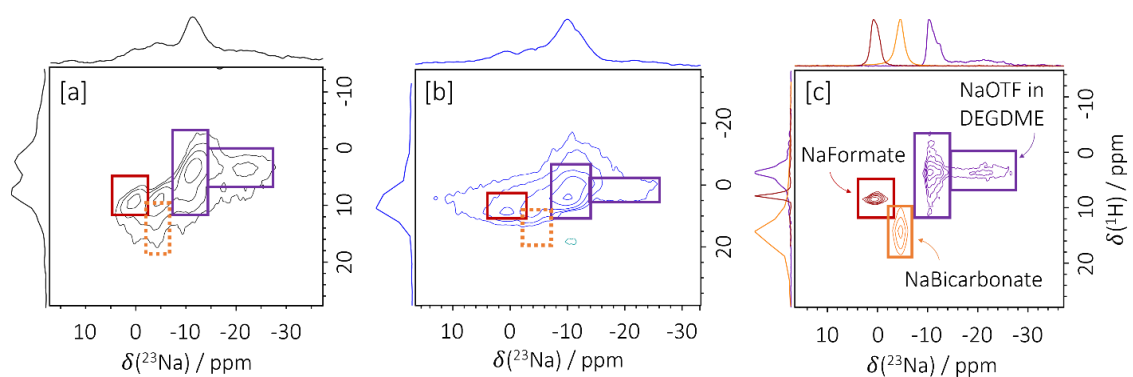


**Figure 4.7.** 2D  $^{23}\text{Na}\{^1\text{H}\}$  D-HMQC spectra of [a] lifetime-cycled 0%- $\text{Ti}_4\text{O}_7$  cathode, [b] lifetime-cycled 90%- $\text{Ti}_4\text{O}_7$  cathode, and [c] combined NaFormate, NaBicarbonate, and dried NaOTF in DEGDM reference materials.

The areas of significant peak intensity in the reference spectra (**Fig. 4.7c**) are highlighted by coloured boxes, these same areas are overlaid on the cathode spectra for a direct comparison of which reference materials appear in the cells. The dotted boxes in the cathode spectra correspond to reference compounds that are not present. The two right-most resonances of the correlated spectra have direct overlap with the reference NaOTF in DEGDME, confirming the assignment. The two left-most resonances that were convoluted in the 1D experiment, with  $^{23}\text{Na}$  shifts at 1 and -5.5 ppm, are now distinctly observed when separated in the indirect  $^1\text{H}$  dimension, with  $^1\text{H}$  shifts of 8.4 and 8.0 ppm, respectively. The 1 ppm  $^{23}\text{Na}$  / 8.4 ppm  $^1\text{H}$  resonance has direct overlap with the reference NaFormate spectrum, and is assigned to NaFormate in both cathodes. The resonance at -5.5 ppm  $^{23}\text{Na}$  / 8.0 ppm  $^1\text{H}$  clearly does not belong to the originally assigned NaBicarbonate product. The identity of this species is not known at this time. However, given the similar  $^1\text{H}$  chemical shift to the assigned NaFormate product, it is possible that it belongs to a hydrate, or DEGDME absorbed species, of NaFormate; similar to what is observed with the NaOTF in DEGDME electrolyte, as Na-oxides are well known to be hygroscopic.<sup>10</sup>

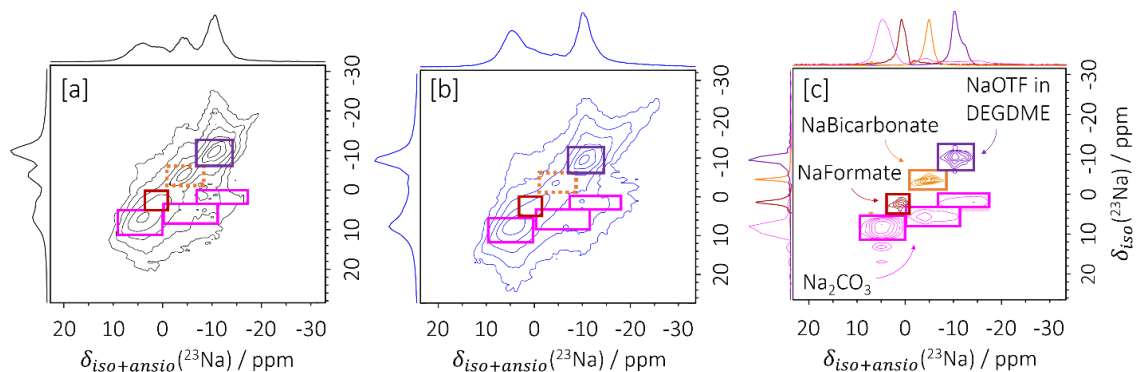


**Figure 4.8.** 2D 3QMAS spectra of [a] lifetime-cycled 0%-Ti<sub>4</sub>O<sub>7</sub> cathode, [b] lifetime-cycled 90%-Ti<sub>4</sub>O<sub>7</sub> cathode, and [c] combined NaFormate, NaBicarbonate, Na<sub>2</sub>CO<sub>3</sub>, and dried NaOTF in DEGDME reference materials.

To further aid in the deconvolution of the electrochemical slurry 2D 3QMAS was used to study the lifetime-cycled cathodes. The 3QMAS experiment is able to separate inequivalent  $^{23}\text{Na}$  resonances to obtain the isotropic quadrupolar lineshape of each species.<sup>50</sup> The 3QMAS spectra of the lifetime-cycled 0%-Ti<sub>4</sub>O<sub>7</sub> and 90%-Ti<sub>4</sub>O<sub>7</sub> cathodes are shown in **Fig. 4.8a** and **4.8b** respectively, with the combined reference spectra of Na<sub>2</sub>CO<sub>3</sub>, NaFormate, and NaOTF in DEGDME in **Fig. 4.8c**. The 3QMAS spectra of each cathode displays 4 main resonances across the diagonal, as well as significant  $^{23}\text{Na}$  intensity in the area of the broader peaks in the Na<sub>2</sub>CO<sub>3</sub> reference spectrum. Notably, the experiment confirms that there are separate Na<sub>2</sub>CO<sub>3</sub> and NaFormate species present by separating the two broad, overlapping, resonances. The resonance of the unconfirmed species at -5.5 ppm is prevalent in each 3QMAS spectrum in the direct area where NaBicarbonate is expected, however the contradictory evidence from the  $^{23}\text{Na}\{^1\text{H}\}$  D-HMQC data rules this out as a possible assignment.

From the combination of the 1D  $^{23}\text{Na}$ , 1D  $^1\text{H}$ , 2D  $^{23}\text{Na}\{^1\text{H}\}$  D-HMQC, and 2D 3QMAS experiments it is clear that Na<sub>2</sub>CO<sub>3</sub> and NaFormate are produced in significant amounts throughout the lifetime of both 0%-Ti<sub>4</sub>O<sub>7</sub> and 90%-Ti<sub>4</sub>O<sub>7</sub> cells. Both Na<sub>2</sub>CO<sub>3</sub> and NaFormate formation have been consistently observed in NaOBs in literature. Na<sub>2</sub>CO<sub>3</sub> is thought to be formed through a direct reaction of precipitated NaO<sub>2</sub> with the carbon of the cathode,<sup>7, 8, 15</sup> while NaFormate is thought to involve proton abstraction by NaO<sub>2</sub> of the glyme electrolyte, with further degradation of the carbon surface to produce the carboxyl group.<sup>15</sup> Each of these mechanisms are consistent with the observed instability of carbon-based materials in the NaOBs employed in this study. These carbon degradation products form an insulating film

over the cathode surface, impeding charge-transfer as cycle-life increases, ultimately ending in cell death.<sup>15, 39, 51</sup> The confirmation that cell death is eventually caused by the accumulation of carbonaceous degradation products agrees with the model proposed above for the mechanism of cell lifetime elongation in Ti<sub>4</sub>O<sub>7</sub> containing NaOBs, where NaO<sub>2</sub> is formed on both the carbon and Ti<sub>4</sub>O<sub>7</sub> proportionally to the amount of available Ti<sub>4</sub>O<sub>7</sub> surface.

#### 4.3.5 – Discharge Mechanism

The experiments above form a distinct model on how the addition of Ti<sub>4</sub>O<sub>7</sub> to carbon paper cathodes can significantly affect the cycle-life of the NaOB. In the context of previous reports, as discussed in the introduction, and outlined in eqn. 1 and 2, Xia et al. rigorously showed that NaO<sub>2</sub> is formed through a solution-based mechanism on discharge, where NaO<sub>2</sub> nucleates out of solution onto the cathode surface.<sup>11, 12</sup> Similarly, the same publication also proves that charge proceeds through the reverse mechanism where NaO<sub>2</sub> crystallites dissolve into the electrolyte to give Na<sup>+</sup> and O<sub>2</sub><sup>-</sup> substituents, before undergoing the reverse OER.<sup>12</sup> In support of this dissolution mechanism on charge, Lui et al. reported the decomposition of NaO<sub>2</sub> at the crystal surface near the electrolyte on charge, and not at the crystal-cathode interface.<sup>15</sup> The confirmed solution-based, precipitation and dissolution, discharge and charge mechanisms fit well with what has been observed here. We propose the following model for the elongation of NaOB lifetimes by Ti<sub>4</sub>O<sub>7</sub> (**Fig. 4.9**):

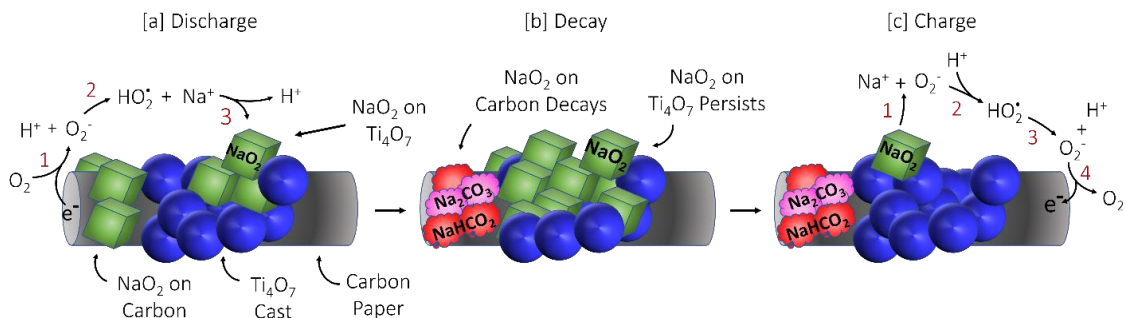


**Figure 4.9.** Proposed schematic on the mechanism by which  $\text{Ti}_4\text{O}_7$  increases cycle-life. [a] Cell discharge;  $\text{O}_2$  is reduced at the carbon surface and  $\text{NaO}_2$  precipitates on both the carbon and  $\text{Ti}_4\text{O}_7$  surfaces via the well-studied solution-based phase transfer catalyst mechanism. [b] Degradation;  $\text{NaO}_2$  in contact with the carbon surface decays. [c] Cell charge;  $\text{NaO}_2$  solvates into solution and  $\text{O}_2^-$  is oxidized at the carbon surface in the reverse phase transfer catalyst mechanism.

When  $\text{Ti}_4\text{O}_7$  is cast on carbon paper, a significant amount of carbon is still accessible to  $\text{O}_2$  in the electrolyte, as a result the highly ORR active carbon surface carries out the bulk of oxygen reduction to produce  $\text{O}_2^-$  in solution.  $\text{O}_2^-$  can then be transported by the  $\text{H}^+$  catalyst to other parts of the cathode where it precipitates either on other carbon surfaces (carbon paper or SuperP), or on the stable  $\text{Ti}_4\text{O}_7$  additive (**Fig. 4.9a**), as visualized by SEM (**Fig. 4.5**).  $\text{NaO}_2$  that precipitates on carbon surfaces will immediately begin to degrade the cathode, while  $\text{NaO}_2$  formed on  $\text{Ti}_4\text{O}_7$  remains stable (**Fig. 4.9b**), as characterized by  $^{23}\text{Na}$  NMR (**Fig. 4.4**). On the charging process,  $\text{NaO}_2$  deposited on conductive  $\text{Ti}_4\text{O}_7$  is dissolved into the electrolyte where the  $\text{H}^+$  catalyst can once again transport  $\text{O}_2^-$  in solution toward the more OER active carbon surface where it can be oxidized into  $\text{O}_2$  (**Fig. 4.9c**), as supported by the discussed dissolution mechanism reported by Xia et al. and Liu et al.<sup>12, 15</sup> Throughout a single cycle the amount of capacity degradation is proportional to the ratio of  $\text{NaO}_2$  formed on  $\text{Ti}_4\text{O}_7$  surfaces to  $\text{NaO}_2$  formed on carbon surfaces. This proportion increases as the proportion of  $\text{Ti}_4\text{O}_7$  in the electrode slurry is increased, resulting in increasing

cycle-lifetimes as the  $\text{Ti}_4\text{O}_7$  wt. % increases, as observed in galvanostatic cycling of NaOB cells (**Fig. 4.2**). Thus,  $\text{Ti}_4\text{O}_7$  significantly increases the stability of the cell without being highly active toward the ORR and OER. This model also predicts that the mechanism of cell death in the 0%- $\text{Ti}_4\text{O}_7$  and 90%- $\text{Ti}_4\text{O}_7$  cells should both relate to the accumulation of  $\text{NaO}_2$  degradation products, such as the observed  $\text{Na}_2\text{CO}_3$  and NaFormate (**Fig. 4.7** and **4.8**), although delayed for the 90%- $\text{Ti}_4\text{O}_7$  cell. Each of the observations from the experiments presented herein reflect this model for the mechanism of capacity enhancement by  $\text{Ti}_4\text{O}_7$  addition to carbon paper cathodes in NaOBs.

#### 4.4 – Conclusions

$\text{Ti}_4\text{O}_7$  was found to significantly increase cell lifetime in limited capacity cycling tests when cast onto carbon paper cathode substrates in NaOB, as compared to cathodes cast with SuperP carbon.  $^{23}\text{Na}$  NMR shows that the primary degradation product after cell death are  $\text{Na}_2\text{CO}_3$  and NaFormate in both the typical carbon-cathode cells and in the lifetime-extended 90%- $\text{Ti}_4\text{O}_7$  cast cathode cells. The discharge chemistry of the 0%- $\text{Ti}_4\text{O}_7$  and 90%- $\text{Ti}_4\text{O}_7$  cells are unaltered. PXRD and  $^{23}\text{Na}$  NMR both identify  $\text{NaO}_2$  as the major discharge product in both 0%- $\text{Ti}_4\text{O}_7$  and 90%- $\text{Ti}_4\text{O}_7$  cast cathodes examined after a single-discharge. The  $\text{Na}_2\text{O}_2 \cdot 2\text{H}_2\text{O}$  product is not identifiable in the  $^{23}\text{Na}$  NMR analysis of either cell. Even though the discharge chemistry is similar,  $\text{NaO}_2$  is shown to degrade to a much lesser degree on the 90%- $\text{Ti}_4\text{O}_7$  cast cathode than on the 0%- $\text{Ti}_4\text{O}_7$  cast cathode. This behaviour was expected from the  $\text{NaO}_2$ - $\text{Ti}_4\text{O}_7$  stability tests and previous reports on the instability of  $\text{NaO}_2$  to

carbon materials. Further, SEM images of discharged cathodes show that  $\text{NaO}_2$  is indeed being formed on the  $\text{Ti}_4\text{O}_7$ -cast surface.

Due to the combination of the increased cell lifetime when  $\text{Ti}_4\text{O}_7$  is cast on the carbon paper, the minimal alteration of the observed discharge chemistry, and the observed enhanced stability of  $\text{NaO}_2$  on the  $\text{Ti}_4\text{O}_7$ -additive cathode, we hypothesise that the high surface area carbon paper fibres themselves are still the main ORR active material on discharge, while the cast  $\text{Ti}_4\text{O}_7$  is acting as a stable nucleation point for  $\text{NaO}_2$  formed in solution. The reduced rate of  $\text{NaO}_2$  degradation when deposited on  $\text{Ti}_4\text{O}_7$  leads to significantly longer cell lifetimes over many cycles.

A natural next step for exploring  $\text{Ti}_4\text{O}_7$  in NaOBs is to replicate the nanosphere synthesis of  $\text{Ti}_4\text{O}_7$ , done by Lee et al. in the context of LiOBs, to see if their observed  $\text{Ti}_4\text{O}_7$  ORR activity translates to the NaOB system.<sup>25</sup> The use of higher surface area  $\text{Ti}_4\text{O}_7$  may also open the door to using alternative cathode substrates such as Ni-foam, removing carbon from the cathode entirely.

## 4.5 – Supporting Information

### 4.5.1 – Further Details on Cathode Manufacturing

All cathodes were prepared with carbon paper substrates of the same diameter, giving each finished cathode has the same circular area,  $0.712 \text{ cm}^2$ . In galvanostatic cycling experiments, areal current densities were used, as is common in NaOB literature.<sup>8, 12, 15, 17, 40, 51</sup> However, gravimetric parameters are still relevant. The amount of active material in each cast varies slightly due to the higher density of  $\text{Ti}_4\text{O}_7$  compared to SuperP carbon. Cast weights vary from 0.7 mg for the 0%- $\text{Ti}_4\text{O}_7$  cast to 0.9 mg for the 90%- $\text{Ti}_4\text{O}_7$  cast. Carbon paper punches weighed 3.0 mg on average,

and since the carbon paper itself is ORR active, the total active masses for each cathode would be 3.7 and 3.9 mg for the 0%-Ti<sub>4</sub>O<sub>7</sub> cathode and 90%-Ti<sub>4</sub>O<sub>7</sub> cathode respectively. This results in gravimetric current densities of 19.3 mA g<sup>-1</sup> for the 0%-Ti<sub>4</sub>O<sub>7</sub> cathode and 18.3 mA g<sup>-1</sup> for the 90%-Ti<sub>4</sub>O<sub>7</sub> cathode, a difference of 5%.

#### 4.5.2 – Details on NMR pulse sequences

All NMR spectra of battery cathodes and reference materials were recorded at a  $B_0 = 132.33$  MHz for <sup>23</sup>Na and at a  $B_0 = 500.25$  MHz for <sup>1</sup>H (both corresponding to a field strength of 11.7 T). All spectra were recorded at spinning speeds of 30 kHz MAS. <sup>23</sup>Na 1D spectra collected used single-pulse experiments. <sup>23</sup>Na pulse lengths were optimized to the NaO<sub>2</sub> signal in the discharged cathode experiments and to the NaOTF signal in the lifetime-cycled cathode experiments (corresponding to 69 kHz (3.6 μs) and 119 kHz (2.1 μs) respectively, at 100 W). The difference in optimal pulse lengths between the two species is due to the low quadrupolar interaction in the cubic NaO<sub>2</sub> product. Delay times of 1 s are used for all recorded spectra. <sup>23</sup>Na chemical shifts are referenced to a 1 M NaCl solution at 0 ppm. All <sup>1</sup>H 1D spectra were collected using a background suppression pulse sequence to remove residual <sup>1</sup>H signal not from the sample. <sup>1</sup>H pulse lengths were optimized to central DEGDME-NaOTF peak in the cathode samples to a bandwidth of 60 kHz (4.167 μs) at 20 W. <sup>123</sup>Na{<sup>1</sup>H} D-HMQC experiment was recorded using the Bruker “hmqcf2” sequence modified to include a pre-saturation pulse train before each scan. SR4 recoupling was used on the <sup>1</sup>H channel with an inversion pulse calibrated to 60 kHz (double the MAS frequency), corresponding to 8.33 μs at 28.84 W, and the recoupling time was optimized to 600 μs. <sup>1</sup>H excitation pulses of 91 kHz bandwidth (2.75 μs at 50 W) were used, as well as <sup>23</sup>Na excitation pulses of 54 kHz bandwidth (4.65 μs at 11.56 W). Cathode spectra

were collected using 5120 direct scans in 80 indirect slices. These parameters were calibrated on  $\text{NaH}_2(\text{PO}_4)$ , the corresponding spectra of which are showed in **Fig.**

#### 4.15S.4.5.3 – $\text{NaO}_2$ Synthesis and Reaction Test

$\text{NaO}_2$  was synthesised as described previously by our group.<sup>7</sup> Ammonia was condensed in a round bottom flask over a dry-ice/acetone bath in a Ar flowing atmosphere.  $\text{O}_2$  gas was then rapidly bubbled through the condensed  $\text{NH}_3$  for approximately 10 minutes to ensure a saturated  $\text{O}_2$  environment (note: glass pipettes are used as the “needle” for all gas addition through septum, use of typical steel needles results in Fe containing side products in the final mixture). Na metal was then added to the flask in small increments, ensuring at all dissolved Na was consumed by  $\text{O}_2$  before adding additional metal (which is easily observed by the disappearance of the characteristic blue colour). We have noticed that if Na is not kept limiting in the reaction,  $\text{Na}_2\text{O}_2$  is formed preferentially over  $\text{NaO}_2$ . After the reaction is complete, the dry ice is removed and  $\text{NH}_3$  is allowed to evaporate freely through an Ar atmosphere oil bubbler. The remaining  $\text{NaO}_2$  product is then dried under vacuum and is stored in the Ar glovebox.

The reactivity of  $\text{Ti}_4\text{O}_7$  toward the synthesized  $\text{NaO}_2$  was evaluated by grinding a mixture of the two in a ceramic mortar and pestle in the Ar glovebox before packing the resulting mixture in a 1.9 mm NMR rotor for characterization by NMR. The  $^{23}\text{Na}$  spectra of both  $\text{NaO}_2$  and the reaction  $\text{NaO}_2 / \text{Ti}_4\text{O}_7$  mixture was recorded at a  $B_0 = 224.88$  MHz (corresponding to a field strength of 19.9 T). The sample was spun at 20 kHz MAS and nuclei were excited using a 2  $\mu\text{s}$  pulse at 45 W, using delay time of 1 s. The reaction mixture was allowed to age in the sealed rotor while being spun over  $\text{N}_2$  gas to ensure no moisture contamination.

#### 4.5.4 – Ti<sub>4</sub>O<sub>7</sub> on Ni Foam Tests

Ti<sub>4</sub>O<sub>7</sub> on Ni foam cathodes were made by washing Ni Foam with concentrated H<sub>2</sub>SO<sub>4</sub> to remove any passivating NiO before dip casting the Ni-Foam in cathode slurries comprised of 90% Ti<sub>4</sub>O<sub>7</sub> and 10% NaCMC binder. Active material loading on Ni foam cathodes ranged from 0.1 to 0.3 mg. Ni foam cathodes were tested in Swagelok style cells fabricated the same manner described in the experimental for cells with the Ti<sub>4</sub>O<sub>7</sub> on carbon paper cathodes (**Fig. 4.11S**). The similarity between the inherent capacity of bare Ni foam and the Ti<sub>4</sub>O<sub>7</sub>-coated Ni foam raises a possible issue in metal-oxygen battery literature. Active material loadings when using metal substrates such as Ni foam are often on the order of 0.1 mg. This can lead to significantly inflated gravimetric capacity values when the Ni foam itself has significant intrinsic capacity. For example, the Ni foam substrate was responsible for 88% of the capacity of the cell in the above example, however if stated in gravimetric terms the Ti<sub>4</sub>O<sub>7</sub>-coated Ni foam cathode reached a modest capacity of approximately 200 mAh g<sup>-1</sup>.

#### 4.5.5 – Additional Figures

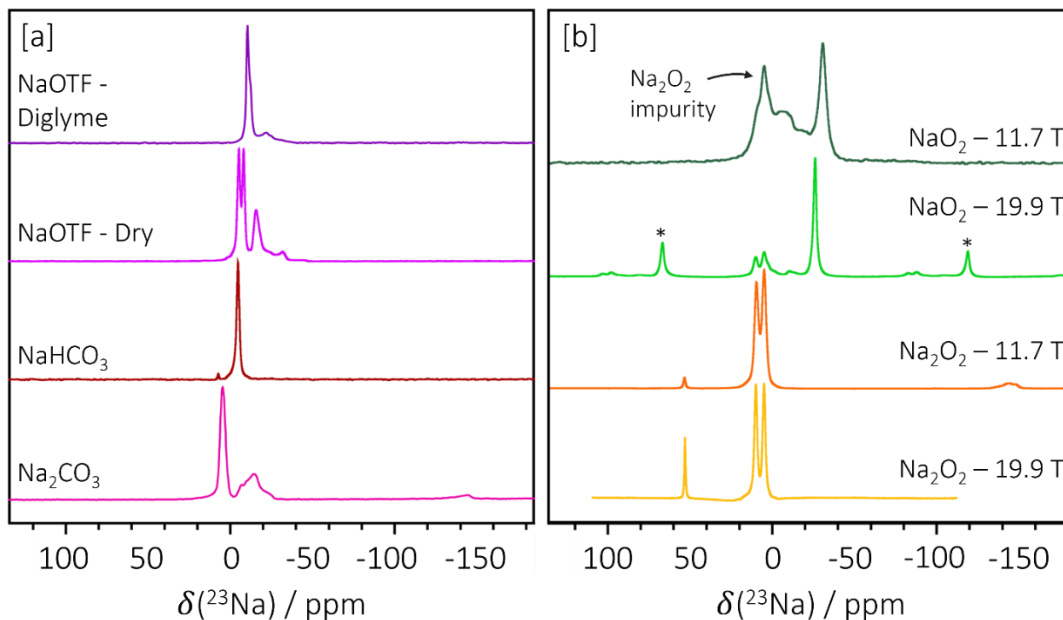


**Figure 4.10S.**  $^{23}\text{Na}$  reference spectra of various Na-containing species expected to form in NaOBs. Spectra in [a] include:  $\text{Na}_2\text{CO}_3$ , NaBicarbonate, Dry NaOTF, and NaOTF in Diglyme electrolyte vacuum dried in the same manner that cycled electrodes are treated. Spectra in [b] include commercial  $\text{Na}_2\text{O}_2$  collected on a 19.9 T NMR spectrometer,  $\text{Na}_2\text{O}_2$  collected on a 11.7 T NMR spectrometer, synthesised  $\text{NaO}_2$  collected on a 19.9 NMR spectrometer, and synthesised  $\text{NaO}_2$  collected on a 11.7 T NMR spectrometer. The  $\text{NaO}_2$  peak shifts between field strengths while the  $\text{Na}_2\text{O}_2$  impurity resonance is static.

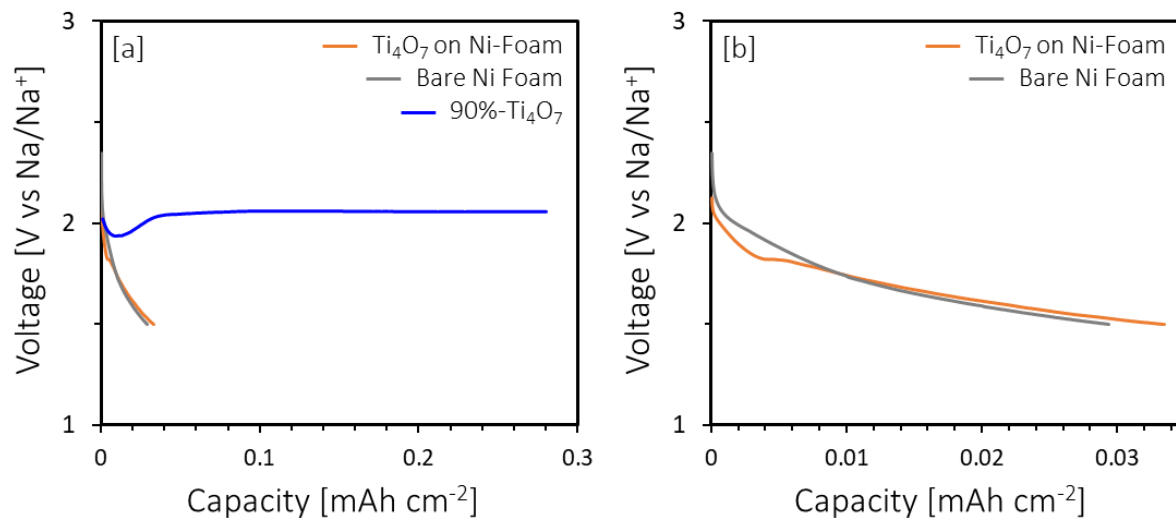


**Figure 4.11S.** [a] The first discharge capacity of NaOBs made with cathodes comprised of Ti<sub>4</sub>O<sub>7</sub> on Ni foam, Bare Ni foam, and 90%-Ti<sub>4</sub>O<sub>7</sub> on carbon paper. [b] The same plot of just the Ti<sub>4</sub>O<sub>7</sub> on Ni foam and Bare Ni foam cells, zoomed in to the low-capacity region. The 90%-Ti<sub>4</sub>O<sub>7</sub> cell is cycled with a current density of 0.1 mA cm<sup>-2</sup>, while the two Ni-foam cells were cycled with a current density of 0.01 mA cm<sup>-2</sup>.

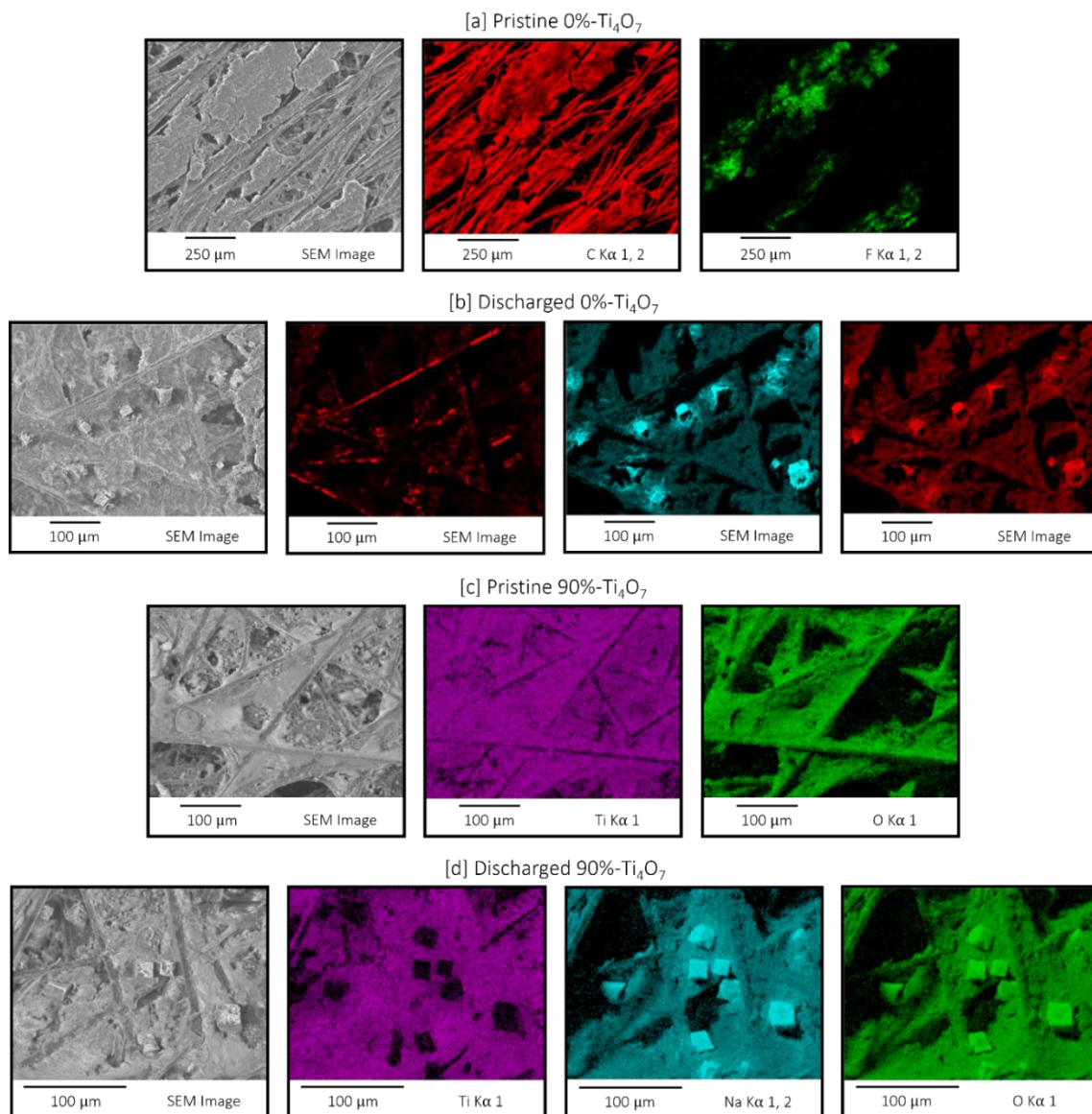


**Figure 4.12S.** SEM and corresponding EDS images of [a] Pristine 0%-Ti<sub>4</sub>O<sub>7</sub>, [b] Discharged 0%-Ti<sub>4</sub>O<sub>7</sub>, [c] Pristine 90%-Ti<sub>4</sub>O<sub>7</sub>, and [d] Discharged 90%-Ti<sub>4</sub>O<sub>7</sub>.

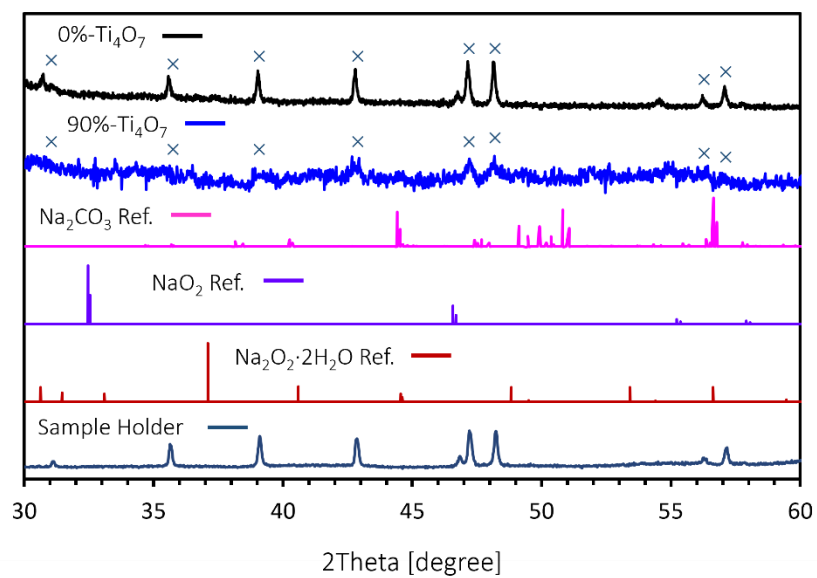


**Figure 4.13S.** PXRD powder patterns of lifetime-cycled 0%-Ti<sub>4</sub>O<sub>7</sub> and 90%-Ti<sub>4</sub>O<sub>7</sub> cathodes. As well as relevant reference patterns.

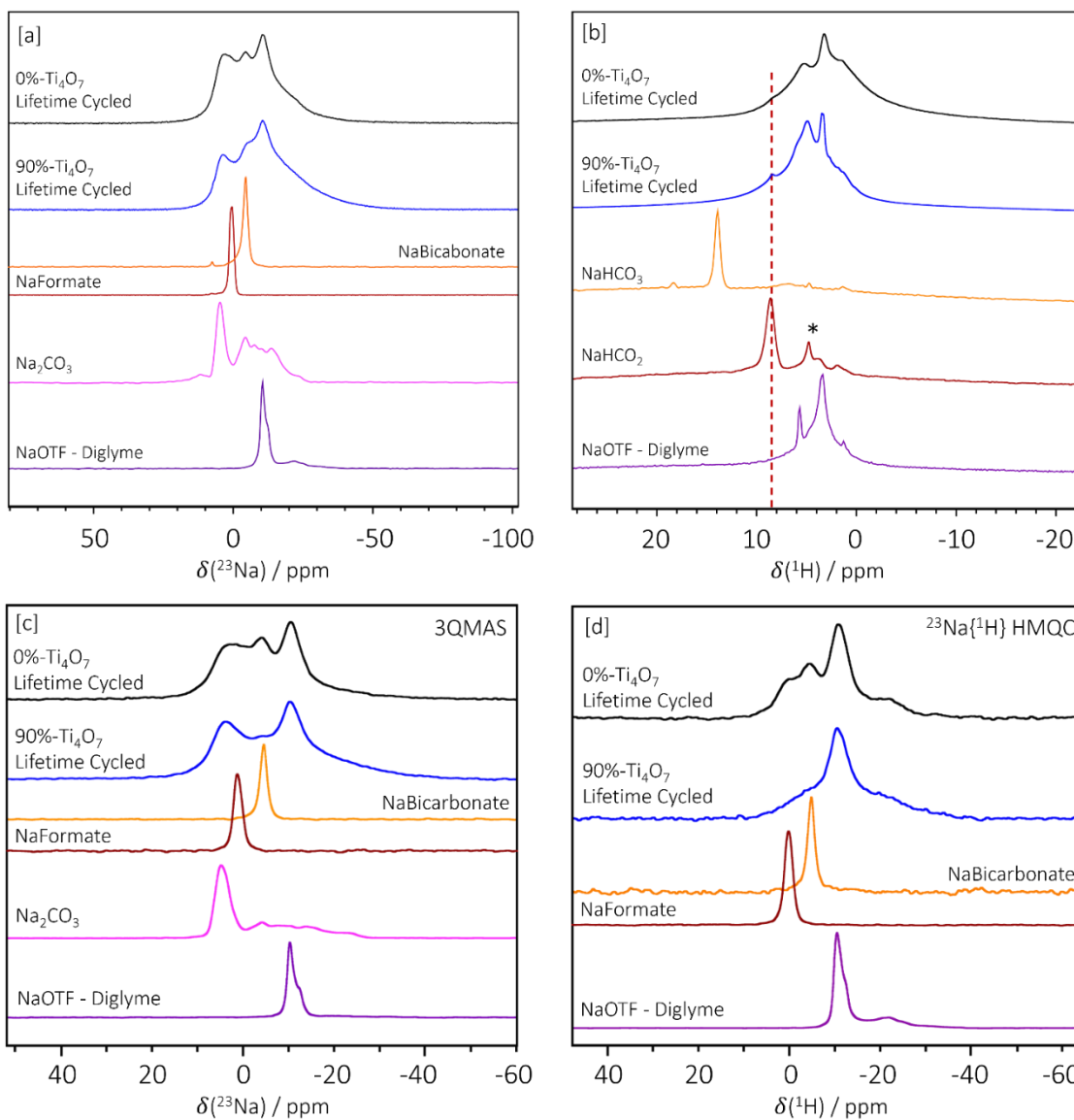


**Figure 4.14S.** [a-b] 1D <sup>23</sup>Na NMR spectra of the 0%-Ti<sub>4</sub>O<sub>7</sub> and 90%-Ti<sub>4</sub>O<sub>7</sub> cathodes with reference spectra. [c] 1D 3QMAS spectra of both the 0%-Ti<sub>4</sub>O<sub>7</sub> and 90%-Ti<sub>4</sub>O<sub>7</sub> cathodes, as well as corresponding reference compounds. [d] 1D <sup>23</sup>Na{<sup>1</sup>H} DHMQC spectra of both the 0%-Ti<sub>4</sub>O<sub>7</sub> and 90%-Ti<sub>4</sub>O<sub>7</sub> cathodes as well as corresponding reference compounds.

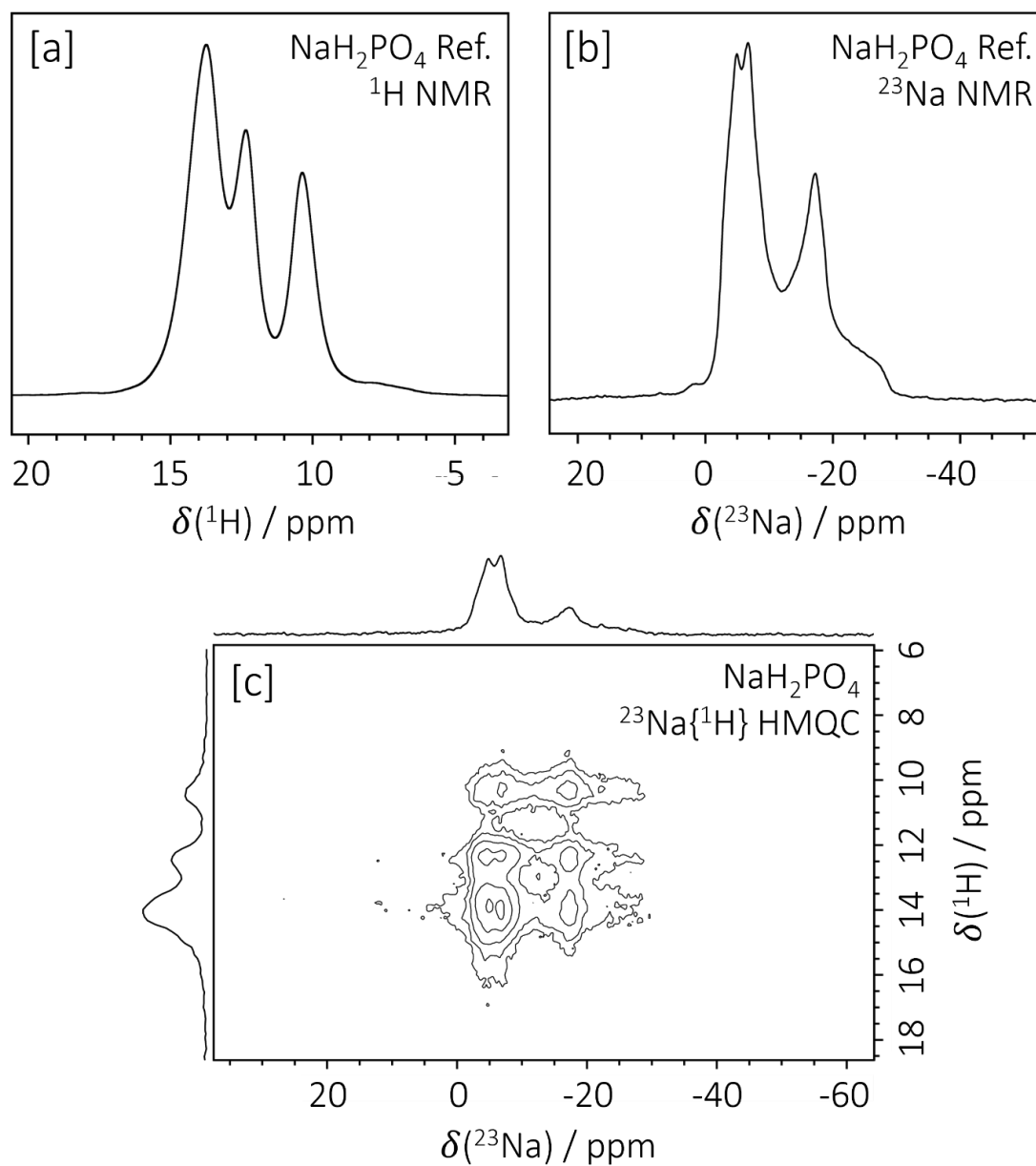


**Figure 4.15S.** Reference [a]  $^1\text{H}$ , [b]  $^{23}\text{Na}$ , and [c]  $^{23}\text{Na}\{^1\text{H}\}$  DHMQC spectra of  $\text{NaH}_2\text{PO}_4$ .

## 4.6 – References

1. Wu, M.; Chen, W. *Sustainability* **2022**, *14* (4), 2206-2219. DOI: 10.3390/su14042206
2. Das, P. K.; Bhat, M. Y. *Environ. Sci. Pollut. Res. Int.* **2022**, *29*, 40612–40622. DOI: 10.1007/s11356-021-18211-w
3. IEA, World Energy Outlook 2016. IEA, Ed. IEA: Paris, 2016.
4. IEA, World Energy Outlook 2021. IEA, Ed. IEA: Paris, 2021.
5. Hartmann, P.; Bender, C. L.; Sann, J.; Durr, A. K.; Jansen, M.; Janek, J.; Adelhelm, P. *Phys. Chem. Chem. Phys.* **2013**, *15* (28), 11661-11672. DOI: 10.1039/c3cp50930c
6. Hirsh, H. S.; Li, Y.; Tan, D. H. S.; Zhang, M.; Zhao, E.; Meng, Y. S. *Advanced Energy Materials* **2020**, *10* (32), DOI: 10.1002/aenm.202001274
7. Reeve, Z. E.; Franko, C. J.; Harris, K. J.; Yadegari, H.; Sun, X.; Goward, G. R. *J. Am. Chem. Soc.* **2017**, *139* (2), 595-598. DOI: 10.1021/jacs.6b11333
8. Yadegari, H.; Franko, C. J.; Banis, M. N.; Sun, Q.; Li, R.; Goward, G. R.; Sun, X. *J. Phys. Chem. Lett.* **2017**, *8* (19), 4794-4800. DOI: 10.1021/acs.jpcclett.7b02227
9. Hartmann, P.; Bender, C. L.; Vracar, M.; Durr, A. K.; Garsuch, A.; Janek, J.; Adelhelm, P. *Nature Materials* **2013**, *12* (3), 228-232. DOI: 10.1038/nmat3486
10. Kim, J.; Lim, H. D.; Gwon, H.; Kang, K. *Phys. Chem. Chem. Phys.* **2013**, *15* (10), 3623-3629. DOI: 10.1039/c3cp43225d
11. Xia, C.; Black, R.; Fernandes, R.; Adams, B.; Nazar, L. F. *Nat. Chem.* **2015**, *7* (6), 496-501. DOI: 10.1038/nchem.2260
12. Xia, C.; Fernandes, R.; Cho, F. H.; Sudhakar, N.; Buonacorsi, B.; Walker, S.; Xu, M.; Baugh, J.; Nazar, L. F. *J. Am. Chem. Soc.* **2016**, *138* (35), 11219-11226. DOI: 10.1021/jacs.6b05382
13. McCloskey, B. D.; Speidel, A.; Scheffler, R.; Miller, D. C.; Viswanathan, V.; Hummelshoj, J. S.; Norskov, J. K.; Luntz, A. C. *J. Phys. Chem. Lett.* **2012**, *3* (8), 997-1001. DOI: 10.1021/jz300243r
14. Bender, C. L.; Hartmann, P.; Vracar, M.; Adelhelm, P.; Janek, J. *Advanced Energy Materials* **2014**, *4* (12), 1301863. DOI: 10.1002/aenm.201301863
15. Liu, T.; Kim, G.; Casford, M. T.; Grey, C. P. *J. Phys. Chem. Lett.* **2016**, *7* (23), 4841-4846. DOI: 10.1021/acs.jpcclett.6b02267
16. Zhao, N.; Li, C.; Guo, X. *Phys. Chem. Chem. Phys.* **2014**, *16* (29), 15646-15652. DOI: 10.1039/c4cp01961j
17. Kang, J.-H.; Kwak, W.-J.; Aurbach, D.; Sun, Y.-K. *Journal of Materials Chemistry A* **2017**, *5* (39), 20678-20686. DOI: 10.1039/c7ta06584a
18. Zhang, S.; Wen, Z.; Rui, K.; Shen, C.; Lu, Y.; Yang, J. *Journal of Materials Chemistry A* **2015**, *3* (6), 2568-2571. DOI: 10.1039/c4ta05427j
19. Hu, Y.; Han, X.; Zhao, Q.; Du, J.; Cheng, F.; Chen, J. *Journal of Materials Chemistry A* **2015**, *3* (7), 3320-3324. DOI: 10.1039/C4TA06287F
20. Ioroi, T.; Senoh, H.; Yamazaki, S.-i.; Siroma, Z.; Fujiwara, N.; Yasuda, K. *J. Electrochem. Soc.* **2008**, *155* (4), B321-B326. DOI: 10.1149/1.2833310
21. Le Canut, J.-M.; Abouatallah, R. M.; Harrington, D. A. *Journal of The Electrochemical Society* **2006**, *153* (5), A857. DOI: 10.1149/1.2179200
22. Bartholomew, R. F.; Frankl, D. R. *Physical Review* **1969**, *187* (3), 828-833. DOI: 10.1103/PhysRev.187.828
23. Szot, K.; Rogala, M.; Speier, W.; Klusek, Z.; Besmehn, A.; Waser, R. *Nanotechnology* **2011**, *22* (25), 254001. DOI: 10.1088/0957-4484/22/25/254001

24. Li, X.; Zhu, A. L.; Qu, W.; Wang, H.; Hui, R.; Zhang, L.; Zhang, J. *Electrochimica Acta* **2010**, *55* (20), 5891-5898. DOI: 10.1016/j.electacta.2010.05.041
25. Lee, S.; Lee, G.-H.; Kim, J.-C.; Kim, D.-W. *ACS Catalysis* **2018**, *8* (3), 2601-2610. DOI: 10.1021/acscatal.7b03741
26. Laoire, C. O.; Mukerjee, S.; Abraham, K. M. *J. Phys. Chem. C* **2009**, *113* (46), 20127–20134. DOI: 10.1021/jp908090s
27. Black, R.; Oh, S. H.; Lee, J. H.; Yim, T.; Adams, B.; Nazar, L. F. *J. Am. Chem. Soc.* **2012**, *134* (6), 2902–2905. DOI: 10.1021/ja2111543
28. Leskes, M.; Moore, A. J.; Goward, G. R.; Grey, C. P. *The Journal of Physical Chemistry C* **2013**, *117* (51), 26929-26939. DOI: 10.1021/jp410429k
29. Frydman, L.; Harwood, J. S. *J. Am. Chem. Soc.* **1995**, *117* (19), 5367–5368. DOI: 10.1021/ja00124a023
30. Medek, A.; Harwood, J. S.; Frydman, L. *J. Am. Chem. Soc.* **1995**, *117* (51), 12779–12787. DOI: 10.1021/ja00156a015
31. Amoureux, J.-P.; Fernandez, C.; Frydman, L. *Chemical Physical Letters* **1996**, *259* (3-4), 347-355. DOI: 10.1016/0009-2614(96)00809-3
32. Lafon, O.; Wang, Q.; Hu, B.; Vasconcelos, F.; Tre' bosc, J.; Cristol, S.; Deng, F.; Amoureux, J.-P. *J. Phys. Chem. A* **2009**, *113* (46), 12864–12878. DOI: 10.1021/jp906099k
33. Bechger, L.; Koenderink, A. F.; Vos, W. L. *Langmuir* **2002**, *18* (6), 2444–2447. DOI: 10.1021/la011485n
34. Park, O. K.; Kang, Y. S. *Colloids and Surfaces A: Physicochemical and Engineering Aspects* **2005**, *257-258*, 261-265. DOI: 10.1016/j.colsurfa.2004.10.014
35. Jaroenworarluck, A.; Sunsaneeyametha, W.; Kosachan, N.; Stevens, R. *Surface and Interface Analysis* **2006**, *38* (4), 473-477. DOI: 10.1002/sia.2313
36. Furusawa, T.; Honda, K.; Ukaji, E.; Sato, M.; Suzuki, N. *Materials Research Bulletin* **2008**, *43* (4), 946-957. DOI: 10.1016/j.materresbull.2007.04.031
37. Resende, S. F.; Nunes, E. H. M.; Houmard, M.; Vasconcelos, W. L. *J. Colloid Interface Sci.* **2014**, *433*, 211-217. DOI: 10.1016/j.jcis.2014.06.033
38. Schwenke, K. U.; Meini, S.; Wu, X.; Gasteiger, H. A.; Piana, M. *Phys. Chem. Chem. Phys.* **2013**, *15* (28), 11830-9. DOI: 10.1039/c3cp51531a
39. Black, R.; Shyamsunder, A.; Adeli, P.; Kundu, D.; Murphy, G. K.; Nazar, L. F. *ChemSusChem* **2016**, *9* (14), 1795-1803. DOI: 10.1002/cssc.201600034
40. Landa-Medrano, I.; Pinedo, R.; Bi, X.; Ruiz de Larramendi, I.; Lezama, L.; Janek, J.; Amine, K.; Lu, J.; Rojo, T. *ACS Appl Mater Interfaces* **2016**, *8* (31), 20120-20127. DOI: 10.1021/acsami.6b06577
41. Kim, J.; Park, H.; Lee, B.; Seong, W. M.; Lim, H. D.; Bae, Y.; Kim, H.; Kim, W. K.; Ryu, K. H.; Kang, K. *Nature Communications* **2016**, *7*, 10670-10678. DOI: 10.1038/ncomms10670
42. Huang, Z.-F.; Wang, J.; Peng, Y.; Jung, C.-Y.; Fisher, A.; Wang, X. *Advanced Energy Materials* **2017**, *7* (23), 1700544. DOI: 10.1002/aenm.201700544
43. Jian, Z.; Chen, Y.; Li, F.; Zhang, T.; Liu, C.; Zhou, H. *Journal of Power Sources* **2014**, *251*, 466-469. DOI: 10.1016/j.jpowsour.2013.11.091
44. Elia, G. A.; Hasa, I.; Hassoun, J. *Electrochimica Acta* **2016**, *191*, 516-520. DOI: 10.1016/j.electacta.2016.01.062
45. Bender, C. L.; Jache, B.; Adelhelm, P.; Janek, J. *Journal of Materials Chemistry A* **2015**, *3* (41), 20633-20641. DOI: 10.1039/c5ta06640a
46. Ortiz-Vitoriano, N.; Batcho, T. P.; Kwabi, D. G.; Han, B.; Pour, N.; Yao, K. P.; Thompson, C. V.; Shao-Horn, Y. *J Phys Chem Lett* **2015**, *6* (13), 2636-43. DOI: 10.1021/acs.jpcclett.5b00919

47. Mason, H. E.; Kozłowski, A.; Phillips, B. L. *Chem. Mater.* **2008**, *20* (1), 294–302. DOI: 10.1021/cm0716598
48. Wu, S.; Qiao, Y.; Jiang, K.; He, Y.; Guo, S.; Zhou, H. *Advanced Functional Materials* **2018**, *28* (13), 1706374. DOI: 10.1002/adfm.201706374
49. He, M.; Lau, K. C.; Ren, X.; Xiao, N.; McCulloch, W. D.; Curtiss, L. A.; Wu, Y. *Angew. Chem. Int. Ed.* **2016**, *55*, 15310–15314. DOI: 10.1002/anie.201608607
50. Frydman, L., Fundamentals of Multiple-Quantum Magic-Angle Spinning NMR on Half-Integer Quadrupolar Nuclei. In *Encyclopedia of Nuclear Magnetic Resonance*, Grant, D. M.; Harris, R. K., Eds. John Wiley & Sons: Chichester, 2002; Vol. 9, pp 262–274.
51. Yadegari, H.; Banis, M. N.; Xiao, B.; Sun, Q.; Li, X.; Lushington, A.; Wang, B.; Li, R.; Sham, T.-K.; Cui, X.; Sun, X. *Chemistry of Materials* **2015**, *27* (8), 3040–3047. DOI: 10.1021/acs.chemmater.5b00435

## 5 – Concentration Dependent Solution Structure and Transport Mechanism in High Voltage LiTFSI – Adiponitrile Electrolytes

This chapter is a reformatted version of an article that has been previously published in the *Journal of the Electrochemical Society* (Franko, C. J., Yim C., Årén F., Åvall G., Whitfield P. S., Johansson P., Abu-Lebdeh Y. A., Goward G. R., *J. Electrochem. Soc.* **2017**, 167 160532, adapted with permission by the *Journal of the Electrochemical Society* © 2020 IOP Publishing). The author was responsible for electrolyte preparation, pulsed field gradient (PFG) NMR experiments, all electrochemical characterizations, and preparation of the manuscript. Differential scanning calorimetry (DSC) data collection was done by Abu-Lebdeh Y. A. and Yim C., x-ray diffraction data was collected by Whitfield P. S, and radial distribution functions were simulated by Årén F., Åvall G., and Johansson P.

In this Chapter, the physiochemical properties of lithium bis(trifluoromethanesulfonyl)imide (LiTFSI) in adiponitrile (ADN) electrolytes are explored as a function of concentration. The phase diagram and ionic conductivity plots show a distinct relationship between the eutectic composition of the electrolyte and the concentration of maximum ionic conductivity in the 25 °C isotherm. A structure-based explanation for the variation of electrolyte ionic conductivity with LiTFSI concentration is proposed, where the eutectic concentration is a transitional region at which the solution structure changes from solvated contact ion pairs to extended units of  $[\text{Li}_z(\text{ADN})_x\text{TFSI}_y]^{z-y}$  aggregates. It is found through diffusion coefficient measurements using PFG NMR that relative  $\text{Li}^+$  diffusion coefficients

( $D_{Li}/D_{TFSI}$  and  $D_{Li}/D_{ADN}$ ) increase with concentration until 2.9 M, where  $Li^+$  becomes the fastest diffusing species, suggesting that ion hopping becomes the dominant transport mechanism for  $Li^+$ . A differentiation in  $Li^+$  transport between the micro and bulk levels that increases with concentration is observed. It is proposed that ion hopping within  $[Li_z(ADN)_xTFSI_y]^{z-y}$  aggregates dominates the micro-scale, while the bulk-scale is governed by vehicular transport. Lastly, it is found that LiTFSI in ADN is a suitable electrolyte system for use in Li-O<sub>2</sub> cells.

## 5.1 – Introduction

A crucial component to the development of higher energy density Li-ion batteries is the production of cells that can operate stably at higher voltages. This is principally achieved through the use of high voltage cathode materials such as the spinel structured  $LiMn_{1.5}Ni_{0.5}O_4$  (LMNO) which deintercalates  $Li^+$  uniformly at 4.7 V, a substantial increase from the commonly used  $LiNi_{1/3}Mn_{1/3}Co_{1/3}O_2$  (LiNMC), which operates at an average voltage of 3.75 V.<sup>1-3</sup> However, this significant increase in voltage results in additional oxidative stress on the liquid electrolyte. Typical carbonate-based electrolyte systems (composed primarily of lithium hexafluorophosphate ( $LiPF_6$ ) salt in ethylene carbonate (EC), dimethyl carbonate (DMC), and diethyl carbonate (DEC) solvents) will decompose above 4.5 V, leaving the 4.7 V voltage plateau of LMNO unachievable.<sup>4, 5</sup>

A possible oxidatively stable alternative to the currently used carbonate solvents is adiponitrile (ADN). Electrolytes composed of lithium bis(trifluoromethanesulfonyl)imide (LiTFSI) in ADN solvent have been shown to resist oxidation beyond 6 V ( $Li/Li^+$ ) in previous studies.<sup>6, 7</sup> In addition to offering a

high voltage stability window, ADN also displays a high thermal stability. The boiling and flash points of ADN are 295 and 163 °C, respectively, alleviating some of the safety concerns prevalent in the aforementioned flammable carbonate solvents used in current Li-ion cells. Further, LiTFSI salt is highly resistant to hydrolysis, a common issue for LiPF<sub>6</sub> salt that affects both the safety and lifetime of the cell.<sup>8</sup>

Even with these enhanced thermal and chemical properties, LiTFSI in ADN has been seldom studied for use in Li-ion batteries. Abu-Lebdeh et al. used 1 M LiTFSI in ADN in graphite (Gr) || LiCoO<sub>2</sub> (LCO) full cells and found that cell capacity degrades rapidly with cycle number as ADN is unable to form a stable solid electrolyte interphase (SEI) on the carbon anode at the low voltage required for Li<sup>+</sup> intercalation.<sup>7</sup> Further studies have used electrolyte additives in an attempt to facilitate stable SEI production. Both vinylene carbonate (VC) and fluoroethylene carbonate (FEC) have been shown to be effective additives in relatively low concentrations at forming fluorine containing stable SEIs at graphite. However, this has only been shown to produce long cycle life batteries with the further addition of a second salt component such as lithium tetrafluoroborate (LiBF<sub>4</sub>), lithium difluoro(oxalato)borate (LiDFOB), or lithium bis(oxalato)borate (LiBOB).<sup>7, 9, 10</sup> This is attributed to the instability of LiTFSI toward the aluminum current collector of the positive electrode. The decomposition of the co-salt provides a passivating layer that protects from long term aluminum corrosion.<sup>11</sup> It has also been suggested that the co-salt may help form a stable SEI on the graphite electrode.<sup>7</sup> At the high voltage LMNO electrode, other carbonate co-solvents such as EC and DMC encourage stable cathode electrolyte interfaces on the LMNO surface, however this has only been shown in LiTFSI-free binary salt formulations.<sup>12</sup>

Notably, these studies have all used ADN in electrolyte formulations at a concentration of approximately 1 M, as this is the approximate concentration of maximum ionic conductivity ( $C_{\max}$ ) for most organic electrolytes. For other electrolyte formulations, the effects of concentrating electrolytes far past this typical 1 M standard composition has been explored as a possible alternative to complicated electrolyte formulations.<sup>13-24</sup> Imide-based lithium salts such as the similarly structured LiTFSI, lithium bis(fluorosulfonyl)imide (LiFSI), and lithium bis(perfluoroethylsulfonyl)imide (LiBETI) are most often used to prepare these super-concentrated solutions due to their low lattice energies, and correspondingly high solubilities, that let these highly concentrated solutions form.<sup>13, 15</sup> This relatively new class of liquid electrolytes has already been shown to successfully suppress dendrite growth when employing high power-density lithium metal anodes,<sup>14, 15, 19</sup> to significantly improve charging rates within graphite anodes,<sup>16, 17, 24</sup> and to facilitate the formation of stable SEI layers in non-EC-based solvents.<sup>13, 16-18, 20, 23</sup>

The surprising appearance of these desirable attributes has led to investigations of the chemical mechanisms behind the improved electrochemical performance.<sup>24-26</sup> Classical electrolyte theory predicts full solvation of the salt component of the electrolyte, with the solvent forming a full four-coordinate solvation sphere around the Li cation in a matrix of uncoordinated free solvent molecules. This, however, is only applicable to dilute concentrations. As concentrations increase, the lowering stoichiometric ratio of solvent causes weaker solvation of the salt, and contact ion pairs (CIP) form where the anion is more closely coordinated to the Li cation.<sup>26</sup> It has been suggested that as salt concentrations reach their saturation point, larger cation-anion-solvent aggregate structures (of the form  $[\text{Li}^+_x(\text{An}^-)_y(\text{Sol})_z]^{x-y}$ ) are present in

solution.<sup>24, 26</sup> Dokko et al. studied the transport behaviour of these theorized aggregate structures in concentrated LiBF<sub>4</sub>-sulfolane electrolytes using pulsed field gradient (PFG) NMR spectroscopy.<sup>24</sup> It was shown that at high concentrations, the Li<sup>+</sup> cation diffuses faster than either the anion or solvent molecules, suggesting a shift in transport from the classical vehicular mechanism to an ion hopping mechanism.

The use of diffusion spectroscopy by Dokko et al. to study the local transport of individual components adds insight toward the effect of structure on ionic conductivity across the concentration range of the electrolyte. The sharp decrease of conductivity observed after C<sub>max</sub> is typically attributed to a drastic increase in dynamic viscosity. Recent studies have challenged this by exploring the relationship between the solution structure of the electrolyte and its ionic conductivity, primarily through ionic conductivity measurements and phase diagram construction.<sup>25, 27</sup> Findings suggest a new empirical model where the conductivity variations as function of concentration are a result of both structural changes in solution and viscosity, as opposed to just viscosity alone.

This investigation expands on the idea that ionic conductivity is highly dependant on the concentration-variable solution structure of the electrolyte through a physical study of electrolytes composed of LiTFSI salt in ADN solvent. A distinct relationship between the eutectic point and the C<sub>max</sub> of the electrolyte is observed, adding support to a structure-based conductivity model. At high concentrations, measurement of diffusion coefficients show conduction is occurring via Li<sup>+</sup> hopping. Variable diffusion time ( $\Delta$ ) PFG-NMR is used to further quantify the level of aggregate formation across the concentration range through the heterogeneity of Li<sup>+</sup> diffusion between the micro- and bulk-level length scales. This type of variable- $\Delta$  diffusional analysis has never

previously been applied to Li-salt electrolytes and allows for greater insight into the short-range ordered structures present in electrolyte solutions.

## 5.2 – Experimental

### 5.2.1 – Electrolyte Preparation

LiTFSI (99.9 %) was purchased from Solvionic (France) and used as received. ADN (99%) was purchased from Millipore Sigma and was purified using a freeze pump thaw method before being stored over 3 Å molecular sieves in an argon-filled glovebox with O<sub>2</sub> and H<sub>2</sub>O concentrations less than 0.1 and 2.0 ppm respectively. Electrolytes were mixed in said glovebox in glass vials with gentle heating for the high concentration samples. Samples were prepared according to molar ratio, and molarities displayed are calculated without volume correction.

### 5.2.2 – Electrolyte Preparation

Ionic conductivity measurements were carried out using AC impedance spectroscopy. The electrolyte was poured into a two-platinum-electrode conductivity cell ( $K = 1 \text{ cm}^{-1}$ ). The frequency range was 1 kHz – 1 Hz swept using a Solartron frequency response analyzer (FRA) 1255B coupled with a Princeton Applied Research (PAR) 263A potentiostat.

Cyclic voltammetry was carried out inside an Ar-filled glovebox with platinum wire used as both the counter and working electrodes. Lithium metal was used as the reference electrode and was constructed by compressing a clean piece of lithium metal through a 1 mL syringe with a copper wire, so that only the bare Li surface is in contact

with the electrolyte. Voltage limits of 6.5 V and -0.2 V were used, with a sweep rate of 10 mV s<sup>-1</sup> and a step size of 2 mV.

Li-O<sub>2</sub> cells were made in a coin cell geometry. Lithium metal rolled onto a stainless-steel current collector was used as the negative electrode, while a carbon paper gas diffusion layer was used as the positive electrode, with a stainless-steel mesh current collector. Celgard 3501 was used as the separator. 40 and 60 uL of electrolyte was added in-between the anode and separator and separator and cathode respectively. A final 20 uL was added on top of the carbon cathode. Coin cell lids were modified with drilled holes to allow for the diffusion of oxygen gas. Cells were crimped inside the glovebox and sealed in airtight chambers, before being brought out of the glovebox to be charged with O<sub>2</sub> gas (Praxair, 4.5 purity). Cells were allowed to rest for a minimum of 2 hours before starting CV measurements to allow for sufficient O<sub>2</sub> dissolution. CVs were run with the Li metal as a dual counter/reference electrode, and the carbon paper as the working electrode. Scan rates of 50 mV s<sup>-1</sup> and a step size of 10 mV were used, with voltage limits of 1.5 and 4.5 V.

### 5.2.3 – Low Temperature XRD measurement of LiTFSI-ADN solutions

For the X-ray diffraction studies, samples were prepared by mixing ADN with the required amount of LiTFSI salt and then the solution was injected into 1 mm capillaries containing ground quartz glass in an Argon-filled glove box and then sealed with wax. Data collected on Bruker D8 with focussing mirror and Vantec PSD. Custom-built, 90° short-nozzle cryoflow system used to control temperature. Samples tended to supercool on quenching so rapid heating to ~20K below melting was used to crystallize them. The cryoflow temperature was calibrated using the thermal

expansion of aluminum metal. Diffractograms were taken at 5 °C intervals from -175 °C until significantly above the melting temperature.

#### 5.2.4 – NMR Spectroscopy

All NMR measurements were done on a Bruker Widebore 300 MHz Avance III spectrometer using a Diff50 gradient probe with a dual resonance 8 mm  $^7\text{Li} / ^{19}\text{F}$  RF insert for  $^7\text{Li}$  and  $^{19}\text{F}$  measurements, and single resonance  $^1\text{H}$  insert for  $^1\text{H}$  measurements. Diffusions coefficients were measured using a bipolar stimulated echo method with diffusion times ranging from 10 to 500 ms for the variable  $\Delta$  dataset. All measurements for the diffusion ratio datasets are from data at a  $\Delta = 500$  ms.

### 5.3 – Results and Discussion

#### 5.3.1 – Conductivity - Phase Diagram Relationship

The measured room temperature ionic conductivity ( $\kappa$ ) and phase diagram of LiTFSI in ADN electrolytes as a function of concentration are shown in **Fig. 5.1a** and **5.1b** respectively. In the dilute stages, ionic conductivity increases rapidly with increasing salt concentration due to a higher density of charge carriers in solution. As concentrations increase further, conductivity plateaus to  $C_{max}$  ( $\approx 0.8$  M), at 2.3 mS  $\text{cm}^{-1}$ , before sharply dropping. Eventually, at the highest concentrated 2.9 M sample,  $\kappa$  begins to level off toward a minimum value of 0.5 mS  $\text{cm}^{-1}$ . Farhat et al. have also studied the conductivity of LiTFSI-ADN solutions and showed a similar trend in conductivity values, reaching 2.3 mS  $\text{cm}^{-1}$  at  $C_{max}$  of  $\approx 0.8 - 0.9$  M.<sup>28</sup> This trend is

typical of most aqueous and non-aqueous electrolyte solutions and fits well to the equation derived by Abu-Lebdeh et al. (supplementary information **eqn. 5.S1**).<sup>25, 27</sup>

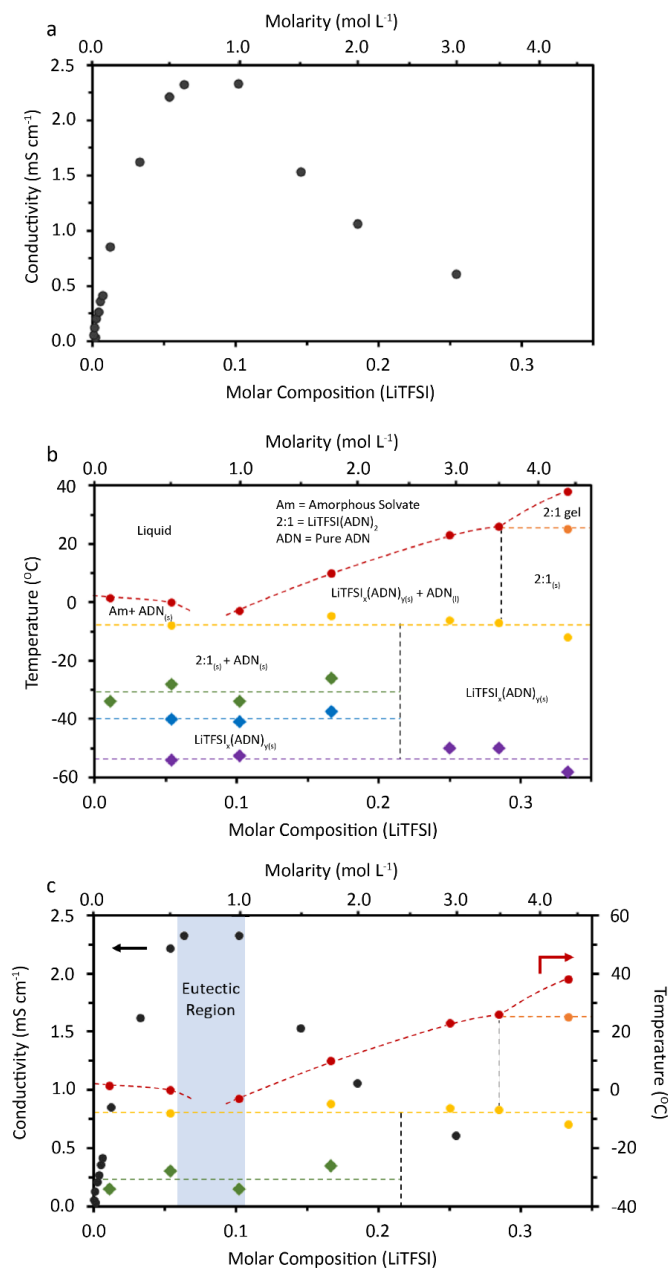


**Figure 5.1.** [a] Ionic conductivity of LiTFSI in ADN solutions as a function of concentration. [b] Extrapolated phase diagram of LiTFSI in ADN measured by DSC. Circles and diamonds represent endothermic and exothermic transitions, respectively. [c] Overlay of the conductivity plot and phase diagram showing the distinct relationship between  $C_{max}$  and  $x_{\epsilon}$ .

The phase diagram of the electrolyte, as constructed via DSC, is shown in **Fig. 5.1b**. It should be noted that crystallization and fusion of LiTFSI in ADN was not uniformly reproducible. A number of unexpected exotherms appear in the DSC plots, and some samples have multiple endothermic peaks (in the case of the 0.33 (LiTFSI molar composition) sample, an endotherm appears far above the temperature range at which the solution can be physically observed to of melted). This odd behaviour in the DSC data has been observed for the same electrolyte by Watanabe and co-workers as well.<sup>29</sup> A more detailed breakdown of how thermatogram peaks were assigned is available in the SI.

In the phase-diagram, the melting point ( $T_m$ ) of the electrolyte decreases steadily with concentration until a eutectic transition in the 0.7 to 0.9 M range, where it drops sharply to the observed solidus temperature at approximately  $-7.5$  °C, which agrees well with findings by Ugata et al.<sup>29</sup>  $T_m$  then recovers and steadily increases up until a peritectic transition at 3.5 M, or an ADN to LiTFSI ratio of 2.5 to 1. This ratio is significant as it is just below the minimum number of solvent molecules typically believed to be necessary to fully solvate  $\text{Li}^+$ .<sup>24, 30, 31</sup> After this point,  $T_m$  increases sharply as the electrolyte can no longer be properly solvated. The observed eutectic composition matches well with the expected composition if calculated using the generalized LeChatelier–Schröder equation ( $x_{\text{LiTFSI}} \approx 0.7$ , SI **eqn. 5.S2**).<sup>32</sup> The observed eutectic temperature is somewhat lower than the predicted value of the equation ( $-2$  °C), which can be attributed to the assumption of ideal activity. This speaks to the strong interactions present between LiTFSI and ADN, which has been seen for LiTFSI in other nitrile solvents.<sup>31</sup>

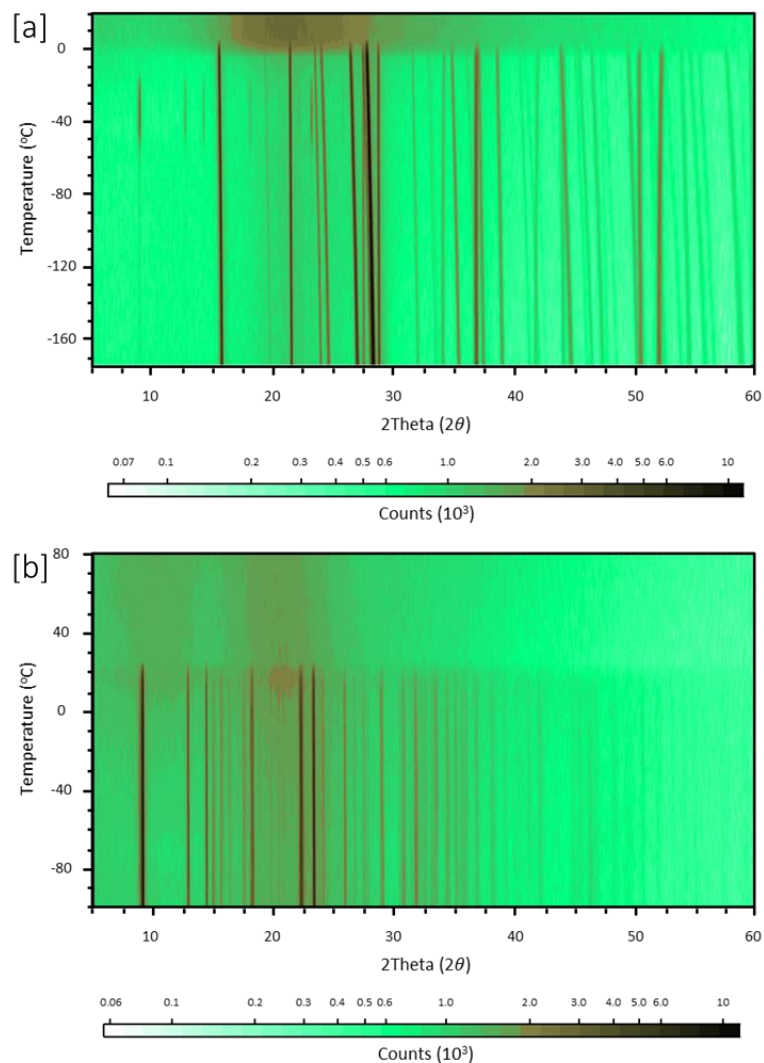


**Figure 5.2.** Variable temperature powder x-ray diffractogram of [a] 4.4 M LiTFSI in ADN electrolyte, corresponding to a 2 to 1 ADN:Li molar ratio, or 0.33  $x_{LiTFSI}$ , and [b] 0.1 M LiTFSI in ADN, corresponding to a 88 to 1 ADN:Li molar ratio, or 0.011  $x_{LiTFSI}$ .

Phase transitions noted in the phase diagram were determined by variable temperature x-ray diffraction on the crystallised electrolyte samples (Fig. 5.2 and Fig. 5.15S – 5.18S). The x-ray reflection temperature-evolution profiles show that many of the transitions seen in the phase diagram are not structural in nature. It is likely that many of the observed transitions in the DSC diffractograms are the dissolution

and solvation of various solvates that are too amorphous to be observed via x-ray diffraction techniques. This is consistent with visual observations of the electrolyte, where the post-eutectic composition samples transitioned between liquids and waxy gels day-to-day, with little to no variation in laboratory room temperature.

Specifically examining the 4.4 M (LiTFSI(ADN)<sub>2</sub>) sample (**Fig. 5.2b**), a uniform reflection profile is observed from -100 °C until the melting point (**Fig. 5.2b**). Comparing this to the most dilute, 0.1 M ( $\approx$  LiTFSI(ADN)<sub>88</sub>) sample (**Fig. 5.2a**), the reflection profile corresponding to pure ADN is observed throughout the entire temperature range, but the LiTFSI(ADN)<sub>2</sub> reflection profile appears as a binary phase from -45 °C to -15 °C. This suggests that the crystallized LiTFSI(ADN)<sub>2</sub> structure is relatively stable and may preferentially form in these electrolytes even when it is stoichiometrically unfavourable, while the vast excess of left over ADN crystallises in the pure form.

To better understand the relationship between ionic transport and structure, an overlay of the conductivity plot and phase diagram is shown in **Fig. 5.1c**. The observed plateau and drop-off of conductivity is typically attributed to the increasing viscosity of the solution and the subsequent decreasing mobility of each electrolyte species. However, in this case, a careful comparison shows distinct correlations between the conductivity plot and phase diagram of the electrolyte. Specifically,  $C_{max}$  correlates directly with the extrapolated eutectic composition ( $x_e$ ). To better understand this distinct relationship between conductivity and structure it is important to summarize a number of recent findings by other research groups.

As discussed above, these observations fit well with the equation and corresponding model of Abu-Lebdeh et al. which suggests that  $C_{max}$  reflects a change

in transport mechanism as a result of structural change near  $x_{\epsilon}$ .<sup>27</sup> The introduction also mentions the theorized formation of long-range aggregate structures in electrolytes at high concentrations,<sup>24, 26</sup> a proposal that fits well with a structurally-based transport model. To further support the formation of aggregates, Farhat et al. used Raman spectroscopy to study LiTFSI/ADN electrolyte solutions and calculated the mean solvation number of  $\text{Li}^+$  by nitrile groups. They found that the solvation number decreases from 4 in dilute solutions to 1.4 at saturation due to a lack of free ADN molecules.<sup>29</sup>

In addition, Watanabe et al. have recently shown that various highly concentrated LiFSI/dinitrile electrolytes (including ADN), in 2 to 1 (dinitrile to LiFSI) molar ratios, form crystal structures with extended networks of  $\text{Li}^+$  – dinitrile –  $\text{Li}^+$  coordination bridges interspaced by the anion.<sup>33</sup> In three-dimensional space these  $\text{Li}^+$  – dinitrile –  $\text{Li}^+$  structures form distinct  $\text{Li}^+$  channels that permeate the crystal structure, hinting that the proposed aggregates formed in these dinitrile electrolytes may contain channels responsible for short range  $\text{Li}^+$  diffusion. Even more recently the same group observed, via Raman spectroscopy, the same dinitrile bridging networks form for the larger LiTFSI anion, with glutaronitrile (GN).<sup>29</sup> It stands to reason that the same bridging structure may be conserved when moving to the larger TFSI<sup>-</sup> anion and longer chain length ADN solvent.

The two to one, dinitrile to anion, bridging network is likely the structure observed in the crystallised LiTFSI(ADN)<sub>2</sub> X-ray data, and thus the same structure observed preferentially forming in more dilute compositions. It is our hypothesis that the observed stability of these networked aggregate structures leads them to form in solution as well, as a part of the local solution structure of the electrolyte. Further we

propose that, due to the formed  $\text{Li}^+$  channels that permeate these networks,  $\text{Li}^+$  diffusion on a local scale may be significantly impacted by the population and connectivity of these networks.

### 5.3.2 – Diffusional Perspective

PFG NMR was used to explore the ramifications of the proposed structural transitions on the transport properties of the electrolyte. Self-diffusion coefficients of each electrolyte component are shown in **Fig. 5.3a**. Each of  $D_{\text{Li}^+}$ ,  $D_{\text{TFSI}}$ , and  $D_{\text{ADN}}$  drop significantly with increasing concentration. As is the case with the decrease of ionic conductivity discussed previously, this is typically attributed to an increase of dynamic viscosity in solution.

However, it is important to note the relative hierarchy of diffusing species in the electrolyte as well. In standard vehicular diffusion, the rate of diffusion is inversely proportional to the hydrodynamic radii of the diffusing species.<sup>34</sup> In dilute electrolytes,  $\text{Li}^+$  is fully solvated and appears in the form of  $[\text{Li}(\text{ADN})_x]^+$  complexes, giving it a large hydrodynamic radius when compared to free ADN, and the much less solvated TFSI. Thus, the order of diffusing species in dilute electrolytes is typically  $D_{\text{Solvent}} > D_{\text{Anion}} > D_{\text{Li}^+}$ .<sup>35, 36</sup> This is in direct agreement with what is observed here in the most dilute samples. ADN is the fastest diffusing species by far, while TFSI outpaces  $\text{Li}^+$  by a much lesser margin.

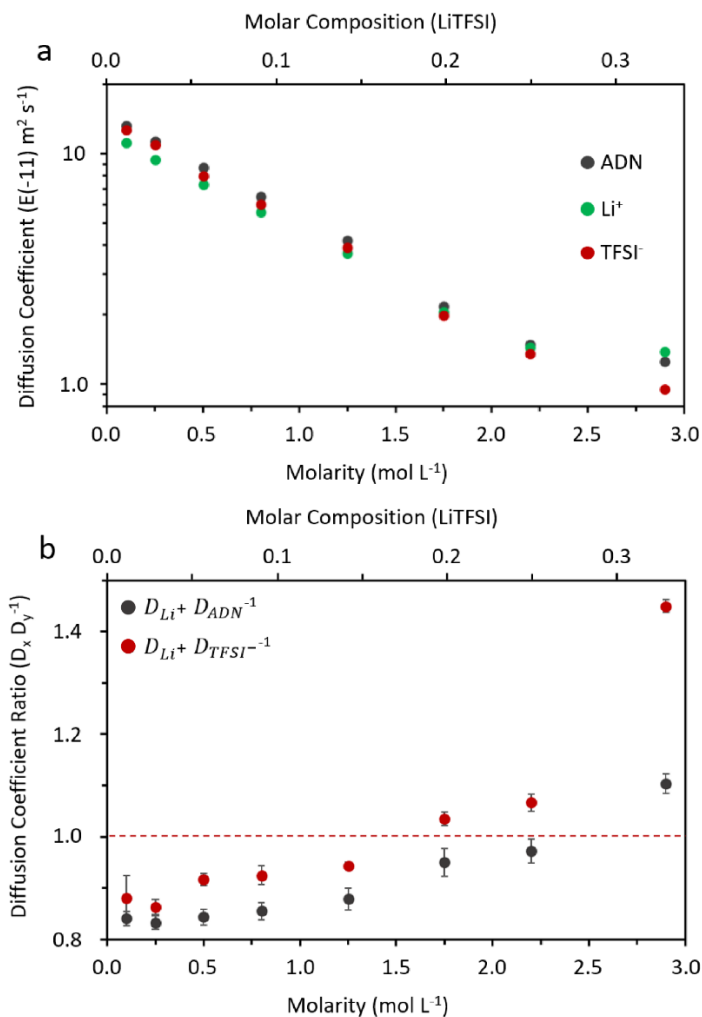


**Figure 5.3.** [a] Diffusion coefficients of  $\text{Li}^+$ , TFSI $^-$ , and ADN measured by  $^7\text{Li}$ ,  $^{19}\text{F}$ , and  $^1\text{H}$  PFG NMR respectively. [b] The quotient of diffusion coefficients as a function of temperature for (red)  $\text{Li}^+$  over TFSI $^-$  and (black)  $\text{Li}^+$  over ADN. The red line represents a ratio of 1, where both species diffuse at the same rate.

To better visualize the evolution of the diffusion coefficient of each species as concentration increases, the ratio of the measured  $\text{Li}^+$  diffusion coefficient to each of the TFSI $^-$  and the ADN coefficients ( $D_{\text{Li}^+}/D_{\text{TFSI}^-}$  and  $D_{\text{Li}^+}/D_{\text{ADN}}$ , respectively) is plotted against concentration in **Fig. 5.3b**. Both  $D_{\text{Li}^+}/D_{\text{TFSI}^-}$  and  $D_{\text{Li}^+}/D_{\text{ADN}}$  increase significantly with concentration. This behaviour is expected as the amount of excess free ADN drops rapidly with the addition of more salt, initiating the formation of less

solvated CIPs, and eventually the proposed larger aggregate structures as well. This results in  $\text{Li}^+$  outpacing TFSI in the 1.75 M sample, and culminates in  $\text{Li}^+$  outpacing both TFSI and ADN in the 2.9 M (3 to 1, ADN to LiTFSI, molar ratio) solution where  $D_{\text{Li}^+}/D_{\text{ADN}}$  exceeds unity and the diffusional order changes to  $D_{\text{Li}^+} > D_{\text{ADN}} > D_{\text{TFSI}}$ .

This is an interesting phenomenon that has been observed previously by Dokko et al. for a variety of sulfolane-based Li electrolytes.<sup>24</sup> They also observed the same increase in diffusional ratios for the LiTFSI in GN system, however  $\text{Li}^+$  never became the fastest diffusing species in that case.<sup>29</sup> As Dokko discussed in their sulfolane study,  $\text{Li}^+$  becoming the fastest diffusing species is particularly significant, because it cannot be explained by the vehicular mechanism. This phenomenon is instead consistent with  $\text{Li}^+$ -ion hopping motion, where a  $D_{\text{Li}^+}/D_{\text{ADN}}$  ratio above unity means that  $\text{Li}^+$  is able to diffuse independently through the electrolyte, leaving its local solvation structure behind.

This stark shift in transport mechanism is reflective of an electrolyte whose solution structure is evolving with concentration and strongly fits the hypothesis concerning the formation of aggregate structures containing  $\text{Li}^+ - \text{ADN} - \text{Li}^+$  networks. Since the individual self-diffusion coefficients are the mean value of transport in the electrolyte through all mechanisms (vehicular and structural), the gradual increase of  $D_{\text{Li}^+}/D_{\text{TFSI}}$  and  $D_{\text{Li}^+}/D_{\text{ADN}}$  with concentration is therefore due to an increasing proportion of  $\text{Li}^+$  ion hopping transport in a concurrently increasing population of networked  $[\text{Li}_z(\text{ADN})_x\text{TFSI}_y]^{z-y}$  aggregates in solution. At the molar ratio of 3:1, these aggregate networks become the majority component of the solution, and  $\text{Li}^+$ -ion hopping is the dominant transport mechanism.

### 5.3.3 – Diffusion Length as a Structural Probe

Measuring diffusion coefficient ratios as employed by Dokko et al. is a powerful tool for identifying the presence of alternative transport mechanisms in electrolyte solutions. We aim to build on this tool by quantifying the evolution of this mechanism using variable diffusion time ( $\Delta$ ) PFG NMR. By varying the central delay,  $\Delta$ , in the PFG experiment, we are able to encode diffusion behaviour as a function of length scale, and thus information on the heterogeneity of the transport mechanism of a material can be obtained. This technique has been previously applied to proton-conducting polyelectrolyte-fluoropolymer (PEF) blend membranes.<sup>37</sup> In these membranes,  $H^+$  conducts through a hierarchal structure of locally aligned conduction domains. As diffusion time increases, the magnitude of the measured diffusion coefficient may be inhibited by the domain boundaries. The end result is a decrease of the observed diffusion coefficient as  $\Delta$  (and thus the diffusional length scale) increases.<sup>37</sup> To the best knowledge of the authors, this technique has never been applied to liquid electrolyte systems.

In a completely homogenous solution with no variability in transport mechanism, the observed diffusion coefficient should not depend on the time scale (and thus length scale) of diffusion. This behaviour is exemplified well by the dataset in **Fig. 5.4a**, which shows the TFSI diffusion coefficient as a function of diffusion time at a variety of concentrations.

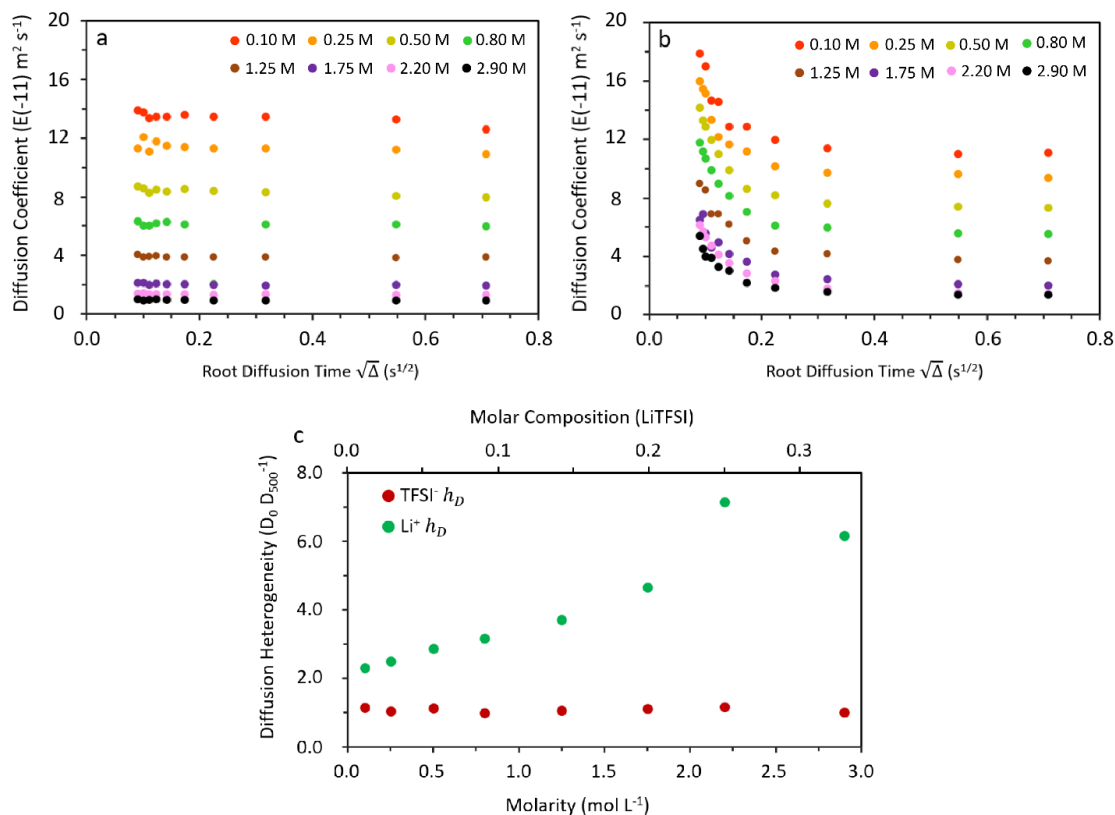


**Figure 5.4.** Diffusion coefficient as a function of diffusion time ( $\Delta$ ) for each concentration of electrolyte for [a] TFSI and (b) Li<sup>+</sup>. (c) The ratio of zero-time diffusion ( $\Delta \rightarrow 0$ ) to bulk diffusion ( $\Delta = 500$ ), diffusion heterogeneity ( $h_D$ ), for both Li<sup>+</sup> and TFSI.

Between each dataset, diffusion drops significantly with concentration as expected. But within each dataset, diffusion remains unaffected by diffusion time. Even at high concentrations where high proportions of bulky  $[\text{Li}_z(\text{ADN})_x\text{TFSI}_y]^{z-y}$  aggregates are expected, TFSI is diffusing purely through the vehicular mechanism as part of the bulk aggregate structure. This vehicular diffusion has no dependence on length scale, and thus the observed diffusional constant is unaffected by changes in  $\Delta$ . This is in contrast to the behaviour of the Li<sup>+</sup> cation (**Fig. 5.4b**). The same expected drop of  $D_{\text{Li}^+}$  with increasing concentration is still present, but now the observed

diffusion coefficient increases significantly as  $\Delta$  becomes very short within each dataset. This implies that  $\text{Li}^+$  diffusion on short length scales is fundamentally different from that of larger length scales. An analogous model to the proton-conducting PEFs can be made for liquid Li electrolyte solutions composed of the as-proposed dinitrile bridged aggregate structures containing  $\text{Li}^+$  channeled networks. Since the observed diffusion coefficient is an average of all apparent processes, we can conclude that as the length-scale of diffusion is shortened,  $\text{Li}^+$  that is diffusing on very short length scales through a hopping mechanism within aligned aggregate domains is preferentially selected for over the comparatively sluggish, longer range vehicular diffusion of the aggregates themselves, causing the observed increase in  $D_{\text{Li}^+}$  as  $\Delta \rightarrow 0$ .

To quantify the extent of heterogeneity in the transport mechanisms, the ratio of the extrapolated diffusion rate at the zero-diffusion time limit ( $\Delta = 0$  ms) to the observed diffusion rate at the bulk diffusion time ( $\Delta = 500$  ms) can be calculated. In the aforementioned PEF membrane study the authors refer to this ratio as tortuosity ( $\tau$ ), which is logical in the context of a polymer membrane.<sup>37</sup> In this work it will be referred to as diffusion heterogeneity ( $h_D$ ). The diffusion rate at zero-diffusion time is simply the y-intercept gained by linear regression of the short diffusion time region ( $\Delta \leq 15$  or 10 ms for TFSI<sup>-</sup> or  $\text{Li}^+$  respectively) of the  $\sqrt{\Delta}$  vs  $D$  curve.  $h_D$  is taken for each of the different concentration datasets to form **Fig. 5.4c**.

When looking at TFSI,  $h_D$  remains close to unity for the entire concentration range. As the solution evolves from having a large excess of free ADN, with fully solvated  $\text{Li}^+$  and free TFSI, toward having little to no free ADN, and being composed

primarily of large aggregates, TFSI diffuses only through the vehicular mechanism. Thus, diffusion remains constant with length scale at all concentrations for TFSI. In the case of  $\text{Li}^+$ ,  $h_D$  is small but still above unity at low concentrations, suggesting that even in the dilute stages, some variation in transport exists between micro and bulk length scales. As concentrations increase,  $h_D$  first increases steadily through the eutectic region then rapidly in the post-eutectic regime. As the solution evolves to being composed of aggregate structures that are continually increasing in population and size, the bulk vehicular diffusion observed at large  $\Delta$  decreases rapidly, while the zero-time hopping diffusion of  $\text{Li}^+$  within said aggregate networks remains rapid. At the highest concentrations, the ion-hopping mechanism observed at low  $\Delta$  becomes the dominant mechanism and is more representative of the bulk, so  $h_D$  begins to decrease. This is observed for the 3 to 1 molar ratio sample, which is where we also observed bulk hopping behaviour when examining the diffusion quotients in the previous section. The evolution of aggregates and the hopping mechanism they bring can now be visualized as a function of concentration.

The formation of aggregate structures is further supported by the calculated radial distribution functions (RDFs) of the LiTFSI in ADN electrolytes (**Fig. 5.19S – 5.21S**). At high concentrations, the RDF of both for the 4.4 M (LiTFSI(ADN)<sub>2</sub>) and 2.9 M (LiTFSI(ADN)<sub>3</sub>) systems show that the TFSI anion is found, with high probability, closer to the  $\text{Li}^+$  cation than the solvent; as expected if aggregates supporting  $\text{Li}^+$  ion hopping are present. This is also observed, but to a much lesser degree, for the low salt concentration 0.8 M (LiTFSI(ADN)<sub>11</sub>) system, suggesting it is not completely composed of fully solvated  $[\text{Li}(\text{ADN})_x]^+$  complexes. This is indeed in agreement with

the measured  $h_D > 1$  for the dilute concentrations. While the presence of  $\text{Li}^+$  - TFSI coordination does not itself guarantee the presence of structures supporting  $\text{Li}^+$ -hopping transport,  $\text{Li}^+$  - TFSI coordination is a pre-requisite to the existence of said structures.

### 5.3.4 – Solvation Structure & Transport Mechanism

Each of the experimental and computational techniques above help us to paint an overall picture of how the structure and transport of the electrolytes evolve as a function of concentration. To better understand the observed behaviour, we split the concentration range into four distinct regimes:

1. In the dilute, pre-eutectic, regime, there is a large amount of free ADN, and the dominating  $\text{Li}^+$  species are  $[\text{Li}(\text{ADN})_x]^+$  complexes (where  $x = 3-6$ ). In this regime, the structure is relatively unaffected by the addition of more salt, but the ionic conductivity increases sharply as the concentration of charge carriers increases. The ion transport is carried out more or less entirely via the vehicular mechanism, and the heterogeneity ( $h_D$ ) of  $\text{Li}^+$  diffusion is also low as few to no large aggregates are present, rendering the transport mechanism homogenous. Both the  $D_{\text{Li}^+}/D_{\text{ADN}}$  and  $D_{\text{Li}^+}/D_{\text{TFSI}}$  quotients are therefore constant as functions of concentration in this regime.
2. In the eutectic regime the structure transitions; the concentration of free ADN separating any complexes formed decreases rapidly, causing formation of CIPs ( $[\text{Li}^+(\text{ADN})_n\text{TFSI}]$ ) and some larger aggregates ( $[\text{Li}_x(\text{ADN})_y\text{TFSI}_z]^{x-z}$ ). However,  $\text{Li}^+$  and  $\text{TFSI}^-$  concentrations are not yet high enough for any long-range structure to form; the electrolyte is rather in a highly disordered state

where the addition of salt has little effect on the ionic conductivity, but a large effect on  $T_m$ , which drops rapidly as  $x_\epsilon$  is reached. Local ordered structures begin to form, causing a slight increase in diffusion heterogeneity,  $h_D$ , but at the bulk level ion conduction is still dominated by a single vehicular mechanism, as shown by the consistent low values of the  $D_{Li^+}/D_{ADN}$  quotient. However,  $D_{Li^+}/D_{TFSI}$  starts to increase as the TFSI anions become involved in the CIPs, and surpasses unity at the end of this regime.

3. In the post-eutectic regime, the concentration of free ADN separating any  $[Li(ADN)_x]^+$  complexes or CIPs decreases rapidly. As these complexes and CIPs become less separated, larger  $[Li_x(ADN)_yTFSI_z]^{x-z}$  aggregates, that contain  $Li^+$  channels formed by the  $Li^+$  – dinitrile –  $Li^+$  bridges, form at an increasing rate. This causes significant increases in both  $D_{Li^+}/D_{ADN}$  and  $D_{Li^+}/D_{TFSI}$  as the hopping mechanism becomes a significant part of the bulk ion transport. This regime exhibits the strongest dichotomy between the short-range ion hopping transport and the bulk vehicular mechanism, and the diffusion heterogeneity,  $h_D$ , reaches its peak. The change in structure also causes a significant viscosity increase.
4. In the ultra-concentrated regime, at ADN to LiTFSI molar ratios  $< 3$ , there is no longer enough ADN to fully solvate LiTFSI. Here  $T_m$  increases rapidly as the electrolyte is dominated by a long-range aggregated structure. Vehicular transport of aggregates still exists, but the dominant conduction mechanism is ion hopping, as shown by  $D_{Li^+}/D_{ADN}$  surpassing unity. Increasing concentration further causes the electrolytes to become more and more

homogenous, as the proportion of the already dominant ion hopping mechanism increases, and thus the diffusion heterogeneity,  $h_D$ , decreases.

### 5.3.5 – Cyclic Voltammetry and Li-O<sub>2</sub> cells Proof of Concept

Cyclic voltammetry (CV) was used to explore any electrochemical ramifications to the high concentration shift in transport mechanism (**Fig. 5.5**). As discussed in the introduction, LiTFSI in ADN is well known for its wide electrochemical stability window, and this is confirmed here.

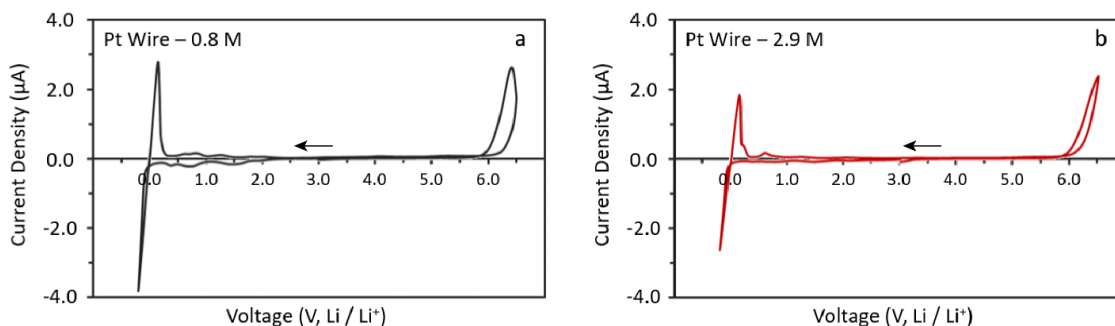


**Figure 5.5.** CV of (a) 0.8 M ( $C_{max}$ ) and (b) 2.9 M (3 to 1 molar ratio) LiTFSI in ADN. Pt wire is used as both the counter and working electrodes, with a Li metal reference electrode.

Both the 0.8 M ( $C_{max}$ ), dilute, and the 2.9 M, highly concentrated, electrolytes show stable Li<sup>+</sup> reduction and reversible oxidation on the cathodic sweep, as well as oxidative stability up to 6 V (vs the Li metal reference electrode) toward the Pt electrode, the latter being a limitation of the TFSI anion, and not ADN.<sup>6, 7</sup> Minor electrolyte degradation is observed below 2 V for both samples as well, as expected of most organic Li electrolytes.<sup>38</sup> There are small differences in the intensity of the low voltage degradation peaks, however, this is likely due to the more sluggish kinetics of the high viscosity 2.9 M electrolyte.

The Li-O<sub>2</sub> battery system was chosen as an appropriate test-case for the high oxidative stability of the electrolytes. LiTFSI is well-known to corrode aluminum current collectors above 4 V,<sup>39</sup> and Li-O<sub>2</sub> cells instead typically employ free-standing carbon-based gas diffusion layers as cathodes with stainless-steel mesh current collectors. Furthermore, Li-O<sub>2</sub> cells often need to reach voltages of 4.5 V during the charging process, which is at the edge of the oxidative limit for the typically used glyme solvents.<sup>40</sup> CV was performed on Li-O<sub>2</sub> coin cells made with both 0.8 M and 2.9 M LiTFSI in ADN electrolytes (**Fig. 5.6c** and **Fig. 5.6d**). On the cathodic sweep, a clear oxygen reduction peak ( $R_1$ ) can be seen for both the 0.8 and 2.9 M electrolytes, corresponding to the formation of lithium superoxide (LiO<sub>2</sub>).<sup>40</sup> The reduction process is much sharper using the 0.8 M electrolyte than the 2.9 M electrolyte, likely due to worse oxygen solvation in the latter.

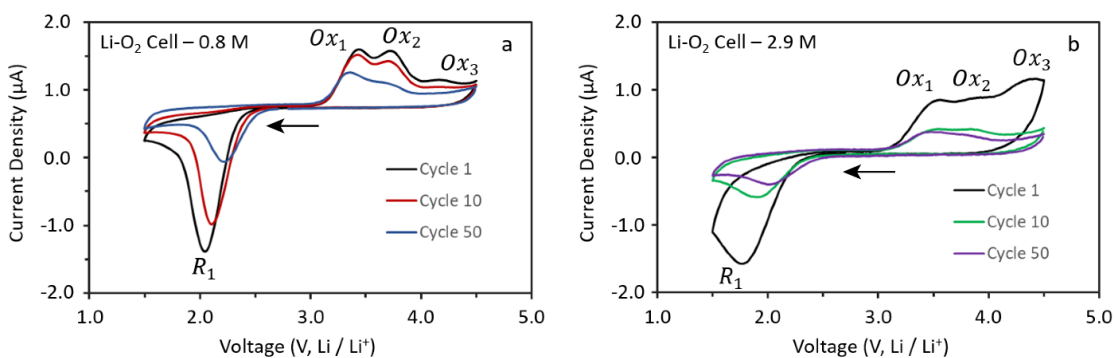


**Figure 5.6.** Cyclic voltammetry of Li-O<sub>2</sub> coin cells in an O<sub>2</sub> atmosphere using (a) 0.8 M ( $C_{max}$ ) and (b) 2.9 M (3 to 1 molar ratio) LiTFSI in ADN electrolyte. Carbon cloth is used as the working electrode, and Li metal as the counter/reference in both cells.

On the anodic sweep, three distinct oxidation peaks are observed for both samples. As was the case for the reduction events, the oxidation peaks are much less resolved in the highly concentrated analog. Ox<sub>1</sub> and Ox<sub>2</sub> correspond to oxidation of LiO<sub>2</sub> and lithium peroxide (Li<sub>2</sub>O<sub>2</sub>), respectively. Trahan et al. have done detailed

similar CV experiments on dimethyl sulfoxide (DMSO) based systems, and found that both  $\text{LiO}_2$  and  $\text{Li}_2\text{O}_2$  oxidation are observed even with a single reduction process.<sup>40</sup> This is due to electrochemically formed  $\text{LiO}_2$  undergoing chemical disproportionation into  $\text{Li}_2\text{O}_2$ .<sup>41</sup> At higher voltages,  $\text{Ox}_3$  is likely the oxidation of any surface groups present in the carbon electrode before cycling, as well as oxidation of passivating  $\text{Li}_2\text{CO}_3$  formed from superoxide attack of the carbon cathode.<sup>42-44</sup> As the CV continues into higher and higher cycle numbers, this  $\text{Li}_2\text{CO}_3$  passivation significantly hinders the oxygen reduction process as active carbon sites become unreachable by dissolved  $\text{O}_2$ , a well-known phenomenon of metal-air battery cells. <Ottakam Thotiyl, 2013 #468> The passivation manifests as a significant drop in current density as cycle number increases. This phenomenon is observed in both samples but is much more pronounced in the 2.9 M electrolyte. It is thought that the solvent plays an important role in stabilizing the superoxide anion in these cells,<sup>45</sup> and with little to no free solvent available in the concentrated sample,  $\text{LiO}_2$  is destabilized/unstable and reacts with the carbon cathode much more aggressively than in the 0.8 M electrolyte cell, resulting in the rapid passivation observed here.

Overall, the wide electrochemical stability window, and clear activity toward the ORR and OER, make LiTFSI in ADN a promising electrolyte system for Li- $\text{O}_2$  cells. However, the highly concentrated electrolyte offers no clear advantages, and even accelerates the carbon passivation process. Further studies on the less concentrated  $C_{max}$  electrolyte can show how its high anodic limit affects the long-term stability of Li- $\text{O}_2$  cells.

## 5.4 – Conclusions

The physiochemical properties of LiTFSI in ADN electrolytes were investigated as a function of salt concentration. A strong relationship between the eutectic point and the concentration of maximum ionic conductivity suggests that there is a strong structural component to the variance in ionic conductivity with concentration. Diffusion constants measured by PFG NMR show that Li<sup>+</sup> diffusion increases relative to the TFSI anion and ADN solvent with increasing concentration, culminating in Li<sup>+</sup> outpacing both components at a LiTFSI molar composition of 0.25. This demonstrates a shift from a dominantly vehicular transport mechanism to an ion hopping transport mechanism at high concentrations. Variable diffusion time PFG further showed the dichotomy existing between small-scale and bulk solution structure, which is theorized to exist due to an ever increasing proportion of  $[\text{Li}_x(\text{ADN})_y\text{TFSI}_z]^{x-z}$  aggregates as the concentration of free ADN decreases.

The change in ion transport mechanism was not shown to have any significant impact on the elementary electrochemical behaviour, but the LiTFSI in ADN electrolytes were confirmed to be strong candidates for use with high voltage cathode materials given their stability limit of 6 V (vs Li/Li<sup>+</sup>). Furthermore, Li-O<sub>2</sub> coin cells were made with the LiTFSI in ADN electrolytes and showed reversible oxygen reduction and evolution reactions. This paired with the high oxidative stability of the electrolyte make LiTFSI in ADN electrolytes extremely useful in the context of metal-air batteries.

Although LiTFSI is well-known to corrode aluminum current collectors at LMNO voltages, recent studies have shown that aluminum corrosion can be suppressed by using electrolyte additives such as fluoroethylene carbonate in low concentrations.<sup>11,</sup>

<sup>46</sup> We suggest further work be done on high voltage LMNO cells using binary electrolyte systems that take advantage of both the suppressed LiTFSI aluminum corrosion gained by using additives, and the high oxidative stability of the LiTFSI in ADN electrolyte solution.

## 5.5 – Supporting Information

### 5.5.1 – Phase Diagram Construction

The phase diagram was constructed using phase transitions observed in the differential scanning calorimetry (DSC) thermatograms. DSC was performed using a TA Instruments Q2000 in hermetically sealed aluminum pans. Samples were heated to 40 °C before being cooled to -90 °C and reheated to 150 °C, or 75 °C in the case of the 0.5 M sample. Cooling and heating rates were both 10 °C per minute. Due to the presence of many unexplained peaks in these samples, not all peaks in the thermatograms are plotted on the phase diagram. Peak picking is shown with the appropriate coloured labelled in the thermatograms for each sample composition below. Generally, melting points (red) were taken as the highest temperature endothermic peak, except for the most concentrated sample, LiTFSI(ADN)<sub>2</sub>, where the an unexplained endothermic transition is seen above 50 °C, which is far above the melting temperature observed visually when working with these samples.

The solidus (and therefore the eutectic transition) was chosen based on the endothermic melting transitions (yellow circles) observed below the melting points. The solidus temperature of -7.5 °C was fit by taking the average of the observed eutectic transition temperatures. No solidus transition is seen for the 1 M (**Fig. 5.10S**) or 0.1 M (**Fig. 5.8S**) samples ( $x_{LiTFSI} = 0.011$  and  $x_{LiTFSI} = 0.10$  respectively). The 1.0

M solidus transition is likely too close in temperature to the large melting peak, and is being consumed in the thermatogram, while the 0.1 M sample may be too dilute for a significant solidus transition to appear. Nonetheless the solidus temperature agrees well with that collected by Ugata et al..<sup>29</sup>

Labeling of the phases in the phase diagram was aided by the variable temperature PXRD experiments. X-ray diffraction data was collected by first preparing samples by mixing ADN with the required amount of LiTFSI salt. The solution was then injected into 1 mm capillaries containing ground quartz glass in an Argon-filled glove box and then sealed with wax. Data collected on Bruker D8 with focussing mirror and Vantec PSD. Custom-built, 90° short-nozzle cryoflow system used to control temperature. Samples tended to supercool on quenching so rapid heating to ~20K below melting was used to crystallize them. The cryoflow temperature was calibrated using the thermal expansion of aluminum metal. Diffractograms were taken at 5 °C intervals from -175 °C until significantly above the melting temperature.

In the 0.1 M ( $x_{LiTFSI} = 0.011$ ) sample (**Fig. 5.2** and **Fig. 5.15S**), pure ADN is observed from -175 °C to melting, with LiTFSI(ADN)<sub>2</sub> phase crystallizing and disappearing briefly from around -45 °C to -15 °C. This agrees roughly with the temperature range between the green crystallisation and yellow solidus transitions observed in the thermatograms for the more dilute samples. We reason that with increasing temperature mixed LiTFSI<sub>x</sub>(ADN)<sub>y</sub> phases are allowed to form, and the LiTFSI(ADN)<sub>2</sub> networks are a favourable composition. However, after the solidus transition, more ADN is solvated into the solid electrolyte and more dilute, amorphous concentrations form, thus causing the LiTFSI(ADN)<sub>2</sub> reflections to

disappear. In the 1 M ( $x_{LiTFSI} = 0.10$ ) sample (**Fig. 5.17S**), on the more concentrated side of the eutectic point, solid ADN is still observed in the temperature range between the green crystallisation and yellow solidus transitions. No reflections are seen above the solidus, in part due to how close it is to the melting temperature, but it is also likely that any  $LiTFSI_x(ADN)_y$  phases formed here would be highly amorphous in nature. Below the crystallization temperature, reflections of an unknown phase are observed, which may be some other solid composition of  $LiTFSI_x(ADN)_y$ .

In the highly concentrated 4.4 M ( $x_{LiTFSI} = 0.33$ ) sample (**Fig. 5.19S**), a single phase is seen throughout the entire temperature range until melting. This is attributed to the  $LiTFSI(ADN)_2$  networked phase, as discussed in the main text. Although melting appears to happen at about 25 °C in the reflection profile, the 2.9 M sample was a wax-like gel at room temperature and would fully melt with mild heating. This is why the DSC peak at 25 °C is attributed to a gelling of the solid, and the higher temperature 38 °C peak is attributed to melting.

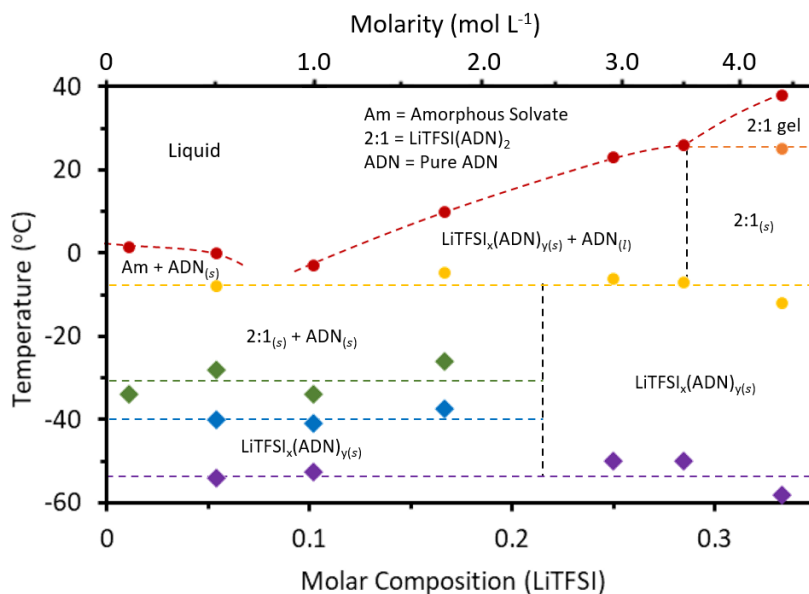


**Figure 5.7S.** Copy of phase diagram seen in the main text. Data points here are labelled as DSC thermatogram peaks in the following figures.

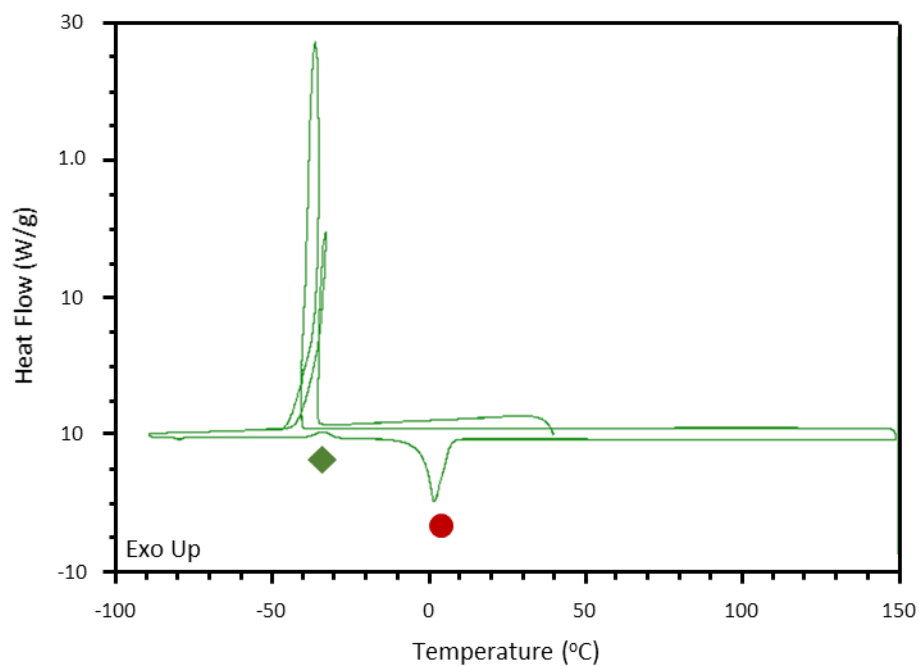


**Figure 5.8S.** DSC plot of 0.1 M LiTFSI in ADN electrolyte, corresponding to a 88 to 1 ADN:Li molar ratio, or 0.011  $x_{LiTFSI}$ .

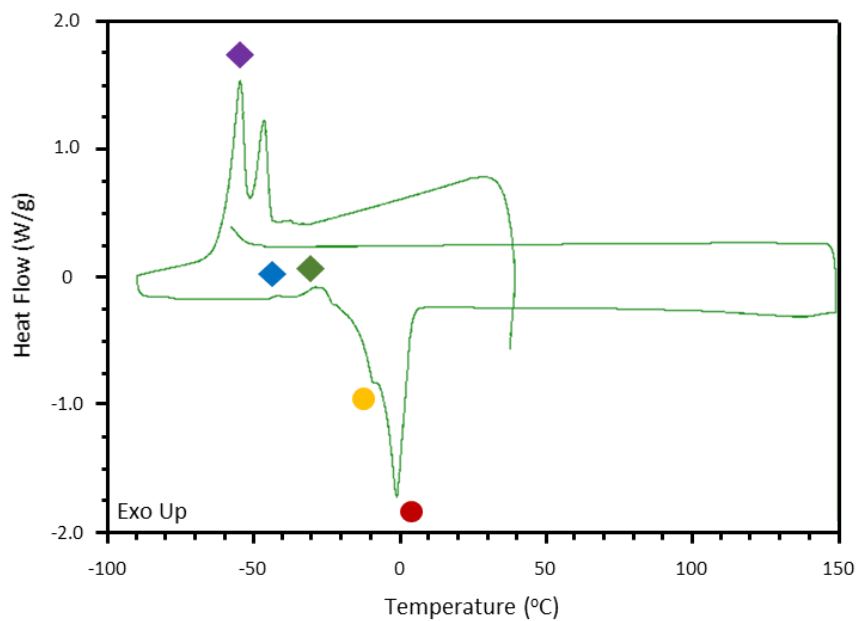


**Figure 5.9S.** DSC plot of 0.5 M LiTFSI in ADN electrolyte, corresponding to a 17.5 to 1 ADN:Li molar ratio, or  $0.054 x_{LiTFSI}$ .

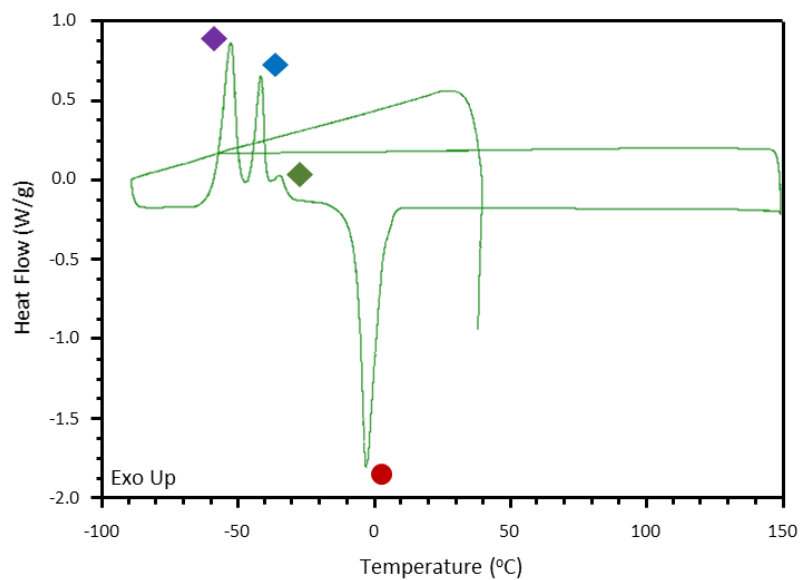


**Figure 5.10S.** DSC plot of 1.0 M LiTFSI in ADN electrolyte, corresponding to a 8.8 to 1 ADN:Li molar ratio, or  $0.10 x_{LiTFSI}$ .

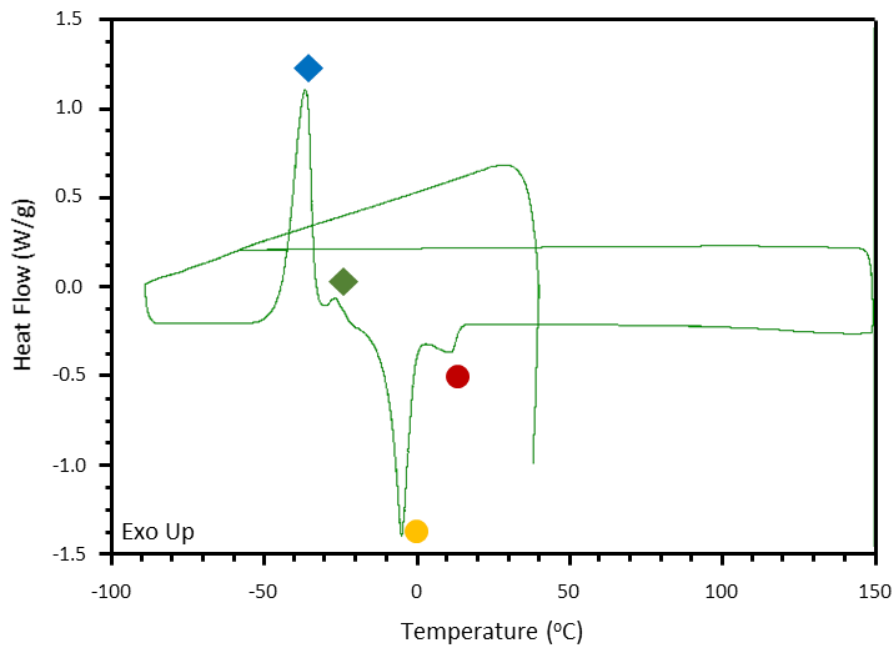


**Figure 5.11S.** DSC plot of 1.8 M LiTFSI in ADN electrolyte, corresponding to a 5 to 1 ADN:Li molar ratio, or  $0.17 x_{LiTFSI}$ .

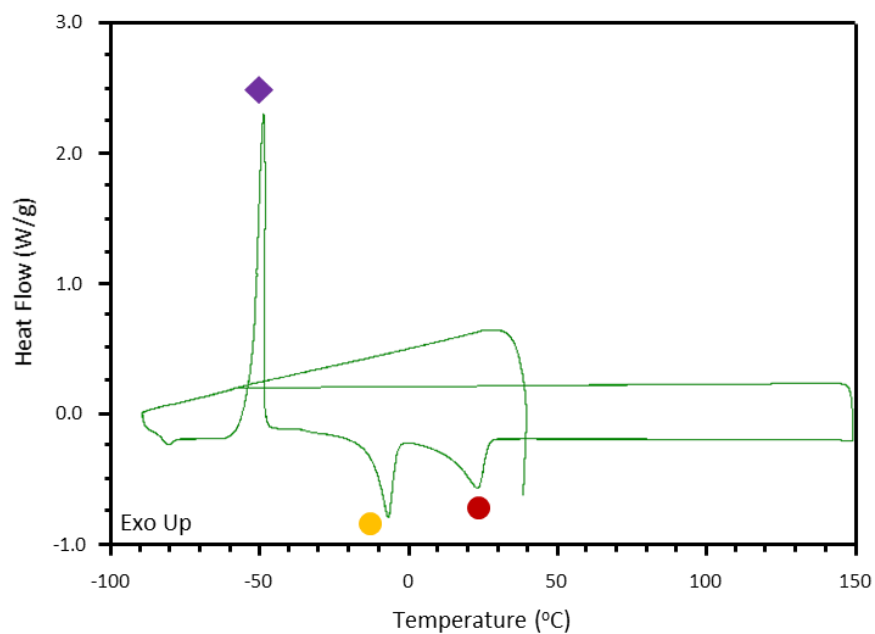


**Figure 5.12S.** DSC plot of 2.9 M LiTFSI in ADN electrolyte, corresponding to a 3 to 1 ADN:Li molar ratio, or  $0.25 x_{LiTFSI}$ .

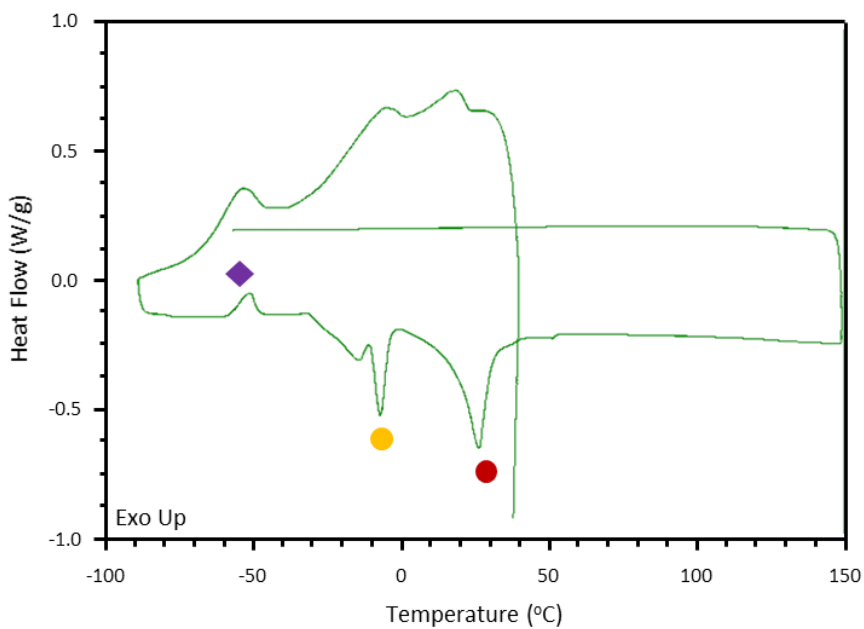


**Figure 5.13S.** DSC plot of 3.5 M LiTFSI in ADN electrolyte, corresponding to a 2.5 to 1 ADN:Li molar ratio, or  $0.28 x_{LiTFSI}$ .

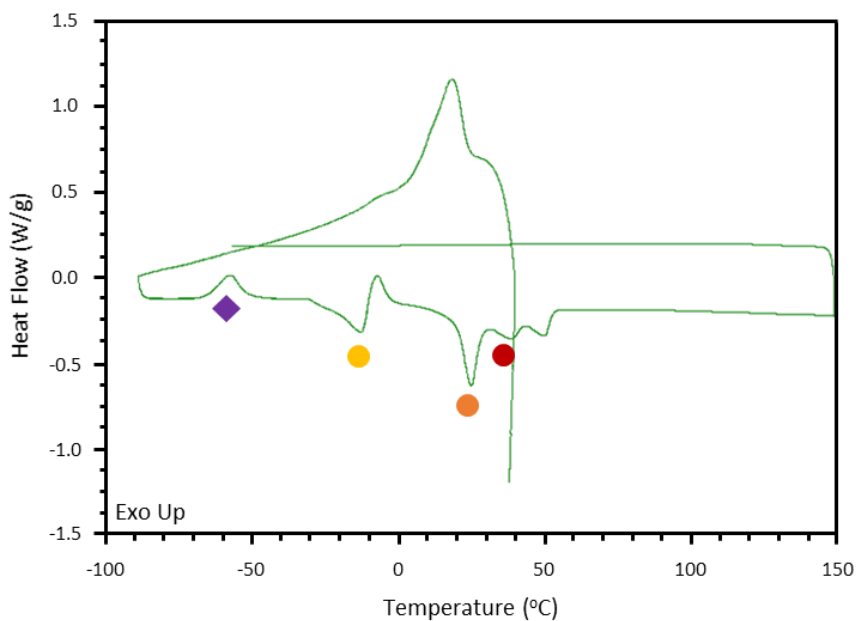


**Figure 5.14S.** DSC plot of 4.4 M LiTFSI in ADN electrolyte, corresponding to a 2 to 1 ADN:Li molar ratio, or  $0.33 x_{LiTFSI}$ .

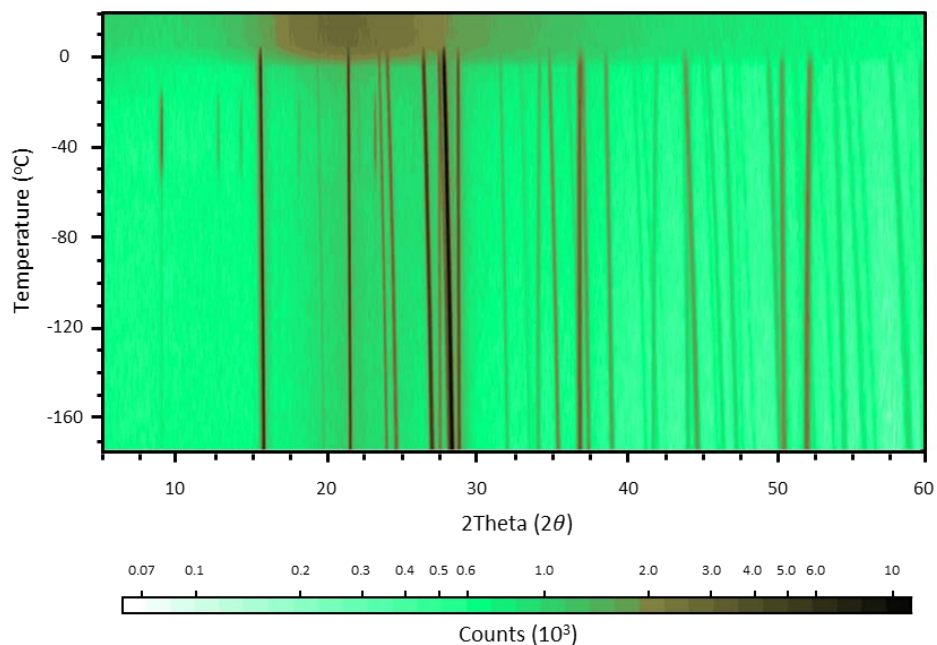


**Figure 5.15S.** Variable temperature powder x-ray diffractogram of 0.1 M LiTFSI in ADN, corresponding to a 88 to 1 ADN:Li molar ratio, or 0.011  $x_{LiTFSI}$ .

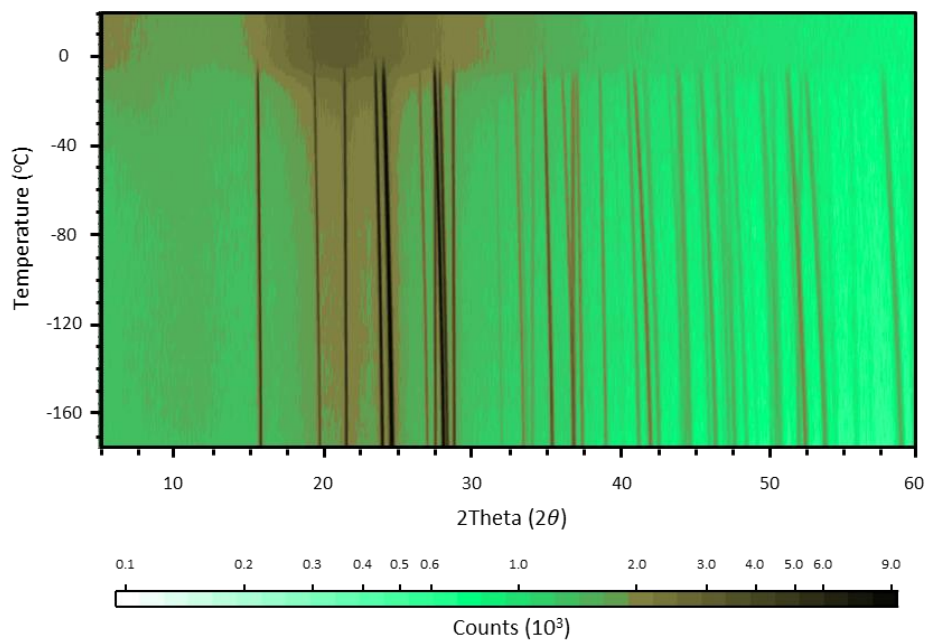


**Figure 5.16S.** Variable temperature powder x-ray diffractogram of 0.5 M LiTFSI in ADN, corresponding to a 17.5 to 1 ADN:Li molar ratio, or 0.054  $x_{LiTFSI}$ .

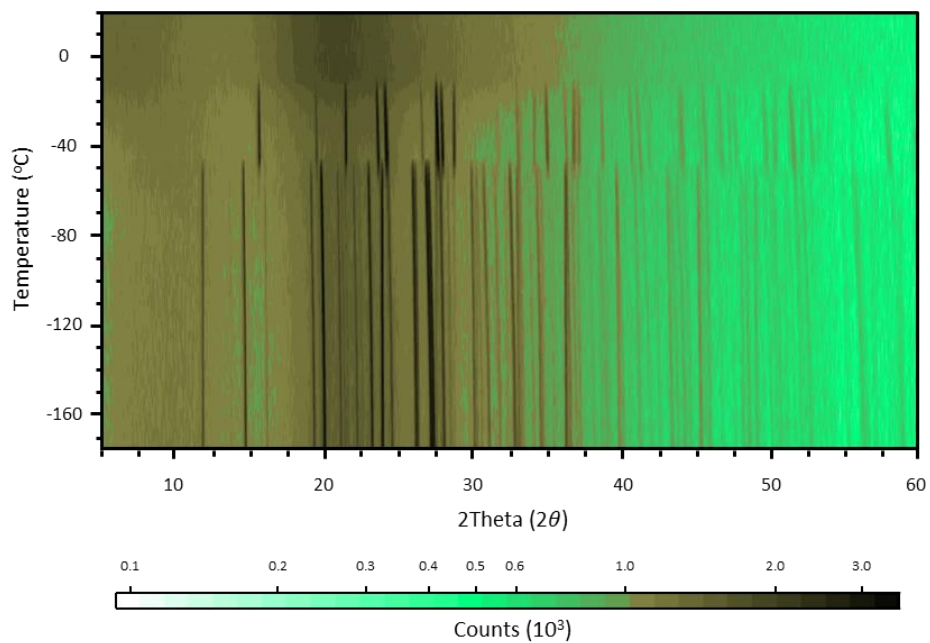


**Figure 5.17S.** Variable temperature powder x-ray diffractogram of 1.0 M LiTFSI in ADN, corresponding to a 8.8 to 1 ADN:Li molar ratio, or  $0.10 x_{LiTFSI}$ .

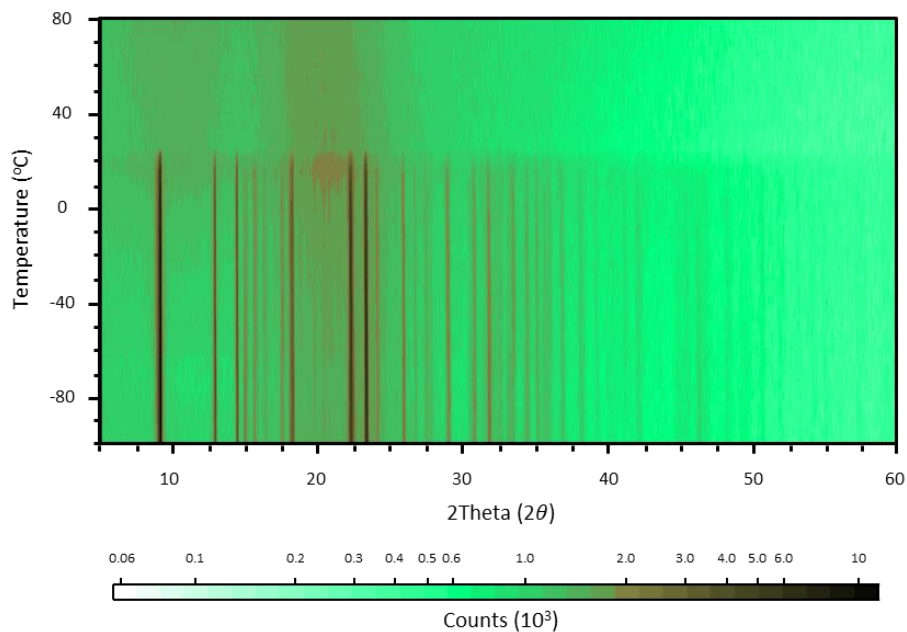


**Figure 5.18S.** Variable temperature powder x-ray diffractogram of 4.4 M LiTFSI in ADN electrolyte, corresponding to a 2 to 1 ADN:Li molar ratio, or  $0.33 x_{LiTFSI}$ .

### 5.5.2 – Fitting of the conductivity isotherm

A close examination of the ionic conductivity isotherm  $\sigma$  vs.  $C$  (**Fig. 5.1a**) shows that it fits well to the equation derived by Abu-Lebdeh et al.<sup>25, 27</sup>

$$\sigma = AC\exp(-BC) \quad 5.S1$$

Where  $\sigma$  is the room temperature ionic conductivity,  $C$  is the concentration in mol L<sup>-1</sup>, and  $A$  and  $B$  are parameters. Table 1 shows the values for  $A$  and  $B$  parameters for ADN other solvents (Acetonitrile, ACN, and water) for comparison. The physical meaning of the two parameters is still not completely understood, but Abu-Lebdeh hypothesises that  $B$  may be related to free volume, the difference in measured liquid volume and the temperature independent minimum occupied volume of the constituent molecules.

**Table 5.1S.** Physical parameters  $A$  and  $B$  for water, ACN and ADN obtained by fitting Equation S1 to their respective conductivity isotherms at room temperature.

Solvent	A	B
Water	3.98	-0.39
ACN	4.34	-0.79
ADN	1.64	-0.78

### 5.5.3 – Calculated Eutectic Composition

The theoretical solid-liquid binary phase diagram was calculated by using the generalized LeChatelier–Schröder equation to approximate each the LiTFSI and ADN liquidus curves:

$$\ln(x_i\gamma_i) = \frac{\Delta H_m}{R} \left( \frac{1}{T_m} - \frac{1}{T} \right) \quad 5.S2$$

$x_i$  is the mole fraction,  $\gamma_i$  is the activity coefficient,  $R$  is the gas constant,  $T$  is the melting temperature of the solution,  $T_m$  is the melting temperature of pure LiTFSI (509.15 K) or ADN (275.15 K) and  $\Delta H_m$  is the melting enthalpy of pure LiTFSI (13.2 kJmol<sup>-1</sup>) or ADN (14.3 kJmol<sup>-1</sup>). Liquidus lines of  $T$  as a function of  $x_i$  are plotted and the intersection is found as the eutectic composition and temperature,  $x_\epsilon$  and  $T_\epsilon$  respectively.  $x_\epsilon$  was found to be 0.07, while  $T_\epsilon$  was found to be -2 °C. The calculated  $x_\epsilon$  matches well with the experimental range of 0.07 to 0.09, while the calculated  $T_\epsilon$  was somewhat higher than the experimental value of -7.5 °C. The latter is a result of the assumption of ideality ( $\gamma=1$ ) and the deviation is an indication of strong interactions between LiTFSI and ADN compared to the pure compounds similar to what was observed for other LiTFSI – nitrile electrolyte solutions.<sup>31</sup>

#### 5.5.4 – Radial Distribution Functions

The radial distribution functions (RDF)  $g(r)$  were calculated as the number  $n(r)$  of atom B at a distance  $r$  from a central atom A within a shell volume  $V = 4\pi r^2 \Delta r$ :  $g(r) = n(r)/V$ . Using the CHAMPION software [R. Andersson, F. Årén, A. A. Franco and P. Johansson, “Ion Transport Mechanisms in Highly Concentrated Electrolytes by Dynamic Structure Discovery using Molecular Dynamics Simulation Trajectories”]. a set of 30 randomized structures were created for each of the LiTFSI:ADN molar ratios 1:2, 1:3, and 1:11, corresponding to 4.4, 2.9 and 0.8 M, with 4, 4, and 2 Li<sup>+</sup>-ions, respectively. Subsequently, geometry optimizations were carried out using MOPAC2016<sup>47</sup> and PM7 with an implicit solvent.<sup>48</sup> included with a permittivity  $\epsilon_r = 32.1$ .<sup>49</sup> Using the stable structures obtained, radial distribution functions (RDF)  $g(r)$

were calculated as the number  $n(r)$  of atom B at a distance  $r$  from a central atom A within a shell volume  $V = 4\pi r^2 \Delta r$ :  $g(r) = n(r)/V$ .

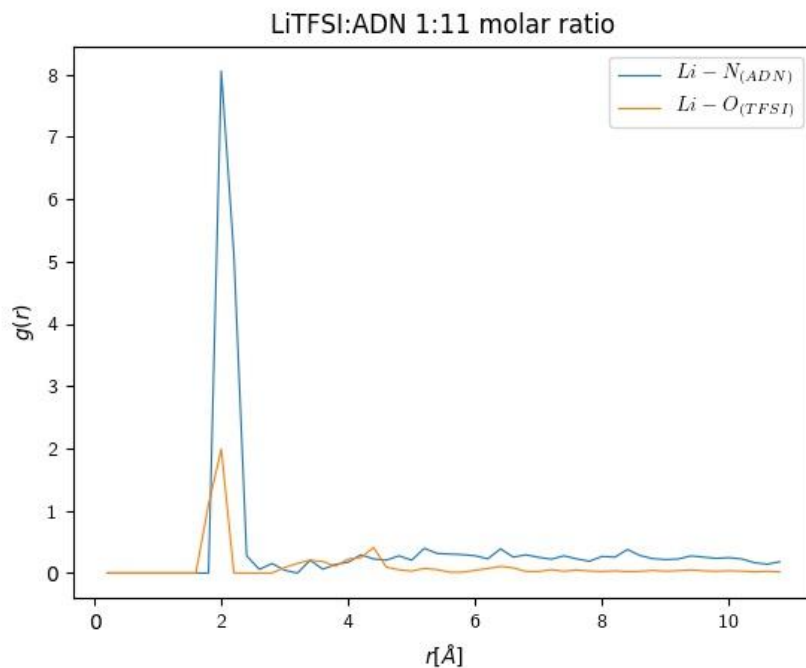


**Figure 5.19S.** RDF profile of dilute  $\text{LiTFSI}(\text{ADN})_{11}$  (0.8 M), the blue line corresponds to the partial RDF of  $\text{Li} - \text{N}_{(\text{ADN})}$ , and the orange line corresponds to  $\text{Li} - \text{O}_{(\text{TFSI})}$ .

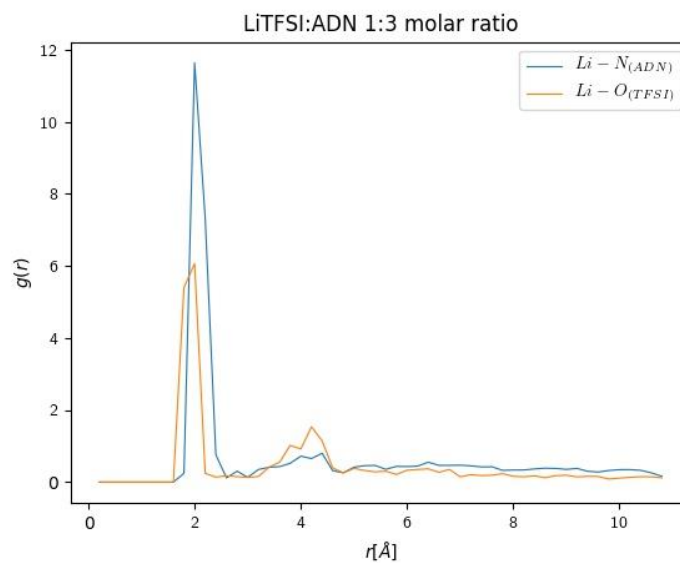


**Figure 5.20S.** RDF profile of highly concentrated LiTFSI(ADN)<sub>3</sub> (2.9 M), the blue line corresponds to the partial RDF of Li - N<sub>(ADN)</sub>, and the orange line corresponds to Li - O<sub>(TFSI)</sub>.

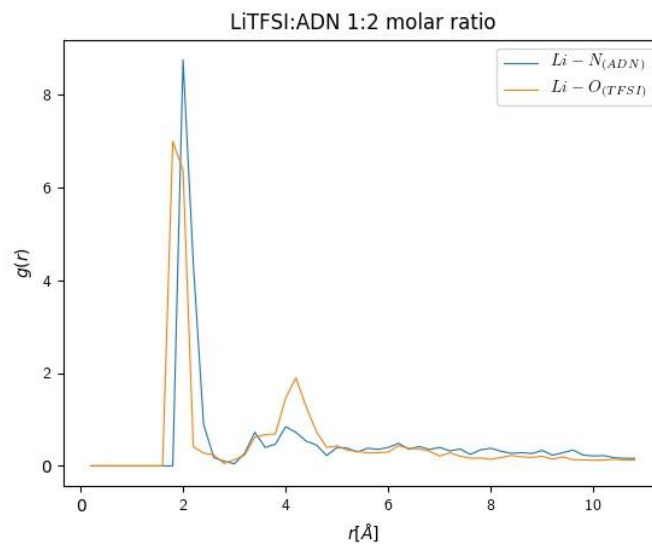


**Figure 5.21S.** RDF profile of highly concentrated LiTFSI(ADN)<sub>2</sub> (4.4 M), the blue line corresponds to the partial RDF of Li - N<sub>(ADN)</sub>, and the orange line corresponds to Li - O<sub>(TFSI)</sub>.

## 5.6 – References

1. Arrebola, J. C.; Caballero, A.; Cruz, M.; Hernán, L.; Morales, J.; Castellón, E. R. *Advanced Functional Materials* **2006**, *16* (14), 1904-1912. DOI: 10.1002/adfm.200500892
2. Kim, J. H.; Pieczonka, N. P.; Yang, L. *Chemphyschem* **2014**, *15* (10), 1940-54. DOI: 10.1002/cphc.201400052
3. Bloom, I.; Walker, L. K.; Basco, J. K.; Abraham, D. P.; Christophersen, J. P.; Ho, C. D. *Journal of Power Sources* **2010**, *195* (3), 877-882. DOI: 10.1016/j.jpowsour.2009.08.019
4. Nelson, K. J.; d'Eon, G. L.; Wright, A. T. B.; Ma, L.; Xia, J.; Dahn, J. R. *Journal of The Electrochemical Society* **2015**, *162* (6), A1046-A1054. DOI: 10.1149/2.0831506jes
5. Xia, J.; Nie, M.; Ma, L.; Dahn, J. R. *Journal of Power Sources* **2016**, *306*, 233-240. DOI: 10.1016/j.jpowsour.2015.12.013
6. Ue, M.; Ida, K.; Mori, S. *J. Electrochem. Soc.* **1994**, *141* (11), 2989.
7. Abu-Lebdeh, Y.; Davidson, I. *Journal of The Electrochemical Society* **2009**, *156* (1), A60-A65. DOI: 10.1149/1.3023084
8. Lu, Z.; Yang, L.; Guo, Y. *Journal of Power Sources* **2006**, *156* (2), 555-559. DOI: 10.1016/j.jpowsour.2005.05.085
9. Gmitter, A. J.; Plitz, I.; Amatucci, G. G. *Journal of The Electrochemical Society* **2012**, *159* (4), A370-A379. DOI: 10.1149/2.016204jes
10. Ehteshami, N.; Eguia-Barrio, A.; de Meatza, I.; Porcher, W.; Paillard, E. *Journal of Power Sources* **2018**, *397*, 52-58. DOI: 10.1016/j.jpowsour.2018.07.004
11. Song, S.-W.; Richardson, T. J.; Zhuang, G. V.; Devine, T. M.; Evans, J. W. *Electrochimica Acta* **2004**, *49* (9-10), 1483-1490. DOI: 10.1016/s0013-4686(03)00930-7
12. Duncan, H.; Salem, N.; Abu-Lebdeh, Y. *Journal of The Electrochemical Society* **2013**, *160* (6), A838-A848. DOI: 10.1149/2.088306jes
13. Jeong, S.-K.; Inaba, M.; Iriyama, Y.; Abe, T.; Ogumib, Z. *Electrochemical and Solid-State Letters* **2003**, *6* (1), A13-A15. DOI: 10.1149/1.1526781
14. Jeong, S.-K.; Seo, H.-Y.; Kim, D.-H.; Han, H.-K.; Kim, J.-G.; Lee, Y. B.; Iriyama, Y.; Abe, T.; Ogumi, Z. *Electrochemistry Communications* **2008**, *10* (4), 635-638. DOI: 10.1016/j.elecom.2008.02.006
15. Suo, L.; Hu, Y. S.; Li, H.; Armand, M.; Chen, L. *Nat Commun* **2013**, *4*, 1481. DOI: 10.1038/ncomms2513
16. Yamada, Y.; Yaegashi, M.; Abe, T.; Yamada, A. *Chem Commun (Camb)* **2013**, *49* (95), 11194-6. DOI: 10.1039/c3cc46665e
17. Yamada, Y.; Furukawa, K.; Sodeyama, K.; Kikuchi, K.; Yaegashi, M.; Tateyama, Y.; Yamada, A. *J Am Chem Soc* **2014**, *136* (13), 5039-46. DOI: 10.1021/ja412807w
18. Yamada, Y.; Usui, K.; Chiang, C. H.; Kikuchi, K.; Furukawa, K.; Yamada, A. *ACS Appl Mater Interfaces* **2014**, *6* (14), 10892-9. DOI: 10.1021/am5001163
19. Qian, J.; Henderson, W. A.; Xu, W.; Bhattacharya, P.; Engelhard, M.; Borodin, O.; Zhang, J. G. *Nat Commun* **2015**, *6*, 6362. DOI: 10.1038/ncomms7362
20. Wang, J.; Yamada, Y.; Sodeyama, K.; Chiang, C. H.; Tateyama, Y.; Yamada, A. *Nat Commun* **2016**, *7*, 12032. DOI: 10.1038/ncomms12032
21. Lee, J.; Lee, Y.; Lee, J.; Lee, S. M.; Choi, J. H.; Kim, H.; Kwon, M. S.; Kang, K.; Lee, K. T.; Choi, N. S. *ACS Appl Mater Interfaces* **2017**, *9* (4), 3723-3732. DOI: 10.1021/acsami.6b14878

22. Yamada, Y.; Yamada, A. *Chemistry Letters* **2017**, *46* (8), 1056-1064. DOI: 10.1246/cl.170284
23. Zeng, P.; Han, Y.; Duan, X.; Jia, G.; Huang, L.; Chen, Y. *Materials Research Bulletin* **2017**, *95*, 61-70. DOI: 10.1016/j.materresbull.2017.07.018
24. Dokko, K.; Watanabe, D.; Ugata, Y.; Thomas, M. L.; Tsuzuki, S.; Shinoda, W.; Hashimoto, K.; Ueno, K.; Umebayashi, Y.; Watanabe, M. *J Phys Chem B* **2018**, *122* (47), 10736-10745. DOI: 10.1021/acs.jpcc.8b09439
25. Yim, C.-H.; Tam, J.; Soboleski, H.; Abu-Lebdeh, Y. *Journal of The Electrochemical Society* **2017**, *164* (6), A1002-A1011. DOI: 10.1149/2.1601704jes
26. Hwang, S.; Kim, D.-H.; Shin, J. H.; Jang, J. E.; Ahn, K. H.; Lee, C.; Lee, H. *The Journal of Physical Chemistry C* **2018**, *122* (34), 19438-19446. DOI: 10.1021/acs.jpcc.8b06035
27. Yim, C.-H.; Abu-Lebdeh, Y. A. *Journal of The Electrochemical Society* **2018**, *165* (3), A547-A556. DOI: 10.1149/2.0641803jes
28. Farhat, D.; Ghamouss, F.; Maibach, J.; Edström, K.; Lemordant, D. *ChemPhysChem* **2017**, *18* (10), 1333-1344.
29. Ugata, Y.; Tatara, R.; Ueno, K.; Dokko, K.; Watanabe, M. *J Chem Phys* **2020**, *152* (10), 104502. DOI: 10.1063/1.5145340
30. Kameda, Y.; Umebayashi, Y.; Takeuchi, M.; Abdul Wahab, M.; Fukuda, S.; Ishiguro, S.-i.; Sasaki, M.; Amo, Y.; Usuki, T. *J Phys Chem B* **2007**, *111*, 6104 - 6109.
31. Seo, D. M.; Borodin, O.; Han, S.-D.; Boyle, P. D.; Henderson, W. A. *Journal of The Electrochemical Society* **2012**, *159* (9), A1489-A1500. DOI: 10.1149/2.035209jes
32. Malinovsky, M. *Chem. zvesti* **1976**, *30* (6), 721 - 729.
33. Ugata, Y.; Thomas, M. L.; Mandai, T.; Watanabe, M. *Physical Chemistry Chemical Physics* **2019**, *21*, 9759-9768.
34. Hayamizu, K.; Akiba, E.; Bando, T.; Aihara, Y. *The Journal of Chemical Physics* **2002**, *117* (12), 5929-5939. DOI: 10.1063/1.1501279
35. Watanabe, M.; Dokko, K.; Ueno, K.; Thomas, M. L. *Bulletin of the Chemical Society of Japan* **2018**, *91* (11), 1660-1682. DOI: 10.1246/bcsj.20180216
36. Hayamizu, K.; Aihara, Y.; Arai, S.; Martinez, C. G. *J Phys Chem B* **1999**, *103* (3), 519-24. DOI: 10.1021/jp9825664
37. Hou, J.; Li, J.; Mountz, D.; Hull, M.; Madsen, L. A. *Journal of Membrane Science* **2013**, *448*, 292-299. DOI: 10.1016/j.memsci.2013.08.019
38. Zhang, X.; Kostecki, R.; Richardson, T. J.; Pugh, J. K.; Ross, P. N. J. *Journal of The Electrochemical Society* **2001**, *148* (12), A1341-A1345. DOI: 10.1149/1.1415547
39. Yang, H.; Kwon, K.; Devine, T. M.; Evans, J. W. *Journal of The Electrochemical Society* **2000**, *147* (12), 4399-4407.
40. Trahan, M. J.; Mukerjee, S.; Plichta, E. J.; Hendrickson, M. A.; Abraham, K. M. *Journal of The Electrochemical Society* **2012**, *160* (2), A259-A267. DOI: 10.1149/2.048302jes
41. Laoire, C. O.; Mukerjee, S.; Abraham, K. M. *J. Phys. Chem. C* **2009**, *113*, 20127-20134.
42. Yadegari, H.; Franko, C. J.; Banis, M. N.; Sun, Q.; Li, R.; Goward, G. R.; Sun, X. *J Phys Chem Lett* **2017**, *8* (19), 4794-4800. DOI: 10.1021/acs.jpcl.7b02227
43. Reeve, Z. E.; Franko, C. J.; Harris, K. J.; Yadegari, H.; Sun, X.; Goward, G. R. *J Am Chem Soc* **2017**, *139* (2), 595-598. DOI: 10.1021/jacs.6b11333

44. Belova, A. I.; Kwabi, D. G.; Yashina, L. V.; Shao-Horn, Y.; Itkis, D. M. *The Journal of Physical Chemistry C* **2017**, *121* (3), 1569-1577. DOI: 10.1021/acs.jpcc.6b12221
45. Laoire, C. O.; Mukerjee, S.; Abraham, K. M.; Plichta, E. J.; Hendrickson, M. A. *J. Phys. Chem. C* **2010**, *114*, 9178–9186.
46. Heine, J.; Hilbig, P.; Qi, X.; Niehoff, P.; Winter, M.; Bieker, P. *Journal of The Electrochemical Society* **2015**, *162* (6), A1094-A1101. DOI: 10.1149/2.0011507jes
47. Stewart, J. J. P. *MOPAC2016*, 20.191M; Stewart Computational Chemistry: 2016.
48. Klamt, A.; Schüürmann, G. *Journal of the Chemical Society, Perkin Transactions 2* **1993**, (5), 799-805. DOI: 10.1039/P29930000799
49. Wohlfarth, C. *Static dielectric constant of hexanedinitrile: Datasheet from Landolt-Börnstein - Group IV Physical Chemistry · Volume 27: "Static Dielectric Constants of Pure Liquids and Binary Liquid Mixtures" in SpringerMaterials ([https://doi.org/10.1007/978-3-662-48168-4\\_116](https://doi.org/10.1007/978-3-662-48168-4_116))*, Springer-Verlag Berlin Heidelberg.

## 6 – Highly Concentrated NaTFSI – Adiponitrile Electrolytes for Na-Ion and Na-O<sub>2</sub> Batteries

This chapter is an adapted version of an article that is currently in preparation for submission to the *Journal of the Electrochemical Society*. The co-authors are Breanna L. Pinto, Olivia Velenosi, Mirna Alhanash, Fabian Åren, Chae-Ho Yim, Patrik Johansson, Yaser Abu-Lebdeh, and Gillian R. Goward. The author was responsible for electrolyte preparation, physical stability tests, NMR characterizations, and preparation of the manuscript. Electrochemical characterizations were conducted by the author with the assistance of Breanna L. Pinto. Na<sub>3</sub>V<sub>2</sub>(PO<sub>4</sub>)<sub>2</sub>F<sub>3</sub> (NVPF) was synthesized by Olivia Velenosi. Differential scanning calorimetry (DSC) data collection was collected by Chae-Ho Yim and Yaser Abu-Lebdeh. Molecular dynamics (MD) simulations were conducted by Mirna Alhanash, Fabian Åren, and Patrik Johansson.

Sodium bis(trifluoromethanesulfonyl)imide (NaTFSI) and adiponitrile (ADN) have attractive high stability and safety properties for application as electrolytes in Na-ion batteries, but are unusable in modern cells due to significant Al corrosion by NaTFSI, and spontaneous ADN degradation by Na metal. In this chapter, the electrochemical properties of NaTFSI – ADN electrolytes are investigated as a function of concentration. The ionic conductivity and phase diagram of NaTFSI – ADN is measured, and molecular dynamics (MD) simulations give insight into the solution structure of the electrolyte. The reductive stability of the electrolyte is found to increase drastically with concentration in cyclic voltammetry (CV) experiments, and the parasitic dissolution of Al by TFSI decreases with concentration in linear

sweep voltammetry (LSV) and chronoamperometry (CA) tests. In Na-ion cells, the dual effect of reductive stability enhancement and Al corrosion suppression allows the 4.4 M electrolyte to reversibly intercalate high voltage  $\text{Na}_3\text{V}_2(\text{PO}_4)_2\text{F}_3$  (NVPF) cathodes for multiple cycles, while no NVPF intercalation is observed with the standard 1.0 M electrolyte. Na- $\text{O}_2$  cells also benefit from the highly concentrated electrolyte, showing significantly longer lifetimes in CV experiments on Na- $\text{O}_2$  coin cells. Concentrating NaTFSI – ADN electrolytes offer practical benefits to Na batteries and should be implemented with further stabilizing strategies going forward.

## 6.1 – Introduction

Lithium-ion batteries (LIBs) are becoming increasingly important in modern society as electric vehicles continue to gain popularity and see widespread market adoption. The global EV market share has increased from 2 to 9 % from 2021 to 2022 alone.<sup>1</sup> As the demand on battery production continues to grow, the limited lithium supply on Earth becomes an ever apparent issue. This has sparked interest in sodium-based battery technologies in recent years. Na has comparatively limitless reserves on Earth compared to Li (23600 ppm Na to 20 ppm Li), and the price of raw sodium carbonate ( $\text{Na}_2\text{CO}_3$ ) as of 2019 is roughly just \$150 per ton, compared to \$13,000 per ton for lithium carbonate ( $\text{Li}_2\text{CO}_3$ ).<sup>2</sup>

Two candidates for sodium-based battery technologies are sodium-ion batteries (SIBs) and sodium-oxygen batteries (NaOBs). NaOBs have drastic energy density advantages, reaching up to 1100 Wh  $\text{kg}^{-1}$  (compared to 550 Wh  $\text{kg}^{-1}$  for  $\text{LiCoO}_2$  based LIBs) but suffer from serious instability issues that limit the lifetime of the cell to just a few cycles at their current state.<sup>3</sup> SIBs are much more reliable in comparison, with

state of the art cells able to achieve close to 100% capacity retention after 150 cycles, however the energy density struggles to compete with that of the LIB, reaching just 360 Wh kg<sup>-1</sup>.<sup>4,5</sup>

One way to improve energy density in SIBs is to utilize higher voltage cathode materials, such as the NASICON-type Na<sub>3</sub>V<sub>2</sub>(PO<sub>4</sub>)<sub>2</sub>F<sub>3</sub> (NVPF), which intercalate above 4 V (Na / Na<sup>+</sup>).<sup>6</sup> The exploration of higher voltage cathode materials calls for additional investigations into alternative electrolyte systems with better oxidation tolerance than the standard sodium hexafluorophosphate (NaPF<sub>6</sub>) in ethylene carbonate (EC) and diethyl carbonate (DEC) electrolyte mixtures that are currently used, which start to degrade at 4.2 V (Na / Na<sup>+</sup>).<sup>7</sup> Recently, electrolytes utilizing an adiponitrile (ADN) solvent have gained significant research attention in LIBs for their unmatched oxidative stability, up to 6.0 V vs Li / Li<sup>+</sup>, which corresponds to approximately 5.7 V vs Na / Na<sup>+</sup>.<sup>8,9</sup> The stability of these systems comes from the exceptional tolerance of the nitrile group to oxidation in ADN.<sup>8</sup> Indeed, research has shown that the choice of electrolyte solvent has a significantly higher influence on the electrochemical and thermal stability of the total electrolyte system than the choice of electrolyte salt.<sup>10</sup> ADN unfortunately comes with the downside of being unable to form stable solid electrolyte interface (SEI) layers after reduction on graphite electrodes.<sup>8</sup> The addition of co-solvents and co-salts, such as ethylene carbonate (EC) and lithium bis(oxalato)borate (LiBOB), are needed to fully stabilize the nitril by getting preferentially reduced at the negative electrode to form a passivating SEI, stopping ADN from being parasitically reduced.<sup>8</sup> Additionally, LiPF<sub>6</sub> is well known to contribute to a healthy fluoride containing SEI, but has very low solubility in ADN and thus alternative salts need to be used.<sup>8,11</sup>

Lithium bis(trifluoromethanesulfonyl)imide (LiTFSI) is a promising candidate for a salt pairing with ADN due to the stability of the TFSI anion to hydrolysis, and subsequent HF formation.<sup>12</sup> ADN has also been shown to significantly lessen the well-studied phenomenon of Al corrosion by TFSI at the positive electrode,<sup>8, 13</sup> although the process is not completely avoided. Full alleviation of Al corrosion can be achieved with further addition of co-salts or electrolyte additives such as lithium tetrafluoroborate (LiBF<sub>4</sub>) or fluoroethylene carbonate (FEC).<sup>14, 15</sup> Along with the previously mentioned EC and LiBOB additives needed to stabilize ADN at the negative electrode, electrolyte compositions can easily become quite complex when trying to prevent both ADN reduction and TFSI Al corrosion, which one would like to avoid when working with a relatively new battery system such as the SIB.

An alternative strategy that has gained traction in LIB literature is the use of highly concentrated electrolytes to avoid using complex additives. In 2014, Yamada et al. found that LiTFSI in acetonitrile (AN) electrolytes exhibited excellent reductive stability at concentrations above 4 M, producing stable SEI layers in early cycles,<sup>16</sup> while a critical evaluation found these electrolytes to be problematic when used high voltage LIB cells.<sup>17</sup> On the cathode side, Matsumoto et al. have observed passivation of the Al current collector, to avoid further decomposition, in LiTFSI in EC / DEC electrolytes at concentrations of just 1.8 M, leading to drastic improvements in cycling lifetime.<sup>18</sup> McOwen et al. extended this further to 7.5 M solutions of LiTFSI in single solvent EC, showing complete passivation of Al in Li coin cells.<sup>19</sup>

The intriguing benefits of concentrated electrolytes have not gone unnoticed in the SIB community. Several experimental and computational studies have explored the properties of highly concentrated Na electrolytes,<sup>20-25</sup> with one notable study

exploring high concentration NaTFSI in propylene carbonate (PC).<sup>24</sup> The study, conducted by Geng et al. observed similar truncation of Al corrosion by TFSI at high concentration that was seen by Matsumoto and McOwen et al. in Li cells.<sup>24</sup> To the knowledge of this author, there have been no attempts to combine the attractive properties of high concentration NaTFSI with the oxidative stability of ADN in the SIB system, nor are there any reports on the use of ADN as an electrolyte solvent in SIBs in general.

Previously we conducted a study on the physical and electrochemical properties of LiTFSI – ADN electrolytes at ranging compositions, and found significant changes in the transport behaviour of Li<sup>+</sup> in the electrolyte at high concentrations.<sup>9</sup> Herein we extend this study to NaTFSI – ADN electrolytes in the context of SIBs. The physical properties such as ionic conductivity and melting temperature of the electrolyte as a function of concentration are determined, and the solution structure of the electrolyte is further explored by molecular dynamics (MD) simulations. The reductive stability of ADN is found to improve dramatically as concentration increases, resulting in improved reversibility in Na deposition and stripping in cyclic voltammetry (CV) experiments. Further, it is found that corrosion of the Al current collector by TFSI is significantly hindered at high concentrations. Lastly, these interesting properties are applied to NaOB and SIB coin cells, leading to long-term stable cycling in Na-O<sub>2</sub> CV experiments, and reversible intercalation in Na || NVPF half cells, phenomenon that are not observed for the standard 1.0 M electrolyte.

## 6.2 – Experimental

### 6.2.1 – Electrolyte Preparation

Adiponitrile (99%, Millipore Sigma) was degassed via three cycles of the freeze pump thaw method before being brought into an Ar filled glovebox to be further dried over 3 Å molecule sieves for one week before using. NaTFSI (99.5%, Solvionic) was used as received. NaTFSI and ADN were mixed in glass vials. NaTFSI readily dissolved in ADN until concentrations of about 2 M, where gentle heating was applied to reach full dissolution. The 4.4 M ((ADN)<sub>2</sub>(NaTFSI)<sub>1</sub>) and 2.9 M ((ADN)<sub>3</sub>(NaTFSI)<sub>1</sub>) solutions are gel-like solids at room temperature, while the 2.2 M ((ADN)<sub>4</sub>(NaTFSI)<sub>1</sub>) solutions is mostly a clear liquid, with a gel precipitate forming on the bottom of the vial occasionally. Solutions of 1.75 M ((ADN)<sub>5</sub>(NaTFSI)<sub>1</sub>) and lower are consistently liquid at room temperature.

### 6.2.2 – Electrode Preparation

Cathode slurries were prepared by mixing synthesized NVPF, polyvinylidene fluoride (PVDF, Atofina, Kynar 741, >99 %), and Super P carbon (Alfa Aesar, >99 %) in weight percentages of 75, 15, and 10 respectively in N-Methyl-2-pyrrolidone (NMP) solvent for 24 hr. The ratio of NMP solvent to powder was 4.2 to 1. After the slurries were thoroughly mixed, they were cast with a doctor blade on Al foil to a height of 500 µm. Cathodes were dried in a vacuum oven overnight at 120 °C before being punched as circular electrodes with a diameter of 1.27 cm. Finished electrodes were dried once again overnight in the vacuum oven at 120 °C and brought into the Ar-filled glovebox.

### 6.2.3 – Electrochemical Characterization

All materials used for battery preparation were stored in an Ar-filled glovebox (MBraun). Na-ion and Na-O<sub>2</sub> cells were prepared in a coin-cell geometry. Coin cells were of the 2032 format and the tops of cells were modified to have holes for O<sub>2</sub> gas diffusion for Na-O<sub>2</sub> cells. For all cells, pure Na metal pressed onto a stainless-steel spacer was used as the anode and two punches of Whatman glass fibre (type GF/A) were used as separators. Na-ion cells were constructed in the order: NVPF cathode, 40 µL electrolyte, glass fibre separator, 40 µL electrolyte, glass fibre separator, 40 µL electrolyte, Na metal anode. Na-O<sub>2</sub> cells were constructed similarly except with the Na anode on the bottom and carbon paper cathode on top, and with a stainless-steel mesh current collector above the cathode. Fabricated Na-O<sub>2</sub> cells were sealed in air-tight chambers before being brought out of the glove box and getting repeatedly vacuumed and subsequently charged with O<sub>2</sub> (Linde, 4.5, 99.995 %) in triplicate to ensure an ample supply of O<sub>2</sub> gas.

Completed coin cells were tested on a Gamry Interface 5000 for linear sweep voltammetry (LSV), chronoamperometry (CA), cyclic voltammetry (CV), and electrochemical impedance spectroscopy experiments (EIS) experiments. EIS experiments used to measure ionic conductivity were collected on a two-electrode vial cell with Pt counter and working electrodes. The cell constant was previously measured using a standard aqueous 0.01 M NaCl solution of known ionic conductivity. Spectra were collected from 5000 to 1 Hz.

EIS experiments on cycled Na || NVPF half cells were collected from 1 MHz to 0.01 Hz, with an AC voltage of 10 mV. EIS spectra were collected at the top of charge (4.4 V) and bottom of discharge (2 V) of galvanostatic cycling. Cells were cycled to the

corresponding voltage with a constant applied current, after which a constant voltage hold was applied to ensure the cell reached an equilibrium state at said voltage. The EIS experiment was then collected with a constant DC offset equal to the final voltage of the cell. This method ensures the cell is at the assumed state of charge throughout the entire EIS experiment.

LSV and CV datasets were collected with a scan rate of 10 mV s<sup>-1</sup>. LSV, CA, and CV datasets concerning Al corrosion (**Fig. 6.5**) were collected on coin cells using a Na metal reference / counter electrode and a bare Al foil punch as a working electrode. CV datasets concerning Na deposition and dissolution (**Fig 2**) were collected on three-electrode cells using a Pt counter and Pt working electrodes, and a Na metal reference electrode.

## 6.3 – Results and Discussion

### 6.3.1 – Transport and Physical Properties

Electrolytes composed of NaTFSI salt in ADN solvent were made in a wide concentration range from 0.1 M to 4.4 M, corresponding to approximate compositions of (NaTFSI)<sub>1</sub>(ADN)<sub>88</sub> to (NaTFSI)<sub>1</sub>(ADN)<sub>2</sub>, or  $\chi_{\text{NaTFSI}} = 0.01$  to  $\chi_{\text{NaTFSI}} = 0.33$  (where  $\chi_{\text{NaTFSI}}$  refers to the NaTFSI molar composition), respectively. Each of the electrolyte solutions appeared as colourless, transparent liquids in the 0.1 M to 1.75 M ((NaTFSI)<sub>1</sub>(ADN)<sub>5</sub>,  $\chi_{\text{NaTFSI}} = 0.17$ ) range. The 2.2 M ((NaTFSI)<sub>1</sub>(ADN)<sub>4</sub>,  $\chi_{\text{NaTFSI}} = 0.2$ ) solution is physically observed to be a transparent liquid at ambient conditions on some days, with a translucent, amorphous, gel-like precipitate appearing at times. Inconsistent crystallization behaviour has been observed

previously for the LiTFSI – ADN analogue by Watanabe et al. and our group separately,<sup>9, 26</sup> and this behaviour carries over to the NaTFSI – ADN system.

The unique phase transformations of these electrolytes are evident when examining the phase diagram built from differential scanning calorimetry (DSC) measurements (**Fig. 6.1a**). Individual DSC thermatograms and description for each sample are provided in the supporting information (**Fig. 6.9S**). The most dilute solution, at 0.1 M ( $\chi_{\text{NaTFSI}} = 0.01$ ), has three distinct transitions: a melting point near that of pure ADN (2 °C, black circles), a eutectic transition at -21 °C (blue circles), and a low temperature devitrification (cold crystallization) event -32 °C (purple circles). Devitrification events are characteristic of amorphous glassy solids.<sup>27</sup> This transition suggests that stable  $(\text{NaTFSI})_x(\text{ADN})_y$  aggregates crystallize out of the amorphous solid electrolyte upon heating.<sup>27</sup> This fits well with the observed amorphous nature of the solid-state samples, and the observed behaviour of the high concentration samples to sporadically precipitate gel-like solvates. This phenomenon has been observed for the LiTFSI – ADN analogues previously, where the  $(\text{LiTFSI})(\text{ADN})_2$  composition was found to crystallize even in dilute compositions,<sup>9, 26</sup> and is unique to ADN in the dinitrile series of systems.<sup>26</sup>

As more NaTFSI is added to the electrolyte the melting point decreases steadily up to the 1.25 M ( $\chi_{\text{NaTFSI}} = 0.12$ ) electrolyte. In this range the eutectic transition stays relatively constant and forms the expected solidus line. In contrast, the devitrification event undergoes much more significant changes. From 0.1 to 0.5 M ( $\chi_{\text{NaTFSI}} = 0.01$  to  $\chi_{\text{NaTFSI}} = 0.05$ ) the devitrification peak increases gradually with temperature, until the event overlaps with the eutectic transition at 0.5 M ( $\chi_{\text{NaTFSI}} = 0.05$ ). Then in the 0.8 to

1.25 M ( $\chi_{\text{NaTFSI}} = 0.08$  to  $\chi_{\text{NaTFSI}} = 0.12$ ) range, the devitrification event suddenly drops to a significantly lower temperature of  $-62$  °C at 0.8 M ( $\chi_{\text{NaTFSI}} = 0.08$ ), and begins a much sharper increase in temperature. This suggests a new stable solvate is forming in this concentration range.

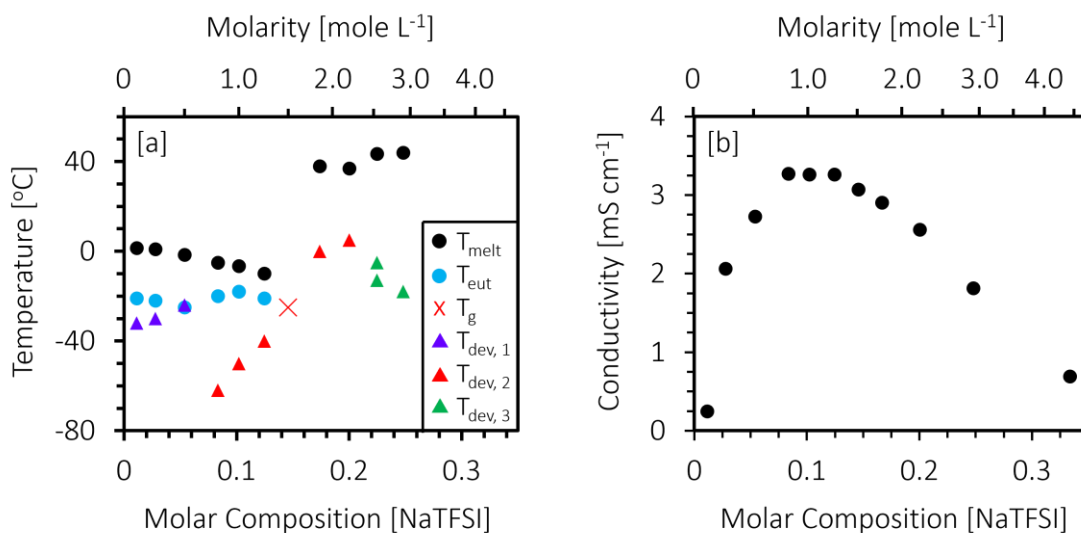


**Figure 6.1.** NaTFSI – ADN (a) Phase diagram measured by DSC and (b) Room temperature ionic conductivity isotherm measured by EIS. In the phase diagram legend:  $T_{\text{melt}}$  stands for melting point,  $T_{\text{eut}}$  is eutectic transition temperature,  $T_{\text{g}}$  is glass transition temperature, and  $T_{\text{dev}}$  is devitrification transition temperature.

A crystallization gap is observed at 1.5 M, as the sample repeatedly shows no discernible peaks in the DSC thermatogram. A glass transition temperature is discernable at this concentration at  $-24$  °C (red “x”), but is not identified in any other sample. After the crystallinity gap, in the 1.85 to 4.4 M ( $\chi_{\text{NaTFSI}} = 0.17$  to  $\chi_{\text{NaTFSI}} = 0.33$ ) range, the melting point has significantly increased to  $38$  °C in 1.85 M ( $\chi_{\text{NaTFSI}} = 0.17$ ) electrolyte, and steadily increases from there. No eutectic transitions is observed in this range, and the devitrification event follows the expected linear trajectory until the 2.55 M sample where the devitrification temperature drops once

again, perhaps again indicating the formation of a higher concentration solvate. It is clear from the phase diagram the NaTFSI – ADN electrolyte undergo significant changes as concentration increases.

The ionic conductivity of each sample was measured by EIS and plotted as a function of concentration in **Fig. 6.1b**. Initially ionic conductivity increases rapidly with concentration as the number of charge carriers in solution increases from 0.1 to 0.8 M, and then plateaus in the 0.8 to 1.25 M region. The 1.0 M sample is taken as the concentration of maximum conductivity ( $C_{\max}$ ) with a value of  $3.26 \pm 0.05 \text{ mS cm}^{-1}$ , as it rests in the centre of the plateau and the measured conductivity of each sample is within error of the others (0.8 M:  $3.27 \pm 0.05 \text{ mS cm}^{-1}$ , 1.0 M:  $3.26 \pm 0.05 \text{ mS cm}^{-1}$ , 1.25 M:  $3.26 \pm 0.05 \text{ mS cm}^{-1}$ ). This value is higher than the maximum conductivity of  $2.3 \text{ mS cm}^{-1}$  measured for the LiTFSI – ADN system.<sup>9</sup> Generally, Na electrolytes have higher ionic conductivities than their Li counterparts due to the lower charge density and thus relative “softness”, in terms of hard-soft acid-base (HSAB) theory, of the Na cation compared to Li.<sup>28, 29</sup> This leads to lesser cation-solvent attraction, allowing  $\text{Na}^+$  to move more freely.

After this plateau, ionic conductivity begins to decrease for the 1.5 to 4.4 M samples. The highest concentration sample, 4.4 M, has a room temperature conductivity of just  $0.69 \text{ mS cm}^{-1}$ . The drop in conductivity at high concentrations is much more gradual for NaTFSI – ADN than what we measured previously for LiTFSI – ADN.<sup>9</sup> For example, the ionic conductivity of 1.0 M NaTFSI – ADN is 40 % larger than that of 1.0 M LiTFSI – ADN, whereas the value of the 2.9 M Na sample is 200 % larger than that of the 2.9 M Li sample ( $3.26$  vs  $2.3 \text{ mS cm}^{-1}$  and  $1.81$  vs  $0.6 \text{ mS cm}^{-1}$ , respectively).<sup>9</sup> Increasing viscosity is typically attributed as the main factor for

decreased conductivity at high concentrations, and studies have shown that Na-based electrolytes tend to have slower increases in viscosity with concentration than Li-based systems, again likely due to lesser ionic interactions between Na and the TFSI pair.<sup>28, 30</sup>

Interestingly, this drop in conductivity coincides with the post-eutectic crystallinity gap and subsequent jump in melting point temperatures in the phase diagram. It has been shown previously that, in addition to viscosity-based effects, the conductivity isotherm is also highly dependant on structural changes within solution, and is intimately related to the phase diagram as a result.<sup>9, 31, 32</sup> For example, the LiTFSI – ADN analogue was shown to transition toward an ion-hopping mechanism at post-eutectic concentrations, from the commonly reported vehicular mechanism at moderate concentrations.<sup>9</sup> In order to probe similar solution structure effects in NaTFSI – ADN, MOPAC simulations of the electrolytes for different concentrations were performed.

The cumulative partial coordination numbers (pCNs) for  $\text{Na}^+ - \text{N}_{\text{ADN}}$  (**Fig. 6.2a**),  $\text{Na}^+ - \text{O}_{\text{TFSI}}$  (**Fig. 6.2b**), and  $\text{Na}^+ - \text{F}_{\text{TFSI}}$  (**Fig. 6.2c**) show large differences between ADN and TFSI coordination. The NaTFSI(ADN)<sub>11</sub> composition (approx. 0.8 M) has no ADN coordination until approximately 1.8 Å, where the cumulative pCN sharply increases to a stable plateau at 3.7. No additional  $\text{N}_{\text{ADN}}$  coordination is seen until a radial distance of approximately 3.8 Å, where a second, more gradual, increase is observed. This behaviour remains as the NaTFSI concentration is increased, with the pCN plateau decreasing from 3.7 for NaTFSI(ADN)<sub>11</sub> to 2.0 for NaTFSI(ADN)<sub>2</sub> (approx. 4.4 M). The sharp increase, and subsequent plateau, implies that ADN solvates  $\text{Na}^+$  in an ordered, network-like fashion; all ADN are found at a specific

distance and no other ADN are arranging within the solvation structure. The pCN plateau of 2.0 also implies that there is no free, uncoordinated ADN in  $\text{NaTFSI}(\text{ADN})_2$ .

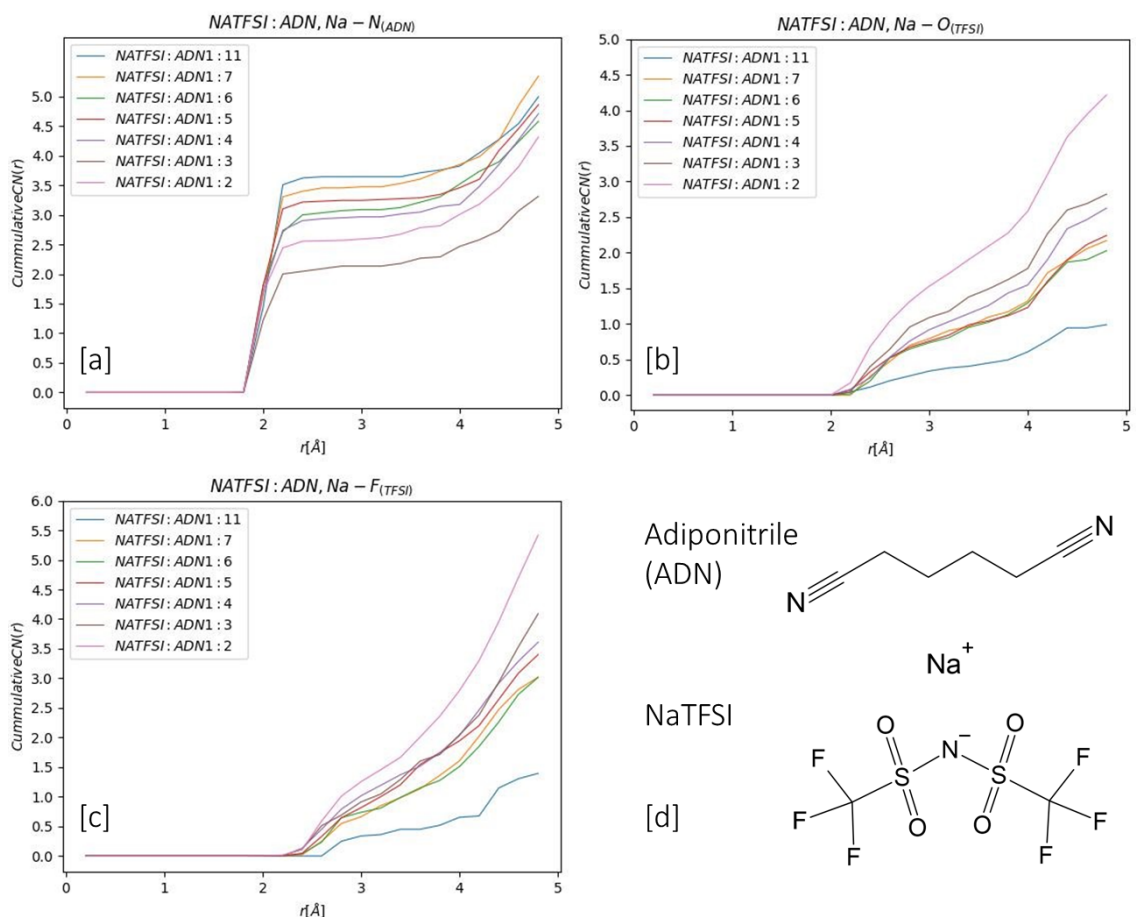


**Figure 6.2.** Calculated cumulative pCNs for (a) Na and N, (b) Na and O, and (c) Na and F in NaTFSI – ADN.

In contrast, both  $\text{Na}^+ - \text{O}_{\text{TFSI}}$  and  $\text{Na}^+ - \text{F}_{\text{TFSI}}$  cumulative pCNs show a much more gradual increase. Coordination begins at a distance of approximately 2.2 Å for  $\text{O}_{\text{TFSI}}$  and 2.6 Å for  $\text{F}_{\text{TFSI}}$ , for the most dilute composition,  $\text{NaTFSI}(\text{ADN})_{11}$ , and the gradual increase continues throughout the entire radial distance. This behavior is consistent for all compositions. The initial  $\text{Na}^+ - \text{O}_{\text{TFSI}}$  and  $\text{Na}^+ - \text{F}_{\text{TFSI}}$  distances

decrease slowly with concentration, while the slope of the cumulative pCN line increases with concentration. This behaviour is indicative of TFSI arranging itself disorderedly around  $\text{Na}^+$ , in stark contrast to the plateau behaviour observed for ADN.

Altogether, this paints a picture of a solvation structure consisting of an ordered  $\text{Na}^+$  – ADN network, with TFSI filling the free volume voids. Such ordered networks have been directly observed via x-ray crystallography for the similar lithium bis(fluorosulfonyl)imide (LiTFSI) – ADN system by Ugata et al.<sup>33</sup>, and indirectly by Raman spectroscopy for LiTFSI – glutaronitrile (GN) by the same group.<sup>26</sup> These structures, however, also involve ordered TFSI arrangements, which is not the case here. This can be explained by significantly weaker  $\text{Na}^+$  – TFSI interactions due to the relative softness of  $\text{Na}^+$  when compared to  $\text{Li}^+$ , and fits well with our findings of NaTFSI – ADN being significantly more amorphous, with less distinct phase transitions, than the LiTFSI – ADN analogue.<sup>9</sup>

### 6.3.2 – Electrochemical Stability.

As discussed thoroughly in the introduction, a number of studies have found significantly enhanced electrochemical stability in highly concentrated electrolytes.<sup>16, 18, 20, 23-25</sup> Two of the most significant findings that concern the currently studied NaTFSI – ADN system are the enhanced reductive stability of the nitrile group of ADN to alkali metals,<sup>16</sup> and the dampening of Al corrosion by TFSI at high voltages.<sup>18</sup> In order to test the stability of NaTFSI – ADN electrolytes to Na metal, small pieces of Na metal were placed in the electrolytes and observed over a period of 48 hr (**Fig. 6.3**).

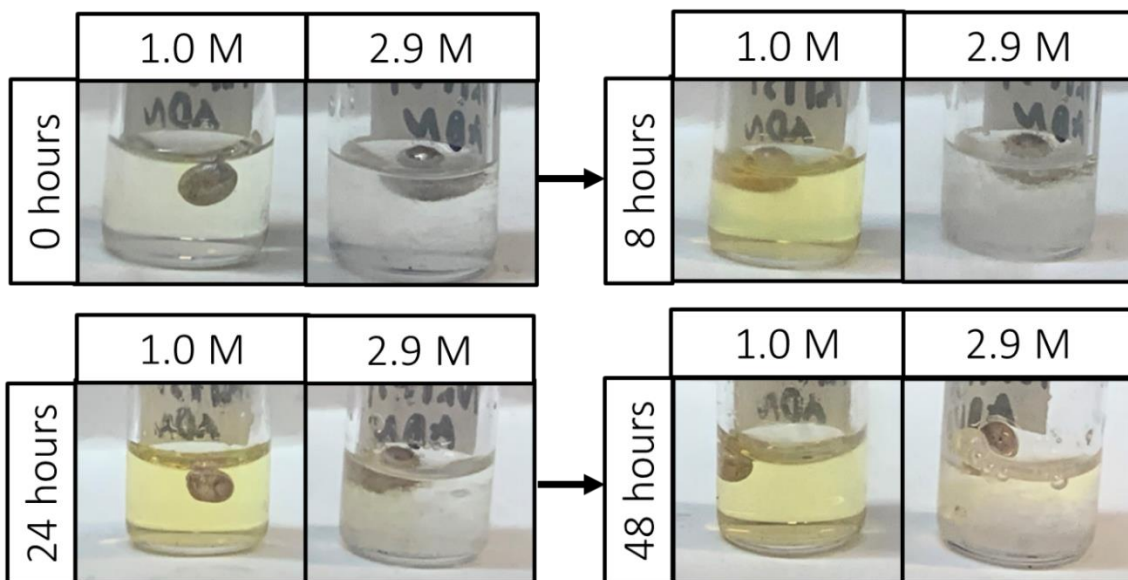


**Figure 6.3.** Reactivity of NaTFSI – ADN electrolyte to Na metal at various concentrations.

The dilute 0.1 M NaTFSI – ADN electrolyte is very unstable toward the reductive Na metal. The nitrile groups of ADN are reduced to form the characteristic yellow colour of reduced organic nitriles.<sup>16,34</sup> The yellow colour comes from a polymerization product that has been observed for both mono and dinitriles when reduced by alkali metals.<sup>34</sup> This reduction is suppressed in the higher concentration 2.9 M sample, which has no visible change even after being in contact with the Na metal for 24 hours. After 2 days have passed, the 2.9 M sample is starting to show a faint yellow colour, signifying some decomposition is occurring. This experiment indicates that concentrating NaTFSI – ADN electrolytes allows the system to overcome the poor reductive stability of ADN. The mechanism for this phenomenon was explored by Yamada et al. for similar stability enhancements in the LiTFSI in acetonitrile (ACN) system.<sup>16</sup> They found through MD simulations that in dilute solutions the lowest unoccupied molecular orbital (LUMO) of the system is that of the nitrile solvent (ACN), whereas in concentrated solutions the LUMO belongs to the TFSI anion,

causing preferential reduction of TFSI instead of the nitrile solvent, and resulting in passivating fluoride containing degradation products on the anode which protect the solvent from further reduction.<sup>16</sup>

In order to test the electrochemical ramification of this stability enhancement, CV of the NaTFSI – ADN electrolyte solutions was conducted in three-electrode cells using a Na metal reference electrode, and Pt wire counter and working electrodes. The cyclic voltammograms for the 1.0 M and 4.4 M electrolytes are shown in **Fig. 6.4a** and **Fig. 6.4b**, respectively. Further voltammograms are given for the entire concentration range in the SI (**Fig. 6.12S**). Each electrolyte possesses the characteristic wide electrochemical stability window of ADN, being stable up to 6 V vs Na / Na<sup>+</sup>. There is however a small irreversible peak at 4 V that is consistent across samples. This peak is not assigned to any particular degradation pathway at this time, although it is clear that the runaway parasitic degradation of the solution does not occur until higher voltages.

The reductive stability of the electrolyte was measured by the analysis of the reversible Na sodium deposition and dissolution event at 0 V. **Fig. 6.4c** and **Fig. 6.4d** show the same CV curves expanded in the low voltage sodium deposition region. It is clear that the high concentration 4.4 M sample displays much smoother Na deposition and dissolution events than the lower concentration, 1.0 M electrolyte. Na deposition also appears to be much more reversible in the higher concentration sample, a phenomenon that has been observed in both the LiTFSI – ACN and LiTFSI – DMSO systems as well.<sup>16, 25</sup> At even lower concentrations, such as 0.25 M, the Na dissolution event is barely present, signalling that the deposition process is thoroughly irreversible (**Fig. 6.12Sb**).

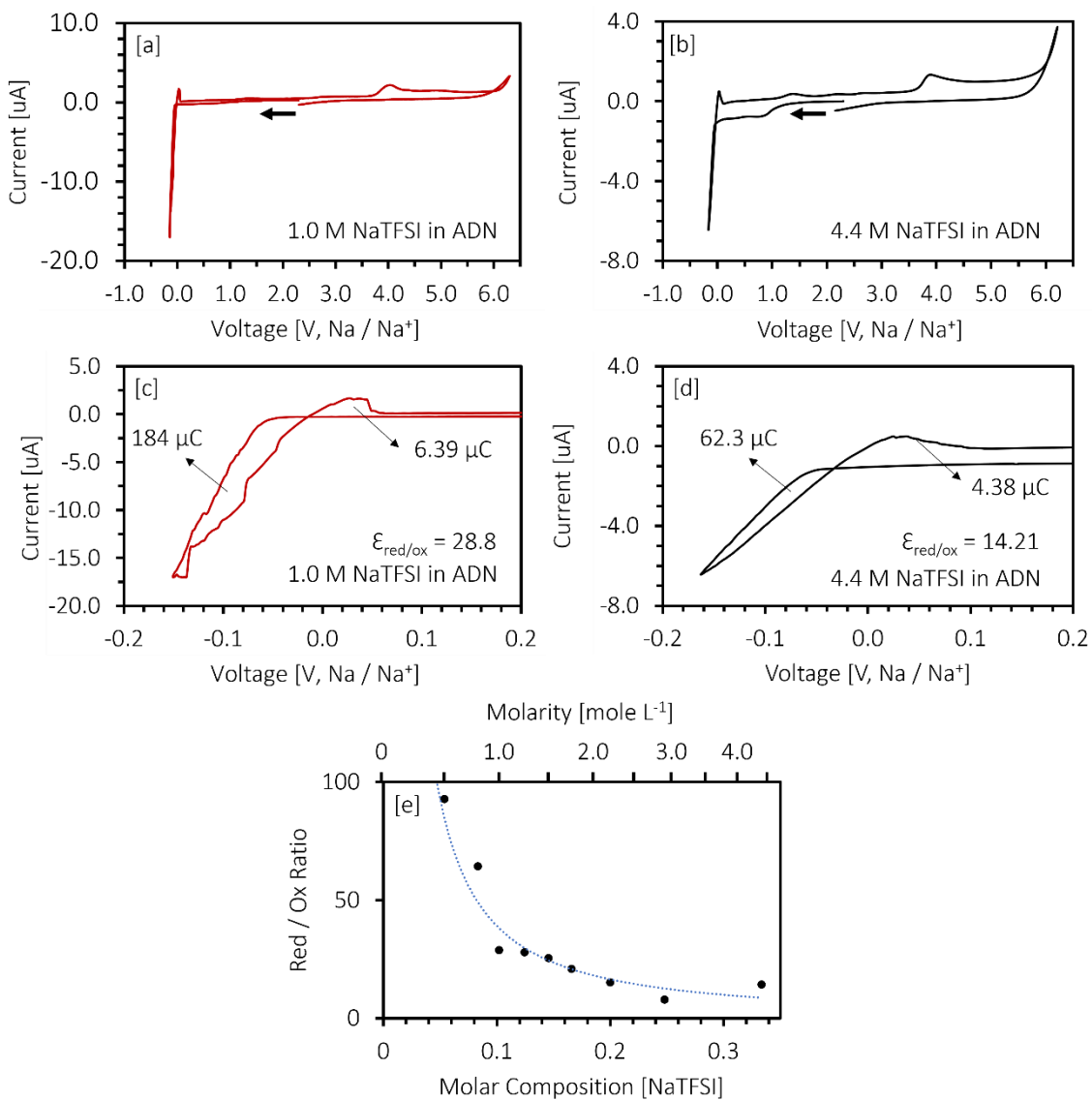


**Figure 6.4.** Cyclic voltammograms of (a) 1.0 M and (b) 2.9 M NaTFSI – ADN. (c – d) The same data sets zoomed into the Na deposition and dissolution region, showing the integrals of the reduction (deposition) and oxidation (dissolution) events, as well as the ratio of the two “ $\epsilon_{\text{red/ox}}$ ”. (e)  $\epsilon_{\text{red/ox}}$  shown as a function of concentration for NaTFSI – ADN electrolytes.

To quantify this, the integral of both the reduction and oxidation regions of the CV curve were taken for each sample, and the ratio of the integral areas ( $\epsilon_{\text{cv}}$ ) was calculated and plotted against concentration in **Fig 6.4e**. There is a distinct trend of decreasing  $\alpha_{\text{cv}}$  as concentration increases, with the minimum being observed for the

2.9 M (NaTFSI(ADN)<sub>3</sub>) sample. This behaviour is a direct consequence of the enhanced reductive stability of the high concentration samples to Na metal. In the low concentration samples, plated Na metal is immediately passivated by the polymerization degradation reaction of ADN and is unable to be reversibly oxidized. This is corroborated by physical observation of the electrolyte solutions gaining a yellow tint after CV experiments. At higher concentrations, as the electrolyte becomes more stable to Na, the Na formed upon reduction is not immediately consumed and the deposition is reversible.

### 6.3.3 – Application to Na-O<sub>2</sub> Batteries.

The enhanced reductive stability at high concentrations, paired with the inherent high oxidative stability of ADN, makes concentrated NaTFSI – ADN electrolytes an attractive choice for use in NaOB systems. Due to the highly oxidizing atmosphere, NaOB electrolytes are prone to oxidative decomposition during the charging process, which approaches voltages of 4.5 V vs Na / Na<sup>+</sup>.<sup>35-37</sup> As such, more oxidatively stable electrolytes need to be examined in the context of NaOBs to improve the viability of the system. One of the reasons nitriles have not yet been considered as candidates is because the NaOB uses a Na metal anode to achieve their quoted extremely high gravimetric capacities on discharge,<sup>3</sup> which of course is unfeasible with dilute nitrile electrolytes as shown in the previous section. To test the effect of the observed reductive stability enhancements on the NaOB system, Na-O<sub>2</sub> coin cells were made with Na metal anodes and carbon paper gas diffusion layer cathodes. CVs were collected for the C<sub>max</sub> sample of 1.0 M NaTFSI – ADN (**Fig. 6.5a**), as well as the high concentration 2.2 M (**Fig. 6.5b**), 2.9 M (**Fig. 6.5c**), and 4.4 M (**Fig. 6.5d**) NaTFSI – ADN samples.

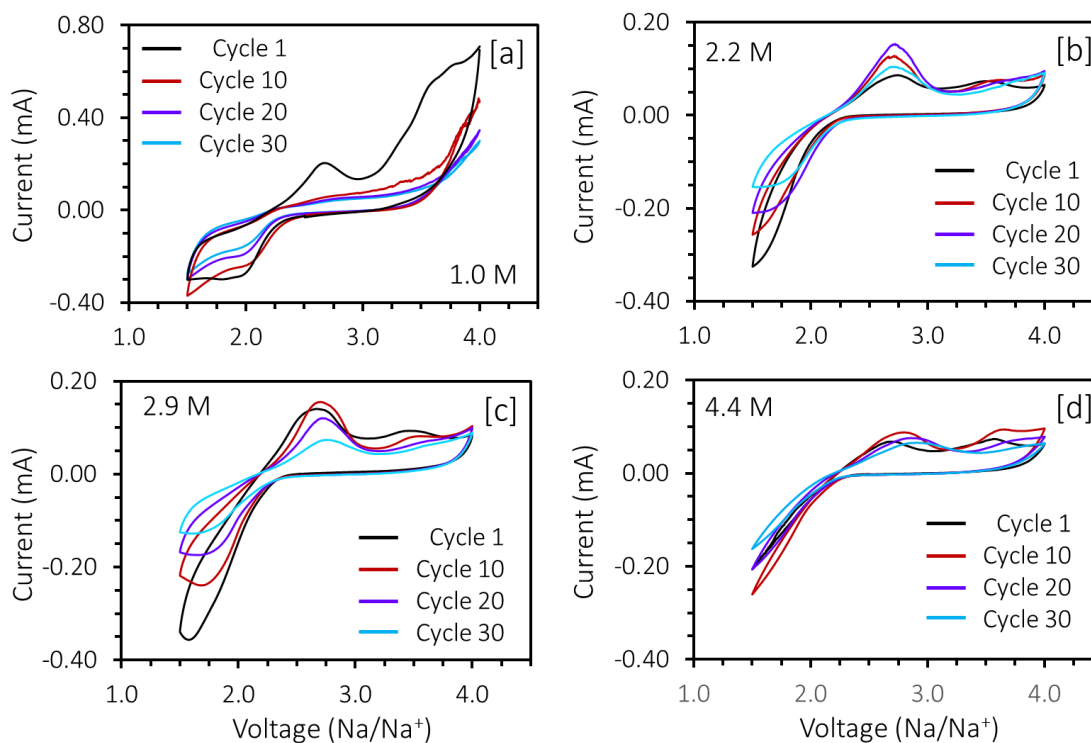


**Figure 6.5.** Cyclic voltammograms of NaOB coin cells using (a) 1.0 M, (b) 2.2 M, (c) 2.9 M, and (d) 4.4 M NaTFSI – ADN electrolytes. Note: the 1.0 M cell is using different y-axis limits to show the large degradation peak.

In the initial cathodic sweep for each cell, there is a reduction event at approximately 2.2 V that corresponds to the oxygen reduction reaction (ORR), and resulting formation of  $\text{NaO}_2$ .<sup>38</sup> On the reverse anodic sweep, the oxygen evolution reaction (OER) is observed at approximately 2.7 V for each sample, corresponding to the degradation of  $\text{NaO}_2$  formed on reduction. In the 1.0 M sample alone, a higher voltage runaway degradation peak is observed at an onset of 3.0 V, signalling electrolyte deterioration. This earlier onset electrolyte decomposition in the presence of Na metal is also observed below in CVs of Na metal coin cells. In subsequent cycles of the 1.0 M sample, the ORR is significantly hindered and there is no discernable

OER peak. Nonetheless, ADN degradation is still observed as the 4.0 V limit is approached.

In the highly concentrated samples, the 3.0 V degradation event observed in the 1.0 M cell is not present, and each cell is able to reversibly undergo the ORR and OER for the full 30 cycles. In each sample however, the ORR current response is tempered as cycle count increases, indicating that the gas diffusion layer cathode is still being passivated over time. Supporting this is the observation of additional peaks observed at 3.5 V and 4.0 V in each of the high concentration samples. These are characteristic of the degradation of sodium peroxide dehydrate ( $\text{Na}_2\text{O}_2 \cdot \text{H}_2\text{O}$ ) that forms from  $\text{NaO}_2$  disproportionation after discharge, and the degradation of sodium carbonate ( $\text{Na}_2\text{CO}_3$ ) formed by  $\text{NaO}_2$  attack of the carbon cathode surface at 3.5V and 4.0V respectively.<sup>35, 39-41</sup> The disproportionation of  $\text{NaO}_2$  to  $\text{Na}_2\text{O}_2 \cdot \text{H}_2\text{O}$  requires a proton source that can either be supplied by  $\text{H}_2\text{O}$  impurities in the electrolyte or from ADN degradation.<sup>39, 42</sup> ADN degradation is certainly plausible, as the high concentration samples did eventually begin to degrade in the stability tests (**Fig. 6.3**), particularly with extended cycling. The effect of cell degradation is lowest in the highest concentration 4.4 M electrolyte, although we also observe that the ORR and OER activity is lower in this cell than in the 2.2 M and 2.9 M samples. This is likely due to the 4.4 M sample being thoroughly solid at room temperature, while the 2.2 M and 2.9 M samples are a viscous liquid and soft gel, respectively. The NaOB discharges through a solution-based formation mechanism that relies on dissolved  $\text{O}_2$  gas in the electrolyte for an efficient ORR,<sup>41, 42</sup> and it has been shown previously that  $\text{O}_2$  solubility can indeed increase with concentration in TFSI-based electrolytes, resulting in higher ORR activity.<sup>43</sup> This effect is observed here for the highly concentrated 2.2

and 2.9 M cells, but as the electrolyte becomes fully solid in the 4.4 M sample, O<sub>2</sub> solubility is likely hindered by the low concentration of free ADN and TFSI molecules, as observed by MD simulations for this composition, and subsequently the ORR and OER activities suffer. Nonetheless, NaTFSI – ADN is shown to be a viable candidate for use in NaOBs at high concentration. Further experiments at elevated cycling temperature could be undertaken to fully explore the viability of these concentrated electrolytes, although negative impacts in terms of side reactions are plausible.

#### 6.3.4 – Aluminum Corrosion Resistance.

As discussed in the introduction, the use of LiTFSI and NaTFSI in moderate concentrations has been avoided in both LIBs and SIBs due to significant Al corrosion of the cathode current collector around 3.5 V vs Na / Na<sup>+</sup>.<sup>44</sup> Concentrating the LiTFSI salt has shown to significantly suppress the observed Al corrosion,<sup>18, 19</sup> but to best of our knowledge no such effect has been measured for organic electrolytes in SIBs. To test NaTFSI – ADN electrolytes for Al corrosion, coin cells were constructed with Na metal counter electrodes and bare Al foil working electrodes, and were subject to LSV, CA, and CV experiments (**Fig. 6.6**).

The LSV experiments show a distinct inverse correlation between concentration and current response (**Fig. 6.6a**). As voltage is increased, Al corrosion begins at approximately 3.5 V vs Na / Na<sup>+</sup>, which is the same onset voltage observed by Matsumoto et al. in the NaTFSI – EC / DEC system.<sup>18</sup> The peak current observed drops from 50. mA cm<sup>-2</sup> in the 1.0 M cell, to just 1.1 mA cm<sup>-2</sup> in the 4.4 M cell. This represents a significant drop in Al corrosion in the highly concentrated sample. The mechanism of Al corrosion in TFSI-containing electrolytes is likely complex and involves a number of reaction pathways,<sup>45</sup> nonetheless recent investigations suggest

that the TFSI anion is too stable to form passivating  $F^-$  containing products on the Al surface. As a result, Al is continually oxidized and leeches into the electrolyte to form Al-TFSI complexes in solution.<sup>19</sup> When the electrolyte is highly concentrated the lack of free solvent and anion molecules makes Al dissolution less favourable, and any Al-TFSI complexes that form are likely insoluble, again due to the lack of free solvent molecules, and therefore passivate the Al surface.<sup>19</sup>

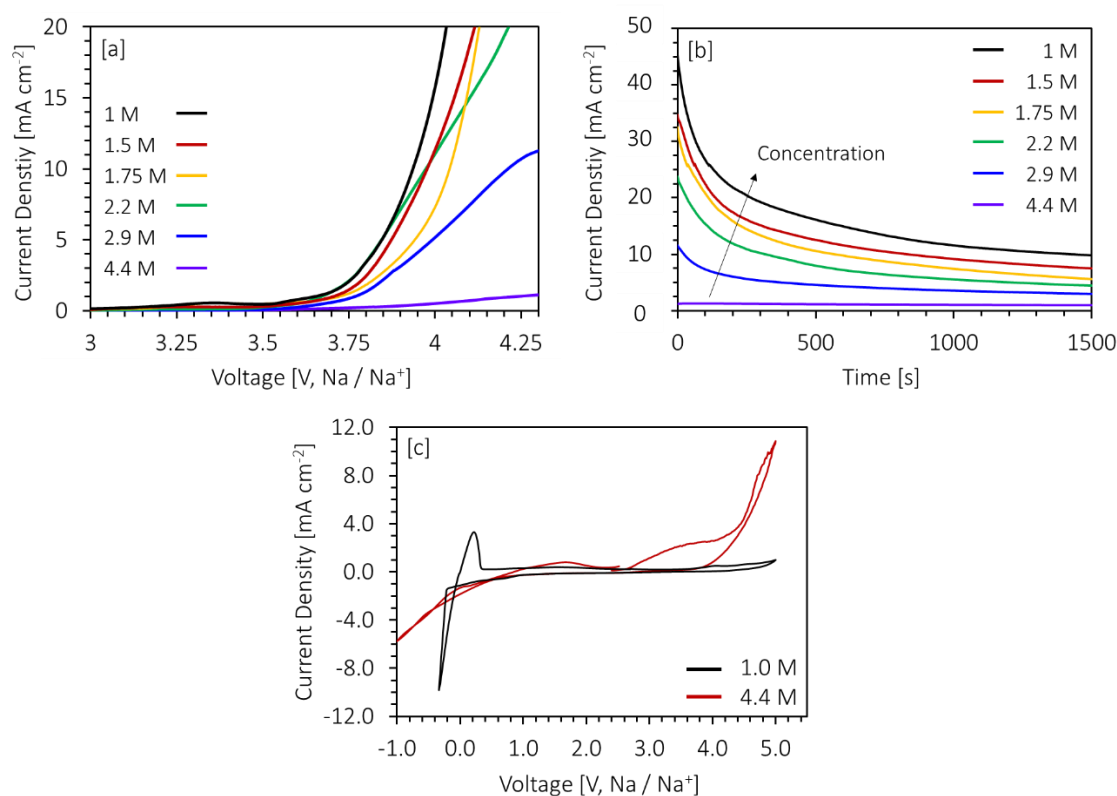


**Figure 6.6.** [a] LSV of Na || Al coin cells with a range of electrolyte concentrations from 3 to 4.3 V vs Na / Na<sup>+</sup>. [b] CA of the same Na || Al coin cells held at 4.3 V vs Na / Na<sup>+</sup> directly after LSV experiments. [c] CV of Na || Al coin cells of 1.0 M and 4.4 M coin cells.

The suppression of Al corrosion is further emphasized by the CA experiments performed immediately after LSV by holding the voltage for 25 minutes after reaching the 4.3 V cut off (**Fig. 6.6b**). In each sample, Al corrosion continues throughout the

entire timeframe, but the current response tappers off to final value of  $9.8 \text{ mA cm}^{-2}$  in the 1.0 M sample, and just  $0.94 \text{ mA cm}^{-2}$  in the 4.4 M cell.

To visualize the dual effects of the enhanced reductive stability to Na metal displayed in **Fig. 6.3** and **Fig. 6.4**, and the reduced rate of Al corrosion observed in the LSV and CA experiments, CVs were taken of the 1.0 M and 4.4 M Na || Al cells over the entire Na deposition and Al corrosion regions (**Fig. 6.6c**). When in the presence of the large Na metal electrode, the 1.0 M electrolyte is unable to undergo reversible Na dissolution, likely due to the rapid reduction and polymerization of ADN on the Na surface as observed in **Fig. 6.3**. The 4.4 M electrolyte on the other hand, undergoes extremely reversible Na dissolution in the coin cell format with an  $\alpha_{cv}$  ratio of just 2.6. As the cells approach higher voltages on the anodic sweep, the 1.0 M cell undergoes a significant irreversible oxidation event starting at just 2.7 V, before the expected Al corrosion event. This is similar to the oxidation event observed in the NaOB CV experiments, and likely involves side products from the significant ADN degradation observed in the previous cathodic sweep at the Na electrode. The 4.4 M cell in contrast is stable throughout the entire anodic sweep as expected from the lack of Al corrosion in the LSV experiments. Considering the reversibility of Na dissolution on the anodic sweep for the 4.4 M sample, no additional oxidative events stemming from ADN degradation products, like that observed in the 1.0 M sample, are expected. The CV experiments demonstrate the multifaceted improvement in stability seen in concentrated NaTFSI – ADN electrolytes.

### 6.3.5 – Half Cell Cycling.

To investigate how the additional stability to Al corrosion translates to practical applications, Na || NVPF coin half cells were constructed with both 1.0 M and 4.4 M

NaTFSI – ADN electrolytes and subjected to galvanostatic cycling from 2 to 4.4 V vs Na / Na<sup>+</sup> for 5 cycles. To solely test the effect of the observed stability enhancements on the charge / discharge behaviour of the cells, and not the rate capability, a low current density of C/20 was used for each cycle. The resulting galvanostatic cycling curves are shown in **Fig. 6.7**.

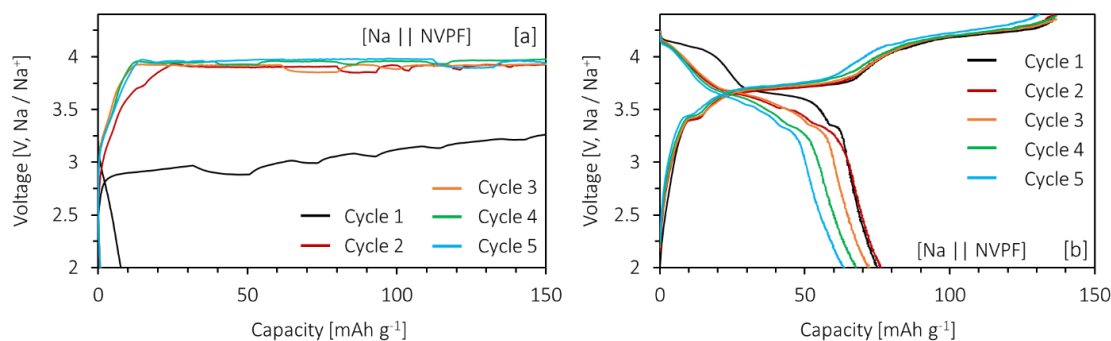


**Figure 6.7.** Galvanostatic cycling curves of Na || NVPF half cells employing [a] 1.0 M NaTFSI – ADN electrolyte and [b] 4.4 M NaTFSI – ADN electrolyte. The x-axis is stated in mAh g<sup>-1</sup> of NVPF.

In the 1.0 M cell, a significant degradation event begins at 2.75 V and the voltage continues to increase gradually in an unstable manner for the remainder of the charge period. The theoretical capacity of NVPF is 128 mA g<sup>-1</sup>, and the material typically undergoes 3 distinct redox events on charge: a relatively small capacity redox event at 3.4 V, a large plateau at 3.6 V, and a second large plateau at 4.1 V.<sup>6, 46</sup> Each of these redox events are higher in voltage than the observed degradation process of the 1.0 M cell. The onset voltage of 2.75 V for the process observed in the 1.0 M half cell agrees with the oxidative degradation event observed in the CV experiment on the Na || Al coin cell using 1.0 M NaTFSI – ADN (**Fig. 6.6c**). Examining the discharge curve, the 1.0 M cell achieves little to no reversible capacity, reaching just 9 mAh g<sup>-1</sup>, confirming that the process observed on charge was indeed the result of cell deterioration, and

not Na insertion into NVPF. In cycles 2 – 5, cell voltage quickly increases to 3.5 V, and continues a sloping increase to 4.0 V, where Al corrosion occurs for the rest of the charging period. Again, this agrees well with the LSV on Na || Al coin cells where the onset of Al corrosion was 3.5 V and the degradation current response increased exponentially to 4 V.

The 4.4 M half cell shows much improved cycling behaviour. Each of the three expected redox plateaus are visible, albeit at slightly higher voltages of 3.4, 3.7, and 4.2 V, possibly due to the relatively high impedance of the solid 4.4 M electrolyte compared to liquid electrolytes used in literature. The cell experiences a significant irreversible capacity, discharging to 75 mAh g<sup>-1</sup> after charging to 136 mAh g<sup>-1</sup> in the first cycle, but is able to recoup the majority of the full charging capacity in each of the five cycles. Nonetheless, the cell is clearly able to intercalate and deintercalate sodium into the NVPF cathode, and no degradation processes are observed. The highly concentrated electrolyte shows significant improvement over the 1.0 M cell.

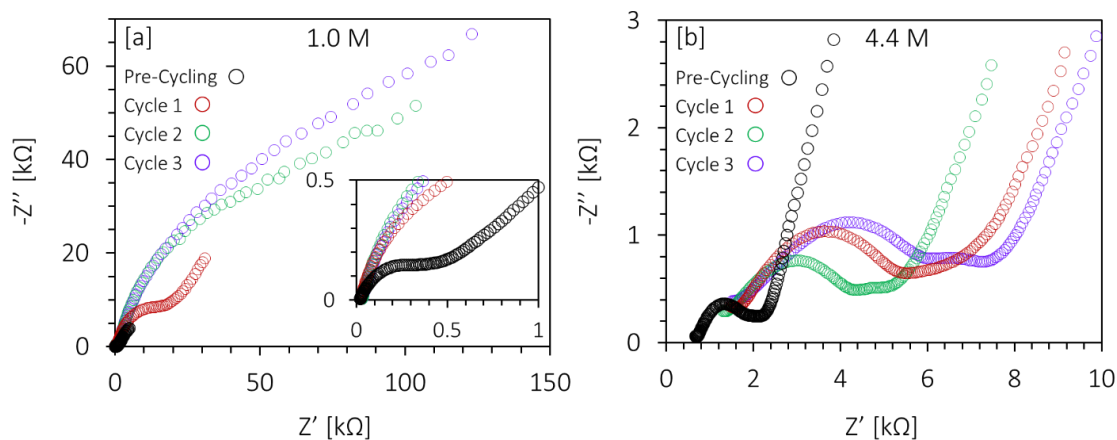


**Figure 6.8.** EIS spectra collected using a frequency range of 1 MHz to 0.01 Hz of Na || NVPF half-cells employing [a] 1.0 M NaTFSI – ADN electrolyte and [b] 4.4 M NaTFSI – ADN electrolyte. The entire frequency range is shown in both figures, and the inset in [a] zooms in on the uncycled 1.0 M cell to emphasize the initially low impedance.

The enhanced stability of the 4.4 M cell is supported further by examining the EIS spectra of each Na || NVPF half-cell during cycling (**Fig. 6.8**). In the initial EIS spectra, taken immediately after cell construction (black), the 1.0 M cell has a significantly lower internal resistance than the 4.4 M analogue (**Fig. 6.8a** (inset) and **Fig. 6.8b**, respectively), corresponding to the significantly higher ionic conductivity of the 1.0 M electrolyte (**Fig. 6.1b**). After a single cycle however (red), the impedance of the 1.0 M cell has drastically increased, to the extent where the entire spectrum of the as-constructed cell is engulfed in the resistive semi-circle of the cycled cell. The 4.4 M cell also experiences an increase in impedance, but the effect is much more reasonable given the lack of extreme degradation events observed during cell cycling. This affect is exacerbated in further cycles in the 1.0 M cell, as further Al corrosion, and likely ADN decomposition, is experienced. While in contrast, the 4.4 M cell experiences a drop in impedance after cycle two, before experiencing a further increase in impedance in later cycles. The eventual increase in cell impedance in the 4.4 M coin cell is expected, as the cell does experience significant capacity fade over time (**Fig. 6.7b**), but the effect is not nearly as extreme as what is observed for the 1.0 M coin cell, which does not undergo any reversible electrochemical processes in the galvanostatic cycling experiments.

The strategy of concentrating electrolytes to improve electrochemical stability has proven fruitful in Na || NVPF half cells. Significant cycling improvements stemming from enhanced reductive stability to Na metal, and improved resistance to Al dissolution, are observed in the 4.4 M system relative to the 1.0 M system, which undergoes no desirable electrochemical processes. Further studies on Na-ion full cells

may prove rewarding since the reductive Na metal would be removed from the system entirely.

## 6.4 – Conclusions

The physiochemical properties of NaTFSI – ADN across a wide concentration range were explored. The phase diagram of the electrolyte was constructed and is representative of an amorphous glass-like system. This is corroborated by MD simulations of the electrolyte, which show the electrolyte arranges itself in a Na<sup>+</sup> – ADN network, with the TFSI anion amorphously filling the void space between the Na and ADN constituents.

The concentrated NaTFSI – ADN electrolytes show desirable electrochemical properties when compared to the moderately concentrated counterparts. The reductive stability of ADN to Na metal increases significantly at high concentrations, especially in the 4.4 M (NaTFSI(ADN)<sub>2</sub>) system. This leads to measurably better Na deposition and dissolution ability by the electrolyte at high concentrations. On the cathode side, the well-studied phenomenon of Al corrosion by the TFSI anion is also drastically suppressed. The dual effect of the additional reductive stability and resistance to Al corrosion significantly improves Na || NVPF half cell cycling. Na || NVPF coin cells using a standard NaTFSI – ADN 1.0 M electrolyte undergo no reversible intercalation chemistry with NVPF, while the 4.4 M electrolyte is able to reversibly deintercalate / intercalate high voltage NVPF cathodes. For the next steps in studying this electrolyte system, we suggest extending the high concentration system to include cosolvents such as EC, which has proven useful in further stabilizing

ADN in LiTFSI – ADN electrolytes,<sup>8</sup> or FEC, which has shown to be effective in forming passivating SEI layers at both the anode and cathode in dinitrile systems.<sup>47</sup>

## 6.5 – Supporting Information

### 6.5.1 – Differential Scanning Calorimetry & Phase Diagram Construction

DSC thermatograms used for building the phase diagram are given in **Fig. 6.9S**. The highest temperature endothermic peak in each DSC thermatogram is assigned as the melting temperature and labelled with a black circle. In the two lowest concentration samples (0.1 M and 0.25 M) there are also distinct exothermic devitrification and endothermic eutectic transition peaks, marked with purple and blue, respectively. The devitrification peak increases in temperature slowly from 0.1 and to 0.5 M, and in the 0.5 M thermatogram the eutectic transition and devitrification event appear to overlap and the eutectic transition is assigned as the sudden dip in the upward slope of the devitrification peak.

In the 0.8 sample, the devitrification peak suddenly drops significantly in temperature to -62 °C and continues to increase in temperature until the 1.25 M sample. The peak is now marked with red to signify it is a unique transition. Throughout this period the eutectic transition does not change in temperature significantly so is continually marked with blue, and the melting temperature continues decreasing slowly.

The crystallization gap then appears in the 1.5 M sample, and a glass transition temperature is observed at the temperature where we would expect the devitrification peak to appear if the current trajectory continues. It is marked with a red “x” symbol.

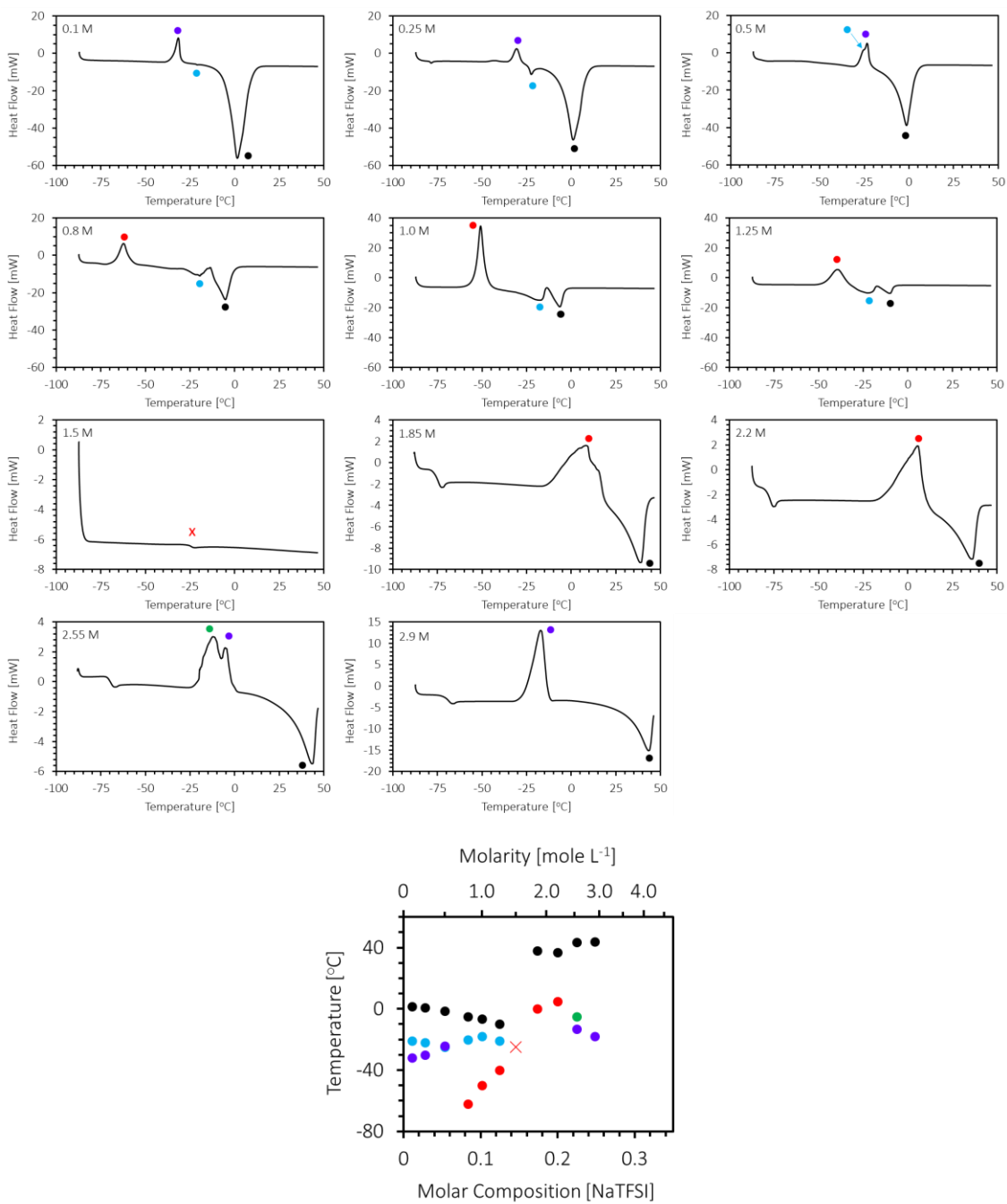


**Figure 6.9S.** DSC thermatograms for each of the NaTFSI – ADN concentrations tested. Each of the peaks in the thermatogram are labelled with the associated data point label used in the phase diagram.

The devitrification peak then appears in the next sample, at 1.85 M at 0 °C, again aligning well with the linear increase in devitrification temperature from the 0.8 to the 1.25 M sample. In the 1.85 M sample the eutectic transition is no longer observed. Interestingly, at this concentration the devitrification peak is very broad and appears to include multiple exothermic transition that are close to each other. The same phenomenon is observed in the 2.2 M sample.

In the 2.55 M sample two separate devitrification peaks are resolved, the lower temperature of which is observed near the original devitrification transition temperature of the 0.1 to 0.5 M sample, so is marked in the original purple colour. The second devitrification peak does not appear to align with any previous transition (except perhaps any exothermic transitions convoluted with the devitrification transitions in the 2.2 and 2.55 M sample), and is marked with green.

Finally in the 2.9 M sample, a single devitrification peak is observed, and again at the temperature of the original devitrification transitions in the 0.1 to 0.5 M sample. For this reason the 2.9 M peaks is also marked with purple.

### 6.5.2 – NMR Characterization

Diffusion coefficients and T1 / T2 relaxation parameters were measured on a Bruker Widebore Avance III 9.9 T spectrometer using a Bruker Diff50 gradient probe with a dual resonance  $^{23}\text{Na}$  /  $^{19}\text{F}$  insert for  $^{23}\text{Na}$  and  $^{19}\text{F}$  measurements, and a separate single resonance  $^1\text{H}$  insert for  $^1\text{H}$  measurements. Diffusion coefficients were characterized using a bipolar stimulated echo pulse sequence with a diffusion time ( $\Delta$ ) of 100 ms and a gradient pulse length ( $\delta$ ) of 2.5 ms. T1 and T2 values were measured using selective inversion and cpmg pulse sequences, respectively.

For electrochemical product characterization, cells were brought into the Ar-filled glovebox immediately after cycling and the cathode was then extracted and dried at room temperature under vacuum for approximately 1 hour. The cathode was then packed into an airtight 2.5 mm diameter solid state NMR rotor. All spectra of battery cathodes were collected on a Bruker Avance I 11.7 T spectrometer using a Bruker 2.5 mm broadband probe. Spectra were collected under MAS conditions using N<sub>2</sub> gas at a spinning speed of 30 kHz. All <sup>23</sup>Na spectra are reference to 1 M NaCl<sub>(aq)</sub> at 0 ppm.

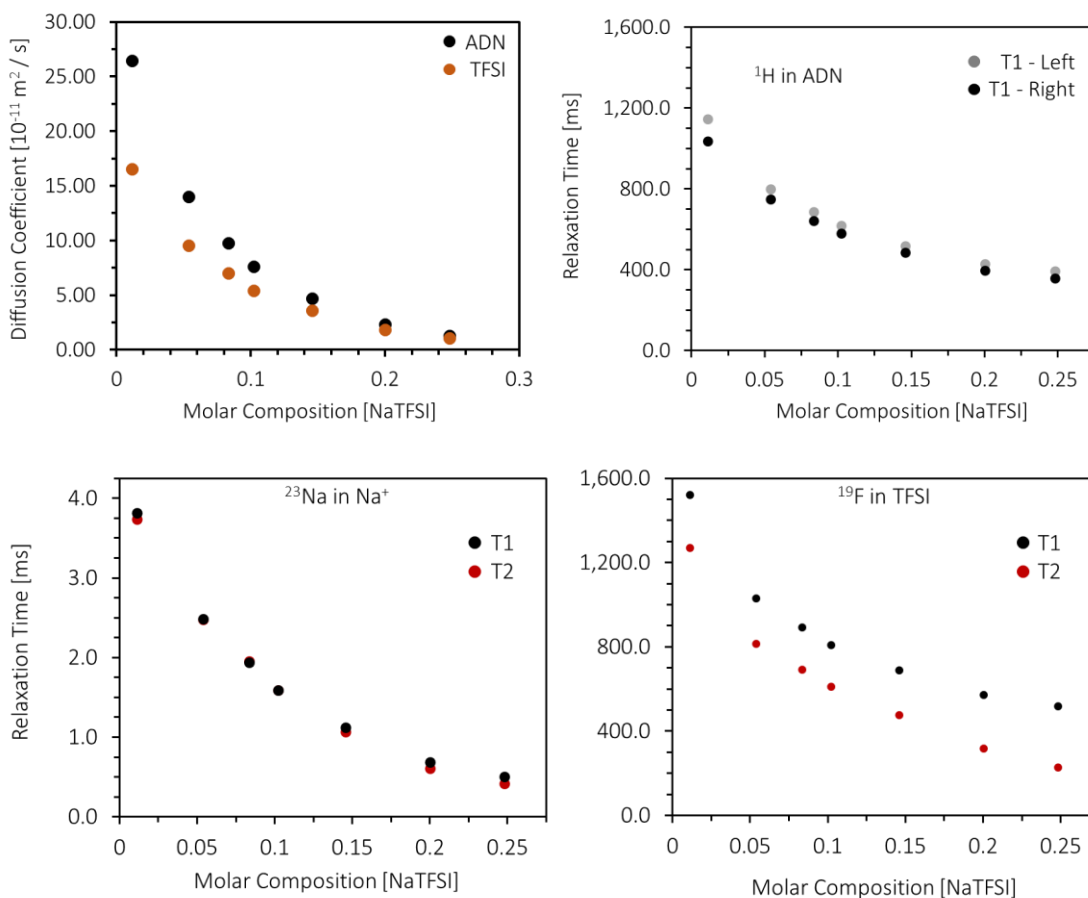


**Figure 6.10S.** [a] Diffusion coefficients of TFSI and ADN as measured by PFG <sup>19</sup>F and <sup>1</sup>H NMR respectively. [b – d] T<sub>1</sub> and T<sub>2</sub> values of [b] ADN, [c] Na<sup>+</sup>, and [d] TFSI.

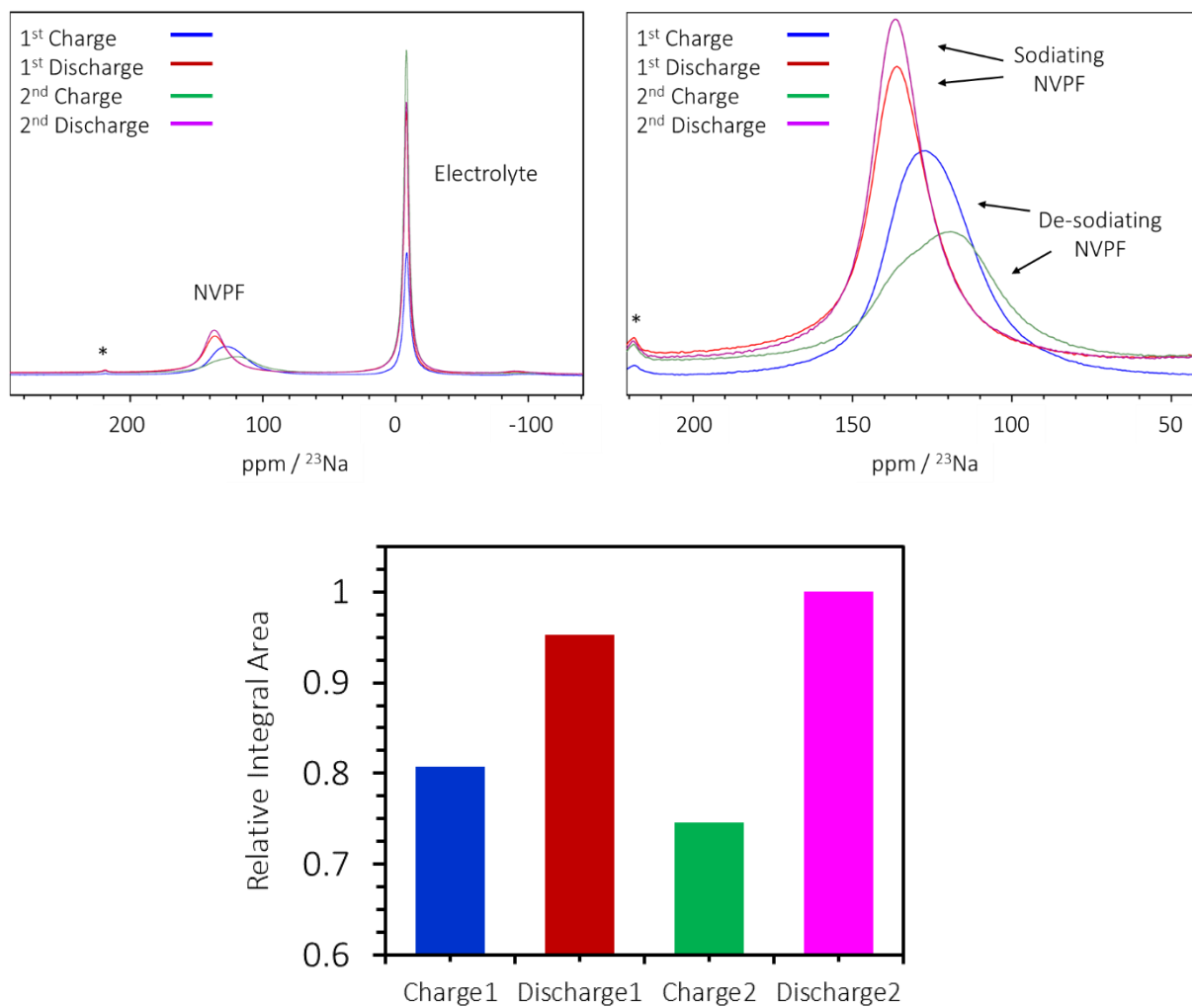


**Figure 6.11S.** [a]  $^{23}\text{Na}$  MAS ssNMR spectra of cycled NVPF cathodes at different states of charge. [b] The same spectra zoomed into the NVPF region. [c] The relative integrals of each of the NVPF peaks in the cycled sample, normalized to the amount of active NVPF material in the cathode.

### 6.5.3 – Additional Cyclic Voltammetry Data

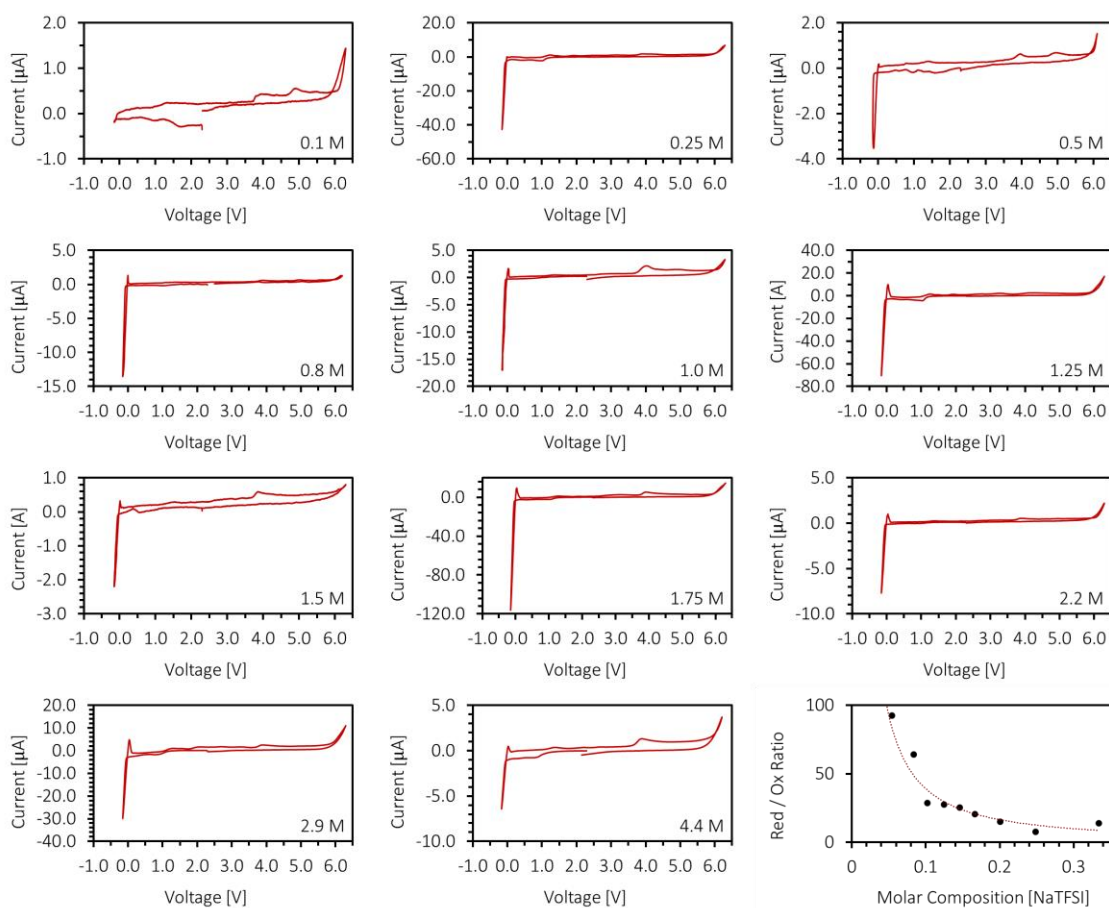


**Figure 6.12S.** Full CV voltammograms of Pt vs Pt (Na Ref.) three electrode cells using each NaTFSI – ADN concentration.

### 6.5.4 – MOPAC simulations

Semi-empirical quantum calculations were run using the PM7 functional as implemented in MOPAC 2016 version 22.067L. 30 uncorrelated simulations were performed for each of the molar ratios NaTFSI:ADN 1:2, 1:3, 1:4, 1:5, 1:6, 1:7, and 1:11, with a constant system size of 320 atoms and starting geometries generated using the CHAMPION geometry creator.<sup>48</sup>

The obtained structural data were analyzed by calculating the total and partial coordination numbers ((p)CN) of the ligands around a central sodium atom by virtue

of the nitrogen<sub>(ADN)</sub>, oxygen<sub>(TFSI)</sub>, and fluoride<sub>(TFSI)</sub> distances. First, the number of neighbours  $n_i(r)$  found within a spherical shell of volume  $V$  was used to calculate  $g_i(r)$ , to generate radial distribution functions (RDFs). The RDFs are expressed as follows,

$$g_i(r) = \frac{n_i(r)}{4\pi r^2 \Delta r} \left[ \frac{1}{\rho_i} \right] \quad [6.S1]$$

where  $\rho_i$  describes the average density of the atomic species and  $g_i(r)$  describes the average distribution of the coordinates at a distance  $r$  from a central atom, here sodium. The pCNs were subsequently calculated by integrating  $g_i(r)$  up to the first minima in the RDFs for each of the three unique coordination sites and the CNs obtained from the sum of all pCNs.

## 6.6 – References

1. IEA, Global EV Outlook 2022. IEA, Ed. IEA: Paris, 2022.
2. Hirsh, H. S.; Li, Y.; Tan, D. H. S.; Zhang, M.; Zhao, E.; Meng, Y. S. *Advanced Energy Materials* **2020**, *10* (32), DOI: 10.1002/aenm.202001274
3. Hartmann, P.; Bender, C. L.; Sann, J.; Durr, A. K.; Jansen, M.; Janek, J.; Adelhelm, P. *Phys. Chem. Chem. Phys.* **2013**, *15* (28), 11661-11672. DOI: 10.1039/c3cp50930c
4. You, Y.; Wu, X.-L.; Yin, Y.-X.; Guo, Y.-G. *Energy & Environmental Science* **2014**, *7* (5), 1643-1647. DOI: 10.1039/C3EE44004D
5. Zhou, A.; Cheng, W.; Wang, W.; Zhao, Q.; Xie, J.; Zhang, W.; Gao, H.; Xue, L.; Li, J. *Advanced Energy Materials* **2021**, *11* (2), 2000943. DOI: <https://doi.org/10.1002/aenm.202000943>
6. Song, W.; Ji, X.; Wu, Z.; Yang, Y.; Zhou, Z.; Li, F.; Chen, Q.; Banks, C. E. *Journal of Power Sources* **2014**, *256*, 258-263. DOI: 10.1016/j.jpowsour.2014.01.025
7. Ould, D. M. C.; Menkin, S.; O'Keefe, C. A.; Coowar, F.; Barker, J.; Grey, C. P.; Wright, D. S. *Angewandte Chemie International Edition* **2021**, *60* (47), 24882-24887. DOI: <https://doi.org/10.1002/anie.202111215>
8. Abu-Lebdeh, Y.; Davidson, I. *Journal of The Electrochemical Society* **2009**, *156* (1), A60-A65. DOI: 10.1149/1.3023084
9. Franko, C. J.; Yim, C.-H.; Årén, F.; Åvall, G.; Whitfield, P. S.; Johansson, P.; Abu-Lebdeh, Y. A.; Goward, G. R. *Journal of The Electrochemical Society* **2020**, *167* (16), 160532. DOI: 10.1149/1945-7111/abcf17
10. Ponrouch, A.; Marchante, E.; Courty, M.; Tarascon, J.-M.; Palacín, M. R. *Energy & Environmental Science* **2012**, *5* (9), 8572-8583. DOI: 10.1039/C2EE22258B
11. Ehteshami, N.; Paillard, E. *ECS Transactions* **2017**, *77* (1), 11-20. DOI: 10.1149/07701.0011ecst
12. Lu, Z.; Yang, L.; Guo, Y. *Journal of Power Sources* **2006**, *156* (2), 555-559. DOI: 10.1016/j.jpowsour.2005.05.085
13. Farhat, D.; Ghamouss, F.; Maibach, J.; Edström, K.; Lemordant, D. *ChemPhysChem* **2017**, *18* (10), 1333-1344.
14. Heine, J.; Hilbig, P.; Qi, X.; Niehoff, P.; Winter, M.; Bieker, P. *Journal of The Electrochemical Society* **2015**, *162* (6), A1094-A1101. DOI: 10.1149/2.0011507jes
15. Song, S.-W.; Richardson, T. J.; Zhuang, G. V.; Devine, T. M.; Evans, J. W. *Electrochimica Acta* **2004**, *49* (9-10), 1483-1490. DOI: 10.1016/s0013-4686(03)00930-7
16. Yamada, Y.; Furukawa, K.; Sodeyama, K.; Kikuchi, K.; Yaegashi, M.; Tateyama, Y.; Yamada, A. *J Am Chem Soc* **2014**, *136* (13), 5039-46. DOI: 10.1021/ja412807w
17. Nilsson, V.; Younesi, R.; Brandell, D.; Edström, K.; Johansson, P. *Journal of Power Sources* **2018**, *384*, 334-341. DOI: <https://doi.org/10.1016/j.jpowsour.2018.03.019>
18. Matsumoto, K.; Inoue, K.; Nakahara, K.; Yuge, R.; Noguchi, T.; Utsugi, K. *Journal of Power Sources* **2013**, *231*, 234-238. DOI: <https://doi.org/10.1016/j.jpowsour.2012.12.028>
19. McOwen, D. W.; Seo, D. M.; Borodin, O.; Vatamanu, J.; Boyle, P. D.; Henderson, W. A. *Energy & Environmental Science* **2014**, *7* (1), 416-426. DOI: 10.1039/C3EE42351D

20. Patra, J.; Huang, H.-T.; Xue, W.; Wang, C.; Helal, A. S.; Li, J.; Chang, J.-K. *Energy Storage Materials* **2019**, *16*, 146-154. DOI: <https://doi.org/10.1016/j.ensm.2018.04.022>
21. Li, K.; Subasinghege Don, V.; Gupta, C. S.; David, R.; Kumar, R. *The Journal of Chemical Physics* **2021**, *154* (18), 184505. DOI: 10.1063/5.0046073
22. Monti, D.; Jónsson, E.; Boschin, A.; Palacín, M. R.; Ponrouch, A.; Johansson, P. *Physical Chemistry Chemical Physics* **2020**, *22* (39), 22768-22777. DOI: 10.1039/D0CP03639K
23. Wang, Y.; Jiang, R.; Liu, Y.; Zheng, H.; Fang, W.; Liang, X.; Sun, Y.; Zhou, R.; Xiang, H. *ACS Applied Energy Materials* **2021**, *4* (7), 7376-7384. DOI: 10.1021/acsaem.1c01573
24. Geng, C.; Buchholz, D.; Kim, G.-T.; Carvalho, D. V.; Zhang, H.; Chagas, L. G.; Passerini, S. *Small Methods* **2019**, *3* (4), 1800208. DOI: <https://doi.org/10.1002/smt.201800208>
25. He, M.; Lau, K. C.; Ren, X.; Xiao, N.; McCulloch, W. D.; Curtiss, L. A.; Wu, Y. *Angew. Chem. Int. Ed.* **2016**, *55*, 15310-15314. DOI: 10.1002/anie.201608607
26. Ugata, Y.; Tatara, R.; Ueno, K.; Dokko, K.; Watanabe, M. *J Chem Phys* **2020**, *152* (10), 104502. DOI: 10.1063/1.5145340
27. Zhang, J.; Wang, F.; Cao, Z.; Wang, Q. *The Journal of Physical Chemistry B* **2021**, *125* (47), 13041-13048. DOI: 10.1021/acs.jpcc.1c08431
28. Kuratani, K.; Uemura, N.; Senoh, H.; Takeshita, H. T.; Kiyobayashi, T. *Journal of Power Sources* **2013**, *223*, 175-182. DOI: <https://doi.org/10.1016/j.jpowsour.2012.09.039>
29. Okoshi, M.; Yamada, Y.; Yamada, A.; Nakai, H. *Journal of The Electrochemical Society* **2013**, *160* (11), A2160-A2165. DOI: 10.1149/2.074311jes
30. Lencka, M. M.; Anderko, A.; Sanders, S. J.; Young, R. D. *International Journal of Thermophysics* **1998**, *19* (2), 367-378. DOI: 10.1023/A:1022501108317
31. Yim, C.-H.; Tam, J.; Soboleski, H.; Abu-Lebdeh, Y. *Journal of The Electrochemical Society* **2017**, *164* (6), A1002-A1011. DOI: 10.1149/2.1601704jes
32. Yim, C.-H.; Abu-Lebdeh, Y. A. *Journal of The Electrochemical Society* **2018**, *165* (3), A547-A556. DOI: 10.1149/2.0641803jes
33. Ugata, Y.; Thomas, M. L.; Mandai, T.; Watanabe, M. *Physical Chemistry Chemical Physics* **2019**, *21*, 9759-9768.
34. Rohan, R.; Kuo, T.-C.; Lin, J.-H.; Hsu, Y.-C.; Li, C.-C.; Lee, J.-T. *The Journal of Physical Chemistry C* **2016**, *120* (12), 6450-6458. DOI: 10.1021/acs.jpcc.6b00980
35. Kim, J.; Lim, H. D.; Gwon, H.; Kang, K. *Phys. Chem. Chem. Phys.* **2013**, *15* (10), 3623-3629. DOI: 10.1039/c3cp43225d
36. Schwenke, K. U.; Meini, S.; Wu, X.; Gasteiger, H. A.; Piana, M. *Phys. Chem. Chem. Phys.* **2013**, *15* (28), 11830-9. DOI: 10.1039/c3cp51531a
37. Liu, T.; Kim, G.; Casford, M. T.; Grey, C. P. *J. Phys. Chem. Lett.* **2016**, *7* (23), 4841-4846. DOI: 10.1021/acs.jpcclett.6b02267
38. Hartmann, P.; Bender, C. L.; Vracar, M.; Durr, A. K.; Garsuch, A.; Janek, J.; Adelhalm, P. *Nature Materials* **2013**, *12* (3), 228-232. DOI: 10.1038/nmat3486
39. Zhao, N.; Li, C.; Guo, X. *Phys. Chem. Chem. Phys.* **2014**, *16* (29), 15646-15652. DOI: 10.1039/c4cp01961j
40. Reeve, Z. E.; Franko, C. J.; Harris, K. J.; Yadegari, H.; Sun, X.; Goward, G. R. *J. Am. Chem. Soc.* **2017**, *139* (2), 595-598. DOI: 10.1021/jacs.6b11333
41. Yadegari, H.; Franko, C. J.; Banis, M. N.; Sun, Q.; Li, R.; Goward, G. R.; Sun, X. *J. Phys. Chem. Lett.* **2017**, *8* (19), 4794-4800. DOI: 10.1021/acs.jpcclett.7b02227

42. Xia, C.; Fernandes, R.; Cho, F. H.; Sudhakar, N.; Buonacorsi, B.; Walker, S.; Xu, M.; Baugh, J.; Nazar, L. F. *J. Am. Chem. Soc.* **2016**, *138* (35), 11219-11226. DOI: 10.1021/jacs.6b05382
43. Lindberg, J.; Endrődi, B.; Ávall, G.; Johansson, P.; Cornell, A.; Lindbergh, G. *The Journal of Physical Chemistry C* **2018**, *122* (4), 1913-1920. DOI: 10.1021/acs.jpcc.7b09218
44. Hatchard, T. D.; Obrovac, M. N. *Journal of The Electrochemical Society* **2014**, *161* (10), A1748-A1752. DOI: 10.1149/2.1131410jes
45. Oldiges, K.; von Aspern, N.; Cekic-Laskovic, I.; Winter, M.; Brunklaus, G. *Journal of The Electrochemical Society* **2018**, *165* (16), A3773-A3781. DOI: 10.1149/2.0461816jes
46. Yan, G.; Mariyappan, S.; Rousse, G.; Jacquet, Q.; Deschamps, M.; David, R.; Mirvaux, B.; Freeland, J. W.; Tarascon, J. M. *Nat Commun* **2019**, *10* (1), 585. DOI: 10.1038/s41467-019-08359-y
47. Ehteshami, N.; Ibing, L.; Stolz, L.; Winter, M.; Paillard, E. *Journal of Power Sources* **2020**, *451*, DOI: 10.1016/j.jpowsour.2020.227804
48. Andersson, R.; Årén, F.; Franco, A. A.; Johansson, P. *Journal of Computational Chemistry* **2021**, *42* (23), 1632-1642. DOI: <https://doi.org/10.1002/jcc.26699>

## 7 – Outlook

In this work, cathode and electrolyte materials for sodium and lithium battery systems were investigated for their physical and electrochemical properties. A summary of the main impacts of each study is given in this chapter.

### 7.1 – Conclusions

The motivation for the research presented in this thesis was to examine novel, oxidatively stable, cathode and electrolyte materials for use in sodium battery systems. This was inspired by observations of the highly oxidative environments encountered in the sodium oxygen battery (NaOB).

In **Chapter 3**, the issue of oxidative instability of carbon cathodes in the NaOB system was identified. The electrochemical discharge slurry of the NaOB were characterized by solid-state nuclear magnetic resonance (ssNMR) for the first time.  $^{23}\text{Na}$  ssNMR identified sodium carbonate ( $\text{Na}_2\text{CO}_3$ ) and sodium fluoride (NaF) as the primary degradation products in discharged carbon black (CB) / polyvinylidene fluoride (PVDF) composite cathodes, while no sodium superoxide ( $\text{NaO}_2$ ) was detected. In subsequent reactivity experiments,  $^{23}\text{Na}$  and  $^{19}\text{F}$  ssNMR were used to show that  $\text{Na}_2\text{CO}_3$  and NaF are produced in NaOBs by  $\text{NaO}_2$  oxidation of CB and PVDF. In an attempt to mitigate  $\text{NaO}_2$  degradation, PVDF-free surface-modified carbon-cloth (CC) cathodes were employed in a subsequent study. Hydrophobic and hydrophilic CC cathode analogues were produced. Analysis of the discharge product morphology by scanning electron microscopy (SEM) showed that the hydrophobic cathodes select for a solution-mediated discharge process, while the hydrophilic cathodes select for a surface-mediated discharge process.  $^{23}\text{Na}$  ssNMR was able to

characterize  $\text{NaO}_2$  production for the first time in the hydrophobic cathode, but ultimately was observed to decay into  $\text{Na}_2\text{CO}_3$  overtime. In contrast, no  $\text{NaO}_2$  was observed by  $^{23}\text{Na}$  ssNMR on the hydrophilic cathode, with  $\text{Na}_2\text{CO}_3$  being the primary discharge product.

**Chapter 4** addressed the issue of carbon cathode instability that was identified in **Chapter 3**.  $\text{Ti}_4\text{O}_7$  was shown to be stable toward  $\text{NaO}_2$ , and was subsequently investigated as a coating material for carbon paper cathodes in NaOBs.  $\text{Ti}_4\text{O}_7$ -coated carbon paper cathodes were found to significantly increase cell lifetimes, when compared to carbon-coated analogues.  $^{23}\text{Na}$  ssNMR of discharged cathodes was able to identify  $\text{NaO}_2$ , and the product was found to be significantly more stable in the  $\text{Ti}_4\text{O}_7$ -coated cathodes. Lifetime cycled cathodes were examined by the  $^1\text{H}$  to  $^{23}\text{Na}$  dipolar heteronuclear multiple quantum correlation ( $^{23}\text{Na}\{^1\text{H}\}$  D-HMQC) and  $^{23}\text{Na}$  triple quantum magic angle spinning (3QMAS) experiments, which showed that  $\text{Na}_2\text{CO}_3$  and  $\text{NaHCO}_2$  are the primary degradation products in both the  $\text{Ti}_4\text{O}_7$ -coated and carbon-coated cells. This result implies that the eventual mechanism of cell death is the decay of the carbon support in both systems. It is proposed that the carbon paper substrate is oxidized by  $\text{NaO}_2$  to produce  $\text{Na}_2\text{CO}_3$  and  $\text{NaHCO}_2$ , but the oxidation process is significantly slowed in  $\text{Ti}_4\text{O}_7$ -coated cathodes, due to the increased stability of  $\text{Ti}_4\text{O}_7$  toward  $\text{NaO}_2$ , leading to the observed longer cell lifetimes in the  $\text{Ti}_4\text{O}_7$ -coated system.

In **Chapter 5**, the oxidatively stable lithium bis(trifluoromethanesulfonyl)imide (LiTFSI) in adiponitrile (ADN) electrolyte system is examined. A relationship between the eutectic point and concentration of maximum ionic conductivity of the electrolyte was observed, suggesting that ion transport is influenced by solution

structure. Pulsed field gradient (PFG) NMR was used to measure the diffusion coefficients of  $\text{Li}^+$ , TFSI, and ADN within the electrolyte, and it was found that there is a shift from a vehicular transport mechanism to an ion-hopping transport mechanism at high concentrations. Variable diffusion time ( $\Delta$ ) PFG NMR diffusion coefficient measurements were used to probe the solution structure of the electrolyte further, and found that the diffusion on the micro- and bulk-scales is increasingly heterogenous as concentration increases, which is theorized to be the result of an increasing proportion of  $[\text{Li}_x(\text{ADN})_y\text{TFSI}_z]^{x-z}$  aggregates that slow vehicular diffusion on bulk length-scales, but facilitate ion-hopping transport at short length-scales. The electrolyte is also found to be extremely oxidation resistant through cyclic voltammetry (CV) experiments.

In **Chapter 6**, the physical and electrochemical properties of the NaTFSI in ADN system were explored as a function of concentration. Molecular dynamics simulations show that Na and ADN are arranged in a network-like structure, but the weak interactions of  $\text{Na}^+$  with TFSI inhibit the formation of a distinct ordered solution structure. The reductive stability of ADN to Na metal was found to significantly improve as concentration increases, leading to more reversible Na plating and stripping in CV experiments. Similarly, Al corrosion by the TFSI anion was found to be suppressed at high concentrations in linear sweep voltammetry (LSV) and chronoamperometry (CA) experiments. The consequences of these effects were tested in  $\text{Na}_{(s)} \parallel \text{Na}_3\text{V}_2(\text{PO}_4)_2\text{F}_3$  (NVPF) half-cells employing both standard 1 M, and highly concentrated 4.4 M, electrolytes. It is found that the 1 M cell facilitates no observable NVPF intercalation chemistry, while the 4.4 M cell is able reversibly intercalate the NVPF cathode for several cycles. Lastly, in CV experiments of NaOB coin cells, high

concentration NaTFSI in ADN was found to undergo reversible oxygen reduction and evolution reactions, showing its utility as an oxidatively stable NaOB electrolyte.

## 7.2 – Future Work

As discussed in the experimental section, **Chapter 6** was originally planned to include a  $^{23}\text{Na}$  PFG NMR study on the NaTFSI in ADN electrolytes, similar to what was conducted on LiTFSI in ADN in **Chapter 5**. However, the  $T_2$  and  $T_1$  relaxation times of the  $^{23}\text{Na}$  nucleus of NaTFSI in ADN were found to be too short for proper diffusional analysis. Other electrolyte systems, such as the sodium trifluoromethanesulfonate (NaOTF) in diethylene glycol dimethyl ether (DEGDME) electrolyte used for NaOB battery studies in this thesis, can be examined to see if their relaxation properties are more amiable to PFG NMR experiments. If so, the variable diffusion time diffusional analysis can be applied to Na electrolytes for the first time.

Further, the electrochemical properties of the NaTFSI in ADN electrolyte can likely be improved upon through the addition of co-solvents such as ethylene carbonate (EC), or additives such as fluoroethylene carbonate (FEC). Both EC and FEC have been shown in literature to stabilize LiTFSI in ADN systems in LIBs,<sup>1,2</sup> but have not been applied to the Na analogue as of yet. Electrochemical studies similar to those presented in **Chapter 6** can be implemented to see if the performance of NaTFSI in ADN can be improved further by co-solvent or additive addition. Particularly, the effect of EC additives on the electrochemical impedance spectroscopy (EIS) data should be examined, as EIS is adept at identifying cell SEI layer formation.<sup>3</sup>

For the Li-analogue, PFG NMR experiments can be used to see how the addition of co-solvents, such as EC, affects the diffusional properties of the electrolyte. In

particular, variable diffusion time experiments can be used to examine if the same evolution of  $\text{Li}^+$  transport mechanism as a function of concentration is observed when co-solvents or additives are added to the electrolyte mixture.

The NaOB needs a significant amount of further development before it can be considered a viable commercial energy storage system. Although **Chapter 4** showed significant stabilization of  $\text{NaO}_2$ , carbon decay was still observed overtime. A natural next step is to try and remove carbon from the system entirely. This has been explored with  $\text{Ti}_4\text{O}_7$  in the lithium oxygen battery (LiOB) system previously by Lee et al., where synthesized  $\text{Ti}_4\text{O}_7$  nanospheres were found to have significant oxygen reduction reaction (ORR) activity without the need of any additional carbon or catalyst material.<sup>4</sup> In **Chapter 4**,  $\text{Ti}_4\text{O}_7$  was found to have negligible capacity in the NaOB, but a high surface area nanosphere material may yield different results. The material could first be deposited on carbon paper substrates, for direct comparison with the cathodes manufactured in **Chapter 4**, as well as on Ni-foam substrates, which would allow for a carbon-free system. For better compatibility with ssNMR techniques, glass fibre substrates could also be employed, but would require relatively large  $\text{Ti}_4\text{O}_7$  active masses to create a sufficiently conductive cathode system.

Another avenue for NaOB research is to attempt to synthesize sodium peroxide dihydrate ( $\text{Na}_2\text{O}_2 \cdot 2\text{H}_2\text{O}$ ) for characterization by ssNMR.  $\text{Na}_2\text{O}_2 \cdot 2\text{H}_2\text{O}$  has been commonly reported as a discharge product in NaOBs, however, the product has never been observed via NMR.  $\text{Na}_2\text{O}_2 \cdot 2\text{H}_2\text{O}$  was attempted to be synthesized by the author previously, but was never successful. The synthesis of  $\text{Na}_2\text{O}_2 \cdot 2\text{H}_2\text{O}$  first involves the synthesis of the octahydrate,  $\text{Na}_2\text{O}_2 \cdot 8\text{H}_2\text{O}$ , which needs to be dried over phosphorus pentoxide ( $\text{P}_2\text{O}_5$ ) in a vacuum desiccator to produce the dihydrate product.

Characterization of  $\text{Na}_2\text{O}_2 \cdot 2\text{H}_2\text{O}$  by ssNMR would allow for a further application of the  $^{23}\text{Na}\{^1\text{H}\}$  D-HMQC experiment, and could give insight into the environments that select for its formation.

Lastly, the two streams of this thesis can be combined through the parallel use of oxidatively stable  $\text{Ti}_4\text{O}_7$  cathodes and oxidatively stable NaTFSI in ADN electrolytes in NaOBs. A brief examination of NaOBs implementing NaTFSI in ADN is given in **Chapter 6**, but a thorough examination of the discharge chemistry using ssNMR is still needed. NaTFSI has been used in NaOBs previously, but, when paired with dimethyl ether, was shown to form parasitic solid electrolyte interfaces (SEIs) at the Na-metal anode, causing rapid cell death.<sup>5</sup> However, a separate study showed that high concentration NaTFSI in dimethyl sulfoxide (DMSO) solvent was able to undergo a reversible ORR for many cycles.<sup>6</sup> The strategy of concentrating NaTFSI electrolytes may prove fruitful in the NaOB system. Clearly, there is more room for the examination of concentrated electrolytes in the NaOB, and the high oxidative stability of the NaTFSI in ADN system makes it a promising candidate.

### 7.3 – References

1. Abu-Lebdeh, Y.; Davidson, I. *Journal of The Electrochemical Society* **2009**, *156* (1), A60-A65. DOI: 10.1149/1.3023084
2. Ehteshami, N.; Paillard, E. *ECS Transactions* **2017**, *77* (1), 11-20. DOI: 10.1149/07701.0011ecst
3. Zhang, S. S.; Xu, K.; Jow, T. R. *Electrochimica Acta* **2006**, *51* (8), 1636-1640. DOI: <https://doi.org/10.1016/j.electacta.2005.02.137>
4. Lee, S.; Lee, G.-H.; Kim, J.-C.; Kim, D.-W. *ACS Catalysis* **2018**, *8* (3), 2601-2610. DOI: 10.1021/acscatal.7b03741
5. Lutz, L.; Alves Dalla Corte, D.; Tang, M.; Salager, E.; Deschamps, M.; Grimaud, A.; Johnson, L.; Bruce, P. G.; Tarascon, J.-M. *Chemistry of Materials* **2017**, *29* (14), 6066-6075. DOI: 10.1021/acs.chemmater.7b01953
6. He, M.; Lau, K. C.; Ren, X.; Xiao, N.; McCulloch, W. D.; Curtiss, L. A.; Wu, Y. *Angew. Chem. Int. Ed.* **2016**, *55*, 15310-15314. DOI: 10.1002/anie.201608607